
Characterization of extended emission from groups and clusters of galaxies

Florian Moritz Käfer



München 2020

Characterization of extended emission from groups and clusters of galaxies

Florian Moritz Käfer

Dissertation
an der Fakultät für Physik
der Ludwig–Maximilians–Universität
München

vorgelegt von
Florian Moritz Käfer
aus Andernach, Deutschland

München, den 12. August 2020

Erstgutachter: Prof. Dr. Kirpal Nandra

Zweitgutachter: Prof. Dr. Jochen Weller

Tag der mündlichen Prüfung: 3. November 2020

Contents

Zusammenfassung	xix
Abstract	xxi
1 Introduction	1
1.1 Prelude	1
1.2 Cosmological model	2
1.3 Structure formation	5
1.3.1 Linear growth of density perturbations	7
1.3.2 Spherical collapse	7
1.3.3 Halo mass function	8
1.4 Clusters and groups of galaxies	10
1.4.1 Composition	11
1.4.2 Emission mechanisms	13
1.4.3 Galaxy cluster profiles	15
1.4.4 Mass determination	16
1.4.5 Self-similar model	19
1.4.6 Scaling relations	21
1.5 Galaxy clusters as cosmological probes	22
1.6 X-ray observatories	25
1.6.1 The ROSAT telescope	25
1.6.2 The eROSITA telescope	26
1.7 Structure detection in X-ray images	28
1.7.1 Sliding cell	28
1.7.2 Wavelet transform	29
1.7.3 Wavelet decomposition	30
2 Toward a characterization of X-ray galaxy clusters for cosmology	33
2.1 Data	35
2.1.1 The sample	35
2.1.2 Data analysis	35
2.1.3 Masses	36
2.2 Analysis	36

2.2.1	Surface brightness profiles	36
2.2.2	Point-spread function	38
2.2.3	Emission measure profiles	38
2.2.4	Scaling relations	39
2.2.5	Cool-core classification	41
2.3	Emission measure profiles	42
2.4	Large-scale center and ellipticity	43
2.5	Analysis of the residuals	47
2.5.1	Discussion: Single β -models	48
2.5.2	Discussion: Core-modeled single β -models	48
2.5.3	Flux comparison	49
2.6	Scaling relations	49
2.7	Summary	55
3	Toward the low-scatter selection of X-ray clusters: Galaxy cluster detection with eROSITA through cluster outskirts	57
3.1	eROSITA and the eROSITA simulator	58
3.1.1	Point-spread function	58
3.1.2	Point sources and background components	59
3.1.3	Extended objects	59
3.1.4	X-ray telescope simulator	59
3.1.5	eROSITA mission planning and survey fields	60
3.2	Source detection and characterization	60
3.2.1	Wavelet decomposition method	61
3.2.2	Adjusting the detection pipeline to eROSITA	63
3.3	Selection criteria	64
3.4	Theoretical predictions	65
3.5	Simulated field	67
3.5.1	Selection function of extended sources	74
3.5.2	Selection	76
3.6	Summary and conclusions	77
4	Future prospects	87
4.1	Measurement of the core-excised luminosity in the eROSITA cluster survey	87
4.1.1	Method	88
4.1.2	Validation of the method	91
4.2	Scaling relations of galaxy groups	96
4.3	Probing the link between the scatter of galaxy cluster characteristics and the mass accretion history	97
5	Brief summary	99

A	Appendix for the characterization of X-ray galaxy clusters	101
A.1	Mass comparison	101
A.2	Priors	103
A.3	HIFLUGCS parameters	103
A.4	HIFLUGCS images and surface brightness profiles	106
	Acknowledgements	150

List of Figures

- 1.1 The galaxy distribution obtained from spectroscopic redshift surveys and from mock catalogues constructed from cosmological simulations. The small slice at the top shows the CfA2 "Great Wall" (Geller and Huchra, 1989), with the Coma cluster at the centre. Drawn to the same scale is a small section of the SDSS, in which an even larger "Sloan Great Wall" has been identified (Gott et al., 2005). This is one of the largest observed structures in the Universe, containing over 10 000 galaxies and stretching over more than 1.37 billion light years. The wedge on the left shows one-half of the 2dFGRS, which determined distances to more than 220 000 galaxies in the southern sky out to a depth of 2 billion light years. The SDSS has a similar depth but a larger solid angle and currently includes over 650 000 observed redshifts in the northern sky. At the bottom and on the right, mock galaxy surveys constructed using semi-analytic techniques to simulate the formation and evolution of galaxies within the evolving dark matter distribution of the "Millennium" simulation (Springel et al., 2005) are shown, selected with matching survey geometries and magnitude limits. Figure and caption taken from Springel et al. (2006). 6
- 1.2 The halo mass function derived from dark-matter-only N-body simulations (DMonly) and hydrodynamical simulations which include baryons (Hydro). The mass function is measured at several redshift slices of the Magneticum simulations, with the lines representing the best-fit functions. The redshift decreases from bottom to top, meaning more and more massive halos are forming with time. Figure taken from Bocquet et al. (2016). 8
- 1.3 Multi-wavelength observations of the "Toothbrush Cluster". Galaxies and stars (upper left) are observed in the optical with the Subaru telescope. The radio (lower left) and X-ray emission (upper right) trace the highly relativistic electrons and the hot ICM, respectively. The gravitational-lensing map (lower right) represents the mass concentration, which is primarily dark matter. The composite image in the center demonstrates that the emission at different wavelengths originates from different populations. Figures taken from <https://chandra.cfa.harvard.edu/photo/2016/archives/>. 12

- 1.4 Expected X-ray emission spectra of a hot and optically-thin plasma for three temperatures of 1 keV (black), 3 keV (red), and 9 keV (green). The continuum emission from thermal bremsstrahlung is the dominant component and shifts to higher photon energies for hotter gas. Toward lower temperatures atomic transitions and recombination radiation become more important, which makes line features, for example the Fe-L and Fe-K complex at approximately 1 keV and 6.8 keV, more prominent. Figure taken from [Reiprich et al. \(2013\)](#). 14
- 1.5 The undistorted (dashed line) CMB spectrum gets distorted when CMB photons pass through the ICM of a galaxy cluster, causing a decrement in the CMB intensity at frequencies below approximately 217 GHz and an intensity increase above this frequency. Therefore, galaxy clusters appear as a negative signal (blue) in the low frequency bands and as a positive signal (red) at higher frequencies compared to the average CMB signal (lower panel). This makes it easier to differentiate the detected clusters at low frequencies from radio-emitting galaxies, which appear as positive "hot spots" in the low and the high passbands. The upper right panel shows the relative spectral distortion. Figures taken from [Carlstrom et al. \(2002\)](#) and <http://sci.esa.int/jump.cfm?oid=47697>. 20
- 1.6 Joint 68.3% and 95.4% credibility regions for different cosmological probes and two sets of cosmological parameters (Ω_m, σ_8) and (Ω_m, w_0). The left panel shows the comparison between constrains of the mean-matter density Ω_m and the amplitude of matter perturbations σ_8 obtained from cluster counts and observations of the CMB power spectrum with the two instruments WMAP and *Planck*. The right panel shows the credibility regions for Ω_m and the dark energy equation of state w_0 from galaxy cluster data and other cosmological probes. In general, the shape and orientation of the credibility regions indicate the degeneracy level between the individual parameters, for example the strong degeneracy between Ω_m and σ_8 for cluster observations. Figures taken from [Mantz et al. \(2015\)](#). . . . 23
- 1.7 Schematic image of the ROSAT telescope. The dashed lines represent X-ray photons entering from the left. The X-rays are focused onto the focal plane assembly through a double reflection on the four nested parabola/hyperbola mirror pairs. Figure taken from <https://projects.mpe.mpg.de/heg/rosat/mission/rosat/payload.html>. 26
- 1.8 Schematic diagram of the eROSITA telescope structure (left panel) and the adaptively smoothed, exposure-corrected image of the interacting galaxy clusters Abel 3391 and Abel 3395. The observation was a target during eROSITA's performance-verification phase and the detection of the filament in between the two clusters demonstrates eROSITA's tremendous capabilities in the soft X-ray regime. Figures taken from [Merloni et al. \(2012\)](#) and <https://www.mpe.mpg.de/7360702/presskit-erosita-firstlight>. 27
- 1.9 Contiguous significant wavelet coefficients for differently-sized features. If features at two successive scales reside within a linking radius, they are considered to belong to the same object. Figure taken from [Starck and Murtagh \(2006\)](#). . . . 29

1.10	A comparison between a simple wavelet analysis (upper right panel) and a wavelet decomposition method (lower left panel) in the case of a bright point source in the vicinity of an extended source (upper left panel). The brightness profiles are extracted within the dashed strip. The point source dominates on all wavelet planes (solid lines) when using a simple wavelet convolution and the two objects will be detected as a single extended source, which might result in a false cluster detection. The wavelet decomposition method separates the point-source emission on small scales from the emission of the extended source on larger scales. Summing up the three smallest and largest scales individually allows for a decomposition of the image into the two components (lower right panel). Figure taken from Vikhlinin et al. (1998)	31
2.1	Surface brightness (left panel) and self-similar scaled emission measure profiles (right panel) for HIFLUGCS objects with temperatures greater than 3 keV. Strong-cool-core, weak-cool-core, and non-cool-core clusters are labeled as SCC, WCC, and NCC, respectively.	42
2.2	Top panels: Weighted mean (left panel) and median (right panel) self-similar scaled emission measure profiles for the individual core types of HIFLUGCS objects with temperatures greater than 3 keV. Bottom panels: Ratio of the self-similar scaled emission measure profiles between the different core type populations. Shown error bars were estimated with 10 000 bootstrapping iterations. The shaded regions represent the intrinsic scatter values of each bin.	44
2.3	Ellipticity as a function of central cooling time of HIFLUGCS objects with temperatures greater than 3 keV. Vertical dashed lines indicate cooling times corresponding to the cool-core classification.	46
2.4	Same as Fig. 2.2, except that the classification is done according to ellipticity.	47
2.5	Median of the fractional residuals from a single β -model (left panels) and a core-modeled single β -model (right panels) in $0.2\text{--}0.5 r_{500}$ radial bins for individual HIFLUGCS objects above a temperature of 3 keV as function of core radius. For the bottom panels the β parameter is fixed to $2/3$ in the surface brightness parameter optimization.	50
2.6	Core radius as a function of temperature for a single β -model (left panel) and core-modeled (right panel) single β -model. The dashed lines and shaded regions represent the medians and their intrinsic scatter of the individual core populations.	51
2.7	Scaling relations between single β -model (left panels) and core-modeled single β -model (right panels) parameters and temperature. The HIFLUGCS clusters with temperatures greater than 3 keV (black points) are used for optimization. Red points mark HIFLUGCS objects below this temperature threshold for visualization. The orange lines and shaded regions show the best-fit relations and their uncertainties, respectively. The blue dashed lines correspond to the intrinsic log-normal scatter.	53

2.8	Single β -model (left panels) and core-modeled single β -model (right panels) parameters as a function of luminosity. The HIFLUGCS clusters with temperatures greater than and below 3 keV are marked as black and red points, respectively.	54
3.1	Galaxy cluster flux limit as a function of redshift for an equatorial, an intermediate, and a deep final eROSITA survey field of approximately 1 ks, 2.5 ks, and 6 ks exposure, respectively. The black solid and black dashed lines show the flux limits corresponding to 40 and 80 counts in the detection region of 1–4' and 1–16' radial scale, respectively.	68
3.2	Same as Fig. 3.1 for the galaxy cluster luminosity limit.	69
3.3	Same as Fig. 3.1 for the galaxy cluster mass limit. The brown solid and brown dashed lines represent the associated overdensity radii (right-hand y-axes).	70
3.4	Galaxy cluster core radius limit as a function of flux for an equatorial, an intermediate, and a deep final eROSITA survey field of approximately 1 ks, 2.5 ks, and 6 ks exposure, respectively. The black solid and black dashed lines show the core radius limits of a 3 keV cluster corresponding to 40 and 80 β -model counts on a 1–4' and 1–16' radial scale, respectively.	71
3.5	Galaxy cluster total count limit as a function of redshift. The black solid and black dashed lines show the total count limit, corresponding to 40 and 80 β -model counts on a 1–4' and 1–16' radial scale.	72
3.6	Differential number of galaxy clusters per square degree as a function of redshift for the three final eROSITA survey fields and the two considered radial scales.	73
3.7	Extended source detection efficiency of our maximally clean (7σ threshold, black contours), our 5σ threshold (brown contour), and the Clerc et al. (2018) threshold (blue contours) in the core radius vs. input flux plain for an equatorial eROSITA survey field of approximately 1 ks exposure.	78
3.8	Maximally clean (7σ) extended source detection efficiency (black contours) in the mass vs. redshift plain for an equatorial eROSITA survey field of approximately 1 ks exposure.	79
3.9	Detection efficiency as a function of input flux for four core radii bins of the 5σ (upper panel) and 7σ (lower panel) detection thresholds. Lines correspond to the model expectation of Eq. 3.8 for core radii of 25'', 50'', 85'', and 150.	80
3.10	Expected differential number of galaxy clusters per square degree as a function of redshift for the final equatorial eROSITA survey field with different selection functions folded in. The solid line serves as comparison and show the 40 aperture count selection on the 1–4' scale of Fig. 3.6.	81
3.11	Detection efficiency as a function of predicted model counts on the 1–4' (upper panel) and 1–16' (lower panel) radial scale for four core radius bins. The dotted vertical lines correspond to 40 and 80 aperture counts, respectively.	82

3.12	Predicted model counts for a 10%, 50%, and 90% detection efficiency as a function of core radius on the 1–4′ (upper panel) and 1–16′ (lower panel) radial scale. The brown values indicate the ratio of the model counts in the 0–1′ and the corresponding angular scale of the individual core radius bin. The dotted horizontal lines correspond to 40 and 80 aperture counts, respectively.	83
3.13	Number density of spurious and misclassified extended sources as a function of detection threshold for an eROSITA survey exposure of approximately 1 ks. . . .	84
3.14	Detection efficiency of extended sources as a function of detection threshold for snapshots in redshift and mass for an eROSITA survey exposure of approximately 1 ks.	85
4.1	Illustrative flow chart to reconstruct the galaxy cluster mass using an MCMC posterior sampling technique with a Poisson likelihood to compare the measured aperture photon counts to the β -model predictions for a given mass estimate. . .	89
4.2	Reconstructed over input mass ratio as a function of central emissivity. The panels correspond to the four discussed extraction regions ([1]–[4]) as summarized in Table 4.1. Data points are gray-scale-coded by their ellipticity. The orange lines and the shaded regions correspond to the median values of the mass ratios and their intrinsic 1σ scatter values.	93
4.3	Reconstructed over input mass ratio as a function of input mass for the non-fixed 0.2–0.5 r_{500} extraction region. Data points are logarithmically gray-scale-coded by their redshift. The orange line and the shaded region correspond to the median value of the mass ratio and its intrinsic 1σ scatter value.	94
4.4	Reconstruction (orange curve) of the true cluster image (blue curve) from a Poisson realization (black points) of the PSF-convolved image (red curve). The ratio between reconstructed and input profile is shown in the bottom panel. Figure taken from Eckert et al. (2020)	96
4.5	Reconstructed core-excised luminosity as a function of input core-excised luminosity (left panel), as well as reconstructed mass as a function of input mass (right panel). The number of reconstructed photon counts is shown as a color code. The solid lines and shaded regions represent the best-fit linear relation and their intrinsic scatter. The dashed line shows the one-to-one relation. Figures taken from Eckert et al. (2020)	97
A.1	Comparison between <i>Planck</i> and hydrostatic mass estimates of HIFLUGCS objects with temperatures greater than 3 keV.	102

A.2	Left panels: ROSAT count rate images for individual galaxy clusters. The large-scale centers are shown as green plus signs. Red contours correspond to wavelet scales used for background modeling. The large scales (the ones above $0.2 r_{500}$) are shown as blue contours. These large scales are used to calculate the center and ellipticities. The extracted SExtractor ellipses are displayed in dashed green. Each box size corresponds to the outer significance radius of the shown cluster. Right panels: The top panels show the measured (black points) surface brightness profiles of individual galaxy clusters. The background models used for the single β -model fits (solid blue lines) are shown as red points. The bottom panels show the residuals of the core-modelled single β -model fits.	106
A.2	Continued.	107
A.2	Continued.	108
A.2	Continued.	109
A.2	Continued.	110
A.2	Continued.	111
A.2	Continued.	112
A.2	Continued.	113
A.2	Continued.	114
A.2	Continued.	115
A.2	Continued.	116
A.2	Continued.	117
A.2	Continued.	118
A.2	Continued.	119
A.2	Continued.	120
A.2	Continued.	121
A.2	Continued.	122
A.2	Continued.	123
A.2	Continued.	124
A.2	Continued.	125
A.2	Continued.	126
A.2	Continued.	127

List of Tables

2.1	Parameters from single β -model and core-modelled single β -model fits to the y -temperature scaling relations. Listed are the slopes, m , normalizations, b , and intrinsic scatter values, λ_y	52
2.2	Correlation coefficients between different galaxy cluster parameters from single β -model and core-modelled single β -model fits. Listed are the correlation coefficient values, λ_{xy} , between the parameters x and y	52
3.1	Best-fit parameters of the analytic selection function (Eq. 3.8) for the 5σ and 7σ detection thresholds.	76
4.1	Overview of the chosen extraction regions and the corresponding redshift ranges for the four cases of aperture definitions. The last two columns show the median mass ratios between reconstructed and input masses \tilde{M}_{ratio} as well as the corresponding intrinsic scatter values $\lambda_{\tilde{M}}$	92
A.1	List of parameters and their priors. We note that the prior of the scaling relation slope is assumed to be uniform in $\sin(\Theta)$ (VanderPlas, 2016), with Θ being the angle between the best-fit line and the x -axis. The term "pos-normal" refers to a probability distribution that follows an ordinary normal distribution but is set to zero for negative parameter values, meaning that the parameter is restricted to be positive.	103

A.2	Galaxy cluster parameters. Column (1) gives the cluster name. Columns (2) and (3) list the equatorial coordinates of the cluster center in decimal degrees based on the large-scale wavelet image. Column (4) gives the offset to an iteratively determined two-dimensional 'center of mass' using an aperture radius of 3' (Reiprich and Böhringer, 2002). Column (5) and (6) list the cluster redshift (Reiprich and Böhringer, 2002) and core-excised temperature (Hudson et al., 2010), respectively. Column (7) and (8) give the β -model slope and core radius for a core-modeled fit. Column (9) lists the luminosity in the 0.1–2.4 keV energy range. The cool-core classification according to Hudson et al. (2010) is given in column (10). Column (11) lists the characteristic radius where the density corresponds to 500 times the critical density at the cluster redshift. Galaxy clusters, whose r_{500} value is marked with a † do not have SZ mass estimates (Planck Collaboration et al., 2016) and the Schellenberger and Reiprich (2017) mass estimate is used to determine the wavelet small scales. These clusters are excluded from further analysis steps which comprise characteristic radii. Column (12) gives the measured large scale ellipticity. The physical to angular scale conversion at the cluster redshift is given in column (13).	104
A.2	Continued.	105

Acronyms

ACIS	Advanced CCD Imaging Spectrometer
AGN	Active Galactic Nuclei
APEC	Astrophysical Plasma Emission Code
BAOs	Baryonic Acoustic Oscillations
BCG	Brightest Cluster Galaxy
CALDB	Calibration Database
CCD	Charge-Coupled Device
CMB	Cosmic Microwave Background
CODEX	COntstrain Dark Energy with X-ray galaxy clusters
DES	Dark Energy Survey
EED	Extended Emission Detection
eFEDS	eROSITA Final Equatorial-Depth Survey
eSASS	eROSITA Science Analysis Software System
EM	Emission Measure
eROSITA	extended ROentgen Survey with an Imaging Telescope Array
HIFLUGCS	Highest X-ray FLUx Galaxy Cluster Sample
HRI	High Resolution Imager
HSC	Hyper Suprime-Cam
ICM	IntraCluster Medium
LoCuSS	Local Cluster Substructure Survey

LSS	Large Scale Structure
MCMC	Markov Chain Monte Carlo
MCXC	Meta-Catalogue of X-ray detected Clusters of galaxies
ML	Maximum Likelihood
NCC	Non-Cool Core
PED	Point-like Emission Detection
PSF	Point-Spread Function
PSPC	Position Sensitive Proportional Counter
PV	Performance Verification
RASS	ROSAT All-Sky Survey
REFLEX	ROSAT-ESO Flux Limited X-ray
ROSAT	ROentgen SATellite
SB	Surface Brightness
SCC	Strong Cool Core
SDSS	Sloan Digital Sky Survey
SPT	South Pole Telescope
SRG	Spectrum Roentgen Gamma
SXS	Soft X-ray Spectrometer
SZ	Sunyaev-Zel'dovich
TM	Telescope Module
tSZ	Thermal Sunyaev-Zel'dovich
XMM-LSS	XMM-Newton Large-Scale Structure
WCC	Weak Cool Core

Zusammenfassung

Im Rahmen des hierarchischen Modells sind die Eigenschaften des heißen Gases innerhalb von Galaxienhaufen eng mit der Strukturbildung im Universum verknüpft, wodurch sich Röntgendurchmusterungen gut für kosmologische Studien eignen. Um kosmologische Parameter mit Hilfe von Galaxienhaufen in aktuellen und zukünftigen Röntgendurchmusterungen genau bestimmen zu können, ist ein besseres Verständnis der Selektionseffekte im Zusammenhang mit der Detektionsmethode von Galaxienhaufen erforderlich. In Kapitel 2 streben wir ein besseres Verständnis der Morphologie von Galaxienhaufen an um Korrekturen zwischen den verschiedenen Kerntypen sowie Kovarianzen mit Röntgenleuchtkräften in die Selektionsfunktionen einzu beziehen. Insbesondere untersuchen wir die morphologischen Abweichungen zwischen einer neu beschriebenen Charakterisierung von Oberflächenhelligkeitsprofilen und einem häufig verwendeten einfachen β -Modell. Wir untersuchen einen neuartigen Ansatz zur Beschreibung von Oberflächenhelligkeitsprofilen, bei dem die überschüssige Kühlkern-Emission in den Zentren der Galaxienhaufen mittels Wavelet-Zerlegung modelliert wird. Morphologische Parameter und die Residuen wurden mit klassischen einfachen β -Modellen verglichen, die an die gesamten Oberflächenhelligkeitsprofile angepasst wurden. Die Verwendung einfacher β -Modelle zur Beschreibung des Ensembles der gesamten Oberflächenhelligkeitsprofile führt im Durchschnitt zu einer von Null verschiedenen Unausgewogenheit ($0,032 \pm 0,003$) im äußeren Teil der Galaxienhaufen, d.h. zu einem systematischen Unterschied der Oberflächenhelligkeit von etwa 3% bei großen Radien. Darüber hinaus zeigen die β -Modelle einen allgemeinen Trend zur Unterschätzung des Flusses im Außenbereich bei kleineren Kernradien. Die Fixierung des β -Parameters auf $2/3$ verdoppelt die Unausgewogenheit und vergrößert die Residuen eines einfachen β -Modells um bis zu mehr als 40%. Die Modellierung des Kernbereichs bei der Anpassung reduziert die Auswirkungen dieser beiden Effekte erheblich. Zusätzlich finden wir eine positive Skalierung zwischen morphologischen Parametern und Temperatur sowie eine negative Korrelation von etwa $-0,4$ zwischen Ausdehnung und Helligkeit. Wir demonstrieren die Einschränkungen bei der Modellierung von Galaxienhaufen mit einfachen β -Modellen und empfehlen diese mit Vorsicht zu verwenden, insbesondere wenn die Systematiken nicht berücksichtigt werden. Unsere nichtparametrische Analyse der selbstähnlich-skalierten "Emission Measure"-Profile zeigt keine systematischen Unterschiede zwischen den verschiedenen Kerntypen in den äußeren Bereichen der Galaxienhaufen wenn man die Medianprofile betrachtet.

Wie bereits erwähnt ist ein Schlüsselfaktor in Röntgendurchmusterungen die Selektionseffekte zu verstehen um Galaxienhaufen in kosmologischen Untersuchungen nutzen zu können. Die Abhängigkeit der Röntgenemission vom Quadrat der Gasdichte führt zu einer vorherrschenden

den Rolle von kühlen Kernen bei der Detektion von Galaxienhaufen. Der Beitrag der kühlen Kerne zur Röntgenleuchtkraft skaliert nicht mit der Masse der Haufen oder der Kosmologie und beeinflusst daher die Verwendung von Röntgenhaufen bei der Berechnung kosmologischer Parameter. Eines der wichtigsten wissenschaftlichen Ziele von eROSITA (extended Roentgen Survey with an Imaging Telescope Array) ist es, kosmologische Modelle mit einer kompletten Himmelsdurchmusterung einzuschränken. In Kapitel 3 schlagen wir ein Schema zur Detektion von Galaxienhaufen in Bezug auf eROSITA vor, das die Verwendung von Galaxienhaufenzentren bei der Detektion vermeidet. Wir berechnen theoretische Erwartungen und charakterisieren die Effizienz dieses Schemas durch Simulationen. Unsere Monte-Carlo-Simulationen der bevorstehenden eROSITA-Mission enthalten bekannte Vorder- und Hintergrundkomponenten. Realistische Simulationen von Punktquellen im Himmeldurchmusterungsmodus erlauben es uns nach räumlichen Skalen zu suchen, bei denen das Signal ausgedehnter Quellen nicht durch den Fluss von Punktquellen verunreinigt wird. Wir leiten eine Kombination von Skalen und Schwellenwerten ab, die zu einem sauberen Katalog von ausgedehnten Quellen führen. Mit Hilfe von diesem Katalog ist es uns möglich die kernaussgeschnittene Leuchtkraft mittels externer Massenmessungen zu kalibrieren. Wir beschreiben eine Methode um die Ergebnisse dieser Kalibrierung in die Berechnung der endgültigen kernaussgeschnitten Leuchtkraft einzubeziehen. Ähnlich wie bei anderen Detektionspipelines für Galaxienhaufen untersuchen wir Stichproben bei verschiedenen Flüssen und Kernradien. Dabei finden wir viele Ähnlichkeiten mit der Pipeline die verwendet wurde um Galaxienhaufen in einer 400 Quadratgrad großen ROSAT PSPC Durchmusterung, der 400d Durchmusterung, zu detektieren. Beide Detektionsmethoden benötigen eine große Anzahl von Photonen für kompakte Galaxienhaufen um die Kontamination durch Punktquellen zu reduzieren. Der Vorteil unserer Pipeline besteht in der Sensitivität gegenüber den äußeren Profilen von Galaxienhaufen. Diese zeichnen sich durch große Kerngrößen aus und haben wenig Variation bei einer fixen Masse des Haufens. Die Detektion von Galaxienhaufen durch deren Außenbereiche verbessert die Charakterisierung der Haufen in der Himmelsdurchmusterung mit eROSITA und wird gut charakterisierte Kataloge von Galaxienhaufen mit einfachen Selektionsfunktionen liefern.

Die Masse eines Galaxienhaufens ist nicht direkt beobachtbar aber ein wichtiger Parameter für kosmologische Studien. Die Messung der kernaussgeschnittenen Röntgenleuchtkraft in Himmelsdurchmusterungen bietet einen streuungsarmen Massenproxy, der für die Charakterisierung von Galaxienhaufen nützlich ist. Bei der Durchführung der Messung muss man die Umrechnung zwischen den für die Messung leicht verfügbaren Winkelskalen und den physikalischen Skalen, in denen der Kern des Haufens definiert ist, berücksichtigen. Ein solches Problem wurde erfolgreich in thermischen Sunyaev-Zel'dovich-Effekt Experimenten gelöst. Der Compton y -Parameter wird iterativ rekonstruiert indem ein universelles Profil des Drucks angenommen wird. In ähnlicher Weise diskutieren wir in Kapitel 4 eine neue Methode die das Wissen über das Röntgenoberflächen-Helligkeitsprofil des Haufens mit der partiellen Messung des Haufenflusses kombiniert, um iterativ die kernaussgeschnittene Leuchtkraft und Masse zu rekonstruieren. In ersten Tests untersuchen wir die Leistungsfähigkeit und Grenzen der Methode mit Hilfe von Simulationen der eROSITA Himmelsdurchmusterung. In einem idealisierten Szenario, d.h. bei Abwesenheit von Punktquellen und Hintergrund, rekonstruiert die aktuelle Implementierung die Massen der Haufen innerhalb eines Faktors von ungefähr fünf.

Abstract

In the framework of the hierarchical model the intra-cluster medium properties of galaxy clusters are tightly linked to structure formation, which makes X-ray surveys well suited for cosmological studies. To constrain cosmological parameters accurately using galaxy clusters in current and future X-ray surveys, a better understanding of selection effects related to the detection method of clusters is needed. In Chapter 2 of this thesis, we aim at a better understanding of the morphology of galaxy clusters to include corrections between the different core types and covariances with X-ray luminosities in selection functions. In particular, we stress the morphological deviations between a newly described surface-brightness-profile characterization and a commonly used single β -model. We investigated a novel approach to describe surface brightness profiles, where the excess cool-core emission in the centers of the galaxy clusters is modeled using wavelet decomposition. Morphological parameters and the residuals were compared to commonly-used single β -models, fitted to the overall surface brightness profiles. Using single β -models to describe the ensemble of overall surface brightness profiles leads on average to a non-zero bias (0.032 ± 0.003) in the outer part of the clusters, that is an approximate 3% systematic difference in the surface brightness at large radii. Furthermore, β -models show a general trend toward underestimating the flux in the outskirts for smaller core radii. Fixing the β parameter to $2/3$ doubles the bias and increases the residuals from a single β -model up to more than 40%. Modeling the core region in the fitting procedure reduces the impact of these two effects significantly. In addition, we find a positive scaling between shape parameters and temperature, as well as a negative correlation of approximately -0.4 between extent and luminosity. We demonstrate the caveats in modeling galaxy clusters with single β -models and recommend using them with caution, especially when the systematics are not taken into account. Our non-parametric analysis of the self-similar scaled emission measure profiles indicates no systematic core-type differences of median profiles in the galaxy cluster outskirts.

As already mentioned, one key ingredient in using galaxy clusters as a precision cosmological probe in large X-ray surveys is understanding selection effects. The dependence of the X-ray emission on the square of the gas density leads to a predominant role of cool cores in the detection of galaxy clusters. The contribution of cool cores to the X-ray luminosity does not scale with cluster mass and cosmology and therefore affects the use of X-ray clusters in producing cosmological constraints. One of the main science goals of the extended ROentgen Survey with an Imaging Telescope Array (eROSITA) mission is to constrain cosmology with a wide X-ray survey. In Chapter 3 of this thesis, we propose an eROSITA galaxy cluster detection scheme that avoids the use of X-ray cluster centers in detection. We calculate theoretical

expectations and characterize the performance of this scheme using simulations. We performed Monte Carlo simulations of the upcoming eROSITA survey, including known foreground and background components. By performing realistic simulations of point sources in survey mode, we searched for spatial scales where the extended signal is not contaminated by the point-source flux. We derive a combination of scales and thresholds which result in a clean extended source catalog. We designed the output of the cluster detection to enable calibration of the core-excised luminosity as a mass proxy using external mass measurements. We provide a way to incorporate the results of this calibration in producing the final core-excised luminosity. Similarly to other galaxy cluster detection pipelines, we sample the detection space of the flux – cluster core radius of our method and find many similarities with the pipeline used to detect clusters in a 400 square degree ROSAT PSPC survey, the 400d survey. Both detection methods require large statistics on compact clusters in order to reduce the contamination from point sources. The benefit of our pipeline consists of the sensitivity to the outer cluster shapes, which are characterized by large core sizes with little cluster to cluster variation at a fixed total mass of the cluster. Galaxy cluster detection through cluster outskirts improves the cluster characterization using eROSITA survey data and is expected to yield well-characterized cluster catalogs with simple selection functions.

The mass of a galaxy cluster is not directly observable but is an important parameter for cosmological studies with galaxy cluster surveys. The measurement of the core-excised X-ray luminosity in cluster surveys offers a low-scatter mass proxy, which is useful for cluster characterization. Performing the measurement, one has to address the conversion between the angular scales readily available to perform the measurement and physical scales in which the cluster core is defined. Such a problem has been successfully addressed by thermal Sunyaev-Zel'dovich effect experiments, which adopt a universal pressure profile to iteratively reconstruct the Compton y -parameter. Similarly, we discuss a new method in Chapter 4 which combines knowledge of the cluster X-ray surface brightness profile with the partial measurement of the cluster flux to iteratively reconstruct the core-excised luminosity and mass. In first tests, we study the performance and limitations of the method on simulations of the eROSITA all-sky survey. In an idealized scenario, that is the absence of point sources and background, the current set-up recovers the cluster masses within a factor of approximately five.

Chapter 1

Introduction

1.1 Prelude

Among other things, modern astronomy tries to expand our knowledge and understanding of cosmology and the driving forces behind the expansion and structure formation histories of our Universe. Galaxy clusters offer a unique probe to study the matter distribution over a wide range of redshifts, allowing us to test different cosmological models independently of other methods, such as supernovae type Ia and the cosmic microwave background. In addition, galaxy clusters are interesting objects from an astrophysical point of view and are studied over a wide range of the electromagnetic spectrum. Imaging in the X-ray band is among the most sensitive and robust methods to detect and analyse galaxy clusters. Current X-ray observatories such as *XMM-Newton* and *Chandra* are designed to make detailed studies of individual objects and allow the statistical analysis of cluster samples with hundreds of objects. In July 2019 a powerful X-ray instrument, the extended ROentgen Survey with an Imaging Telescope Array (eROSITA), was launched to investigate the nature of dark energy by detecting approximately one hundred thousand groups and clusters of galaxies, reaching out above a redshift of one. However, the challenge of translating these into cosmological constraints goes well beyond the simple detection of sources in the all-sky-survey data. It is important to understand the characteristics of the sample and the detected sources themselves. To exploit the full observational capability of eROSITA, one requires an accurate surface-brightness model of galaxy clusters, as well as a suitable detection method, including a handle on the observational systematics to determine the level of completeness and purity. In this thesis work we explore novel approaches to addresses both.

This thesis is structured as follows. In Chapter 1, we present the theoretical background of current cosmological models and structure formation. We introduce general properties of and science with galaxy groups and clusters, including cosmological studies. We discuss the basic concept of X-ray observatories, in particular ROSAT and eROSITA. Finally, we highlight the importance and challenges with structure detection in X-ray images.

In Chapter 2, we introduce a new and unbiased approach to characterize surface brightness profiles of galaxy clusters and compare it to a commonly used model. We study the scaling between shape parameters and cluster temperature, as well as the correlations between shape

parameters and luminosity at fixed temperature.

In Chapter 3, we propose a novel galaxy cluster detection method, discuss it in the framework of eROSITA and compare its performance to existing detection schemes through simulations.

In Chapter 4, we discuss applications and prospects with eROSITA that are currently ongoing. This includes a self-consistent framework to measure core-excised luminosities and a brief discussion of eROSITA's capabilities to improve our understanding of scaling relations.

Finally, we conclude the thesis in Chapter 5 with a brief summary of the main results. This thesis, in particular Chapter 2 and 3 include sections of the peer reviewed publications Käfer et al. (2019) and Käfer et al. (2020), respectively.

1.2 Cosmological model

According to current measurements, the Universe formed around 13.8 Gyr ago (Planck Collaboration et al., 2018) after an initial acceleration from a very hot and dense state, often referred to as the Big Bang. As a result of the finite speed of light, we are not able to observe the entire Universe but regions inside a sphere with cosmological-model-dependent radius, the Hubble radius. Since light needs a finite time to travel from the origin of the emission to the observer, we always look back into the past. The Universe is considered homogeneous and isotropic on large enough scales, which is called the cosmological principle. Based on these assumptions, we can theoretically describe the evolution and composition of the Universe using a theory of gravity. The most established geometric theory is Einstein's general relativity, which describes the space-time structure by the distribution of matter or energy in the Universe. The space-time is a four-dimensional continuum, consisting of a three-dimensional spatial vector and a time variable.

The expansion of space increases the relative distances of the fixed points on the grid on which the spatial vector is defined. This evolution of the Universe's length scales due to its radial expansion is described in the time-dependent cosmic scale factor $a(t)$. The position of a matter element at arbitrary time t is then defined with respect to the 3-dimensional position on the fixed grid at time t_0 according to

$$\vec{r}(t) = a(t)\vec{r}(t_0). \quad (1.1)$$

Choosing the time t_0 to be the current age of the Universe, the scale factor today is $a(t_0) = 1$ by convention. Distances in the Universe are defined with a metric and one solution to Einstein's field equations is the Robertson-Walker metric (Robertson, 1935; Walker, 1935), which describes the distance between two objects in space-time ds^2 according to

$$ds^2 = c^2 dt^2 - a^2(t) \left[d\chi^2 + f_K^2(\chi) (d\theta^2 + \sin^2 \theta d\psi^2) \right]. \quad (1.2)$$

The spatial position is described with the spherical coordinates χ , θ and ψ . The comoving angular diameter distance $f_K(\chi)$ is a function of the comoving radial coordinate χ and depends on the space curvature parameter K according to

$$f_K(\chi) = \begin{cases} K^{-1/2} \sin(K^{1/2}\chi) & (K > 0) \\ \chi & (K = 0). \\ (-K)^{-1/2} \sinh[(-K)^{1/2}\chi] & (K < 0) \end{cases} \quad (1.3)$$

In case of electromagnetic radiation, θ and ψ are constant and $ds = 0$. The comoving distance between an observer and an object that emits at time t is therefore

$$\chi(t) = \int_t^{t_0} \frac{c}{a(t')} dt'. \quad (1.4)$$

This implies a cosmological redshift z for photons, which is defined as the relative change between observed and emitted wavelength

$$z := \frac{\lambda_{\text{obs}} - \lambda_{\text{em}}}{\lambda_{\text{em}}} = \frac{1}{a(t)} - 1. \quad (1.5)$$

The dynamics of the Universe, that is the evolution of the scale factor, are described by the two independent Friedmann equations

$$\left(\frac{\dot{a}}{a}\right)^2 = \frac{8\pi G}{3}\rho + \frac{1}{3}c^2\Lambda - \frac{Kc^2}{a^2} \quad (1.6)$$

$$\frac{\ddot{a}}{a} = \frac{4\pi G}{3}\left(\rho + \frac{3p}{c^2}\right) + \frac{1}{3}c^2\Lambda, \quad (1.7)$$

where G is the gravitational constant, ρ the total energy density, p the total pressure, Λ is Einstein's cosmological constant, and K is the space-time curvature constant. The second Friedmann equation defines the rate of the accelerated expansion of the Universe. The expansion rate of the Universe is defined by the first Friedmann equation and commonly known as the Hubble parameter

$$H(t) := \frac{\dot{a}(t)}{a(t)}. \quad (1.8)$$

According to current measurements, today's expansion rate, the so-called Hubble constant, is $H_0 = (67.66 \pm 0.42) \text{ km s}^{-1} \text{ Mpc}^{-1}$ (Planck Collaboration et al., 2018), where $1 \text{ pc} \approx 3.1 \cdot 10^{16} \text{ m}$. The first Friedmann equation demonstrates that the total energy-density value depends on the geometry of the Universe and requires a precise calibration in case of a flat universe with $K = 0$, referred to as critical density

$$\rho_{\text{crit}}(t) = \frac{3H(t)^2}{8\pi G}. \quad (1.9)$$

In case the density is greater than the critical density, K is positive and the space-time geometry is defined as closed. If the density is smaller than the critical density, K is negative and the geometry is considered open. The dimensionless density parameters of the individual energy components i are defined as ratios with respect to the critical density

$$\Omega_i(t) := \frac{\rho_i(t)}{\rho_{\text{crit}}(t)}. \quad (1.10)$$

The total energy density today and the curvature of the Universe is defined as $\Omega_0 = \sum_i \Omega_i(t_0)$ and $\Omega_K = 1 - \Omega_0$. Current measurements are consistent with a flat geometry of the Universe, measuring Ω_K values close to zero with $\Omega_K = 0.0007 \pm 0.0037$ (Planck Collaboration et al., 2018).

The current concordance model is known as the Lambda Cold Dark Matter model (Λ CDM) and establishes that the Universe is composed of four energy components that contribute to the total energy budget: radiation, baryonic matter, dark matter, and dark energy. Neutrinos have a special role because they contribute differently to the energy budget, depending on their masses and present-day velocities. The effective total number of neutrino families $N_{\text{eff}} = 2.99 \pm 0.17$ (Planck Collaboration et al., 2018) is in agreement with the Standard Model of particle physics prediction of $N_{\text{eff}} = 3.046$. The sum of the neutrino masses is with $\sum m_\nu < 0.12 \text{ eV}$ very small but the observational evidence of neutrino oscillations implies that these leptons have masses greater than zero. We describe the four energy components in more detail.

Radiation

Radiation includes electromagnetic radiation and relativistic particles with velocities much larger than their rest mass energy, for example photons and neutrinos, respectively. In addition to the expansion of space-time ($\propto a^{-3}$) the radiation density is proportional to a cosmic-redshift-induced energy shift ($\propto a^{-1}$) such that $\rho_r(a) = \rho_{r,0}a^{-4}$.

Baryonic matter

Baryons are particles with velocities much smaller than the speed of light which interact strongly electromagnetically. Due to their negligible gravitational pressure support, the evolution of the baryon density scales with the cosmic expansion as $\rho_b(a) = \rho_{b,0}a^{-3}$. Time evolutions of other matter components have the same proportionality.

Dark matter

The existence of an additional invisible matter component in galaxy clusters was postulated because the measured velocity dispersion in the Coma Cluster was higher than expected from the calculated masses of the galaxies (Zwicky, 1933). Dark matter is a type of matter assumed to be non-baryonic with very low interaction cross-sections. Therefore, direct detections have not yet been accomplished, but we indirectly observe its gravitational impact on baryonic matter. The three categories hot, warm, and cold dark matter are defined according to the particle velocities. An example for hot and warm dark matter are relativistic and non-relativistic neutrinos, respectively. A common model for cold dark matter is weakly interacting massive particles (WIMPS) like the neutralino. Dark matter characteristics inferred from the history of structure formation favour a mixture of warm and cold dark matter. Generally, we label the total dark-matter energy density as ρ_{DM} .

Dark energy

Supernovae type Ia measurements of the relation between observed distances and redshifts indicate an accelerated expansion of the Universe caused by a form of energy density with negative pressure which makes up roughly two thirds of the total energy budget, the so-called dark energy (Riess et al., 1998; Perlmutter et al., 1998). The general time evolution of the dark-energy

density is

$$\rho_{\text{DE}} = \rho_{\text{DE},0} \cdot \exp \left[-3 \int_1^a \frac{1 + w(a')}{a'} da' \right]. \quad (1.11)$$

If the equation of state w is equal to minus one, the dark-energy density is constant and referred to as cosmological constant. Beyond the Λ CDM more generalized models are under discussion, for example w_0 CDM with a constant equation of state with $w \neq -1$ or w CDM with a time-evolving equation of state.

Total matter energy density

The total matter energy density of the Universe is defined as the sum of the baryonic and dark matter component

$$\Omega_{\text{m}} = \Omega_{\text{b}} + \Omega_{\text{DM}}. \quad (1.12)$$

The total energy budget is then

$$\Omega_0 = \Omega_{\text{r}} + \Omega_{\text{m}} + \Omega_{\text{DE}} + \Omega_{\text{K}}. \quad (1.13)$$

Assuming a cosmological constant as dark energy, the first Friedmann equation can be rewritten as

$$H(t)^2 = H_0^2 (\Omega_{\text{r}} a^{-4} + \Omega_{\text{m}} a^{-3} + \Omega_{\Lambda} + \Omega_{\text{K}} a^{-2}) = H_0^2 E(a)^2. \quad (1.14)$$

Often the dimensionless Hubble function, $E(a)$, is written in a redshift dependent way using Eq. 1.5 through

$$E(z) = \sqrt{\Omega_{\text{r}}(1+z)^4 + \Omega_{\text{m}}(1+z)^3 + \Omega_{\text{K}}(1+z)^2 + \Omega_{\Lambda}}. \quad (1.15)$$

1.3 Structure formation

In contrast to the cosmological principle, observations of, for example the distribution of galaxies or galaxy clusters as tracers (e.g., [Colless et al., 2001](#); [Eisenstein et al., 2011](#)) indicate that the present day Universe is not homogeneous on scales smaller than approximately 100 Mpc (see Fig. 1.1). The observed structure evolved from tiny density perturbations in the early Universe driven by quantum fluctuations and increased to macroscopic scales by an inflation phase ([Guth, 1981](#); [Linde, 1982](#)). This initiated the accretion of matter into regions of increasing overdensity, so-called filaments and corresponding underdense regions, so-called voids. The intersection points of filaments are called knots, which eventually experience mergers with other overdense regions and collapse into virialized objects decoupled from the expansion of the Universe. The most massive virialized objects are galaxy clusters. Observing the spatial and mass distribution of galaxy clusters allows to study the evolution of structure formation, which strongly depends on the cosmological model and cosmological parameters. In the following two subsections, we provide a qualitative description of the density perturbations and their collapse that lead to the global distribution of matter in the Universe, the so-called Large Scale Structure (LSS).

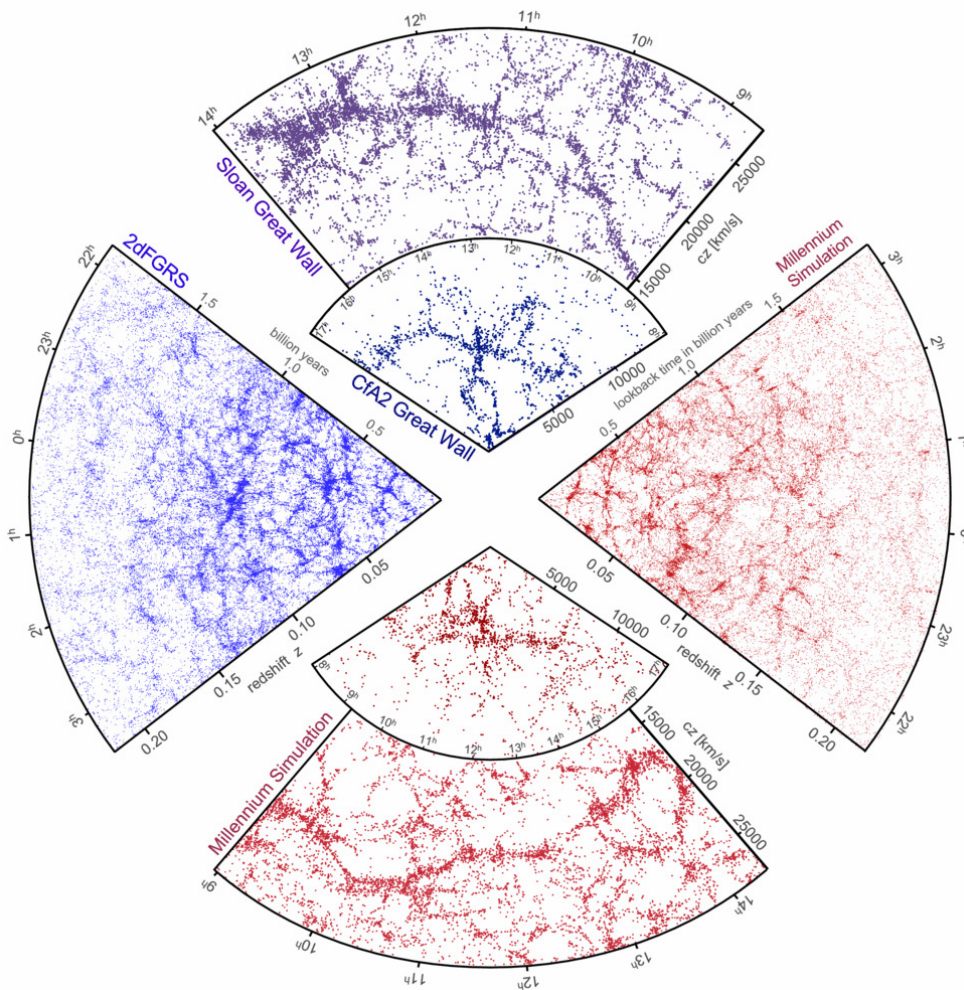


Figure 1.1: The galaxy distribution obtained from spectroscopic redshift surveys and from mock catalogues constructed from cosmological simulations. The small slice at the top shows the CfA2 "Great Wall" (Geller and Huchra, 1989), with the Coma cluster at the centre. Drawn to the same scale is a small section of the SDSS, in which an even larger "Sloan Great Wall" has been identified (Gott et al., 2005). This is one of the largest observed structures in the Universe, containing over 10 000 galaxies and stretching over more than 1.37 billion light years. The wedge on the left shows one-half of the 2dFGRS, which determined distances to more than 220 000 galaxies in the southern sky out to a depth of 2 billion light years. The SDSS has a similar depth but a larger solid angle and currently includes over 650 000 observed redshifts in the northern sky. At the bottom and on the right, mock galaxy surveys constructed using semi-analytic techniques to simulate the formation and evolution of galaxies within the evolving dark matter distribution of the "Millennium" simulation (Springel et al., 2005) are shown, selected with matching survey geometries and magnitude limits. Figure and caption taken from Springel et al. (2006).

1.3.1 Linear growth of density perturbations

The matter density at given comoving coordinates and time $\rho(\vec{x}, t)$ and the mean matter density $\bar{\rho}(t)$ characterize the primordial density field by the matter density contrast

$$\delta(\vec{x}, t) = \frac{\rho(\vec{x}, t) - \bar{\rho}(t)}{\bar{\rho}(t)}. \quad (1.16)$$

The time evolution of the density contrast is driven by gravitational interaction and depends on the component dominating the total energy density in addition to the considered perturbation scale. For the scope of the thesis, we focus on the epoch of matter domination, assuming a negligible contribution of radiation. The linear evolution of the density contrast for small perturbations is found by solving the continuity, Euler, and Poisson equation which characterize mass conservation, momentum conservation, and the potential field, respectively. With the competition between pressure support and gravity, as well as the friction represented by the Hubble parameter, the equation reads

$$\ddot{\delta} + 2H\dot{\delta} = \delta \left(4\pi G\bar{\rho}(t) - \frac{c_s k^2}{a^2} \right), \quad (1.17)$$

with the speed of sound c_s . The solution of this differential equation is a linear combination of a decaying D_- and a growing mode D_+ , where only the growing mode is of broader physical interest. For cold dark matter the pressure is zero and the growing mode in the Λ CDM framework reads

$$D_+(z) = \frac{2}{5}\Omega_m E(z) \int_z^\infty \frac{1+z'}{E(z')^3} dz', \quad (1.18)$$

which is the so-called linear growth factor. Due to the strong $E(z)$ dependency, the growth factor is sensitive to cosmological parameters.

1.3.2 Spherical collapse

The formation of galaxy clusters can be expressed by a simple non-linear and spherically-symmetric model, the so-called top-hat model. An overdense region that accretes matter has a decreasing expansion compared to its environment because of the greater gravitational potential and eventually expands up to a maximum radius. Then, the overdense sphere decouples from the general Hubble flow of the Universe and recollapses into a virialized object with half the radius at the turnaround. Solving the equation of motion of a sphere $\ddot{r} = -GM/r^2$ in the spherical collapse framework for an Einstein-deSitter Universe with $\Omega_m = \Omega_0 = 1$ results in a mean density of the collapsed perturbation within the virialized region with respect to the critical density of

$$\frac{\rho_{\text{coll}}}{\rho_{\text{crit}}(z)} = 18\pi^2 \approx 178 =: \Delta_{\text{vir}}. \quad (1.19)$$

The final overdensity at the time of equilibrium, Δ_{vir} , shows only a weak dependence on cosmology and is commonly used to define the virial radius of galaxy clusters. The total cluster mass is

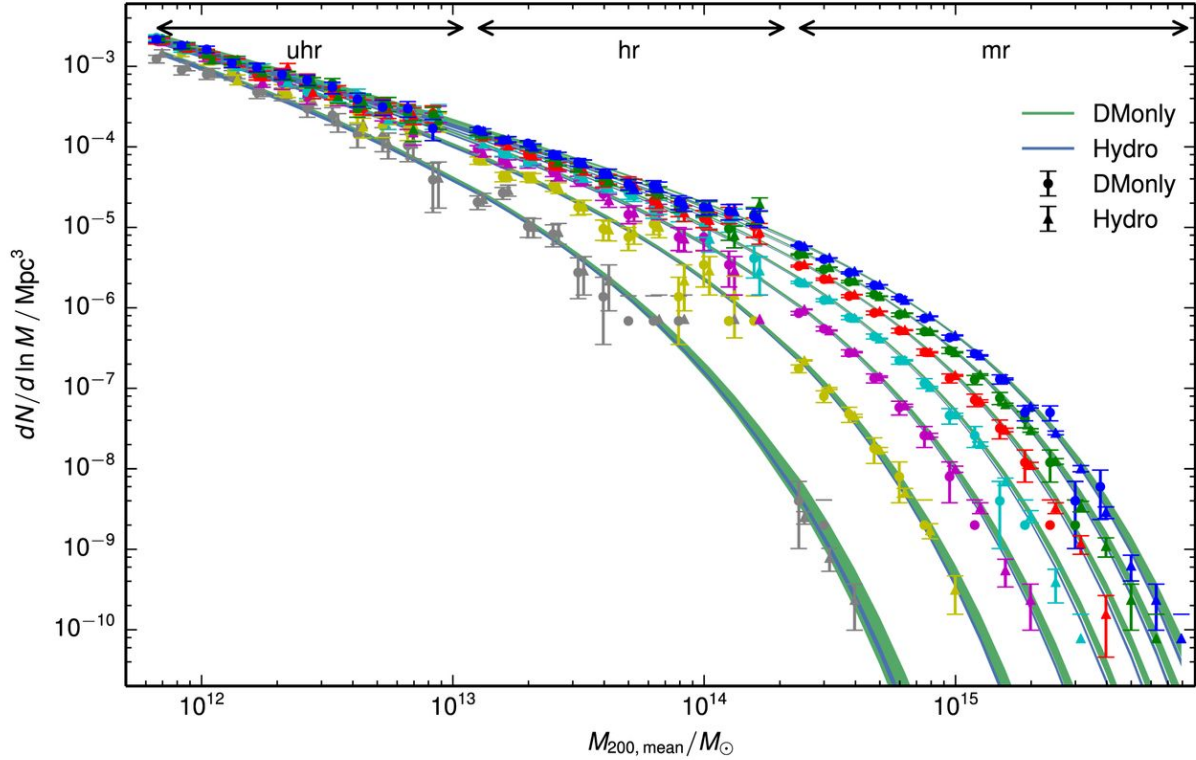


Figure 1.2: The halo mass function derived from dark-matter-only N-body simulations (DMOnly) and hydrodynamical simulations which include baryons (Hydro). The mass function is measured at several redshift slices of the Magneticum simulations, with the lines representing the best-fit functions. The redshift decreases from bottom to top, meaning more and more massive halos are forming with time. Figure taken from [Bocquet et al. \(2016\)](#).

usually defined within a certain overdensity radius

$$M_{\text{tot}}(< r_{\Delta}) := \frac{4}{3}\pi\Delta\rho_{\text{crit}}(z)r_{\Delta}^3, \quad (1.20)$$

where $\Delta = 200$ is used as virial radius. A perturbation will collapse and form a virialized structure if its overdensity with respect to the initial density field is $\delta_+(t_{\text{vir}}) \approx 1.69$ at the time of virialization.

1.3.3 Halo mass function

The dependence between the time evolution of galaxy clusters and cosmological parameters makes clusters interesting observational targets to constrain cosmological models. However, observations of the formation history of individual objects is unfeasible due to the large cosmological time scales. Instead, we study the population in a statistical way as a function of mass and redshift. The distribution of dark matter haloes, in which galaxy clusters are believed to reside,

is called the halo mass function and describes the number density of haloes of a given mass at a particular redshift (see Fig. 1.2). The general functional form of the halo mass function is described by the fraction of the total volume that collapses into a halo of given mass divided by the occupied comoving volume of these haloes and is given by (Sheth and Tormen, 1999)

$$\frac{dn(M, z)}{dM} = \frac{\bar{\rho}_{m,0}}{M} \left(\frac{d \ln \sigma^{-1}(M, z)}{dM} \right) f(\sigma, z). \quad (1.21)$$

The mean matter density at redshift zero is given by $\bar{\rho}_{m,0} = \rho_{\text{crit},0} \Omega_m$. The variance of the linear density field, $\sigma(M, z)$, holds the dependence on cosmology and the power spectrum, $P(k, z)$. The power spectrum is a function of redshift and wavenumber $k = 2\pi/\lambda$, with length scale λ . Assuming that the initial density field is described by a Gaussian distribution with a density contrast that spatially averages to zero, the variance of the perturbed density field is

$$\sigma^2(M, z) = \frac{1}{2\pi^2} \int P(k, z) |\tilde{W}(k)| k^2 dk. \quad (1.22)$$

The Fourier transform of the top-hat window function

$$\tilde{W}(k) = \frac{3[\sin(kR) - kR \cos(kR)]}{(kR)^3} \quad (1.23)$$

smooths fluctuations whose scales are smaller than the size of the initial perturbations needed to obtain an object of mass M , namely $R(M) = (3M/4\pi\rho_m)$. The redshift evolution of the variance is expressed by the growth factor

$$\sigma(M, z) = \sigma(M, 0) \frac{D_+(z)}{D_+(0)}. \quad (1.24)$$

A statistical characterization of the large scale structure is the matter power spectrum

$$P(k, z) = T^2(k) \left(\frac{D_+(z)}{D_+(0)} \right)^2 A \cdot k^{n_s}. \quad (1.25)$$

The modification of the power spectrum's shape as a result of non-gravitational effects is described by the transfer function $T(k)$. The index, n_s , and amplitude at redshift zero, A , characterize the primordial power spectrum. An index value of one would correspond to a scale-invariant power spectrum and measured power-spectrum indices are slightly smaller than unity $n_s \sim 0.966$ (Planck Collaboration et al., 2018). The amplitude needs to be measured observationally and is defined as the present variance of the matter distribution for a comoving radius of $R = 8 h^{-1} \text{Mpc}$ for a top-hat window function. This choice of R comes from galaxy-counts results which found that the variance of the galaxy number density on these spatial scales is close to unity (Davis and Peebles, 1983). The variance on these scales determines the number of haloes in the Universe by the height of the density peaks and is referred to as σ_8 . It is expected that the profile of the halo mass function is universal and its shape therefore independent of cosmology. The halo mass function is calibrated using structure formation simulations by fitting the halo abundance function $f(\sigma, z)$ (Sheth and Tormen, 1999; Jenkins et al., 2001; Reed et al., 2003; Warren et al., 2006;

Reed et al., 2007; Watson et al., 2013; Bocquet et al., 2016; Despali et al., 2016). A widely used model in galaxy-cluster studies is the one by Tinker et al. (2008)

$$f(\sigma, z) = A_T(z) \left[\left(\frac{\sigma}{b_T(z)} \right)^{-a_T(z)} - 1 \right] \exp(-c_T(z)/\sigma^2), \quad (1.26)$$

with overall mass-function amplitude A_T , slope and amplitude of the low-mass power law a_T and b_T , as well as the cut-off scale where the halo abundance decreases exponentially c_T . The parameters A_T , a_T , b_T , and c_T depend on redshift and the overdensity Δ

$$A_T(z) = A_{T,0}(1+z)^{-0.14}, \quad (1.27)$$

$$a_T(z) = a_{T,0}(1+z)^{-0.06}, \quad (1.28)$$

$$b_T(z) = b_{T,0}(1+z)^{-\alpha_T(\Delta)}, \quad (1.29)$$

$$c_T(z) = c_{T,0}, \quad (1.30)$$

$$\log_{10}(\alpha_T(\Delta)) = - \left[\frac{0.75}{\log_{10}(\Delta/75)} \right]^{1.2}. \quad (1.31)$$

The importance of the halo mass function for cosmology lies in the strong dependence of its shape on cosmological parameters. This makes abundance studies of galaxy groups and clusters as a function of redshift a powerful tool for precision cosmology. However, to exploit the full cosmological potential with the 100 000 galaxy clusters expected to be detected with eROSITA, we require an accuracy of the mass-function of a few percent.

1.4 Clusters and groups of galaxies

In our Universe galaxies are not uniformly distributed in space but rather tend to group in so-called galaxy groups and clusters. The clustering of galaxies is seen in the projection of observed galaxies on the sky (e.g., Sharp, 1986; Colless et al., 2001; Eisenstein et al., 2011). Originally, groups and clusters were identified by the spatial concentration of galaxies and the definition of the categorization into groups or clusters was based on the number of member galaxies within a sphere of characteristic diameter D . A group consists of typically more than three and less than 50 galaxies within $D \lesssim 1.5 h^{-1} \text{Mpc}$ and a cluster has more than 50 galaxies and extends beyond $D \gtrsim 1.5 h^{-1} \text{Mpc}$ (Abell, 1958). The space between the galaxies is filled with diffuse and collisionally ionized gas, the intracluster medium (ICM). The main component of the total galaxy-cluster mass is in the form of dark matter. Galaxy clusters are considered the most massive relaxed cosmic structures in our Universe and thus are believed to reside in the knots of the large-scale structure. Therefore, clusters are interesting targets for observational cosmology and to study structure-formation history. In addition, diverse astrophysical aspects can be studied, amongst others shocks, the metal-enrichment history, or the physics of Active Galactic Nuclei (AGN). In this section we review the properties of galaxy groups and clusters in more detail.

1.4.1 Composition

Galaxy groups and clusters extend over a total mass range of $10^{12} M_{\odot}$ to a few $10^{15} M_{\odot}$. Four main components contribute to the total mass budget.

Dark matter

Dark matter makes up approximately 80% of the total galaxy-cluster mass and provides the gravitational attraction needed for the ICM to be gravitationally bound as well as the galaxies in the halo that it forms. Typical mass-to-light ratios of clusters are $M/L \approx 300 h M_{\odot}/L_{\odot}$, which means at least a factor of ten larger than mass-to-light ratios of early-type galaxies. Therefore, clusters of galaxies must contain significantly more mass than is visible in galaxies and the majority of the cluster masses must be in the form of non-baryonic dark matter, the so-called missing mass problem (Zwicky, 1933).

Intracluster medium

Approximately 15% of the total cluster mass is comprised of baryonic gas, the so-called intra-cluster medium (ICM). This gas originates from ambient baryonic matter, which is accreted onto larger structures like clumps and knots during the structure-formation process. In this process the potential energy of the baryonic matter is converted into kinetic energy, which in turn is converted into heat by adiabatic compression and shocks (e.g., Borgani and Kravtsov, 2011). As a result of the deep potential wells of clusters, the baryonic gas is heated to typical temperatures of 1–15 keV, where $1 \text{ keV}/k_{\text{B}} \approx 1.16 \times 10^7 \text{ K}$ using the Boltzmann constant k_{B} . Hydrogen and helium atoms are fully collisionally ionized at these temperatures and metals are in hydrogen- or helium-like states. With densities of 10^{-3} – 10^{-1} particles cm^{-3} the ICM is an optically thin plasma and has metallicities of approximately 0.3 times the solar abundance (Arnaud et al., 1992).

Galaxies

Galaxies provide approximately 5% of the total cluster mass. As a result of tidal interactions with other galaxies and ram-pressure stripping within the ICM, clusters show greater fractions of elliptical galaxies than the field. This makes member galaxies of clusters redder than field galaxies at similar redshift. Cluster members can be determined by their position in galaxy colour versus magnitude diagrams (Gladders and Yee, 2000). This so-called red-sequence technique is used in cluster-finder algorithms for optical identification. A giant elliptical galaxy close to the cluster centre is referred to as the brightest cluster galaxy (BCG).

Relativistic particles and magnetic fields

The energy content of relativistic particles and magnetic fields, which are of the order of a few μG , is a negligible fraction compared to the total thermal energy of clusters. However, non-thermal relativistic particles that are for example accelerated due to shocks driven in the ICM by interactions (Bonafede et al., 2014), gyrate in the magnetic field, and thus emit synchrotron

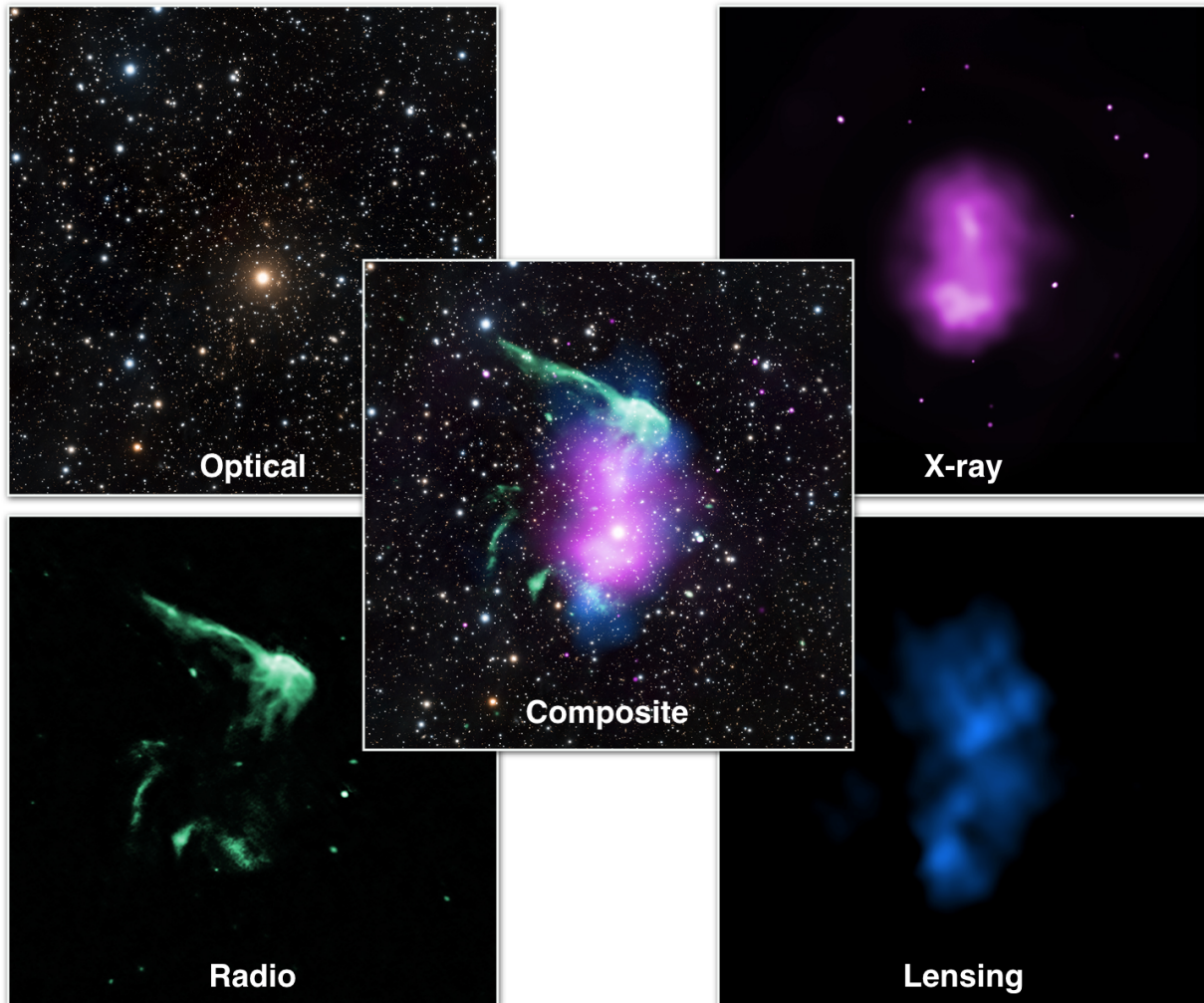


Figure 1.3: Multi-wavelength observations of the "Toothbrush Cluster". Galaxies and stars (upper left) are observed in the optical with the Subaru telescope. The radio (lower left) and X-ray emission (upper right) trace the highly relativistic electrons and the hot ICM, respectively. The gravitational-lensing map (lower right) represents the mass concentration, which is primarily dark matter. The composite image in the center demonstrates that the emission at different wavelengths originates from different populations. Figures taken from <https://chandra.cfa.harvard.edu/photo/2016/archives/>.

emission that can be observed at radio wavelengths. This diffuse and extended synchrotron emission is usually categorized into radio relics, meaning elongated radio sources in the peripheral regions of galaxy clusters with steep radio spectra ($S_\nu \gtrsim \nu^{-1.2}$) as well as radio haloes, which are large-scale radio sources with low surface brightness found in the centre of some clusters that typically follow the morphology of the ICM.

1.4.2 Emission mechanisms

The emission processes of the ICM in X-ray are thermal bremsstrahlung, line emission and recombination. We discuss these processes in more detail in this section and show typical X-ray spectra of galaxy clusters in Fig. 1.4. We assume that the electrons are in thermal equilibrium with the other gas particles, which is a reasonable assumption for galaxy cluster studies because the equilibration time scales are with a few 10^8 yr within r_{500} , rather short compared to the Hubble time (Reiprich et al., 2013).

Bremsstrahlung

Above electron temperatures of $k_B T_e \gtrsim 2$ keV the primary component of the ICM spectrum is thermal bremsstrahlung of electrons that are accelerated in the vicinity of atomic nuclei, so-called free-free emission. The acceleration of the nuclei and therefore their contribution to this emission process is negligible due to their much greater mass. The bremsstrahlung emissivity at frequency ν , with elementary charge e , electron mass m_e , ion charge Z , as well as ion and electron densities n_i and n_e , respectively is

$$\epsilon_\nu^{\text{ff}} = \underbrace{\frac{2^5 \pi e^6}{3 m_e c^3} \left(\frac{2\pi}{3 m_e k_B} \right)^{1/2}}_{= 6.8 \cdot 10^{-38} \text{ erg K}^{1/2} \text{ cm}^3 \text{ s}^{-1} \text{ Hz}^{-1}} g_{\text{ff}}(Z, T_e, \nu) Z^2 n_e n_i T_e^{-1/2} \exp\left(-\frac{h_P \nu}{k_B T_e}\right). \quad (1.32)$$

The Gaunt factor g_{ff} corrects for quantum effects and for the impact of distant collisions. For a hydrogen plasma the Gaunt factor slowly decreases with frequency (Karzas and Latter, 1961; Kellogg et al., 1975). The thermal bremsstrahlung spectrum is smooth overall and continuous, with a power-law shape at low energies ($h_P \nu \ll k_B T_e$) and an exponential drop at high frequencies ($h_P \nu \gtrsim k_B T_e$). The bremsstrahlung cutoff shifts to higher energies for higher gas temperatures and can therefore be used to determine the electron temperature in measured X-ray spectra of galaxy clusters. The emissivity integrated over all frequencies is approximately

$$\epsilon^{\text{ff}} \propto T_e^{1/2} n_e^2. \quad (1.33)$$

Line emission

At typical ICM temperatures the wavelengths of emission lines caused by a transition between quantized energy states of heavy elements, so-called bound-bound emission, are in the X-ray regime. The Fe-K complex for example composes of a helium- α -like iron multiplet around 6.7 keV and hydrogen-like ion lines around 6.97 keV. Below electron temperatures of $k_B T_e \lesssim$

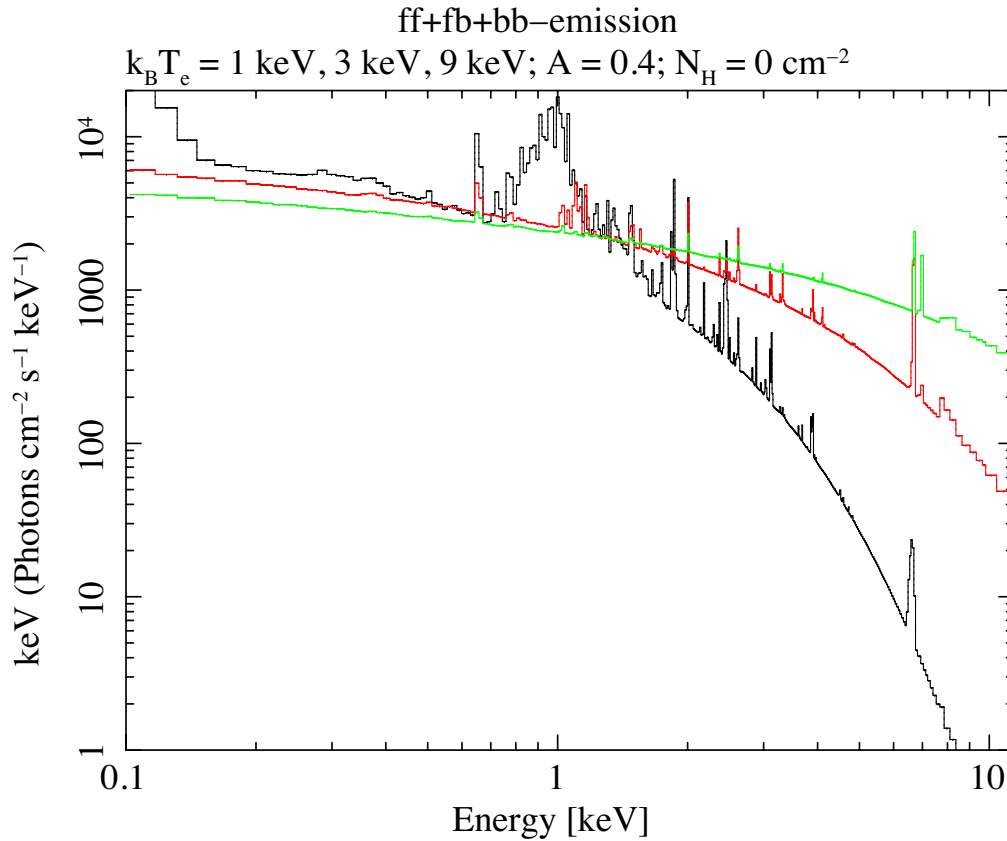


Figure 1.4: Expected X-ray emission spectra of a hot and optically-thin plasma for three temperatures of 1 keV (black), 3 keV (red), and 9 keV (green). The continuum emission from thermal bremsstrahlung is the dominant component and shifts to higher photon energies for hotter gas. Toward lower temperatures atomic transitions and recombination radiation become more important, which makes line features, for example the Fe-L and Fe-K complex at approximately 1 keV and 6.8 keV, more prominent. Figure taken from [Reiprich et al. \(2013\)](#).

2.5 keV the Fe-L complex at approximately 1 keV has a significant contribution to the total emissivity. The labels L and K denote electron transitions to a principal quantum number of 2 and 1, respectively. The line emission can be modelled to determine the redshift and the abundance of galaxy clusters. X-ray calorimeters like the Soft X-ray Spectrometer (SXS) aboard the Hitomi X-ray Observatory allow measurements of Doppler shifts and broadening of emission lines to infer bulk and turbulent motions with high precision (Hitomi Collaboration et al., 2016).

Recombination

Recombination processes have a minor contribution to the continuum radiation spectrum in the form of radiative recombination, dielectronic recombination and two-photon transitions. The Ar xvii dielectronic recombination line, for example, is discussed in the explanation of weak unidentified emission features in stacked galaxy-cluster spectra (Bulbul et al., 2014). The total emissivity of recombination and line emission is approximately

$$\epsilon^{\text{fb+bb}} \propto T_e^{-0.6} n_e^2, \quad (1.34)$$

and therefore decreases with increasing electron temperature because more and more metals become fully ionised (Sarazin, 1986).

1.4.3 Galaxy cluster profiles

Galaxy clusters are spatially extended objects in the X-ray with diameters of up to a few megaparsecs for massive objects. In this section we describe the most important radial density parameterizations for this work.

Density profiles of dark matter haloes

Numerical simulations allow the study of the dark matter haloes in which galaxy groups and clusters form. Within the Λ CDM framework, virialized objects have a universal density profile of the dark matter halo matching the so-called NFW profile (Navarro et al., 1997),

$$\rho_{\text{NFW}}(r) = \frac{\rho_s}{x(1+x)^2} \quad (1.35)$$

$$x := \frac{r}{r_s}. \quad (1.36)$$

The scale radius r_s represents the radius at which the logarithmic slope of the profile is equal to minus two and ρ_s is the corresponding density at the scale radius. The NFW profile has a cusp at radii much smaller than the scale radius, with an inner slope of $\rho_{\text{NFW}}(r) \propto r^{-1}$. At radii much greater than the scale radius, the outer slope is $\rho_{\text{NFW}}(r) \propto r^{-3}$. Observations in the optical and X-ray support this parametric form of the density profile (e.g., Pointecouteau et al., 2005).

The β -model

One of the most common models used to describe the gas-density distribution of clusters is the β -model (Cavaliere and Fusco-Femiano, 1976), which assumes that the matter distribution in the potential well follows the model of a self-gravitating isothermal sphere and that the galaxy density is described by a so-called King-profile (King, 1962). Under the assumption that the underlying total matter density is well traced by the gas, the gas-density distribution is described by the β -model

$$\rho_g(r) = \rho_{g,0} \left[1 + \left(\frac{r}{r_c} \right)^2 \right]^{-\frac{3}{2}\beta}, \quad (1.37)$$

with central gas density $\rho_{g,0}$. The slope $\beta = \mu m_p \sigma^2 / k_B T$ encapsulates the ratio between the specific kinetic energies in galaxies and gas. The core radius r_c parameterizes the extent scale of the profile. All three parameters $\rho_{g,0}$, β , and r_c need to be constrained by observations because they cannot be derived from theory. The density distribution is not a direct observable but is closely related to the X-ray surface brightness

$$S_X = \frac{1}{4\pi(1+z)^4} \int_{-\infty}^{\infty} \epsilon dl, \quad (1.38)$$

which is proportional to the total emissivity ϵ integrated along the line of sight l . As $\epsilon \propto n_e^2$ (see Eqs. 1.34 and 1.33) and $\rho_g \propto n_e$, the surface brightness can be rephrased using Eq. 1.37 to

$$S_X(R) = S_{X,0} \left[1 + \left(\frac{R}{r_c} \right)^2 \right]^{-3\beta + \frac{1}{2}}, \quad (1.39)$$

with projected radius from the cluster centre R . The outskirts of observed surface brightness profiles are in general well described by a β -model. In the presence of central excess emission the β -model underestimates the central part and a double β -model $S_X = S_{X_1} + S_{X_2}$ can improve the quality of the fit.

1.4.4 Mass determination

The total mass is a fundamental property of a galaxy cluster and can be derived from observations at different wavelengths by applying suitable theoretical models. The determination of galaxy cluster masses is relevant for precision cosmology in order to study the evolution of the halo mass function. In addition individual mass measurements are needed to calibrate observed scaling relations.

Galaxy velocity dispersion

Photometric and spectroscopic observations of galaxies can be used to follow-up and identify cluster candidates by obtaining their redshifts and measuring the galaxies radial velocities. Assuming that the velocity distribution of member galaxies is Gaussian due to being in a common

gravitational potential, a fit to the velocity distribution of the targeted galaxies allows to separate member galaxies from projected galaxies at different redshifts. Typical velocity dispersions in galaxy clusters are of the order of 10^3 km s^{-1} (Sarazin, 1986), which corresponds to crossing times of approximately 1 Gyr. This lead to the assumption that galaxy groups and clusters are relaxed systems, which allow us to calculate the total mass using the virial theorem because the total kinetic energy of the galaxies is related to the total gravitational potential energy for a stable, self-gravitating, spherical distribution of objects with equal mass. A spherically symmetric system with gravitational radius r_G and mass-weighted radial velocity dispersion σ_r has a total virial mass of

$$M_{\text{vir}} = \frac{3r_G\sigma_r^2}{G}. \quad (1.40)$$

We note that the assumption of spherical symmetry and relaxation might not be valid in interacting systems that undergo dynamical formation.

Gravitational lensing

General relativity predicts that the path of photons traveling from a distant source to the observer gets bent by an intervening distribution of matter, a so-called gravitational lens (e.g., Schneider et al., 1993). The deflection of light and thus the distortion of the background source is inversely proportional to the distance to the optical axis defined perpendicular to the source and lens plane. Photons that pass closer to the lens are therefore bent more and the source appears more tangentially stretched. One distinguishes two main regimes of lensing, depending on the geometrical configuration expressed by the critical surface density of the lens $\Sigma_{\text{crit}} = c^2 D_S / (4\pi G D_L D_{LS})$. Here, D_S , D_L , and D_{LS} are the distances between observer and source plane, observer and lens plane, as well as source and lens plane, respectively. If the projected lens-mass density is greater than the critical surface density, multiple magnified and distorted source images are observed. This regime is referred to as strong lensing. In the weak lensing regime just slightly distorted single images of the background sources are observed. This requires a statistical analysis by averaging over many lensed images to determine the mass distribution of the lens out to large radii. This is done by creating a shear profile by measuring the intrinsic alignment and shear induced due to gravitational lensing of each background source. This shear profile is fitted by a model that reconstructs the mass distribution of the lens as a function of radius. One of the simplest model is the singular isothermal sphere, which describes the mass distribution according to $\rho = \sigma^2 / 2\pi G r^2$. Another common model is the NFW profile (see Eq. 1.35). If a galaxy cluster acts as a lens (Zwicky, 1937), weak lensing allows to determine the cluster's mass independent of its dynamical state or the type of matter the cluster is made off. This makes lensing masses reliable cluster mass estimates. There are however systematic biases in cosmic shear results, for example due to the incomplete knowledge of a telescope's point-spread function (PSF) shape and size (Massey et al., 2013). In addition, the LSS of the Universe acts as lens too, a weak effect that is the so-called cosmic shear. This, together with the superposition of other mass distributions along the line of sight, reduces the accuracy in the measurement of weak gravitational lensing.

Hydrostatic X-ray mass

In the X-ray regime, galaxy cluster masses are derived under the main assumptions of spherical symmetry and hydrostatic equilibrium between the gas and the gravitational potential Φ

$$\frac{1}{\rho_g} \frac{dP_g}{dr} = -\frac{d\Phi}{dr} = -\frac{GM(< r)}{r^2}, \quad (1.41)$$

where the total mass within radius r defines the gravitational potential. The pressure is characterized by the ideal gas equation

$$P_g = \frac{k_B}{\mu m_p} \rho_g T_g, \quad (1.42)$$

with mean molecular weight μ and the proton mass m_p . The hydrostatic mass of a galaxy cluster is derived by combining Eqs. 1.41 and 1.42 to

$$M(< r) = -\frac{k_B T_g r}{G \mu m_p} \left(\frac{d \ln \rho_g}{d \ln r} + \frac{d \ln T_g}{d \ln r} \right). \quad (1.43)$$

The measurement of the total hydrostatic mass therefore relies on extracting gas density and temperature profiles out to large radii. The assumptions of spherical symmetry and hydrostatic equilibrium might be violated for interacting systems. In addition, numerical simulations imply that neglecting kinetic gas motions, mainly turbulence and bulk motions, might bias hydrostatic mass estimates low by approximately 10% to 15% as a result of a fraction of the galaxy cluster's energy content that is not yet thermalized (Nagai et al., 2007; Meneghetti et al., 2010). A similar bias is found when comparing hydrostatic masses to weak lensing masses (e.g., Mahdavi et al., 2013; Applegate et al., 2016). X-ray measurements of the non-thermal pressure support to calibrate the biases in hydrostatic mass estimates find a lower bias of approximately 6% at r_{500} (Eckert et al., 2019). Once substructure is excised properly, profiles of ICM properties tend to follow the predictions of simple gravitational collapse beyond the cooling region (Ghirardini et al., 2019).

Gas mass

The gas mass within a given radius r can be derived by integrating the gas-density profile over the corresponding volume according to

$$M_g(< r) = \int_V \rho_g(r) dV' \quad (1.44)$$

$$= 4\pi \int_0^r r'^2 \rho_g(r') dr', \quad (1.45)$$

where the last equation holds under the assumption of spherical symmetry. The ratio between gas mass and total mass of a cluster defines the gas-mass fraction $f_g := M_g/M_{\text{tot}}$. Compared to the mass fraction of hot gas $f_g(z) = \Upsilon(z)(\Omega_b/\Omega_m)$ (Allen et al., 2011), the gas-mass fraction in cluster outskirts typically converges toward the cosmological ratio of $\Omega_b/\Omega_m \approx 15\%$. Star formation and other baryonic effects are taken into account by $\Upsilon(z)$.

Thermal Sunyaev-Zel'dovich effect

Cosmic microwave background (CMB) photons that pass through the galaxy cluster interact in approximately 1% of the cases through inverse-Compton scattering with the energetic electrons of the ICM. As a result, the CMB spectrum is blue-shifted on average. This spectral distortion is known as the Sunyaev-Zel'dovich (SZ) effect (Sunyaev and Zeldovich, 1972) and is observed in the millimeter-wavelength regime. The interaction of the CMB radiation with the hot electrons of the ICM causes a less than 1 mK distortion of the blackbody spectrum of the CMB by boosting the energies of CMB photons by approximately $k_B T_e / m_e c^2$ per collision. As a result, the CMB intensity below 217 GHz decreases, whereas the intensity at greater frequencies increases compared to the average CMB signal (see Fig. 1.5). This spectral distortion of the thermal SZ (tSZ) effect can be expressed as a relative change in the CMB temperature

$$\frac{\Delta T_{\text{SZ}}}{T_{\text{CMB}}} = f_\nu(x)y = f_\nu(x) \int n_e \frac{k_B T_e}{m_e c^2} \sigma_T dl, \quad (1.46)$$

where $x := hv/k_B T_{\text{CMB}}$ represents a dimensionless frequency, y the Compton- y parameter, $m_e c^2$ the electron's rest mass, σ_T the Thompson cross-section, and $f_\nu(x)$ is the frequency dependent function including relativistic corrections δ_{SZ} according to

$$f_\nu(x) = \left(x \frac{e^x + 1}{e^x - 1} - 4 \right) [1 + \delta_{\text{SZ}}(x, T_e)]. \quad (1.47)$$

The total SZ-signal is calculated by integrating the Compton- y parameter over the projected surface area

$$Y_{\text{SZ}} = \int y d\Omega \propto \int n_e T_e dV \propto M_g T_g. \quad (1.48)$$

The so-called integrated y -parameter Y_{SZ} depends directly on the mass and temperature of the gas and is therefore expected to have a tight correlation with the total cluster mass for a given gas mass fraction. The linear dependence of the tSZ signal on the electron density makes it less sensitive to inhomogeneities of the ICM than X-ray emission. Comparing Eq. 1.46 to the pressure of an ideal gas (see Eq. 1.42) shows that the Compton- y parameter is proportional to the integrated pressure along the line of sight. The absolute calibration therefore requires additional data. The advantage of the tSZ effect is its redshift independence, making it a unique tool to observe galaxy clusters at high redshift.

1.4.5 Self-similar model

Kaiser (1986) introduced a theoretical framework to describe observables of galaxy groups and clusters based on the following main assumptions. Galaxy clusters form from initial peaks of the density field due to gravitational collapse in a scale-free or self-similar manner. There is no preferred scale of the initial density fluctuations such that the amplitude of the density contrast is described by a power-law $\Delta(k) \propto k^n$. During the formation and evolution of clusters gravity is the dominant source of energy input into the ICM such that other physical processes do not

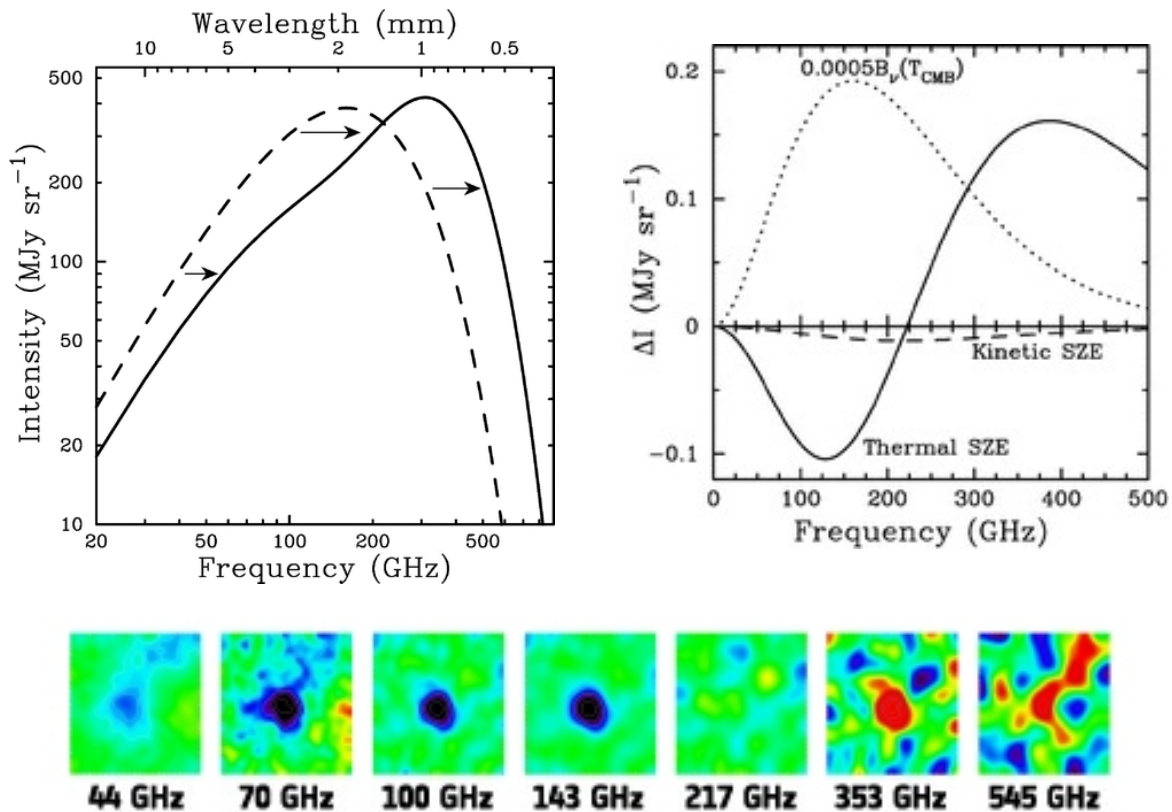


Figure 1.5: The undistorted (dashed line) CMB spectrum gets distorted when CMB photons pass through the ICM of a galaxy cluster, causing a decrement in the CMB intensity at frequencies below approximately 217 GHz and an intensity increase above this frequency. Therefore, galaxy clusters appear as a negative signal (blue) in the low frequency bands and as a positive signal (red) at higher frequencies compared to the average CMB signal (lower panel). This makes it easier to differentiate the detected clusters at low frequencies from radio-emitting galaxies, which appear as positive "hot spots" in the low and the high passbands. The upper right panel shows the relative spectral distortion. Figures taken from [Carlstrom et al. \(2002\)](#) and <http://sci.esa.int/jump.cfm?oid=47697>.

introduce additional scales. With these assumption, the self-similar model considers galaxy clusters as identical versions of one another, scaled by redshift evolution, $\rho_{\text{crit}}(z) = \rho_{\text{crit}}(0)E(z)^2$, and virial mass. Due to the assumed similar formation history, the self-similar model predicts simple power-law relations between different galaxy cluster properties, such as mass and observables. These so-called scaling relations are discussed in more detail in Sect. 1.4.6.

1.4.6 Scaling relations

Scaling relations describe the correlation between different galaxy cluster properties as power laws derived from the self-similar model. For cosmological purposes, it is particularly interesting to relate cluster quantities that are easy to measure to the unobservable cluster mass. An approximate relation exists between cluster mass and radius $M \propto r^3$. However, the redshift evolution of scaling relations in general depends on the chosen radius with in which the mass is calculated. This redshift evolution can be expressed in different parametric forms (Voit, 2005) and we choose a scale radius calculated from the spherical collapse model according to

$$M_{\Delta} = \frac{4\pi}{3} \cdot \Delta \cdot \rho_{\text{crit},0} E^2(z) r_{\Delta}^3. \quad (1.49)$$

We will provide a brief overview of the most relevant scaling relations that include X-ray properties.

Mass-temperature relation

The mass-temperature scaling directly links the energy budget of the ICM to the total mass and is therefore expected to show low scatter of the order of approximately 10–15%. Under the assumption of virial equilibrium, the mass-temperature correlation is

$$T \propto \frac{M}{r} \propto M^{2/3} E^{2/3}(z) \Delta^{1/3} \quad (1.50)$$

$$M \propto \frac{T^{3/2}}{E(z) \Delta^{1/2}}. \quad (1.51)$$

This implies that clusters of the same mass are hotter at higher redshifts. The slope of the mass-temperature relation for clusters obtained from simulations (e.g., Kravtsov et al., 2005; Nagai et al., 2007) and observations (e.g., Chen et al., 2007; Zhang et al., 2008; Vikhlinin et al., 2009b) are generally in agreement with the self-similar prediction. However, precise measurements of cluster temperatures from observed spectra require a few hundred photon counts.

Luminosity-temperature relation

Assuming a pure bremsstrahlung emissivity (Eq. 1.33), the luminosity of a galaxy cluster is expressed as

$$L \propto \epsilon r^3 \propto T^{1/2} n_e^2 r^3 \propto T^2 f_g^2 \Delta^{1/2} E(z), \quad (1.52)$$

where the last proportionality assumes $n_e \propto \rho_g$ and uses Eq. 1.51. This relation has the advantage that both observables are determined almost independently of each other. Observationally, the slope of the luminosity-temperature is found to be steeper than self-similar predictions (e.g., [Pratt et al., 2009](#); [Reichert et al., 2011](#); [Eckmiller et al., 2011](#)) and are found to be even steeper in low-mass galaxy group studies ([Ponman et al., 1996](#); [Balogh et al., 1999](#); [Maughan et al., 2012](#)).

Luminosity-mass relation

Replacing the temperature according to Eq. 1.50 in Eq. 1.52 derives the luminosity-mass relation

$$L \propto M^{4/3} f_g^2 \Delta^{7/6} E^{7/3}(z), \quad (1.53)$$

which implies that objects of the same mass are more luminous at higher redshifts. The X-ray luminosity can be determined by measuring the flux and redshift of a source, meaning that the luminosity-mass relation is particularly interesting to constrain masses in the low-photon regime, for example in all-sky surveys or for clusters at high redshift. However, the intrinsic scatter of the relation is approximately 40% (e.g., [Vikhlinin et al., 2009a](#)), driven by non-gravitational processes in the cores of clusters. Excising the cluster-core regions typically reduces the scatter by more than half (e.g. [Markevitch, 1998](#); [Mittal et al., 2009](#); [Pratt et al., 2009](#)).

1.5 Galaxy clusters as cosmological probes

Two general approaches to study cosmology rely on measuring distances to infer the geometry of the Universe or studying the evolution of structure formation. Galaxy clusters offer the opportunity to study several independent cosmological tests of different physical origin which comprise both of the aforementioned strategies. These complementary tests allow us to check for consistency among one another and to additional cosmological probes such as supernovae type Ia experiments. We summarize key aspects in this section and refer to [Allen et al. \(2011\)](#) for a more detailed review. An example of parameter constrains from various cosmological probes is shown in Fig. 1.6.

Galaxy cluster number counts

For cosmological studies, galaxy clusters are considered to occupy dark matter haloes which reside in the knots of the LSS. Clusters therefore trace the dark matter, which is a dominant part in the history of structure formation. In a nutshell, the matter density and amplitude of the density fluctuations can be constrained by measuring the number density of galaxy clusters as a function of mass and redshift, meaning by measuring the halo mass function, which is explained in detail in Sect. 1.3.3. In addition, the redshift evolution of cluster number counts puts constrains on the linear growth of density perturbations, which depends on the matter and dark energy density.

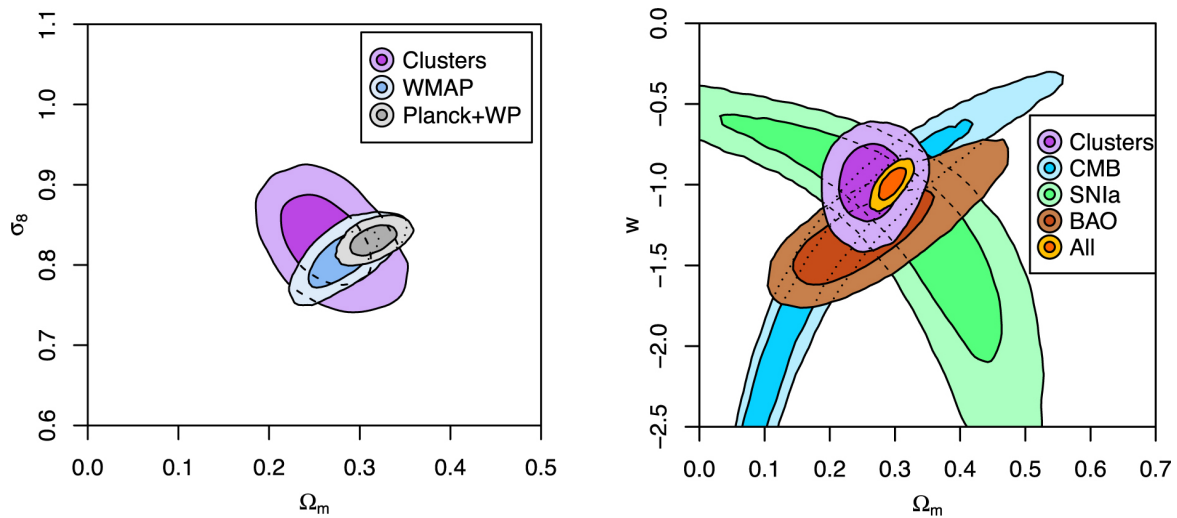


Figure 1.6: Joint 68.3% and 95.4% credibility regions for different cosmological probes and two sets of cosmological parameters (Ω_m, σ_8) and (Ω_m, w_0). The left panel shows the comparison between constraints of the mean-matter density Ω_m and the amplitude of matter perturbations σ_8 obtained from cluster counts and observations of the CMB power spectrum with the two instruments WMAP and *Planck*. The right panel shows the credibility regions for Ω_m and the dark energy equation of state w_0 from galaxy cluster data and other cosmological probes. In general, the shape and orientation of the credibility regions indicate the degeneracy level between the individual parameters, for example the strong degeneracy between Ω_m and σ_8 for cluster observations. Figures taken from [Mantz et al. \(2015\)](#).

Clustering of clusters and matter power spectrum

Measurements of the spatial distribution of clusters constrain cosmological parameters in a complementary way to other cosmological tests, which helps to break degeneracies and to improve constraining capabilities. The large-scale distribution of galaxy groups and clusters is characterized by the correlation function and constrains the matter and dark-energy densities. The matter power spectrum is the Fourier transform of the correlation function and probes the matter density and the density-fluctuation amplitude by its shape and amplitude. Large area surveys are required to obtain reliable measurements of the clustering. Clustering signals have been measured in the X-ray (e.g., [Moscardini et al., 2000](#); [Allevato et al., 2012](#); [Finoguenov et al., 2015](#); [Pacaud et al., 2016](#)), as well as in the optical with the Sloan Digital Sky Survey ([Mana et al., 2013](#)).

Baryonic acoustic oscillations

Baryonic Acoustic Oscillations (BAOs) are periodic density fluctuations of baryons and observed by wiggles in the matter power spectrum originating from the time period after photon decoupling, when the baryons and the dark matter were settling into each other's potentials. The position and amplitude of these oscillations are primarily sensitive to the geometry, as well as the baryon and dark energy content of the Universe (e.g., [Hu and Dodelson, 2002](#); [Anderson et al., 2012](#)).

Baryon fraction measurements

As discussed in Sect. 1.4.4, the total matter density can be inferred if one assumes that the baryon fraction f_b is universal and that the fraction in galaxy clusters does not differ significantly from the cosmic mean. The baryon fraction in galaxies however is affected more by non-gravitational processes due to their small extent and shallower potential well. In addition to stars as tracers of baryons in galaxies, the cosmic baryon density can be predicted by primordial nucleosynthesis models. The total matter density is then calculated according to $\Omega_m = \Omega_b/f_b$.

Absolute distance measurements as standard candles

The relation between the angular size on the sky and the physical size of a cluster determines the angular diameter distance. Once the angular diameter distance is measured, the Hubble constant can be determined according to

$$D_A = \frac{1}{1+z} \frac{c}{H_0} \int_0^z \frac{dz'}{E(z')}. \quad (1.54)$$

This approach relies on the combination of X-ray and SZ observations due to their different dependences on the gas density $\Delta T_{\text{CMB}} \propto \int n_e T_e dl$ and $S_X \propto \int n_e^2 \Lambda_{ee} dl$, respectively. The Λ_{ee} parameter is the X-ray cooling function. Defining the line-of-sight increment $dl = D_A d\theta$, the two integrals can be jointly solved for the angular diameter distance

$$D_A \propto \frac{\Delta T_{\text{CMB}}^2 \Lambda_{ee}}{S_X T_e^2} \propto \frac{cz}{H_0} \quad (1.55)$$

Combined with the redshift information of the cluster and a model of the density distribution, the Hubble parameter serves as normalization of the theoretical angular diameter distance relation. This allows galaxy clusters to be used as standard candles (Carlstrom et al., 2002; Bonamente et al., 2006).

1.6 X-ray observatories

Cosmic X-ray emission is absorbed and scattered in the earth's atmosphere and cannot be directly observed from the ground. High-energy X-ray photons can penetrate the atmosphere more easily than low-energy X-rays. Thus, one requires larger altitudes to detect softer X-ray emission. To observe galaxy clusters in X-ray for example requires observatories at at least a few hundred kilometers altitude. Due to these circumstances, X-ray astronomy developed only after the Second World War with the technology of the Aggregat 4 rocket. The first direct detection of a cosmic X-ray source, the Sun, was performed in 1949 by the United States Naval Research Laboratory. In 1962, Giacconi et al. (1962) intended to study fluorescence X-ray lines created by the interaction of the moon's surface with solar X-rays and discovered the first X-ray source outside our solar system, Scorpius X-1, as well as the cosmic X-ray background. Longer observations compared to rocket and balloon experiments were made possible with the launch of the first earth-orbiting X-ray observatory, the Uhuru satellite (Giacconi et al., 1971), in 1970. Within 3 years, Uhuru performed the first X-ray all-sky survey and detected 339 sources. Several successful X-ray missions followed this pioneering work, and we describe the two most relevant ones for this thesis in Sects. 1.6.1 and 1.6.2.

1.6.1 The ROSAT telescope

The ROentgen SATellite (ROSAT, Truemper 1982) was launched on the 1st of June 1990 and performed the first X-ray all-sky survey with an imaging telescope within the first 6 months of the mission using the Position Sensitive Proportional Counter (PSPC) detectors in the focal plane (see Fig. 1.7). Each of the two redundant PSPC detectors on-board ROSAT, PSPC-B and PSPC-C, consists of two counters. One counter is used to determine the position and energy of X-ray events by two perpendicular cathode grids and an anode grid, respectively. Another anode grid is used as anti-coincidence counter to reject background events. All grids are placed in a housing with a thin plastic entrance window. The gas mixture inside the housing absorbs an incoming X-ray photon through the photoelectric effect. The emitted primary electron ionizes the gas, causing an amount of secondary electrons approximately proportional to the photon's energy. This secondary electron cloud is amplified through the electric field between the cathode and anode grid and, as well as the induced cathode signal, further processed by pre-amplifiers. The gas supply required to operate the PSPC ran out in 1994 and until ROSAT's shutdown in February 1999, observations were performed only with the third detector on-board, the High Resolution Imager (HRI).

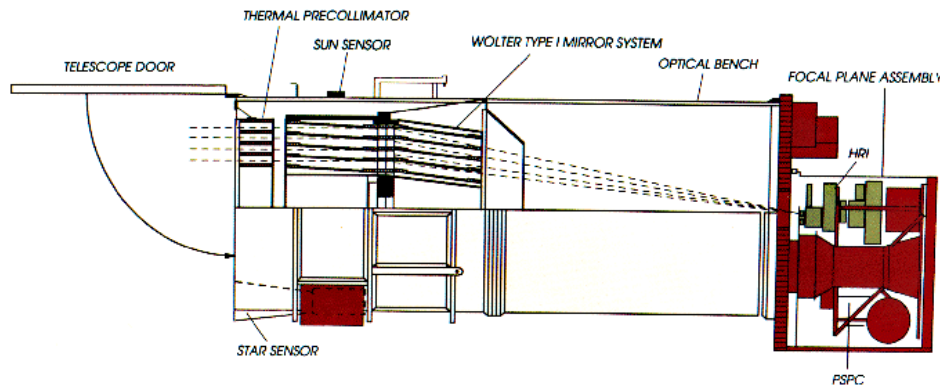


Figure 1.7: Schematic image of the ROSAT telescope. The dashed lines represent X-ray photons entering from the left. The X-rays are focused onto the focal plane assembly through a double reflection on the four nested parabola/hyperbola mirror pairs. Figure taken from <https://projects.mpe.mpg.de/heg/rosat/mission/rosat/payload.html>.

1.6.2 The eROSITA telescope

The extended ROentgen Survey with an Imaging Telescope Array (eROSITA, [Merloni et al. 2012](#); [Predehl et al. 2018](#)) is the soft (0.3–10 keV energy range) X-ray instrument on-board of the Russian/German Spectrum Roentgen Gamma (SRG) mission. It was launched on the 13th of July 2019 from the Baikonur Cosmodrome and consists of 7 identical mirror modules, each with 54 nested Wolter-I type ([Wolter, 1952](#)) shells, as well as an X-ray baffle that reduces the stray light caused by single reflections at the mirror's surface by more than 90% ([Friedrich et al., 2014](#)). Each mirror system has its own charge-coupled device (CCD) detector ([Meidinger et al., 2014](#)). A schematic diagram of eROSITA is shown in Fig. 1.8. The pn-CCD chips are back-side illuminated silicon based semiconductor detectors and are operated fully depleted. The p- (positive-) and n- (negative) layers are doped to obtain excess electron holes, that is the lack of electrons, and loosely bound excess electrons in the outer shells of the atoms used for doping, respectively. Incident radiation generates electron-hole pairs and the charge is separated and amplified. In single photon counting, the signal amplitude is proportional to the deposited charge. An improved quantum efficiency and the response to low-energy X-ray photons is achieved by a very thin pn-junction. Five of the seven CCD chips have on-chip filters in addition to the filter wheel, which block visible and ultra-violet light from the detector to minimize a potential shift or broadening of the measured X-ray lines. The two telescope modules (TMs) without on-chip filter, TM-5 and TM-7, are affected by an unexpected optical light leak, which lead to contamination with high event rates per frame in the beginning of the mission. In order not to accumulate optical-irradiation data of limited scientific use in the mass memory, the primary threshold of the analogue-to-digital converter was raised to 150 ADU. After a successful calibration and performance-verification phase (see Fig. 1.8), as well as entering its operating orbit around the second Lagrangian point (L2), the all-sky-survey phase of the SRG spacecraft started on the 8th of December 2019. eROSITA will perform eight all-sky surveys within the next four

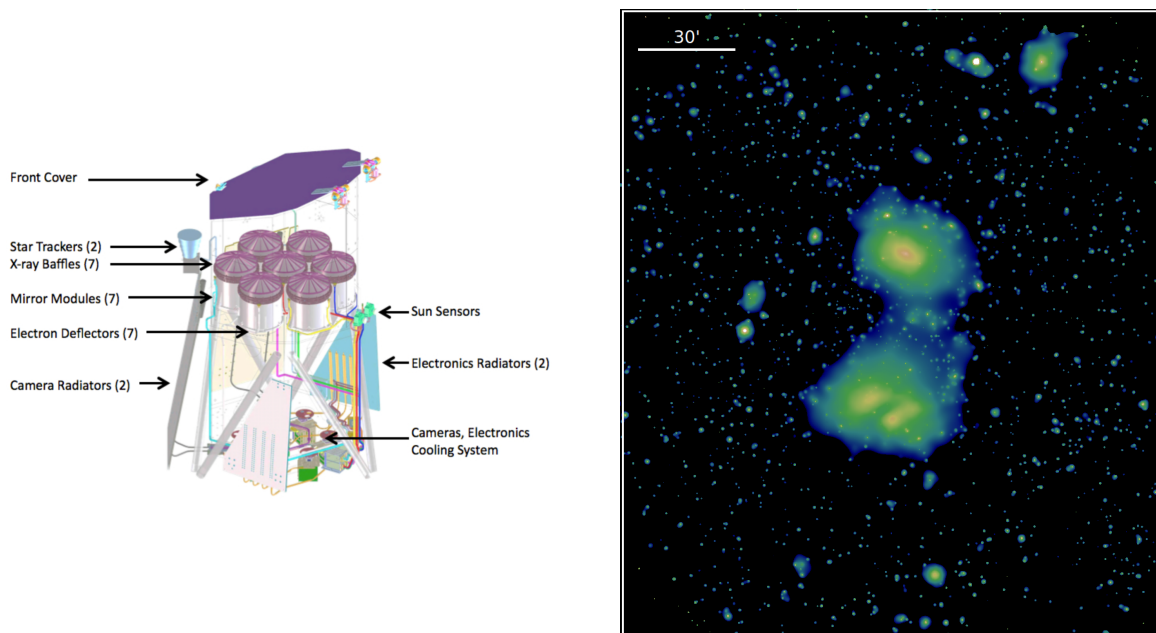


Figure 1.8: Schematic diagram of the eROSITA telescope structure (left panel) and the adaptively smoothed, exposure-corrected image of the interacting galaxy clusters Abel 3391 and Abel 3395. The observation was a target during eROSITA's performance-verification phase and the detection of the filament in between the two clusters demonstrates eROSITA's tremendous capabilities in the soft X-ray regime. Figures taken from [Merloni et al. \(2012\)](#) and <https://www.mpe.mpg.de/7360702/presskit-erosita-firstlight>.

years. In the 0.5–2 keV band eROSITA is expected to be approximately 20–30 times deeper than the RASS and in the hard band (2–10 keV) it will provide the first ever true imaging survey of the whole sky. The main science goal of the eROSITA mission is the observation of approximately one hundred thousand groups and clusters of galaxies to derive tight constraints on cosmological parameters. Furthermore, eROSITA offers the opportunity for numerous additional science topics, including AGNs, time domain astrophysics (e.g., tidal disruption events, transients, X-ray flares, gamma-ray burst afterglows, AGN variability), stars (e.g., activity cycles, stellar emission lines, X-ray irradiation of exoplanets), Solar System (e.g., charge exchange emission), diffuse emission (e.g., supernova remnants, galactic structures of soft diffuse X-ray emission), normal galaxies, and compact objects (e.g., neutron stars, pulsars, quiescent black holes).

1.7 Structure detection in X-ray images

The detection of sources in X-ray images is crucial for subsequent scientific analysis and achieved by locating regions which have a statistically significant overdensity of photons over the background. Most often this task is complicated because X-ray images contain few photons. This is particularly challenging for extended sources for which the photons are spread over a large area. In addition, different background components and instrumental characteristics make the analysis of X-ray images more difficult. The latter includes PSF effects and vignetting, meaning the decrease of the effective area with off-axis angle, which are both a function of the photon energy and the location on the detector. Detected objects are typically classified into two categories, point-like and extended sources. Extended sources, such as galaxy groups and clusters, show extended X-ray emission that might exceed the instrument's PSF. Point-like sources, such as AGNs, are unresolved objects with sizes smaller than the PSF of the telescope. The complicated shape of the PSF however might make point-like sources appear as extended or compact galaxy clusters might appear point-like. This makes a proper classification, for example by comparing PSF-model to PSF-convolved-extent-model fits to the detected sources, difficult. Possible strategies to find X-ray clusters are through optical follow-up observations (e.g., [Klein et al., 2018](#)) or analyzing the spectra of the sources. In Chapter 3 we explore a novel approach for eROSITA, namely the direct detection of sources by their extended emission. In the following subsections, we give a general overview of two relevant source-detection algorithms for this thesis.

1.7.1 Sliding cell

The sliding cell method scans an X-ray image in incremental steps using a detection cell of a predefined size and shape. In each step, the signal-to-noise ratio within the detection cell is compared to a threshold value or to the local background and the cell position is marked as source if a signal-to-noise ratio criterion is fulfilled. The cell shapes range from a simple box to a matched filter. The cell size can, for example, be fixed, adaptive as a function of observational characteristics, or increasing with successive runs of the algorithm to gain sensitivity for extended objects. However, this method has drawbacks in the detection of extended objects, especially for those with an extent that is larger than the cell size. The method can split extended sources into multiple

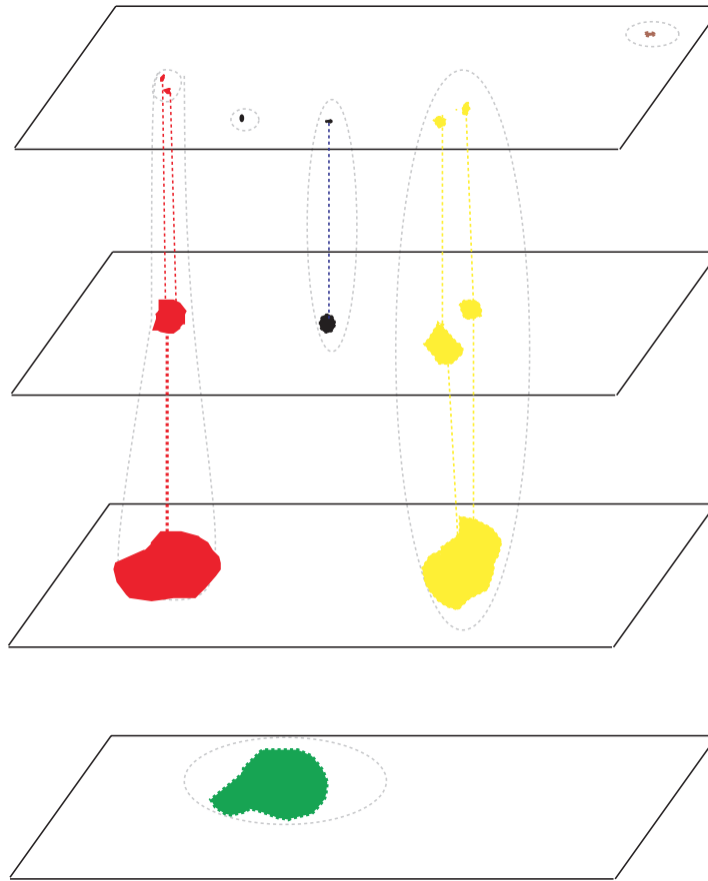


Figure 1.9: Contiguous significant wavelet coefficients for differently-sized features. If features at two successive scales reside within a linking radius, they are considered to belong to the same object. Figure taken from [Starck and Murtagh \(2006\)](#).

detections or merge close by sources within a cell and is therefore mostly robust in the detection of isolated point sources. The splitting of close-by sources and the source characterization can be improved by a subsequent maximum likelihood analysis.

1.7.2 Wavelet transform

A wavelet algorithm can isolate structures of different sizes by a multi-scale decomposition of the image through wavelet transforms ([Slezak et al., 1990](#)). The wavelet functions are scalable, oscillating, have a null normalisation, and are zero outside a given spatial regime. An image $I(x, y)$ is convolved with the a wavelet function W to obtain wavelet-coefficients planes w_a of given scale a through

$$w_a = I(x, y) * W\left(\frac{x}{a}, \frac{y}{a}\right). \quad (1.56)$$

This allows decomposition of the image into a set of wavelet coefficients planes of different scales in which structures with sizes similar to the corresponding scale are isolated (see Fig. 1.9). Wavelet transforms like the à trous (Holschneider et al., 1989) make it possible to reconstruct the original image by summing up the individual planes

$$I(x, y) = \sum_{i=1}^n w_i(x, y). \quad (1.57)$$

The significance of structures over the Poisson noise needs to be evaluated on each scale to remove insignificant features. Different statistical models have been proposed to evaluate if a wavelet coefficient is significant, meaning not as a result of noise. These include the methods of Slezak et al. (1994) who used the Anscombe transformation to transform X-ray images with high enough photon counts into an image with Gaussian noise; Vikhlinin et al. (1995) and Damiani et al. (1997) who defined significant thresholds based on the assumption of Gaussian local noise and Monte Carlo simulations, respectively; the method based on wavelet function histogram by Starck and Pierre (1998) to calculate the probability that a wavelet coefficient originated from noise. Regardless of the statistical method used, significant wavelet coefficients at each wavelet scale are kept and cross-matched between the different scales. The wavelet algorithm is sensitive to extended, low-surface-brightness objects with a variety of shapes. In addition, no prior knowledge about flat background components is necessary.

1.7.3 Wavelet decomposition

The wavelet decomposition method uses the wavelet transform to reveal structures of particular angular size within an image. In a simple wavelet analysis, the image is convolved with a family of kernels of different sizes. Significant local maxima in the convolved image represent detected sources. Similar to the sliding cell algorithm, this approach works well if the sources are isolated. If there are two (or more) sources located close-by this simple analysis might fail, especially if one of the sources is significantly brighter than the other. This is demonstrated in Fig. 1.10. The wavelet decomposition method minimizes this effect by detecting the point sources first, subtracting them from the image and then detecting extended sources in the residual image. More details about this method can be found in Chapters 2.2.1 and 3.2.1 of this thesis.

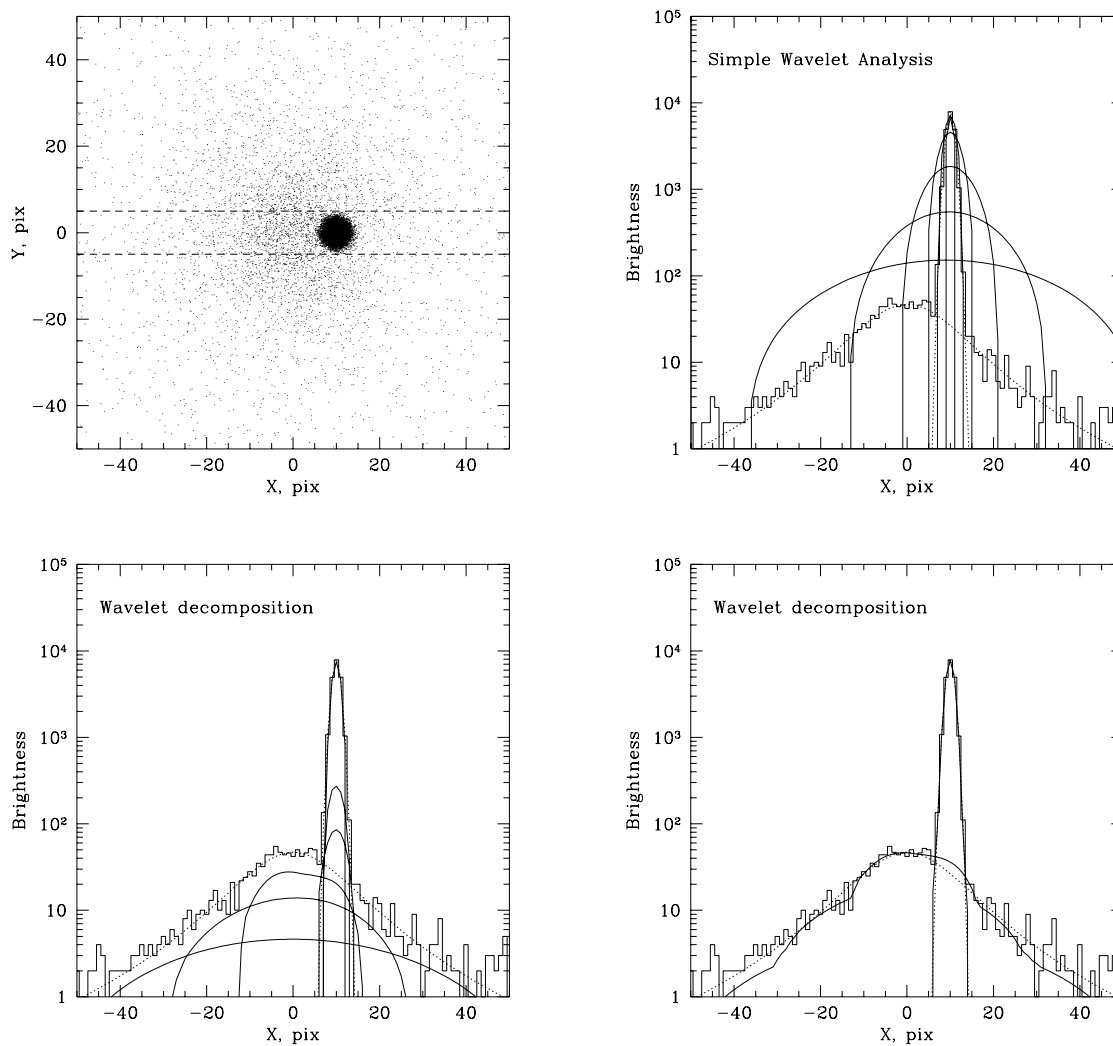


Figure 1.10: A comparison between a simple wavelet analysis (upper right panel) and a wavelet decomposition method (lower left panel) in the case of a bright point source in the vicinity of an extended source (upper left panel). The brightness profiles are extracted within the dashed strip. The point source dominates on all wavelet planes (solid lines) when using a simple wavelet convolution and the two objects will be detected as a single extended source, which might result in a false cluster detection. The wavelet decomposition method separates the point-source emission on small scales from the emission of the extended source on larger scales. Summing up the three smallest and largest scales individually allows for a decomposition of the image into the two components (lower right panel). Figure taken from [Vikhlinin et al. \(1998\)](#).

Chapter 2

Toward a characterization of X-ray galaxy clusters for cosmology

Clusters of galaxies are formed from the collapse of initial density fluctuations in the early Universe and grow hierarchically to the densest regions of the large-scale structure. This makes them the most massive ($M_{\text{tot}} \sim 10^{14} - 10^{15} M_{\odot}$) gravitationally bound structures in our universe and their virialization timescales are less than the Hubble time. The gas between the galaxies, the intra-cluster medium (ICM), has been heated to temperatures¹ of several 10^7 K by gravitational collapse. The primary emission mechanism of this hot, fully-ionized thermal plasma is thermal bremsstrahlung and line emission of heavy elements, such as iron. The majority (approximately 85 %) of the baryonic component is in the form of the hot ICM. Therefore, the most massive visible component can be traced by X-ray emission, which makes X-ray astronomy a great and important tool to study galaxy clusters. However, flux-limited galaxy cluster samples compiled from X-ray surveys suffer from selection effects like Malmquist bias, that is the preferential detection of intrinsically brighter sources (a more detailed discussion of different selection effect biases is compiled in e.g., [Hudson et al. 2010](#); [Giodini et al. 2013](#)). Another form of selection effect arises from the different core-types of galaxy clusters. In the central regions of galaxy clusters, gas is able to cool more efficiently compared to the outskirts. Several diagnostics were proposed to identify and categorize galaxy clusters according to their different core-types, for example a central temperature decrease ([Sanderson et al., 2006](#)), mass-deposition rates ([Chen et al., 2007](#)), cuspidity ([Vikhlinin et al., 2007](#)), or surface brightness concentration ([Santos et al., 2008](#)). Galaxy clusters exhibiting cool-cores show centrally-peaked surface brightness profiles, whereas non-cool-core clusters have flat profiles. In surveys differently shaped profiles are detected with different efficiencies. Even for the same brightness, cool-core clusters may be more easily detected since their surface brightness profiles are more peaked. Therefore, the central emission sticks out more above the background. The preferential detection of cool-core objects close to the detection threshold of flux-limited samples leads to the so-called cool-core bias (e.g., [Eckert et al., 2011](#); [Rossetti et al., 2017](#)). It is crucial to take such selection effects into account in cosmological studies to obtain unbiased results. One possibility to quantify these biases is running the source detection chain on well-defined simulations. The quantification of the completeness, that is the fraction of detected clusters as function of mass and redshift, requires an

accurate galaxy cluster model as input for such simulations.

Outside the core regions, scaled radial profiles (e.g., temperature, pressure, or entropy profiles) of galaxy clusters show a so-called "self-similar" behavior (e.g., [Zhang et al., 2007](#); [Ghirardini et al., 2018a](#)). It is believed that this is the result of a similar formation process of galaxy clusters, namely that tiny density perturbations in the early universe are amplified by gravitational instabilities and grow hierarchically, yielding the large-scale structure observed today. Galaxy clusters are then believed to correspond to the densest regions of the large-scale structure. This formation history motivated the theoretical consideration of the self-similar model (e.g., [Kaiser, 1986](#)), where all galaxy clusters share the same average density and evolve with redshift and mass according to prescriptions given by spherical gravitational collapse. Therefore, galaxy cluster observables such as X-ray luminosity, spectral temperature, or gas mass are correlated to the total cluster mass. Assuming gravity is the dominant process, the self-similar model predicts simple power-law relations between those cluster observables and the total mass, so-called scaling relations (e.g., [Maughan, 2007](#); [Pratt et al., 2009](#); [Mantz et al., 2010, 2016](#); [Maughan et al., 2012](#)).

In this work, we aim toward a proper characterization of galaxy cluster shapes using different surface brightness parameterizations. We investigate scaling relations between surface brightness parameters and temperature by use of the HIghest X-ray FLUX Galaxy Cluster Sample (HIFLUGCS), a statistically complete, X-ray-selected, and X-ray flux-limited sample of 64 galaxy clusters compiled from the ROSAT all-sky survey (RASS, [Voges et al. 1999](#)). In addition we study the covariances between shape and other galaxy cluster parameters. The impact of the different core-types on the obtained scaling relations and covariances are quantified. The goal of this study is to improve our understanding of galaxy cluster shapes. This serves as a basis for simulations quantifying selection effects, amongst others, for the future X-ray all-sky survey performed by the extended ROentgen Survey with an Imaging Telescope Array (eROSITA, [Merloni et al. 2012](#); [Predehl et al. 2018](#)). In addition, the obtained covariance matrices can be implemented in current cosmological studies using the COntstrain Dark Energy with X-ray galaxy clusters (CODEX) sample, for example.

Throughout this chapter a flat Λ CDM cosmology is assumed. The matter density, vacuum energy density, and Hubble constant are assumed to be $\Omega_m = 0.3$, $\Omega_\Lambda = 0.7$, and $H_0 = 70 \text{ km s}^{-1} \text{ Mpc}^{-1}$ with $h_{70} := H_0/70 \text{ km s}^{-1} \text{ Mpc}^{-1} = 1$, respectively. The natural logarithm is referred to as 'ln' and 'log' is the logarithm to base ten. All errors are 1σ unless otherwise stated.

The majority of the work in this chapter is based on the peer reviewed publication [Käfer et al. \(2019\)](#).

¹X-ray gas temperatures are often expressed in kiloelectronvolt (keV). Using the Boltzmann constant k_B , $1 \text{ keV}/k_B \approx 1.16 \cdot 10^7 \text{ K}$.

2.1 Data

2.1.1 The sample

The Highest X-ray FLUX Galaxy Cluster Sample (HIFLUGCS, [Reiprich and Böhringer, 2002](#); [Hudson et al., 2010](#)) comprises 64 galaxy clusters, constructed from highly complete cluster catalogs based on the ROSAT all-sky survey (RASS). The final flux limit of $f_X(0.1\text{--}2.4\text{ keV}) = 20 \cdot 10^{-12} \text{ erg s}^{-1} \text{ cm}^{-2}$ defines the X-ray-selected and X-ray flux-limited sample of the brightest galaxy clusters away from the Galactic plane. Although statically complete, HIFLUGCS is not necessarily representative or unbiased with respect to the cluster morphology ([Hudson et al., 2010](#); [Mittal et al., 2011](#)). [Eckert et al. \(2011\)](#) calculated a significant bias in the selection of X-ray clusters of about 29% in favor of centrally peaked cool-core objects compared to non-cool-core (NCC) clusters. We minimize these kind of selection effects by restricting our study to objects above a temperature of 3 keV. This temperature threshold excludes the low mass galaxy groups, which are closer to the HIFLUGCS flux threshold and therefore have a high cool-core fraction as discussed in the introduction of Chapter 2. Originally, the cluster RX J1504.1-0248 was not included in HIFLUGCS. This object is a strong cool-core (SCC) cluster that appears only marginally extended in the RASS, meaning that its extent is comparable to the ROSAT survey point-spread function (PSF). To avoid biasing our results because of the small extent of this system compared to the ROSAT PSF, this cluster is excluded in our full analysis. In total, we consider 49 galaxy clusters above our selected temperature threshold of 3 keV.

2.1.2 Data analysis

Pointed ROSAT observations were used whenever available. The pointed data is reduced with the ROSAT Extended Source Analysis Software package ([Snowden et al., 1994](#)) as described in [Eckert et al. \(2012\)](#). Otherwise RASS data from the public archive are used. There are 4 objects without pointed observations above our representative temperature threshold of 3 keV and excluding those from the analysis does not change our results significantly. Therefore, we do not expect our results to be affected by the use of heterogeneous data. All images for count rate measurements are restricted to the ROSAT hard energy band (channels 42–201 \approx 0.4–2.0 keV) due to higher background levels in the soft band. Luminosities are taken from [Reiprich and Böhringer 2002](#), which means that they are based on ROSAT data and are not corrected for cooling flows. The central temperature drop of the ICM in cool-core clusters biases the estimation of the cluster virial temperature, that is the temperature of the hot gas which is in hydrostatic equilibrium with the potential well of the cluster. This bias is a source of scatter in scaling relations related to temperature and can be minimized by excluding the central region for the temperature fitting. Since we are interested in how the galaxy cluster shape parameters scale with temperature, we adapt core-excised HIFLUGCS temperatures measured by [Hudson et al. 2010](#) using *Chandra*'s Advanced CCD Imaging Spectrometer (ACIS) data. We re-scale all temperatures greater than 2 keV due to the *Chandra* calibration package updates according to the [Mittal et al. \(2011\)](#) best-fit relation

$$T_{4.1.1} = 0.875 \cdot T_{3.2.1} + 0.251, \quad (2.1)$$

which links temperature measurements (in keV) between the Calibration Database (CALDB) 3.2.1 and CALDB 4.1.1. The reader is referred to the aforementioned papers in this subsection for a detailed description of individual data analysis steps.

2.1.3 Masses

We adapt M_{500} values of the "Union catalog" (Planck Collaboration et al., 2016) calculated by *Planck* Sunyaev-Zel'dovich (SZ) observations, which contains detections with a minimum signal-to-noise of 4.5. We note that SZ mass uncertainties are small due to being purely statistical and are not propagated when rescaling radii. The advantage of using masses calculated by the use of the $Y_{\text{SZ}} - M$ relation in this study is that they are statistically not covariant with X-ray parameters and less affected by galaxy cluster core states (Lin et al., 2015). Above our selected temperature threshold of 3 keV there are four galaxy clusters without counterpart in the *Planck* catalog (Hydra-A, A1060, ZwCl1215, A2052). These clusters are rejected for studies that require characteristic masses or radii. Assuming spherical symmetry, the galaxy cluster masses can be transformed into r_{500} values according to

$$r_{500} = \left(\frac{3M_{500}}{4\pi \cdot 500\rho_{\text{crit},z}} \right)^{1/3}. \quad (2.2)$$

2.2 Analysis

2.2.1 Surface brightness profiles

Using King's (1962) analytical approximation of an isothermal sphere, measured X-ray surface brightness profiles of galaxy clusters are well described² by a β -model (Cavaliere and Fusco-Femiano, 1976)

$$s_{\text{X}}(R) = \sum_{j=1}^N s_{0,j} \left[1 + \left(\frac{R}{r_{c,j}} \right)^2 \right]^{-3\beta_j+0.5}. \quad (2.3)$$

For each component j , $s_{0,j}$ is the central surface brightness, which means at projected radial distance $R = 0$, $r_{c,j}$ is the core radius of the gas distribution, and the slope β_j is motivated by the ratio of the specific energy in galaxies to the specific energy in the hot gas. For galaxy clusters exhibiting a central excess emission due to the presence of cool cores, a double ($N = 2$) β -model can improve the agreement between model and data as one component accounts for the central excess emission while the other accounts for the overall cluster emission. However, the two components are highly degenerate and except for very nearby galaxy clusters, the ROSAT point-spread function is insufficient to resolve the core regions since the apparent size of the objects is smaller. Therefore, a single ($N = 1$) beta model is used to describe the galaxy cluster emission and the central excess emission is included in the background model. Simulations (Navarro et al., 1995; Bartelmann and Steinmetz, 1996) indicate that the measured β values are biased systematically low if the range of radii used for fitting is less than the virial radius of the cluster. The advantage of using ROSAT PSPC data to determine the surface brightness profiles is

in the large field-of-view and the low background, allowing to trace the galaxy cluster emission to relatively large radii.

Wavelet decomposition

We use a wavelet decomposition technique as described in [Vikhlinin et al. \(1998\)](#). The technique is implemented as `wvdecomp` task of the publicly available ZHTOOLS³ package. The basic idea is to convolve the input image with a kernel which allows the isolation of structures of given angular size. Particular angular sizes are isolated by varying the scale of the kernel. The wavelet kernel on scale i used in `wvdecomp` is approximately the difference of two Gaussians, isolating structures in the convolved image of a characteristic scale of approximately 2^{i-1} . The input image is convolved with a series of kernels with varying scales, starting with the smallest scale. In each step, significantly detected features of the particular scale are subtracted from the input image before going to the next scale. This allows, among other things, to decompose structures of different sizes into their components, for instance in the case of point-like sources in the vicinity of an extended object. Wavelet kernels have the advantage of a simple linear back transformation, meaning that the original image is the sum of the different scales. We define a scale around $0.2 r_{500}$ up to which all emission from smaller scales is classified as contamination and is included in our background modeling for the core-modeled single β -model approach. The galaxy clusters $0.2 r_{500}$ wavelet scales are around 3–5 (2–3) for pointed (survey) observations. This corresponds to 4–16 pixel (2–4 pixel), with a pixel size of 15'' (45''). The detection threshold of a wavelet kernel convolved image is the level above which all maxima are statistically significant. [Vikhlinin et al. \(1998\)](#) performed Monte-Carlo simulations of flat Poisson background to define detection thresholds such that one expects on average 1/3 false detections per scale in a 512×512 pixel image. We adapt a slightly more stringent threshold of 5σ .

Likelihood function

Under the assumption that the observed counts are Poisson distributed, the maximum-likelihood estimation statistic to estimate the surface brightness profile parameters is chosen to be the Poisson likelihood. The so-called Cash statistic ([Cash, 1979](#)) is derived by taking the logarithm of the Poisson likelihood function and neglecting the constant factorial term of the observed counts

$$\ln \mathcal{L} \propto \sum_i O_i \ln(M_i) - M_i, \quad (2.4)$$

where M_i and O_i are the model and observed counts in bin i , respectively. The model counts of the background sources using wavelet decomposition, $B_{wv,i}$, are not Poissonian. We assume this background component without error, meaning that just the total amount of counts show dispersion. Thus, we can add this background component to the model counts ([Greiner et al.](#),

²We note that the assumption of single β -models is that the hot gas and the galaxies are in hydrostatic equilibrium and isothermal.

³Please contact A. Vikhlinin for the latest version of ZHTOOLS (avikhlinin@cfa.harvard.edu).

2016). In the same way, we add an additional particle background component, $B_{p,i}$, to Eq. 2.4 for pointed observations. Then, the likelihood function becomes

$$\ln \mathcal{L} \propto \sum_i O_i \ln (M_i + B_{wv,i} + B_{p,i}) - (M_i + B_{wv,i} + B_{p,i}). \quad (2.5)$$

A single β - plus constant background model is used to describe the surface brightness of each cluster (see Eq. 2.3, using $N = 1$ and dropping the index j)

$$s_i(R_i) = s_0 \left[1 + \left(\frac{R_i}{r_c} \right)^2 \right]^{-3\beta+0.5} + b_c. \quad (2.6)$$

The projected radii, R_i , are placed at the center of the bins. By use of the exposure map, we calculate the proper area, α_i , and the vignetting corrected mean exposure time, $\epsilon_{\text{mean},i}$. The model counts in each bin are then calculated by multiplying Eq. 2.6 with the corresponding area and exposure time

$$M_i = s_i(R_i) \cdot \alpha_i \cdot \epsilon_{\text{mean},i}. \quad (2.7)$$

2.2.2 Point-spread function

The ability of an X-ray telescope to focus photons, in other words its response to a point source, is characterized by its point-spread function. More peaked cool-core objects are affected more by PSF effects compared to non-cool-core objects. The ROSAT PSF depends amongst others on photon energy, off-axis angle and observation mode. A detailed description of the ROSAT PSF functions is presented in Boese (2000). We use the Python package `pyproffit`⁴ to calculate PSF mixing matrices based on Eqs. 7 and 30 of Boese (2000) for pointed and survey observations, respectively. These matrices are folded in our surface-brightness-profile-fitting method to obtain PSF unconvolved parameters.

2.2.3 Emission measure profiles

This subsection describes our approach to obtain background subtracted self-similar scaled emission measure profiles. First, the outer significance radius and background level of each galaxy cluster are iteratively determined using the growth curve analysis method (Böhringer et al., 2000; Reiprich and Böhringer, 2002). The outer significance radius determines the maximum radius out to which galaxy cluster emission is detected and thus to which radius each profile is extracted. Background-subtracted and logarithmically binned surface-brightness profiles are converted into emission measure profiles using the normalisation of a partially absorbed Astrophysical Plasma Emission Code (APEC) model

$$\frac{10^{-14}}{4\pi[D_A(1+z)]^2} \int n_e n_H dV. \quad (2.8)$$

The total weighted hydrogen column density (calculated with the method of Willingale et al. (2013))⁵ is used to describe the absorption by the atomic and molecular Galactic column density

⁴<https://github.com/domeckert/pyproffit>

⁵<http://www.swift.ac.uk/analysis/nhtot/index.php>

of hydrogen. Metallicities are fixed to $0.35 Z_\odot$ and the abundance table compiled by [Anders and Grevesse \(1989\)](#) is used. The emission measure along the line-of-sight,

$$EM(R) = \int n_e n_H dl, \quad (2.9)$$

is self-similar scaled according to [Arnaud et al. \(2002\)](#) and

$$T \propto (E(z)M_{500})^{2/3} \quad (2.10)$$

by

$$\Delta_z^{3/2} (1+z)^{9/2} \left(\frac{E(z)M_{500}}{2 \cdot 10^{15} M_\odot} \right)^{1/3}, \quad (2.11)$$

where Δ_z is calculated using the density contrast, Δ_c , and matter density parameter at redshift z , $\Omega_z = \Omega_m(1+z)^3/E(z)^2$, according to

$$\Delta_z = \Delta_c \Omega_m / (18\pi^2 \Omega_z). \quad (2.12)$$

Under the assumption that the cluster has just virialized, [Bryan and Norman \(1998\)](#) derived an analytical approximation of Δ_c for a flat universe from the solution to the collapse of a spherical top-hot perturbation

$$\Delta_c = 18\pi^2 + 82w - 39w^2, \quad (2.13)$$

with $w = \Omega_z - 1$.

2.2.4 Scaling relations

In this subsection we describe the basic principle of our linear regression routine to obtain scaling relations. A set of two variates, x/y , is fitted by a power-law relation according to

$$\log y/n_y = m \cdot \log x/n_x + b. \quad (2.14)$$

The pivot elements, $n_{x/y}$, are set to the median along a given axis, such that the results of the slope and normalisation are approximately uncorrelated.

Likelihood function

Linear regression of the scaling relations is performed using a Markov chain Monte Carlo (MCMC) posterior sampling technique. We adapt an N dimensional Gaussian likelihood function

$$\mathcal{L} = \prod_{n=1}^N \frac{1}{2\pi \sqrt{\det(\Sigma_n + \Lambda)}} \exp\left(-\frac{1}{2} \tilde{r}_n^T (\Sigma_n + \Lambda)^{-1} \tilde{r}_n\right), \quad (2.15)$$

extended compared to [Kelly \(2007\)](#) to account for intrinsic scatter correlation. The intrinsic scatter tensor, Λ , is described in more detail in Sect. 2.2.4. The uncertainty tensors Σ_n account

for measurement errors in the independent and the dependent variables and \tilde{r}_n denote the residual vectors. For illustration purposes, this is how these two objects would look like in a bivariate example:

$$\tilde{r}_n = \begin{pmatrix} x_n - \tilde{x}_n \\ y_n - m \tilde{x}_n - b \end{pmatrix} \quad (2.16)$$

$$\Sigma_n = \begin{pmatrix} \sigma_{x,n}^2 & 0 \\ 0 & \sigma_{y,n}^2 \end{pmatrix} \quad (2.17)$$

In this study, the correlation between different measurement errors in the uncertainty tensor is set to zero. The "true" coordinate \tilde{x}_n is normal-scattered according to the intrinsic scatter tensor via

$$\begin{pmatrix} \hat{x}_n \\ \hat{y}_n \end{pmatrix} \sim \mathcal{N} \left(\begin{pmatrix} \tilde{x}_n \\ m \tilde{x}_n - b \end{pmatrix}, \Lambda \right). \quad (2.18)$$

We integrate out, which means that we marginalize over, \hat{x}_n and \hat{y}_n . The scatter along the independent axis, λ_x , of the intrinsic scatter tensor is fixed to avoid degeneracies. This means that for this study the intrinsic scatter in temperature is fixed to 20%, that is $\lambda_T = 0.11$ (Kravtsov et al., 2006). The correlation between the intrinsic scatter values of the two variates x and y , λ_{xy} , is of particular interest for this study and will be described in more detail in Sect. 2.2.4. We use the emcee algorithm and implementation (Foreman-Mackey et al., 2013) for optimization. A chain is considered as converged when the integrated autocorrelation time is greater than one-hundredth of the chain length.

Covariance

The linear relationship and thus the joint variability between two or more sets of random variables can be quantified by the covariance between those variates. In the simple case of two variables x and y , each with a sample size of N and expected values \bar{x} and \bar{y} , the covariance is given by

$$\text{cov}(x, y) := \frac{1}{N-1} \sum_{i=0}^N (x_i - \bar{x}_i)(y_i - \bar{y}_i). \quad (2.19)$$

The degree of correlation can be calculated by normalizing the covariance to the maximum possible dispersion of the single standard deviations λ_x and λ_y , the so-called Pearson correlation coefficient:

$$\lambda_{xy} := \frac{\text{cov}(x, y)}{\lambda_x \lambda_y}. \quad (2.20)$$

The Pearson correlation coefficient can take values between -1 and $+1$, where 0 means no linear correlation and $+1$ (-1) means total positive (negative) linear correlation. In the general case of n

sets of variables $\{X_1\}, \dots, \{X_n\}$, the covariances can be displayed in a matrix, where the first-order covariance matrix is defined by

$$\Lambda_{l,m} := \text{cov}(X_l, X_m). \quad (2.21)$$

In the previous example of two variables x and y , the covariance matrix reads

$$\Lambda = \begin{pmatrix} \text{cov}(x, x) & \text{cov}(y, x) \\ \text{cov}(x, y) & \text{cov}(y, y) \end{pmatrix} = \begin{pmatrix} \lambda_x^2 & \lambda_{xy}\lambda_x\lambda_y \\ \lambda_{xy}\lambda_x\lambda_y & \lambda_y^2 \end{pmatrix}. \quad (2.22)$$

The latter equality makes use of Eq. 2.19, which implies that the covariance of a variate with itself, that is $\text{cov}(x, x)$, reduces to the variance of x or the square of the standard deviation of x . The off-axis elements are rewritten by solving Eq. 2.20 for the covariance and using the symmetry $\lambda_{xy} = \lambda_{yx}$.

Calculating the Pearson correlation coefficient between the ranked variables is a non-parametric measure of a monotonic relationship between the variables and is called the Spearman rank-order correlation coefficient.

Selection effects

As already discussed in the introduction of Chapter 2, centrally peaked galaxy clusters are more likely to enter an X-ray selected sample due to their enhanced central emission. [Mittal et al. \(2011\)](#) investigated this effect by applying the HIFLUGCS flux limit to Monte Carlo simulated samples. Assuming HIFLUGCS being complete, one can vary the input fractions of different core-types in the simulations to match the observed ones. The intrinsic scatter increases the normalization of the luminosity-temperature relation because up-scattered clusters have a higher chance of lying above the flux threshold. In this study, we are not trying to determine the true luminosity-temperature relation but are interested in the residuals of the sample with respect to the mean to study the intrinsic scatter covariances. Therefore, we are neglecting Malmquist bias in the parameter optimization, although it is present in HIFLUGCS. To investigate the effect of Malmquist bias on the best-fit shape-temperature relation parameters and the intrinsic scatter correlation coefficients, we artificially decrease the luminosity-temperature relation normalization and find that the differences are insignificant.

2.2.5 Cool-core classification

[Hudson et al. \(2010\)](#) used HIFLUGCS to compare 16 different techniques to differentiate cool-core and non-cool-core clusters. The central cooling time, t_{cool} , was found to be suited best and used to classify clusters into three categories. Clusters with central cooling times shorter than 1 Gyr are classified as strong-cool-core (SCC) clusters. They usually show characteristic temperature drops toward the center and low central entropies. Clusters exhibiting high central entropies and cooling times greater than 7.7 Gyr are classified as non-cool-core (NCC) clusters. In intermediate class with cooling times in between those of SCC and NCC clusters are classified as weak-cool-core (WCC) clusters. We adapt the [Hudson et al. \(2010\)](#) classification scheme and

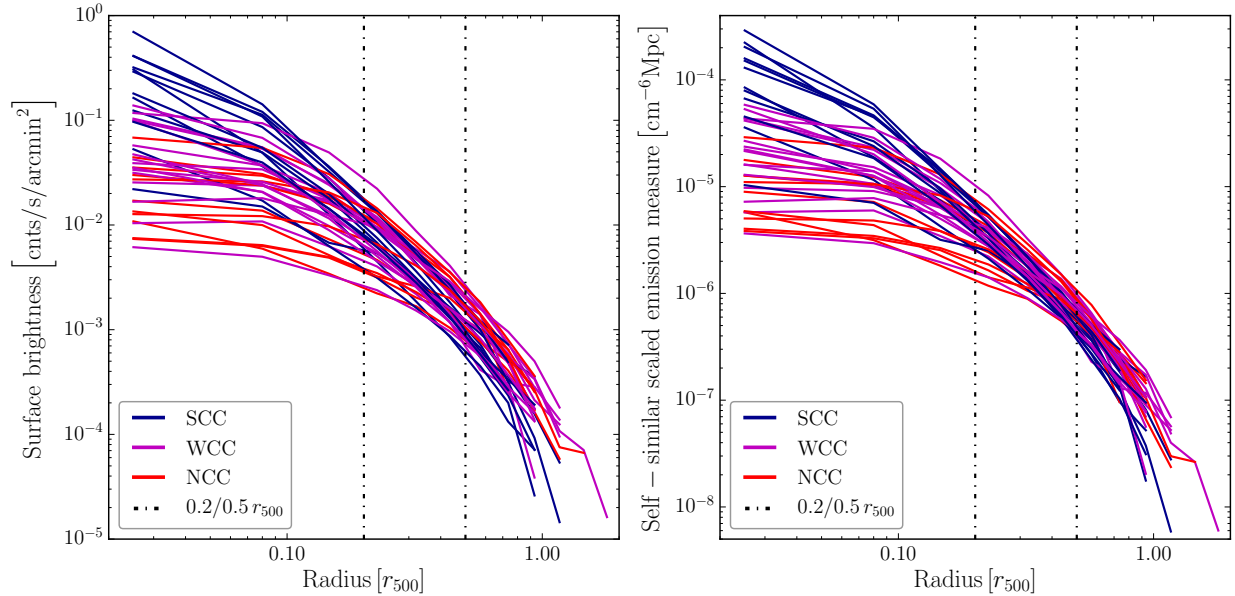


Figure 2.1: Surface brightness (left panel) and self-similar scaled emission measure profiles (right panel) for HIFLUGCS objects with temperatures greater than 3 keV. Strong-cool-core, weak-cool-core, and non-cool-core clusters are labeled as SCC, WCC, and NCC, respectively.

categorization of HIFLUGCS clusters for this study. There are 45 galaxy clusters above our selected temperature threshold of 3 keV with mass estimates in the *Planck* "Union catalog". The amount of each core-type category is 15, 16, and 14 for SCC, WCC, and NCC, respectively. For one of the SCC and three of the WCC objects, no ROSAT pointed observations are available and RASS data is used.

2.3 Emission measure profiles

This section describes a model-independent way to test the surface brightness (SB) behavior between different core-type populations by comparing their background subtracted self-similar scaled emission measure (EM) profiles. We show the SB and self-similar scaled EM profiles in Fig. 2.1. Outside the cluster core the galaxy clusters show self-similar behavior, as already discussed in several previous studies (e.g., [Vikhlinin et al. 1999](#)). The self-similar scaled EM profiles show a smaller intrinsic scatter compared to the surface brightness profiles in the 0.2–0.5 r_{500} range. It is reduced by 28% (33%) with respect to the median (weighted mean). To investigate possible differences between the core-type populations, the EM profiles are stacked according to their core types by calculating the weighted mean and the median, as shown in the top panel of Fig. 2.2. The bottom panel of Fig. 2.2 shows the ratio of the average EM profiles sorted according to their core types. The statistical errors on the weighted means or medians are very small. The error bars indicated on the plot correspond to uncertainties calculated by bootstrapping the data, that is by shuffling the profiles with repetition, repeating the operation

10 000 times and computing the median and percentiles of the output distribution. The bootstrap errors thus include information on the sample variance and non-Gaussianity of the underlying distribution.

The weighted mean profiles reveal in a model-independent way the existence of subtle differences between the galaxy cluster populations. The amplitude of this effect between SCC and NCC clusters in the $0.2\text{--}0.5 r_{500}$ radial range is up to 30% and confirms the finding of [Eckert et al. \(2012\)](#). Compared to the heterogeneous sample of [Eckert et al. \(2012\)](#) HIFLUGCS is statistically complete, which confirms the result in a more robust way. If true, this finding implies that the outskirts are affected by the core-type and a detection algorithm tailored to the galaxy cluster outskirts will be more sensitive to the more abundant NCC objects, which needs to be taken into account in selection functions. In addition one could determine the statistical likelihood for the core-state of a particular galaxy cluster. However, the asymmetric bootstrap errors indicate an underlying non-Gaussian distribution or that the sample is affected by outliers. The median profiles, which are more robust against outliers, do not reveal the same trend of the emission measure ratios. As a test, we exclude the strong cool-core profile that deviates most with respect to the median within $0.2\text{--}0.5 r_{500}$ (Abell 3526). This cluster also shows the smallest statistical errors in this radial range. The weighted mean ratios resembles well the trend of the median when excluding this single cluster from the analysis. This reveals that the weighted mean is driven by an outlier with small statistical errors. Therefore, we conclude that there is no indication of a systematic core-type differences in the galaxy clusters $0.2\text{--}0.5 r_{500}$ radial range. Nevertheless, this comparison is useful because outliers like Abell 3526 will affect the selection function. The investigation of a possible redshift evolution of this analysis is left to a future study. Beyond $0.5 r_{500}$ the difference between SCC and NCC clusters become larger. [Eckert et al. \(2012\)](#) discussed gas redistribution between the core region and the outskirts as possible explanation. In this scenario, the injected energy due to a merging event flattens the density profile of interacting objects. Assuming that NCC clusters are more likely to have experienced a recent merging event, their self-similar scaled EM profiles would be different compared to CC objects. Another explanation could be the current accretion of large-scale blobs. Clusters with higher mass accretion rates show a larger fraction of non-thermal pressure in simulations ([Nelson et al., 2014](#)). Again assuming that NCC objects are merging clusters, the discrepancies can be explained by the different non-thermal energy content. However, this scenario seems unlikely since we expect to detect such structures in our wavelet images. An additional explanation can be that the dark matter halos of NCC and CC objects have different shapes and thus a different concentration at a given radius.

2.4 Large-scale center and ellipticity

The wavelet decomposition allows us to study galaxy cluster parameters on large scales. The one scale around $0.2 r_{500}$ is used to determine the center and ellipticities using the `SExtractor` program ([Bertin and Arnouts, 1996](#)). This minimizes the impact of the different core states on these parameters. The chosen scale contains most of the cluster counts outside the core region and is therefore a good tracer for large-scale properties. Including scales up to around $0.5 r_{500}$

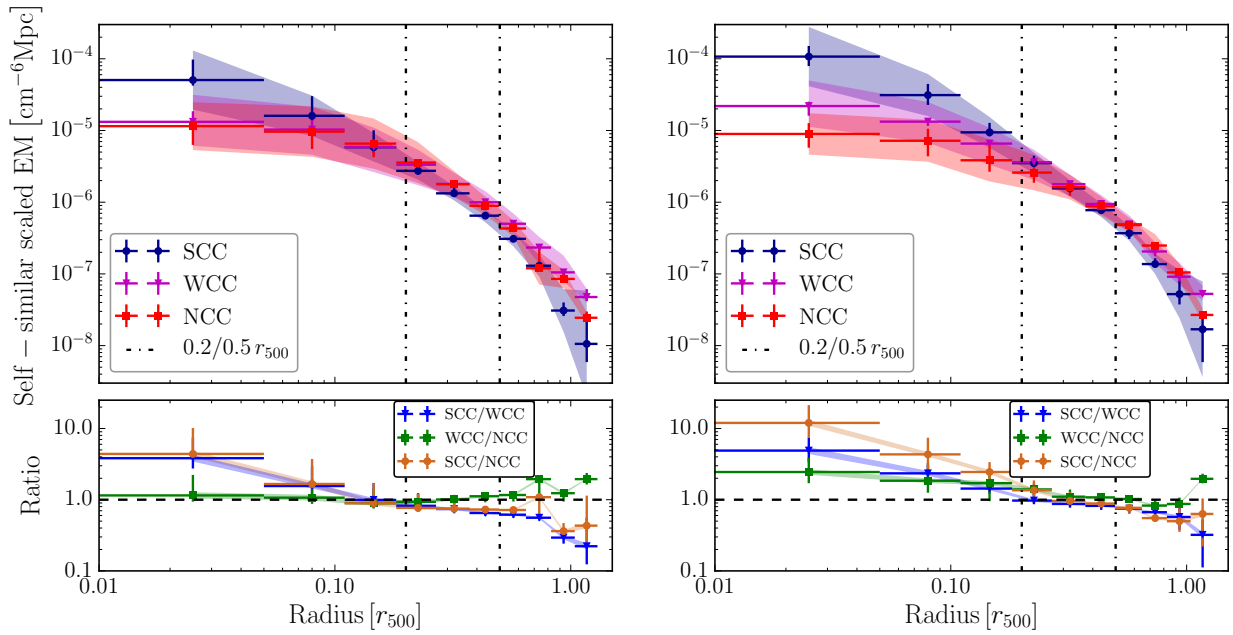


Figure 2.2: Top panels: Weighted mean (left panel) and median (right panel) self-similar scaled emission measure profiles for the individual core types of HIFLUGCS objects with temperatures greater than 3 keV. Bottom panels: Ratio of the self-similar scaled emission measure profiles between the different core type populations. Shown error bars were estimated with 10 000 bootstrapping iterations. The shaded regions represent the intrinsic scatter values of each bin.

(an additional 1–3 scales) shows that the median and mean difference in ellipticity is just about 10%. The ellipticity, e , of an ellipse with major-axis, e_1 , and minor-axis, e_2 , is defined as

$$e = 1 - e_2/e_1 \quad (2.23)$$

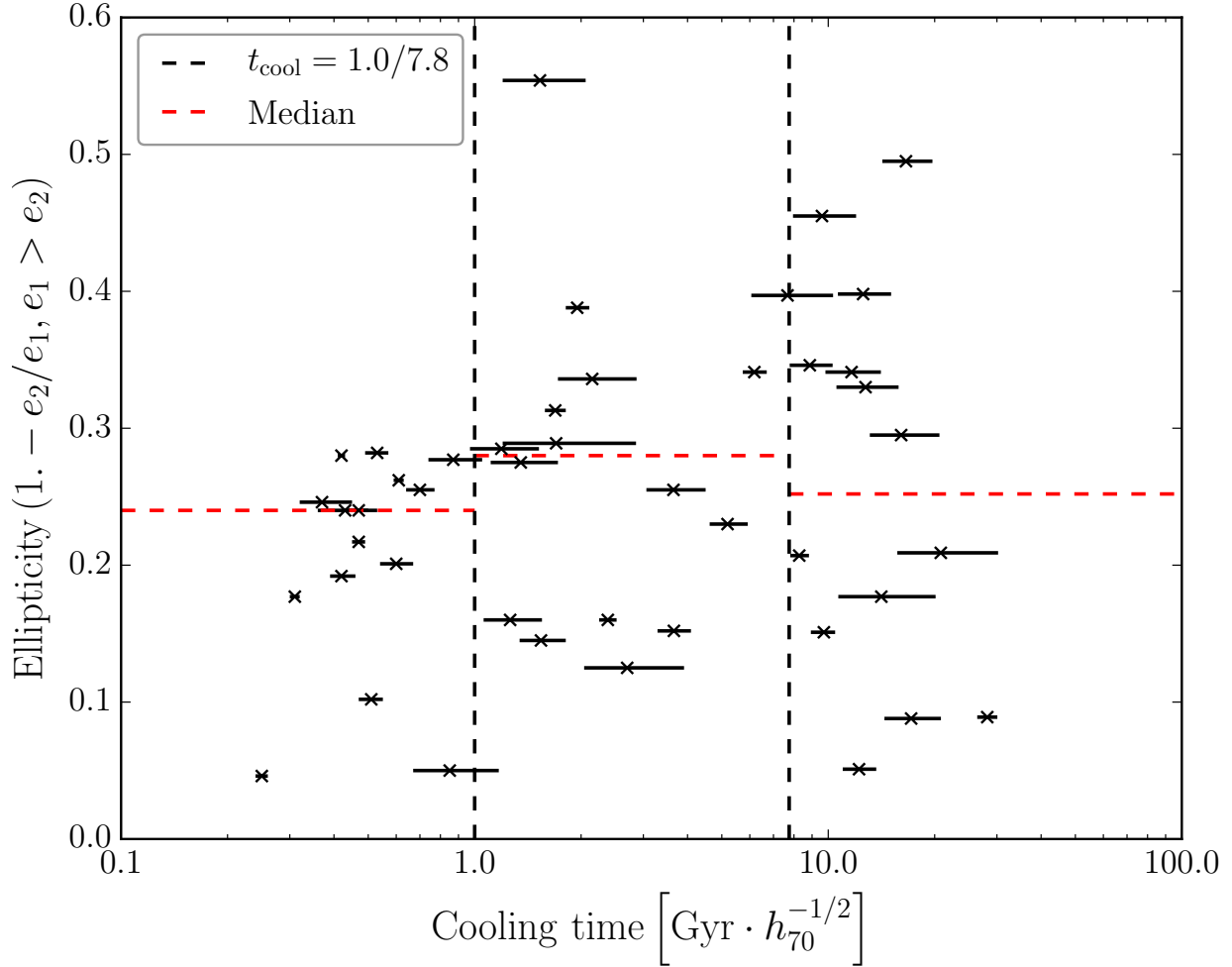
and is shown as function of the cooling time in Fig. 2.3. The two parameters do not show a significant correlation (Spearman rank-order correlation coefficient of 0.17). The medians and sample standard deviations in the three bins are (0.24, 0.28, 0.25) and (0.08, 0.12, 0.14), respectively. There are no highly elliptical clusters with short cooling times. Therefore, selecting clusters above an ellipticity of approximately 0.3 creates a sample without SCC objects. The universality of this result needs to be confirmed with galaxy cluster samples of larger sizes.

We perform a similar stacking analysis as in Sect. 2.3, where the sample is divided into 3 sub-classes according to ellipticity, rather than core-state. The weighted mean and median profiles are shown in Fig. 2.4. The median profiles do not show a difference between the sub-classes except in the core region and the very outskirts.

We quantify the covariance between ellipticity and core radius in kpc. For a core-modeled single β -model and fixed β -parameter, the Spearman rank-order correlation coefficient is 0.20, which is no strong indication for a correlation. Allowing the β -parameter to vary introduces a small positive correlation coefficient of 0.33. We see a similar behavior for best-fit core radii using a single β -model.

Clusters with large cooling times show a large range of 2D ellipticities. Assuming that they originate from the same population in 3D, the large scatter of ellipticity might be explained by projection effects, meaning that triaxial halos with random orientations will yield a wide range of observed 2D ellipticities. The verification of this effect using simulations is left to a future study. Considering ellipticity adds supplementary information since it is not significantly correlated with the core radius. The ellipticity in the galaxy cluster outskirts traces the amount of baryon dissipation (Lau et al., 2012). Thus, ellipticity is linked and may help to constrain cosmological parameters like the amplitude of the matter power spectrum, σ_8 . Halos form later for lower σ_8 values and are therefore on average more elliptical (Allgood et al., 2006; Macciò et al., 2008). In addition, measuring ellipticity on several scales allows to indirectly study large-scale gas rotation in galaxy clusters (Bianconi et al., 2013). This allows us to test if the ICM is in hydrostatic equilibrium, an often made assumption in X-ray mass measurements. This makes the ellipticity an interesting survey measure for the future eROSITA X-ray all-sky survey, where we expect a range of ellipticities. The ratio of the weighted mean profiles between objects with low and high ellipticity shows a slight offset. Since this offset is not visible in the median profile, it cannot solely be explained by the larger non-Gaussianity per bin of elliptical surface brightness distributions extracted in circular annuli.

Hashimoto et al. (2007) studied the relationships between the X-ray morphology and several other cluster properties using a heterogeneous sample of 101 clusters taken from the *Chandra* archive, out of which 18 objects are represented in HIFLUGCS. The ellipticity measurements are in agreement with our study within a factor of approximately two, except for A0399. For this cluster, the ellipticity calculated by Hashimoto et al. (2007) is a factor of 5.6 larger (0.284 compared to 0.051). We note that the semi-major and semi-minor axis are calculated in the



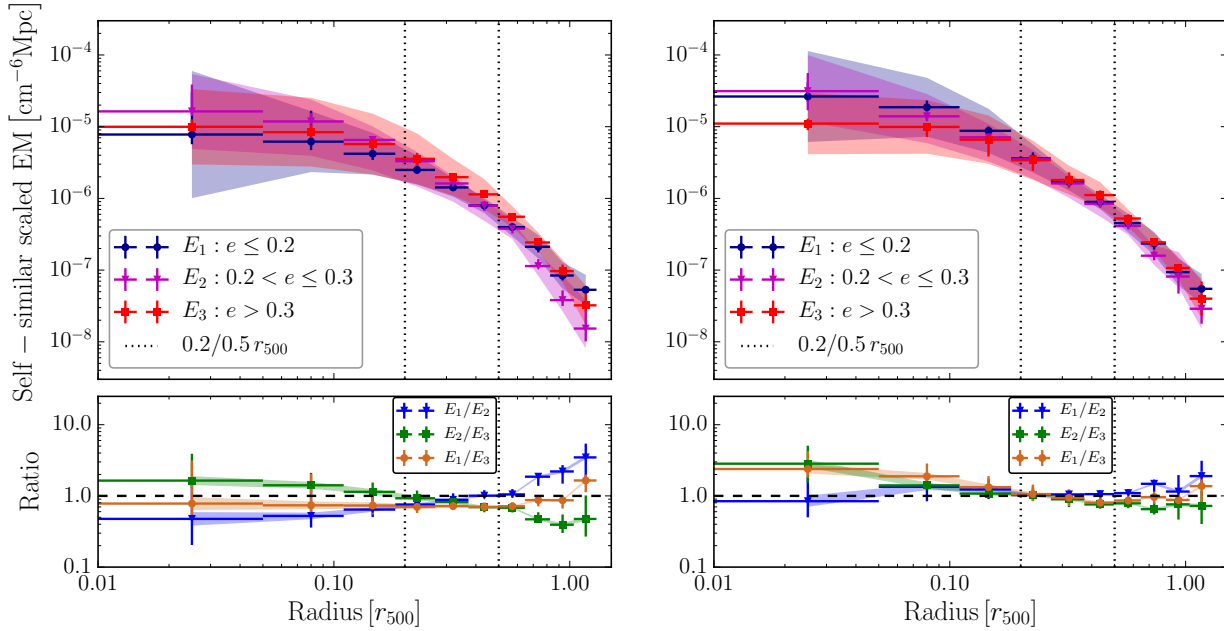


Figure 2.4: Same as Fig. 2.2, except that the classification is done according to ellipticity.

same way, that is by the 2nd-order moments but we subtracted the central excess emission of the cluster before. Including the central excess emission brings our results in better agreement with [Hashimoto et al. \(2007\)](#), especially in the case of A0399. For a single β -model description of the surface brightness profile, they find a slightly larger Spearman rank-order correlation coefficient of 0.37, compared to 0.26, between ellipticity and core radius in kpc.

2.5 Analysis of the residuals

In this section we quantify how well the different model parameterizations represent the underlying HIFLUGCS surface brightness profiles. All profiles are fitted over the full extracted radial range (see Fig. A.2) using an MCMC posterior sampling technique, taking uncertainties in the measured surface brightness into account. In case of the core-modeled single β -model all contaminating sources, including the excess emission in the cluster core, are modeled according to Eq. 2.5. For the single β -model fitting procedure we perform a classical approach of masking contaminating sources that are detected on the wavelet images. This includes point-like sources or extended emission like substructure but not emission from the cluster core. Thus the likelihood functions for the two cases are different because for a single β -model, $B_{wv,i}$ in Eq. 2.5 is equal to zero for all i . The choice of priors is discussed in Appendix A.2. The background is modeled with an additive constant. We note that not subtracting the background before fitting introduces a positive degeneracy between the best-fit slope of the β -model and the background level. In this framework, residuals are defined as (data-model)/model, meaning that positive (negative) residuals indicate that the model under- (over-) predicts the observed surface brightnesses. We focus

particularly on the $0.2\text{--}0.5 r_{500}$ radial range because most of the galaxy cluster counts outside the non-scalable core regions are expected there.

2.5.1 Discussion: Single β -models

A single β -model is a widely used description to fit surface brightness profiles, especially in the low statistics regime. Therefore, it is also commonly used to detect extended sources in X-ray surveys. In Fig. 2.5 (top left panel), we show the fractional median of the residuals from a single β -model in the $0.2\text{--}0.5 r_{500}$ radial range as function of core radius. There is a clear trend of positive residuals toward smaller core radii. This means that the flux in the outskirts is systematically under-predicted, especially for SCC objects (see Sect. 2.5.3). In addition, the core radii of objects that exhibit cool-cores are systematically biased low since a single β -model lacks degrees of freedom to model the central excess emission. Due to higher photon statistics in the core region, a single β -model fit tends to be driven by the inner radial bins. As an additional test we reduce the weight of the core region in the fitting procedure by assuming that the variance in the Gaussian likelihood function is underestimated by a given fractional amount $f = 0.1$. The qualitative behavior of the residuals remains the same. In cases where the cluster outskirts are poorly fitted, the background level is not determined properly as well because its level compensates for the poor fit in the outskirts. This influences the β value determination as already discussed. The median of the β parameters is 0.59 and thus smaller than the often assumed generic value of $2/3$. The best-fit values of the surface brightness parameters are in good agreement with [Reiprich and Böhringer \(2002\)](#).

The single β -model residuals for individual clusters have a wavy form. We investigate different functional forms to describe the common deviations from a single β -model, but no significant common form of the residuals could be found. The scatter around zero and bias in the $0.2\text{--}0.5 r_{500}$ radial bin are 0.092 and 0.032 ± 0.003 , respectively. The non-zero bias reflects the same finding as discussed above.

The residuals in the $0.2\text{--}0.5 r_{500}$ radial range from a single β -model with fixed β parameter ($\beta = 2/3$) is shown in the bottom left panel of Fig. 2.5. The amplitude of the residuals for SCC objects increases up to over 40%. Fixing the β parameter increases the scatter and bias to 0.161 and 0.066 ± 0.003 , respectively.

2.5.2 Discussion: Core-modeled single β -models

The negative effects of a single β -model as described in Sect. 2.5.1 are reduced when modeling the excess core emission by adding the counts on the small scales of the wavelet decomposition to the model counts in the Poisson likelihood function (see Sect. 2.2.1). The residuals in the $0.2\text{--}0.5 r_{500}$ radial range are shown in Fig. 2.5 (top right panel). The measured residuals scatter around zero and there is no bias between individual core types visible. The scatter around zero in the $0.2\text{--}0.5 r_{500}$ radial bin is slightly reduced compared to the single β -model (0.074). Most importantly, the bias gets more consistent with zero (-0.004 ± 0.003). In case of a fixed β parameter (bottom right panel of Fig. 2.5), the bias of a core-modeled single β -model is consistent with zero (-0.001 ± 0.003) and the scatter is slightly increased (0.087). The median of the β

parameters is larger compared to the single β -model case and with 0.696 close to the generic value of $2/3$.

To verify our core-modeling method and to confirm its results we excise the core region ($< 0.2 r_{500}$) in the single β -model fitting procedure. This is an independent way to avoid the single β -model fit to be driven by the non-scalable core emission and to reduce residuals between model and data in the cluster outskirts. In more than 90% of the cases, we find that this approach delivers comparable best-fit parameters for β and core-radii as when modeling the core emission. Due to excluding data, the constraining power is reduced and the degeneracy of the shape parameters with the β -model normalization is larger. In several cases, this results in a larger mismatch of the β -model fluxes compared to the real flux of the objects.

2.5.3 Flux comparison

This section compares the overall model flux, as well as the model flux in the cluster outskirts for the single β -model and core-modeled single β -model to the measured flux in the corresponding radial range. For each model, we calculate the cluster count rate by integrating a single β -model with the corresponding best-fit parameters in a given radial range, that is $0-r_x$ (the outer significance radius) for the overall model flux and $0.2-0.5 r_{500}$ for the flux in the outskirts. We are interested in flux ratios, in which the count rate to flux conversion factors of individual clusters cancel each other out. We calculate the total flux of the single β -model including the central excess emission and subtract the wavelet-detected central excess emission in the core-modeled case. The median of the measured fluxes in the outskirts and the overall fluxes of the NCC and WCC objects agree very well with each other. The measured overall single β -model fluxes of the SCC objects are on average approximately 23% larger compared to the measured overall core-modeled fluxes and the flux ratio has an intrinsic scatter of approximately 14% around the median. The median accuracy between model and measured total flux is within approximately 4% (2%) for the (core-modeled) single β -model, regardless of the core-type or if the β value is free to vary or fixed to $2/3$. The flux in the outskirts of the core-modeled single β -model has the same median accuracy of 2%. For the single β -model, the accuracy stays at the 4% level for WCC and NCC objects. For SCC objects, for the single beta-model case, the flux in the outskirts is biased low by 6% and increases to 10% when β is fixed to $2/3$; meaning that the bias is 3–5 times larger than for the core-modeled case. In all cases, the intrinsic scatter values of the ratios are below 6%. The Spearman rank-order correlation coefficients do not reveal a significant correlation between the flux underestimation and the cluster temperature.

2.6 Scaling relations

This section describes how the shape parameters scale with temperature and how they correlate with luminosity. In Fig. 2.6, we show the core radius as a function of temperature, where the β parameter is fixed to $2/3$ to avoid degeneracies between the surface brightness parameters. We note that the overall picture does not change when fixing β to the median of the full population or the medians of the individual core-type populations. To account for a possible temperature de-

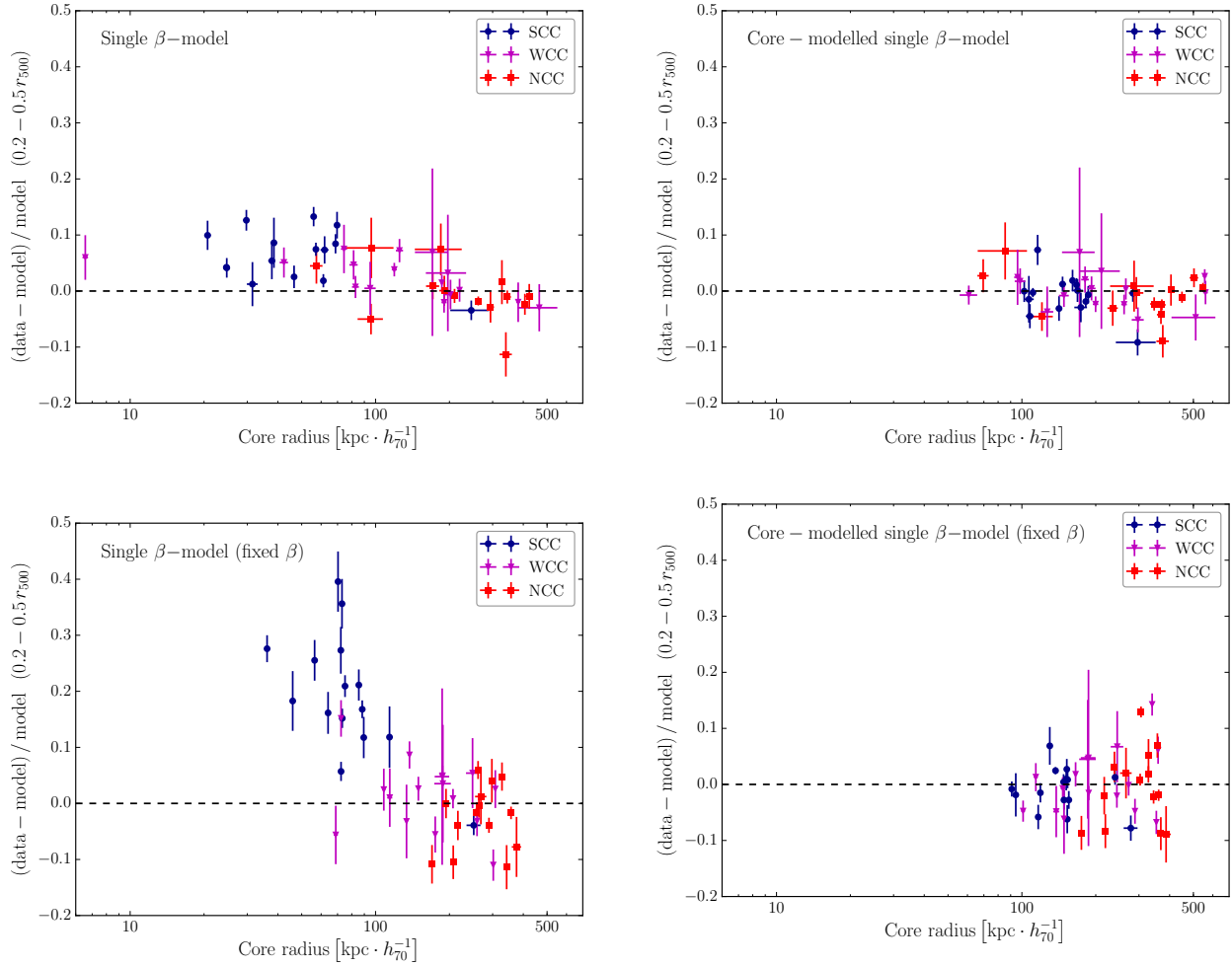


Figure 2.5: Median of the fractional residuals from a single β -model (left panels) and a core-modeled single β -model (right panels) in $0.2-0.5 r_{500}$ radial bins for individual HIFLUGCS objects above a temperature of 3 keV as function of core radius. For the bottom panels the β parameter is fixed to $2/3$ in the surface brightness parameter optimization.

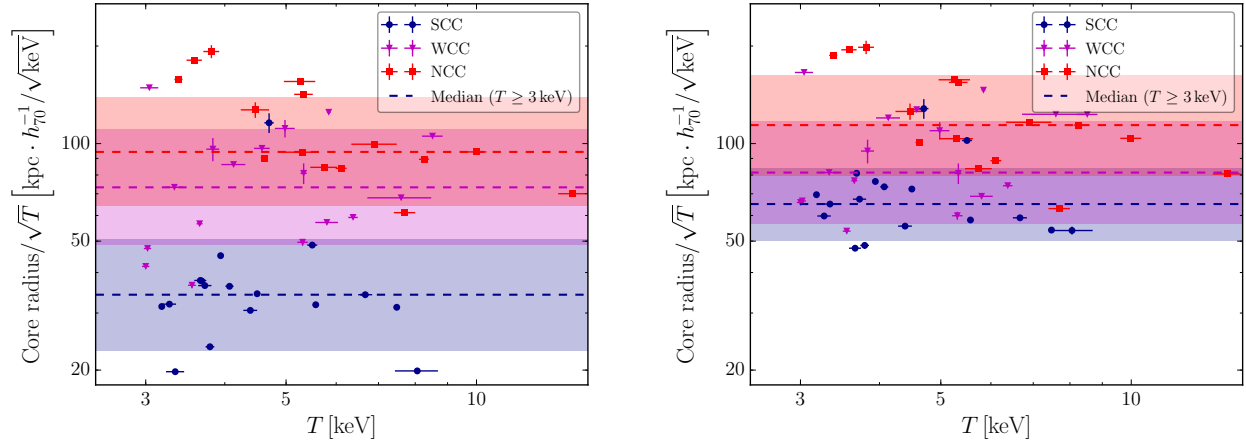


Figure 2.6: Core radius as a function of temperature for a single β -model (left panel) and core-modeled (right panel) single β -model. The dashed lines and shaded regions represent the medians and their intrinsic scatter of the individual core populations.

pendence, the core radii are divided by the square-root of the corresponding cluster temperatures (see below for more details). The figure emphasizes the systematic differences between the individual core types in the modeling with a single β -model. The discrepancies get less prominent when modeling the core region using the wavelet decomposition. In addition, the intrinsic scatter is reduced by 8%, 11%, and 35% for NCC, WCC, and SCC objects, respectively. In both modeling cases, the Spearman rank-order correlation coefficients indicate a stronger negative (-0.7), a mild positive (0.3) and no significant (0) correlation for the NCC, WCC, and SCC populations, respectively.

We determine scaling relations as outlined in Sect. 2.2.4. The best-fit relations between shape parameters and temperature (Fig. 2.7), as well as luminosity and temperature are determined simultaneously. This allows studying the covariances between shape and luminosity from the joint fit. The best-fit values are shown in Tables 2.1 and 2.2. In Fig. 2.8, we show the correlation between the shape parameters and luminosity. The Spearman rank-order correlation coefficients between luminosity and β , as well as luminosity and core radius are 0.37 and 0.12 (0.32 and 0.22) for the (core-modeled) single β -model, respectively. When the β value is fixed to $2/3$, the luminosity-core radius correlation coefficients become mildly negative with -0.23 (-0.22).

The best-fit parameters of the single β -model and core-modeled single β -model scaling relations agree approximately on the 1σ level, except that in the latter case the intrinsic scatter value of the core radius is reduced by almost a factor of two. In both modeling approaches the shape parameters show a positive correlation with temperature. The shape parameters of galaxy clusters are often fixed to generic values (e.g., $\beta = 2/3$) or scaling relations (e.g., $r_c \propto r_{500}$, Pacaud et al. (2018)). The assumption that the core-radius is proportional to r_{500} , together with Eq. 2.10 results in a self-similar scaling of $r_c \propto T^{1/2}$. We find a core-radius-temperature relation with a marginally steeper slope of 1.04 ± 0.37 (0.75 ± 0.20) for the (core-modeled) single β -model compared to this expectation. Fixing the value of β to $2/3$ results in 0.77 ± 0.14 (0.50 ± 0.16), consistent with the self-similar value when modeling the excess core emission. We study the

Table 2.1: Parameters from single β -model and core-modelled single β -model fits to the y -temperature scaling relations. Listed are the slopes, m , normalizations, b , and intrinsic scatter values, λ_y .

y	Single β -model					
				$\beta = 2/3$		
	m	b	λ_y	m	b	λ_y
β	$0.19^{+0.06}_{-0.06}$	$-0.82^{+0.09}_{-0.09}$	$0.13^{+0.02}_{-0.01}$	-	-	-
r_c	$1.04^{+0.37}_{-0.37}$	$2.94^{+0.61}_{-0.60}$	$0.88^{+0.10}_{-0.09}$	$0.77^{+0.14}_{-0.14}$	$3.73^{+0.25}_{-0.25}$	$0.62^{+0.06}_{-0.05}$
$E(z)^{-1}L_{0.1-2.4\text{ keV}}$	$1.90^{+0.23}_{-0.23}$	$99.16^{+0.37}_{-0.38}$	$0.49^{+0.07}_{-0.06}$	$2.26^{+0.14}_{-0.14}$	$98.58^{+0.24}_{-0.24}$	$0.52^{+0.06}_{-0.05}$
y	Core-modelled single β -model					
				$\beta = 2/3$		
	m	b	λ_y	m	b	λ_y
β	$0.16^{+0.07}_{-0.07}$	$-0.63^{+0.11}_{-0.11}$	$0.16^{+0.02}_{-0.02}$	-	-	-
r_c	$0.75^{+0.22}_{-0.22}$	$4.10^{+0.36}_{-0.36}$	$0.52^{+0.06}_{-0.05}$	$0.50^{+0.16}_{-0.16}$	$4.48^{+0.26}_{-0.26}$	$0.40^{+0.05}_{-0.04}$
$E(z)^{-1}L_{0.1-2.4\text{ keV}}$	$1.86^{+0.22}_{-0.23}$	$99.22^{+0.37}_{-0.38}$	$0.50^{+0.07}_{-0.06}$	$1.90^{+0.22}_{-0.23}$	$99.17^{+0.37}_{-0.37}$	$0.49^{+0.07}_{-0.06}$

Table 2.2: Correlation coefficients between different galaxy cluster parameters from single β -model and core-modelled single β -model fits. Listed are the correlation coefficient values, λ_{xy} , between the parameters x and y .

x	y	Single β -model		Core-modelled single β -model	
		$\beta = 2/3$		$\beta = 2/3$	
		λ_{xy}		λ_{xy}	
β	r_c	$0.60^{+0.09}_{-0.11}$	-	$0.67^{+0.08}_{-0.10}$	-
β	$E(z)^{-1}L_{0.1-2.4\text{ keV}}$	$-0.02^{+0.17}_{-0.17}$	-	$0.02^{+0.16}_{-0.16}$	-
r_c	$E(z)^{-1}L_{0.1-2.4\text{ keV}}$	$-0.43^{+0.16}_{-0.13}$	$-0.43^{+0.15}_{-0.13}$	$-0.32^{+0.16}_{-0.15}$	$-0.50^{+0.15}_{-0.13}$

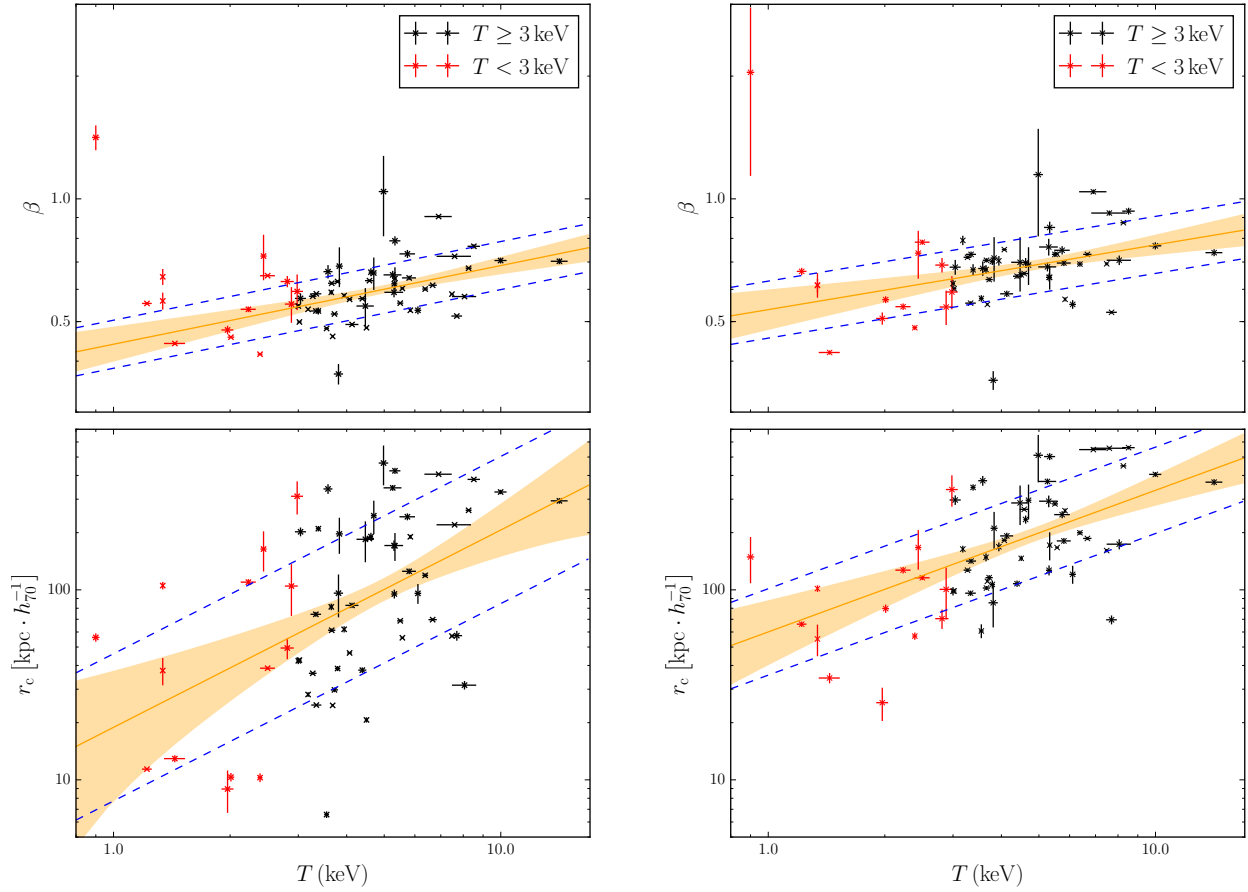


Figure 2.7: Scaling relations between single β -model (left panels) and core-modeled single β -model (right panels) parameters and temperature. The HIFLUGCS clusters with temperatures greater than 3 keV (black points) are used for optimization. Red points mark HIFLUGCS objects below this temperature threshold for visualization. The orange lines and shaded regions show the best-fit relations and their uncertainties, respectively. The blue dashed lines correspond to the intrinsic log-normal scatter.

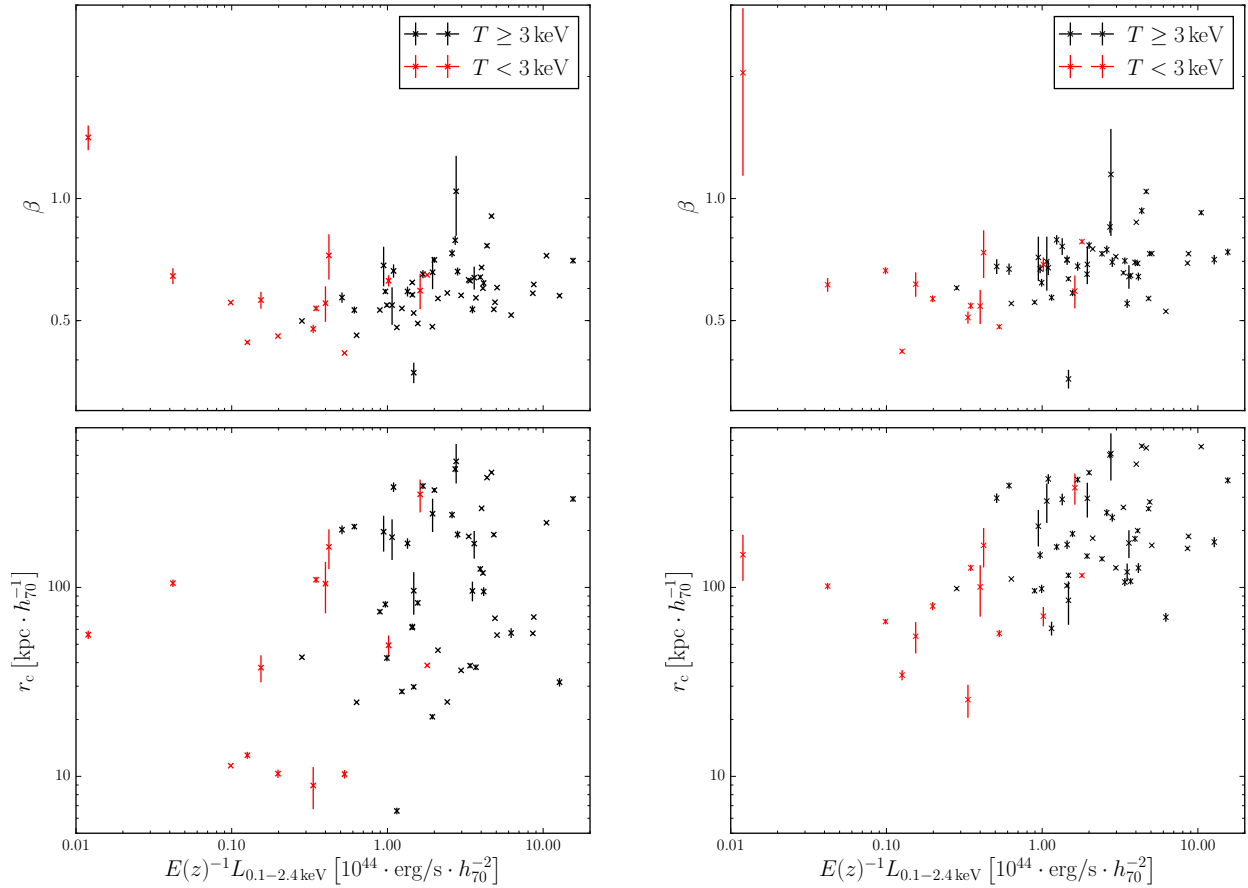


Figure 2.8: Single β -model (left panels) and core-modeled single β -model (right panels) parameters as a function of luminosity. The HIFLUGCS clusters with temperatures greater than and below 3 keV are marked as black and red points, respectively.

correlation coefficients (Table 2.2) between the different galaxy cluster parameters by simultaneously fitting for the scaling relations and the intrinsic scatter tensor. We expect some degeneracy between the single β -model parameters in the fitting, amongst others that a larger core-radius is compensated by a steeper slope. This is reflected in the strong positive correlation between core-radius and β . We do not find a significant correlation between β and luminosity. There is a strong negative correlation between core radius and luminosity, meaning that at a given temperature, more luminous objects tend to be more compact. For all modeling cases, the best-fit correlation coefficients are consistent on a 1σ level. This implies, that the measured correlation between core radius and luminosity is not significantly affected by modeling the central excess emission. Neither this covariance nor the shape-temperature relations are taken into account in existing simulations for eROSITA but may play a crucial role in understanding selection effects related to the detection of clusters in X-ray surveys, which is a key ingredient for using X-ray galaxy clusters as a precision cosmological probe. The findings presented here can be used to perform more realistic simulations and a comparison between different sets of simulations allows to study the impact of these covariances on obtained cosmological parameters.

2.7 Summary

X-ray morphologies of galaxy clusters play a crucial role in the determination of the survey selection function. We compare self-similar scaled emission measure profiles of a well defined galaxy cluster sample (HIFLUGCS) above a representative temperature threshold of 3 keV. One outlier (Abell 3526) with small statistical errors drives the weighted mean profiles of sub-populations according to different core properties toward a different behavior of strong cool-core and non-cool-core objects in the $0.2\text{--}0.5 r_{500}$ radial range. Excluding this object from the analysis or calculating the median profiles reveals no systematic difference in the aforementioned radial range. We conclude that there is no indication for a correlation between the behavior in the $0.2\text{--}0.5 r_{500}$ radial range and the core state, although the overall shapes of the SCC and NCC populations are different. The median SCC profile shows a larger normalization toward the center and is steeper compared to the median NCC profile. This leads to a turnover of the profile ratio at approximately $0.3 r_{500}$. The difference in the center can be explained by the core state but the difference in the outskirts is still under debate. As discussed in Sect. 2.3 possible explanations are gas redistribution between the core region and the outskirts, the current accretion of large-scale blobs, or different shapes of the dark matter halos leading to different concentrations at a given radius. Characterizing galaxy cluster surface brightness profiles with single β -models is still state-of-the-art in the determination of selection functions. We investigate the residuals of a single β -model fit to the overall cluster profile, revealing that this description tends to underestimate the flux in the galaxy cluster outskirts for less extended clusters. Fixing the β parameter to $2/3$ increases this effect dramatically, that is up to over 40%. In both cases, the core-radius measurement for SCC objects are biased low. In addition, the intrinsic scatter values with respect to the medians of the self-similar scaled extent parameters show a more than 1σ tension between strong and non-cool-core objects. These three effects can be minimized by adapting a wavelet decomposition based surface brightness modeling that is sensitive to the galaxy cluster outskirts and models the

excess emission in the core region. Then, the fit is not driven by the local processes in the core. Compared to a single β -model approach the residuals in the $0.2\text{--}0.5 r_{500}$ radial range are much smaller and the core radii depend much more mildly on the core state. Our method to model the excess core emission has very interesting applications for future galaxy cluster surveys, for example with eROSITA. The performance study for high redshift objects with small angular extent and establishing the most robust method for clusters where r_{500} is unknown is left to a future work. Using wavelet decomposition allows to determine large-scale ellipticities of the clusters. The ellipticity is an interesting new survey measure for eROSITA since its determination does not require many photon counts and it adds additional information to the β -model shape parameters and core-excised luminosities. A detailed study of measuring galaxy cluster ellipticities with eROSITA and its implications is left to a future work.

We study how shape parameters and luminosity scale with temperature. There is no significant difference of the best-fit values between a single β -model and core-modeled single β -model, except that the intrinsic scatter of the core radius is almost twice as large for the single β -model case. The slope of the core radius-temperature relation is steeper than the self-similar prediction of $1/2$ but gets in agreement when fixing the β parameter to $2/3$ in the surface brightness profile modeling. More interestingly, the shape parameters are covariant with luminosity, meaning that at a given temperature, more compact objects are more luminous. These covariances are usually neglected in simulations to determine the survey selection function (Pacaud et al., 2007; Clerc et al., 2018). In addition, these previous studies assumed a fixed β value, while we find that β is a function of temperature. Taking shape-temperature scaling relations and shape-luminosity covariances into account will lead to a more realistic set of simulated galaxy clusters and will provide a better understanding of the survey completeness.

Chapter 3

Toward the low-scatter selection of X-ray clusters: Galaxy cluster detection with eROSITA through cluster outskirts

The expansion and structure formation history of the Universe is imprinted on the spatial distribution and number density of its largest collapsed entities, galaxy clusters. This makes galaxy clusters powerful probes for constraining cosmological parameters such as the dark energy equation of state (e.g., [Vikhlinin et al. 2009b](#); [Allen et al. 2011](#) for a review). Among others, X-ray observations of galaxy clusters are of particular interest because they trace the bulk of the baryonic component, the hot intracluster medium (ICM). With the launch of the extended ROentgen Survey with an Imaging Telescope Array (eROSITA, [Merloni et al. 2012](#); [Predehl et al. 2018](#)) in July 2019, X-ray astronomy ushers in a new era. As the primary instrument of the Russian-German Spektrum-Roentgen-Gamma (SRG) mission, eROSITA will perform eight all-sky surveys within four years. The unprecedented survey speed and capability over a wide range of energies mean that the final all-sky survey will be approximately 20–30 times deeper than that of its predecessor (the ROSAT all-sky survey, [Voges et al. 1999](#)) in the 0.5–2 keV energy range and will provide the first ever imaging all-sky survey in the 2–10 keV energy band. With the expected detection of 10^5 galaxy clusters ([Pillepich et al., 2012](#)), eROSITA will place tight constraints on the dark energy equation of state, among others.

Understanding selection effects is an essential but complicated requirement for precision cosmology. Determining the selection function is especially complex for extended X-ray sources because the detection probability and proper classification depend on their morphology, for example ([Eckert et al., 2011](#); [Rossetti et al., 2016, 2017](#); [Andrade-Santos et al., 2017](#); [Lovisari et al., 2017](#)). The cluster outskirts ($0.2\text{--}0.8 r_{500}$) are found to evolve with redshift in a self-similar fashion ([McDonald et al., 2017](#); [Käfer et al., 2019](#)) and exhibit low scatter ([Ghirardini et al., 2018b](#); [Käfer et al., 2019](#)). Therefore, cluster samples that are selected based on the properties of cluster outskirts will closely trace the selection by cluster mass and reduce the systematics of cluster use in cosmological studies. Another important aspect of detailed image decomposition consists of the removal of point sources. In the extragalactic sky, the X-ray point-source population is dominated by active galactic nuclei (AGN). Active galactic nuclei cause false detections

through the noise in the realization of their photon distribution. In addition, they contribute to the total flux of the cluster because the AGN halo occupation distribution extends to high masses, especially at high redshifts (Allevato et al., 2012; Oh et al., 2014). The importance of AGN in contaminating cluster fluxes of eROSITA observations has been highlighted by Biffi et al. (2018).

Spatial filtering of X-ray images to describe the emission that is produced on different spatial scales has been introduced by Starck and Bijaoui (1991) and was successfully applied for source detection in cluster cosmology (Vikhlinin et al., 1998; Pacaud et al., 2006). Finoguenov et al. (2009, 2010b, 2015), Erfanianfar et al. (2013), Mirkazemi et al. (2015), and Gozaliasl et al. (2019) applied the method to detect groups and clusters of galaxies using only the large scales of the X-ray emission. In this study, we present the adaptation of the wavelet decomposition method for eROSITA.

The chapter contains the characterization of the eROSITA point-spread function, simulations of eROSITA observations of the extragalactic fields, calibration of the point-source model, description of the cluster detection pipeline, and its characterization using synthetic simulations.

Throughout this chapter we assume a WMAP9 cosmology with a matter density, vacuum energy density, and Hubble constant of $\Omega_m = 0.282$, $\Omega_\Lambda = 0.719$, and $H_0 = 69.7 \text{ km s}^{-1} \text{ Mpc}^{-1}$, respectively (Hinshaw et al., 2013). The dimensionless Hubble function is defined as $E(z) = \sqrt{\Omega_m(1+z)^3 + (1 - \Omega_m - \Omega_\Lambda)(1+z)^2 + \Omega_\Lambda}$. Quoted errors are 1σ unless otherwise stated.

The majority of the work in this chapter is based on the peer reviewed publication Käfer et al. (2020).

3.1 eROSITA and the eROSITA simulator

eROSITA is a new X-ray telescope that was launched in July 2019 on board the SRG. The full description of the telescope can be found in Predehl et al. (2018).

3.1.1 Point-spread function

The point-spread function (PSF) of an X-ray telescope describes its ability to focus photons. The image produced by a point source is blurred, mostly as a result of misalignments and micro-roughnesses or is caused by the support structures of the instrument's grazing incidence mirrors. The shape and size of the PSF depends among others on the photon energy and its distance from the optical axis. The current eROSITA PSF model is based on measurements made at the PANTER X-ray test facility, where the PSF is sampled on an 11×11 grid, plus an additional central 6×6 grid to increase the small off-axis angle density. Each grid is spaced by $6'$, and the two grids are displaced by $3'$ with respect to one another. The energy dependence is sampled using X-ray emission lines at photon energies of 0.3, 0.9, 1.5, 3.0, 4.5, 6.4, and 8.0 keV. The PSF image at each position and energy is described by shapelets (Refregier, 2003), that is, by a linear image decomposition into a series of differently shaped basis functions of characteristic scales. The shapelet description is a convenient way to compress the PSF information over a few coefficients. Two different scale parameters with individual shapelet coefficients are used in order to reproduce the complex behavior of the PSF core on small scales and the PSF wings on

large scales. Each of the seven eROSITA mirror modules are made out of 54 nested Wolter-I type (Wolter, 1952) shells and have their individual PSF measurements. However, in the current implementation of the X-ray telescope simulator (Sect. 3.1.4), the PSFs of all seven modules are assumed to be the same, using only the shapelet reconstruction of flight module number 2. We note that the eROSITA PSF will be different in orbit, for example, due to shaking of the telescope during launch or temperature and gravitational effects. During the performance-verification and all-sky survey phases, the eROSITA PSF will be determined and calibrated against ground-based measurements.

3.1.2 Point sources and background components

We followed the recipe of Clerc et al. (2018) and used SIXTE¹ (Dauser et al., 2019, see Sect. 3.1.4) to simulate eROSITA fields containing AGN and unresolved X-ray background. Individual AGNs were drawn from a luminosity function down to a field exposure time-dependent flux threshold and uniformly distributed in a field. Thus spatial clustering of AGNs and spatial correlations between AGNs and galaxy clusters are not considered; this is the topic of a future study. The AGN spectra of the low-luminosity tail of the distribution were stacked and redistributed uniformly to construct an unresolved X-ray background component. Emission of the hot plasma in the halo and disk of our Galaxy was simulated using a double MEKAL model (Mewe et al., 1985, 1986; Liedahl et al., 1995) with temperatures of 0.081 keV and 0.204 keV (Lumb et al., 2002). In addition, a non-vignetted eROSITA instrument particle background component according to the expected radiation level at the Lagrange point L2 was simulated (Tenzer et al., 2010).

3.1.3 Extended objects

We here focus on the detection of extended sources. To compare our results to previous studies, we characterize the spatial flux distributions by spherically symmetric β -models (Cavaliere and Fusco-Femiano, 1978) with $\beta = 2/3$ on a discrete grid of core radii. The cluster emission was characterized by a partially absorbed Astrophysical Plasma Emission Code (APEC, Brickhouse et al., 2000) model with a fixed abundance of $0.3 Z_{\odot}$ (Anders and Grevesse, 1989) and a survey-field-dependent Galactic column density of hydrogen. The Galactic absorption was described by a phabs model (Balucinska-Church and McCammon, 1992) and was fixed to $3 \cdot 10^{20} \text{ cm}^{-2}$, $8.8 \cdot 10^{20} \text{ cm}^{-2}$, and $6.3 \cdot 10^{20} \text{ cm}^{-2}$ for the equatorial, intermediate, and deep field, respectively (see Sect. 3.1.5). Cluster temperatures, redshifts, and fluxes were sampled on a grid and ranged between 1–5 keV, 0.05–1.2, and $2 \cdot 10^{-15}$ – $5 \cdot 10^{-15} \text{ erg s}^{-1} \text{ cm}^{-2}$, respectively.

3.1.4 X-ray telescope simulator

The simulations of the extragalactic eROSITA sky were performed using the Monte Carlo based SIXTE simulator (Dauser et al., 2019). A sample of photons was produced based on the effective

¹<http://www.sternwarte.uni-erlangen.de/research/sixte/>

area of the instrument and input source characteristics, for example, a source spectrum, or if necessary, a model of the extent. These photons were virtually propagated through the instrument simulator. Based on the telescope specifications, a list of impact times, positions, and energies of the photons was produced. The final output event list was then created by simulating the read-out characteristics. The simulator already provides an implementation of the eROSITA characteristics described by the PSF, vignetting, response matrix files, and ancillary response files.

3.1.5 eROSITA mission planning and survey fields

We assumed a simple survey strategy for the four-year all-sky survey, where the scanning axis is pointed toward the Sun and eROSITA scans one great circle every four hours (Merloni et al., 2012). One full coverage of the sky is achieved every half year. We note that the final survey strategy will be more complicated due to additional constraints. Since the attitude file we used was created, the movable antenna was replaced by a fixed antenna, thus the spacecraft needs to perform compensating motions to maintain the angular constraints with respect to the Earth and the Sun. In addition, the antenna opening angle and the spacecraft-Sun-vector constraints were changed. This leads to a more inhomogeneous exposure in ecliptic longitude, among others.

We studied three $3.6^\circ \times 3.6^\circ$ sky tiles with approximately 2 ks, 4 ks, and 10 ks exposure. We refer to these fields as equatorial, intermediate, and deep, respectively. Taking vignetting into account, the median net exposures of the fields were roughly halved, that is, approximately 1 ks, 2.5 ks, and 6 ks, respectively. The equatorial field shows a uniform exposure, but the deep field has a large exposure gradient (Clerc et al., 2018).

3.2 Source detection and characterization

The standard technique when source catalogs are created is to split source detection and characterization because different optimized software packages perform better on the individual tasks. After the initial detection, a maximum likelihood (ML) source characterization is used to separate extended and point-like sources, based on the value and the significance of the extent (Vikhlinin et al., 1998; Burenin et al., 2007; Pacaud et al., 2016; Clerc et al., 2018). The approach of splitting detection and characterization is also implemented in the standard eROSITA data-processing pipeline based on the eROSITA Science Analysis Software System (eSASS)². The forward-fitting routine employed by the ML fitting ensures the best sensitivity toward detecting an object with the assumed characteristics. However, the assumed symmetric $\beta = 2/3$ model is too simplistic for many extended sources. The goal of our investigation is to provide a framework that selects extended sources based on their extended emission rather than relying on a blind fitting method. Our galaxy cluster detection scheme is physically motivated and sensitive to the outer self-similar cluster regions. This ensures cluster selection from the point of view of best cluster characterization because the outer cluster regions show less scatter at a given cluster mass.

²<https://erosita.mpe.mpg.de/eR0doc/>

3.2.1 Wavelet decomposition method

The general idea of wavelet decomposition is the isolation of differently sized structures by convolving the input image with kernels of variable scales. Starting with the smallest scale, significant emission is subtracted before continuing on the next larger scale. This allows us to model point-source emission based upon their detection on scales that are unresolved or are the size of the PSF. The angular sizes of these scales depend on instrumental and observational characteristics and can vary from arcseconds for the *Chandra* observatory to arcminutes for ROSAT all-sky-survey data. We refer to these small scales as point-like emission detection (PED) scales, and greater scales are labeled extended emission detection (EED) scales. The removal of point sources based on the PED-scale detection and a PSF model prior to running the wavelet decomposition on EED scales is a natural step within the philosophy of wavelet decomposition and was introduced by [Finoguenov et al. \(2009\)](#). Following this approach, the general concept of our algorithm is to detect point sources and extended sources separately. An overview of the general steps of our procedure is as follows:

1. Calibration of the point-source model on point-source-only simulations by obtaining normalization coefficients of PSF templates on PED scales.
2. Extended source detection and characterization on realistic simulations.
 - (a) Detection of point sources on PED scales.
 - (b) Model the predicted point-source emission using normalization coefficients and PSF templates.
 - (c) Check for residual signal over the background and point-source emission on EED scales.
 - (d) Catalog extended sources.

[1.] The first step is the calibration of point-source modeling, which means addressing which angular sizes the PED scales have in the particular science case. We only used the simulated image of point sources, which contains resolved and unresolved sources. The background level was determined by iterating the detection of point-source emission and excising point sources from the background estimates, as was done for *XMM-Newton* and *Chandra* in [Finoguenov et al. \(2015\)](#). Next, we modeled the instrument PSF with a sum of Gaussians without assuming any prior knowledge about its shape. This has the advantage of being robust and fast to implement. We modeled the PSF up to a scale on which the emission is almost free of point-source contamination. These scales are defined as PED scales. Using the converged background estimate, we ran the detection of point sources on the PED scales to obtain a wavelet image of resolved point sources. This point-source image was smoothed with Gaussians of different widths to obtain fitting templates. We fit these templates to the wavelet-subtracted image to derive the amplitude of the image that best describes the residuals. We did this by cross-correlating the maps in order to take the covariance of the templates into account. The results are individual normalization coefficients for the used templates. These normalization coefficients were used to model the PSF

effect in the simulations that contain extended sources. We note that including actual PSF measurements might improve the description of the PSF wings, which cannot be characterized by our approach of combining several Gaussians. The point-source subtraction technique has proven to be very efficient in deep X-ray fields and has also allowed the separation of extended sources due to inverse Compton scattering of the cosmic microwave background photons on the relativistic plasma of radio jets (Finoguenov et al., 2010a; Jelić et al., 2010). The detection threshold is the level in the convolved image above which the peaks are statistically significant. For the purpose of subtracting or modeling point-source contamination, the detection thresholds considered extended to 3σ (Vikhlinin et al., 1998).

[2.(a/b)] After the calibration of the point-source model, we ran the detection of point sources on the realistic simulations, which contain both point and extended sources. We smoothed the resulting point-source wavelet image with Gaussians of the same widths as in the calibration. These templates were multiplied by the normalization coefficients obtained in the calibration and were added to the unsmoothed wavelet image to model the point-source emission on the PED scales.

[2.(c/d)] To preserve the Poisson statistics, we added the point-source model to the background estimate and searched for residual signal over the background plus point-source model to detect and catalog extended objects. As a result, we obtained maps that were free of point-source emission. The maps retain the spatial shape of the extended source emission, such that ellipticity can be measured, for example. In addition, the maps allow for a simple visual characterization of the detected emission. This can be a complicated task, for instance, if the cluster does not look like a β -model because of extended source confusion. Furthermore, maps obtained by different satellites can be combined, as was done for *Chandra* and *XMM-Newton* observations in Finoguenov et al. (2015). The choice of the detection thresholds for cataloging the extended sources depends on the objective, and they were adjusted to the desired level of completeness and purity of the catalog, as discussed in Sect. 3.5.1. Typically, the detection thresholds were at least 4σ .

The goal of our pipeline is to select sources based on the extended emission, compared to selecting sources based on a symmetric $\beta = 2/3$ model fit to some angular range. Thus, our catalogs include sources with a greater variety of shapes. This detection scheme has obvious benefits at low-mass halos, such as galaxy groups, because they exhibit a wide variety of X-ray morphologies (e.g., Finoguenov et al., 2006, 2007). From the point of view of source selection, the effect of contaminating sources is very different between this pipeline and classical wavelets. Here, the ability to detect and select a cluster as an extended source might be reduced due to the large noise caused by point-source induced background, while in other methods, the source might be classified as a cluster because of the point-source contribution to the total flux.

If we were to only keep the emission above the selected detection threshold, we would discard the bulk of the source flux. Wavelets provide a secondary filtering threshold for estimating the region around the detected maximum where significant flux is detected. A lower filtering threshold compared to the detection threshold therefore minimizes the loss of source flux by keeping a larger region around the detected maximum. This region can be used in the flux estimation of the source in the point-source-subtracted map. However, setting the filtering threshold too low has the drawback of potentially including secondary peaks within the region around the

main peak, which would normally not be detected. These secondary peaks might increase the number of spurious detections. Flux measurements within a wavelet reconstructed region have been extensively tested in [Connelly et al. \(2012\)](#). Together with the source flux, the detection efficiency of galaxy clusters depends on their extent. To achieve a comparison to previous studies, we considered the performance of our pipeline by adopting the same framework as for β -model profiles. Within the β -model approach, the extent is characterized by the value of the core radius. A discussion to extend the existing β -model tools to capture the wide variety of expected source shapes is beyond the scope of this study.

In addition to the standard β -model characterization, our pipeline can be calibrated using any set of cluster characterization. In addition, the catalog of extended sources can be fed back into the β -model-extent fitting routine to identify why certain sources are lacking from the cluster list. This approach is similar to the XMM-XXL survey pipeline ([Pacaud et al., 2006](#)). We note that compared to our method, the flux estimate of the XMM-XXL pipeline includes potential excess cool-core emission.

3.2.2 Adjusting the detection pipeline to eROSITA

As described in Sect. 3.2.1, the proposed source detection algorithm needs to be tuned to the characteristics of the particular observation. In this section, we focus on how to adapt the general framework to eROSITA. Currently, our training is limited to the pre-flight calibration, and a further tuning of the pipeline is required in-flight. Compared to similar pipelines for *Chandra* and *XMM-Newton*, we have not yet addressed the minor deficiencies associated with wavelet flux redistribution between adjacent scales. This will be accomplished as a part of the in-flight calibration and will serve to reduce the root mean square of the residual image. Right now, we propose an effective scheme of the procedure and apply it to current eROSITA-survey mock observations. We follow this path because the incorporation of in-orbit PSF calibration data into the software analysis has proven to be time consuming in our experience.

Similar to *Chandra* and *XMM-Newton*, the off-axis degradation of the eROSITA PSF is driven by the fact that the detector plane is out of focus. Thus, we can directly apply our experience with developing the source detection algorithm for *Chandra* and *XMM-Newton* to eROSITA. However, the eROSITA maximum degradation in terms of the half-energy width is 20% ([Predehl et al., 2010](#)), which is lower than for *XMM-Newton* and far lower compared to *Chandra*. The eROSITA PSF does not have a core, but a typical survey half-energy width of 28'' at 1 keV. In scanning mode, the eROSITA PSF is roughly uniform across sky tiles. The detector pixel size corresponds to 9.6'', and sky tiles are rebinned into images with 4'' pixel size. In our simulations, the impact position of each photon is known. In the eROSITA survey, the rebinning will be made by reconstructing split events using the charge division among adjacent pixels, allowing for subpixel resolution ([Dennerl et al., 2012](#)). We detect sources in eROSITA-survey images in the 0.5–2 keV energy band. Events are not split or selected based on their off-axis angles.

[1.] First, we study the limitations of the point-source-model process on the eROSITA cluster detection. The goal is to answer the questions whether we can reliably model the point-source contribution and to define the angular scales required for this. The angular scales on which point sources are first detected is a strong function of the survey depths, instrument PSF, and assumed

background. A discussion of the effects is presented in [Mirkazemi et al. \(2015\)](#). With respect to eROSITA survey observations, we are not able to reliably predict the residual point-source emission on scales below $32''$ because most of the point sources are only detected on the $32''$ wavelet scale. Even on scales of $64''$, we detect point sources that are not detected on any smaller scales. The point-source contamination on scales starting from $128''$ is minimal. In training for the point-source model, we ran the wavelet decomposition up to a scale of $32''$. Because we are interested in a complete source subtraction, we adopted a low detection and filtering threshold of 3.3σ and 1σ , respectively. These small scales are smoothed with Gaussians of $64''$ and $128''$ widths and fitted to the $32''$ wavelet-subtracted image. The two Gaussian-smoothed templates describe the residual image best, with normalization coefficients of 0.47 and 0.1, respectively. We did not include the $64''$ scale in modeling the point-source flux on the EED scales because we wished to retain sensitivity for extended objects on this scale.

[2.(c/d)] The prediction of the point-source emission on PED scales was included in the background model, and we ran the wavelet decomposition on the EED scales in order to detect and catalog extended objects. A widely adopted way for cleaning catalogs is to set the detection threshold for extended sources higher, which reduces the chance of including misclassified point sources as extended. For eROSITA, we did not detect point sources on the $64''$ scale when we set the detection threshold to 7σ . On the other hand, scales starting from $128''$ are already very clean from the point-source contamination, and the lowest statistically motivated thresholds can be adopted there. This is very good news for the science of galaxy groups with eROSITA, as well as for studies of the unresolved background fluctuation. For this work, we illustrate the performance of the pipeline using two detection thresholds: one maximally sensitive, of 4σ , and another maximally clean, of 7σ . The filtering thresholds were set to 1.6σ and 3σ for high-sensitivity and low-contamination wavelet detection, respectively. In addition, we adapt a 5σ detection threshold with a 1.6σ filtering threshold in Sect. 3.5.1 for a better comparison with an existing study. We motivate these thresholds further in Sect 3.5.2. Our current simulations do not consider spatial AGN clustering, and the quantification of this effect is topic of a future study. We note that a potential AGN clustering might create false fluctuations on larger scales.

Considering the shallow depths of the eROSITA survey, the limitation of using EED scales is primarily for detecting sources at high redshift ($z \sim 1$). There, using smaller scales for fitting the cluster shapes will be complicated by the enhanced AGN activity in clusters ([Biffi et al., 2018](#)) and might present a fundamental limitation of the survey to achieve clean high- z cluster flux estimates in any case, as opposed to merely detecting a cluster. When the in-orbit background is higher than we assume here, the detection threshold can be lowered, staying the same in terms of the source flux. Thus, our results in terms of source flux detection will be quite representative for a wide range of in-orbit conditions.

3.3 Selection criteria

The point-source-cleaned maps provide a way to detect extended sources and to measure their flux. From the point of view of the flux extraction, it is clear that the flux on the spatial scales used to estimate the point-source flux will be partially removed. On the other scales, the work

on eROSITA sample construction has put forward a demand on defining the simplest possible observable on which the selection is made with a preferable step-function-like selection (Grandis et al., 2018). In our method, this is the residual cluster flux in the 1–4′ range. This represents a simple aperture extraction, which is linked to the total cluster flux. The radial range is not directly motivated by the wavelet analysis, except that we need to consider scales above 1′ due to point-source confusion (see Sect. 3.5.1). In addition, we also present a consideration of the source flux in the 1–16′ range. This allows us to study the effects of using a larger aperture. Our experiments with cluster detection in the equatorial fields led to a conclusion of using 40 and 80 counts for these two detection ranges, respectively. This assumes a lower detection threshold for the large area. Previous studies (e.g., Pillepich et al., 2012; Borm et al., 2014) neglected aperture effects in addition to a count threshold and assumed a fixed minimum number of total photons to classify a source as cluster. This leads to an artificially high sensitivity toward a detection of X-ray emission from low-redshift galaxy groups. For cosmological studies, however, these systems are not the intended targets and can be neglected. In the following we derive the analytical description of the cluster selection based on these two thresholds.

It is clear that the redshift range for which our technique is the most attractive is also the range where the selected radial range samples the part of the cluster with the lowest scatter against the total mass. This corresponds to typical clusters of, for example, $10^{14} M_{\odot}$ at redshift 0.4. The sampled part of the cluster changes with redshift as well as mass, and we prefer to model this effect as opposed to changing the extraction region as a function of the redshift-dependent limiting mass. The actual reconstruction of the cluster properties does not have to follow this prescription, and several efforts are underway to provide the core-excised luminosity for the eROSITA clusters (e.g., Eckert et al., 2020).

Using the integrated counts (or count rates) is just one of the possibilities for cluster selection based on our maps. Our source lists can be used with the ML fitting in its standard form and in the modified form, in which the core radii of the clusters are examined only at large radii. This avoids the influence of the cool cores on the estimate, as found by Käfer et al. (2019).

3.4 Theoretical predictions

When we assume the minimum number of counts to detect a galaxy cluster as an extended object (C_{det}) in a field with a given exposure time (T_{exp}), we can iteratively calculate the corresponding cluster flux ($f_{500,\text{lim}}$), luminosity ($L_{500,\text{lim}}$), and mass limit ($M_{500,\text{lim}}$) as a function of redshift. Given an initial cluster mass and temperature-limit guess, the corresponding overdensity radii are calculated assuming spherical symmetry through

$$r_{500,\text{lim}} = \left(\frac{3M_{500,\text{lim}}}{4\pi \cdot 500\rho_{\text{crit},z}} \right)^{1/3}. \quad (3.1)$$

The core radii are assumed to scale with the overdensity radii ($r_c = r_{500}/3$). This ensures that the apparent size scales with redshift, that is, clusters at higher redshift have a smaller angular extent. The relation between core and overdensity radii is calibrated on non-cool-core clusters at low redshift (Käfer et al., 2019) and holds at high redshift, where the relative contribution of the cool

core to the outer parts of the cluster becomes minor (McDonald et al., 2013). The compactness of clusters at high redshift matters for the detection. In practice, we need to characterize the detected population of groups and clusters and correct the numbers for the differential sensitivity of the detection method. With the core radius estimate, the count rate of a cluster is calculated by integrating a single β -model with fixed slope ($\beta = 2/3$) in a given radial range. Realistic deviations from the $\beta = 2/3$ assumption have little impact on the shown thresholds because the actual distribution of the counts is less important. We denote the β -model count rate on the 1–4' scale as $R(1', 4')$ and the count rate within r_{500} as $R(0', r_{500})$. Both predicted β -model count rates are independent of PSF redistribution effects. We used the X-ray spectral-fitting program XSPEC (Arnaud, 1996) as well as the temperature guess to calculate the conversion factor of count rate to flux (λ_{RF}) by dividing the model flux of a partially absorbed APEC model (see Sect. 3.1.3) with unity normalization by the corresponding APEC-model count rate. The conversion factors of count rate to flux range between $(6.45\text{--}7.65) \cdot 10^{-13} \text{ erg count}^{-1} \text{ cm}^{-2}$. The cluster flux limit is derived according to

$$f_{500,\text{lim}} = \lambda_{\text{RF}} \cdot \frac{C_{\text{det}}}{T_{\text{exp}}} \cdot \frac{R(0', r_{500})}{R(1', 4')}. \quad (3.2)$$

Using the redshift, we calculated the conversion factor of count rate to luminosity (λ_{RL}) by shifting the desired rest-frame energy band (0.5–2 keV) to the observed one. This is in order to correct for the fact that the energies of detected photons in a given passband are $(1+z)$ times lower than in the cluster rest-frame. The intrinsic APEC-model luminosity is calculated by multiplying the unabsorbed APEC-model flux in the observed band with 4π times luminosity distance squared and divided by the APEC-model count rate to obtain λ_{RL} . The luminosity conversion factor as a function of redshift is roughly a broken power law, in the form of monomials, with break point around $z = 0.1$. It ranges between $2 \cdot 10^{39}\text{--}2 \cdot 10^{43} \text{ erg count}^{-1}$ for redshifts between 0.001 to 0.1 and steepens to values of $2 \times 10^{46} \text{ erg count}^{-1}$ at $z = 2$. Replacing λ_{RF} in Eq. 3.2 with λ_{RL} yields the cluster luminosity limit. Then, the cluster temperature and mass are updated according to the Giles et al. (2016) temperature-luminosity,

$$kT_{\text{lim}} = 3 \text{ keV} \left[\frac{L_{500,\text{lim}}}{3 \cdot 10^{43} \text{ erg s}^{-1}} \left(\frac{E(z)^{-1.64}}{0.71} \right) \right]^{\frac{1}{2.63}}, \quad (3.3)$$

and the Lieu et al. (2016) mass-temperature scaling relation

$$M_{500,\text{lim}} = \frac{10^{13.56} M_{\odot}}{E(z)} \left(\frac{kT_{\text{lim}}}{\text{keV}} \right)^{1.69}. \quad (3.4)$$

With these updated temperature and mass estimates, the procedure starts over and iterates until the change in mass is lower than 0.1%. As outlined above, we calculated the different selection thresholds for a step-function-like cluster detection (see Sect. 3.3) with 40 and 80 counts on the 1–4' and 1–16' scale, respectively. The flux and luminosity limit of the two angular scales in fields with different exposures are shown in Fig. 3.1 and Fig. 3.2, respectively. Figure 3.3 shows the analytical cluster mass and overdensity radius limit as a function of redshift. The 1–16' scale has a lower sensitivity at higher redshift because the area is larger, but it performs better at lower

redshift than the 1–4′ scale. This is promising for galaxy group studies with eROSITA, assuming that the considered scaling relations hold at these low masses. The core radius limit as a function of flux is shown in Fig. 3.4. The optimal core radius to detect clusters is approximately 1′. For a smaller extent, the flux threshold increases because the surface brightness profiles decline faster, such that there are fewer counts in the outskirts. For a larger extent, the flat inner core of the beta model profile causes more photons to lie beyond 4′ and 16′. This also causes the crossing of the scales around 2′. As expected, the flux threshold decreases with increasing net exposure time. Figure 3.5 shows the total count limit of clusters on the two considered angular scales as a function of redshift. Toward low redshift, increasingly larger statistics are required to detect a cluster because the angular extent increases. This emphasises the challenge for eROSITA to securely detect very nearby extended sources.

We used the Python packages COLOSSUS (Diemer, 2018) and Astropy (Astropy Collaboration et al., 2013, 2018) to calculate the differential number of galaxy clusters per square degree at a given redshift by integrating the cluster mass function (dn/dM , Tinker et al. 2008) in units of Mpc^{-3} multiplied by the differential comoving volume (dV/dz) in units of $\text{Mpc}^3/\text{deg}^2$ over mass,

$$\frac{dN}{dz \text{ deg}^2} = \int_{M_{\text{lim}}(z)}^{M_{\text{max}}} \frac{dn}{dM} \frac{dV}{dz} dM. \quad (3.5)$$

The lower integration limit, $M_{\text{lim}}(z)$, corresponds to the cluster mass limit at the corresponding redshift, and we set the upper limit, M_{max} , to $10^{16} M_{\odot}$, above which the contribution of the mass function to the integral is negligible. Figure 3.6 shows the differential number of galaxy clusters per square degree as a function of redshift for the three final eROSITA survey fields. We computed the total number of clusters in a given survey area A_s detected by eROSITA according to

$$N = A_s \int_{M_{\text{lim}}(z)}^{M_{\text{max}}} \int_0^{z_{\text{max}}} \frac{dn}{dM} \frac{dV}{dz} dM dz. \quad (3.6)$$

For the performance verification (PV) phase of eROSITA, a program to reach the average equatorial depth of the final survey on a smaller patch of the sky is planned, the eROSITA Final Equatorial-Depth Survey (eFEDS). This will demonstrate the survey capabilities of eROSITA and will allow us to calibrate the scaling relations of galaxy clusters. When we assume an upper redshift limit of $z_{\text{max}} = 2$, 3 ks net exposure, and a survey area of 180 square degree, the analytical expectation is to detect approximately 625 clusters using the proposed detection scheme. An in-depth cosmological forecast for galaxy cluster observations with eROSITA is left to a future study.

3.5 Simulated field

This section demonstrates the performance of the source detection based on wavelet decomposition and characterization on a simulated equatorial eROSITA survey field. It serves as an exemplification of the method, and the final adjustments and fine-tuning of the pipeline need to be made on real eROSITA data. We simulated the field as described in Sect. 3.1 and processed

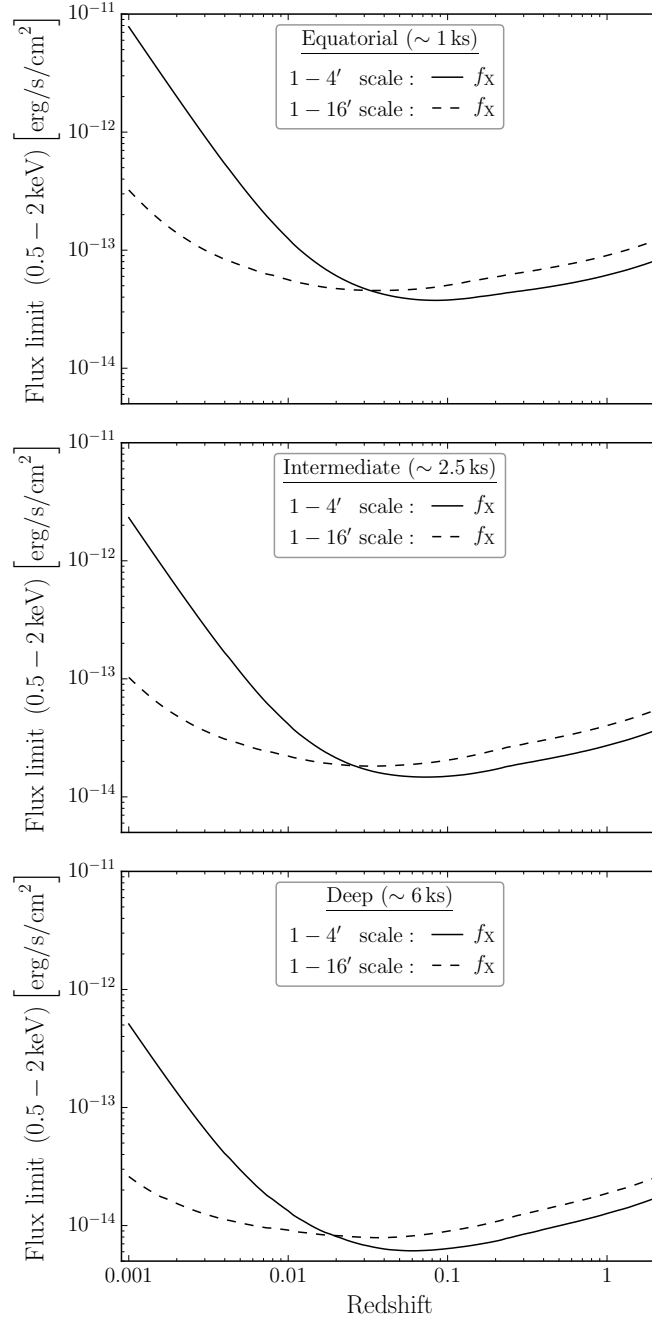


Figure 3.1: Galaxy cluster flux limit as a function of redshift for an equatorial, an intermediate, and a deep final eROSITA survey field of approximately 1 ks, 2.5 ks, and 6 ks exposure, respectively. The black solid and black dashed lines show the flux limits corresponding to 40 and 80 counts in the detection region of 1–4' and 1–16' radial scale, respectively.

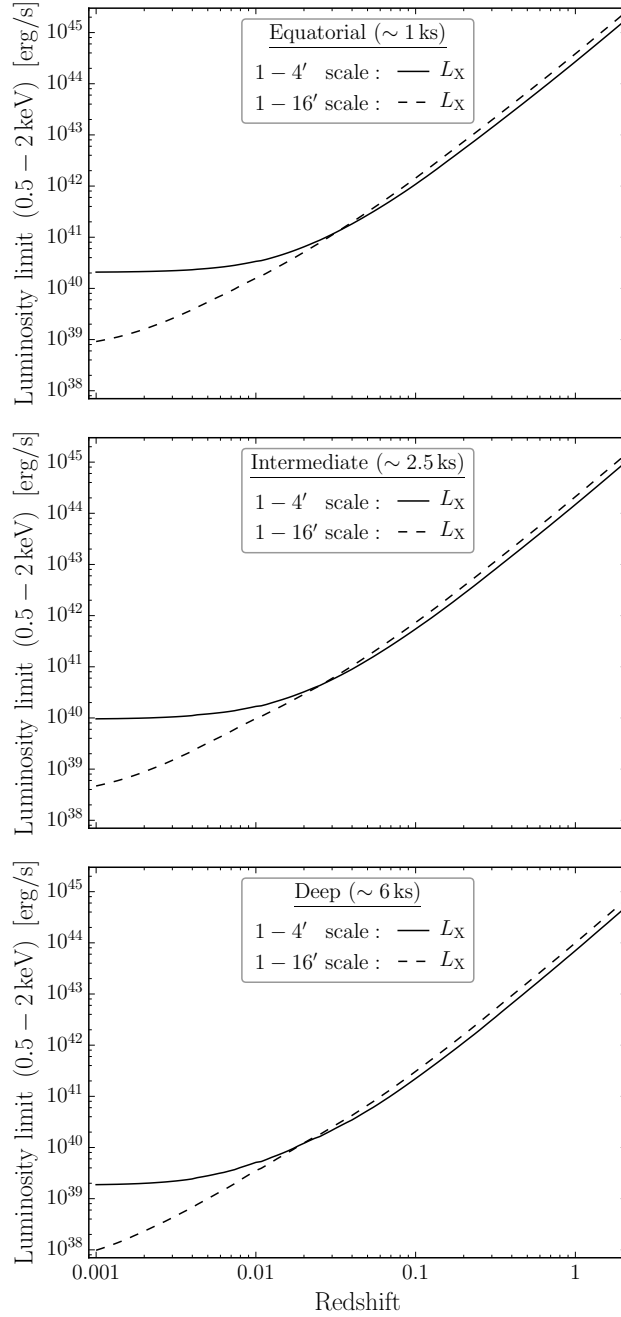


Figure 3.2: Same as Fig. 3.1 for the galaxy cluster luminosity limit.

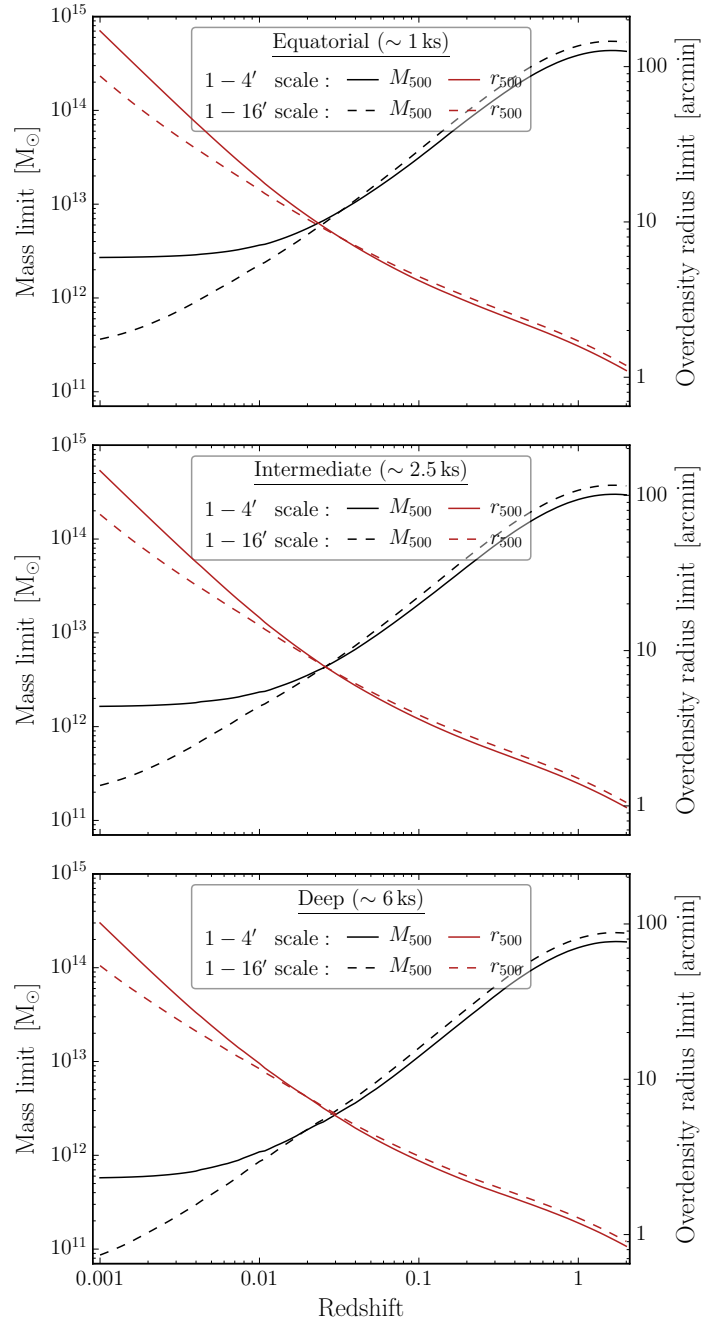


Figure 3.3: Same as Fig. 3.1 for the galaxy cluster mass limit. The brown solid and brown dashed lines represent the associated overdensity radii (right-hand y-axes).

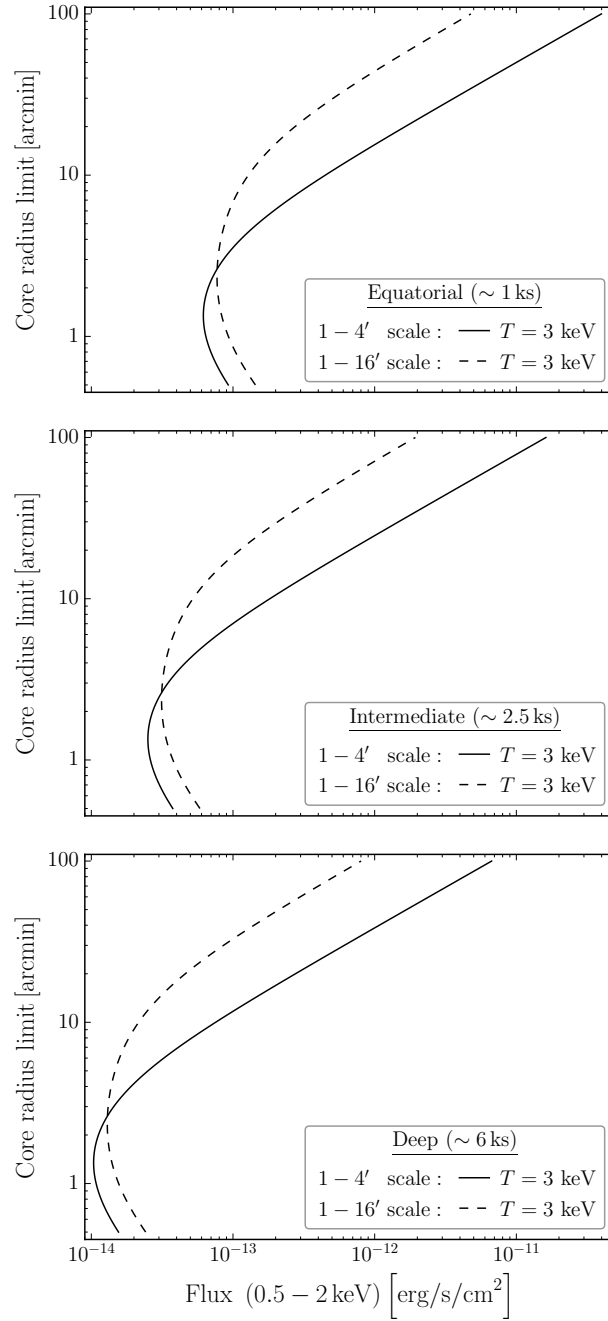


Figure 3.4: Galaxy cluster core radius limit as a function of flux for an equatorial, an intermediate, and a deep final eROSITA survey field of approximately 1 ks, 2.5 ks, and 6 ks exposure, respectively. The black solid and black dashed lines show the core radius limits of a 3 keV cluster corresponding to 40 and 80 β -model counts on a 1–4' and 1–16' radial scale, respectively.

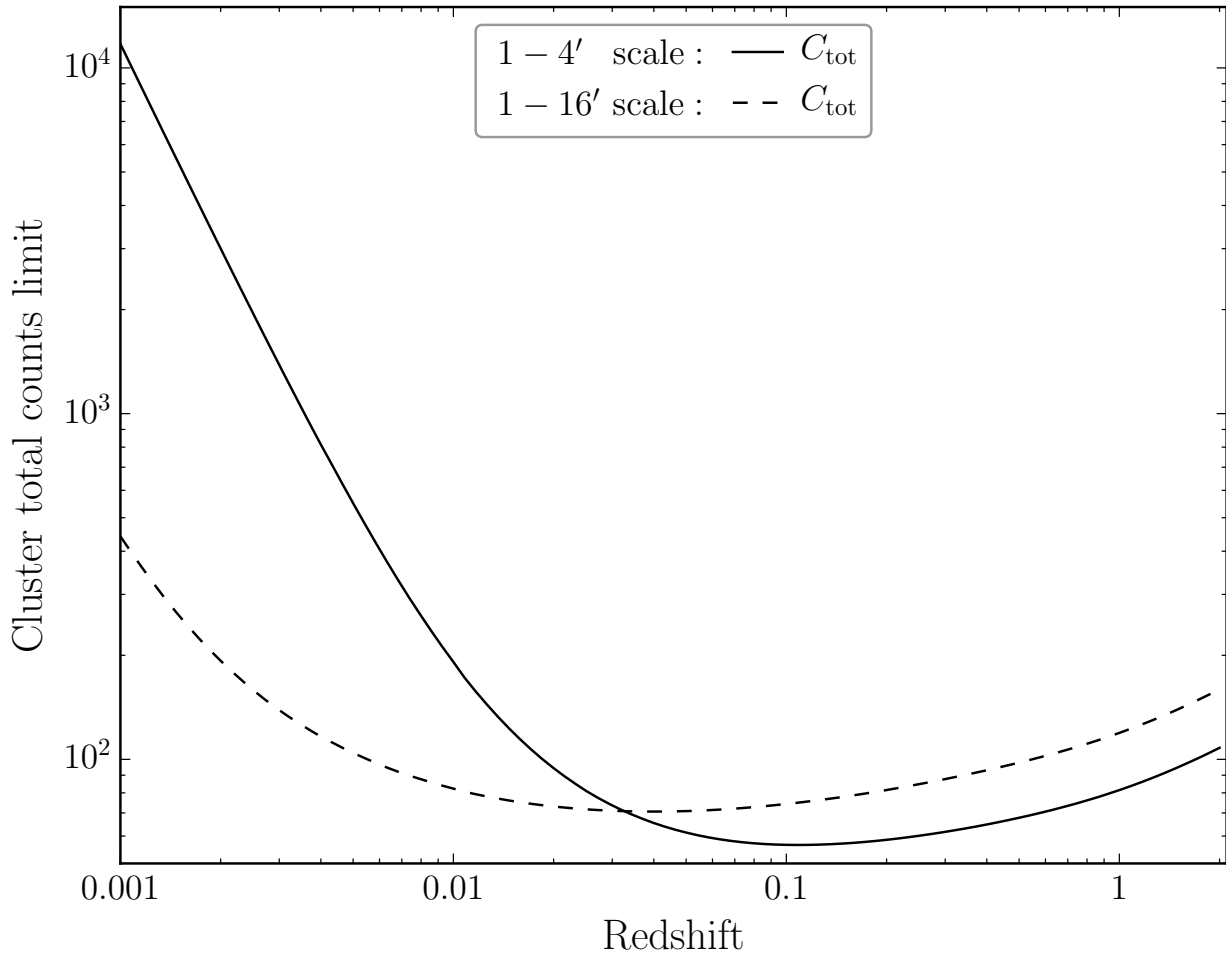


Figure 3.5: Galaxy cluster total count limit as a function of redshift. The black solid and black dashed lines show the total count limit, corresponding to 40 and 80 β -model counts on a 1–4' and 1–16' radial scale.

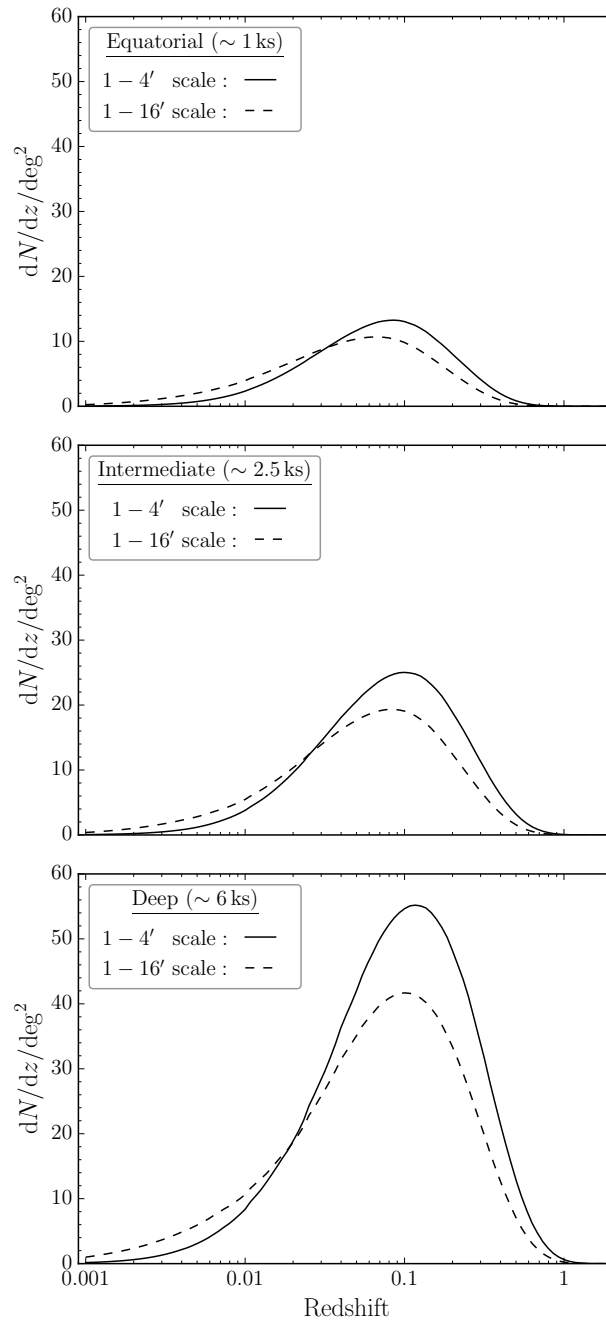


Figure 3.6: Differential number of galaxy clusters per square degree as a function of redshift for the three final eROSITA survey fields and the two considered radial scales.

the output of the simulator using a preliminary version of the eSASS package (User release of 2018 April 20).

3.5.1 Selection function of extended sources

The determination of X-ray survey extended source catalogs and the corresponding selection functions is a trade-off between completeness and purity. The completeness describes the fraction of clusters as function of mass and redshift. Determining it requires an accurate galaxy cluster model because the extended source detection probability depends on the cluster shape. The purity characterizes the contamination of the final sample and requires realistic synthetic simulations. Contamination occurs as a result of point sources that are misclassified as extended or detections that cannot be associated with any input source within a given search radius (spurious detections). We simulated clusters on a predefined spatial grid with a source density such that the emission from neighboring sources did not overlap. This prevented source confusion. The source detection is primarily on the 1–4′ scale, and we cross-matched extended sources within this typical detection scale of 4′ to the input catalogs. This radius is much smaller than the grid size and slightly larger than the maximum simulated core radius of 3.3′. We show the maximally clean (i.e., 7σ threshold) extended source detection efficiency in the final equatorial survey field as a function of core radius and input flux in Fig. 3.7. Similar to the wavelet decomposition techniques of [Vikhlinin et al. \(1998\)](#) and [Burenin et al. \(2007\)](#), our method requires larger photon statistics on compact sources to reduce point-source contamination. The deficiency of detecting compact objects is the topic of a future study, which relates the angular size to physical scales of the galaxy cluster. A study of the trade-off between cool-core bias and detection efficiency is also deferred to a future work. The question of how to clean the PED scales is still open. One possibility is to perform a blind analysis by feeding the maximally sensitive source candidate list into the eSASS ML fitting routine. For each candidate, a set of source parameters (position, count rate, and extent) was determined by fitting a PSF-convolved β -model to the spatial distribution of the source counts. The final extended source catalog was compiled by exploring the output parameter space (detection likelihood, extent parameter, and extent likelihood) and by determining appropriate classification thresholds, for instance, to distinguish point-like and extended sources or reduce contamination. This resembles the approach used in [Clerc et al. \(2018\)](#) to characterize extended sources that are detected by a sliding-cell algorithm, which scans the X-ray image with a sliding square box of different sizes and weights the counts in the detection box with a β -model kernel. This method is a modified version of a sliding-cell and ML fitting adapted for the *XMM-Newton* Science Analysis Software. [Valtchanov et al. \(2001\)](#) compared the performances of several source detection algorithms and found serious drawbacks of this method for the analysis of extended sources because a relatively large number of spurious detections are made and extended sources are split. The sliding-cell method has a high detection rate of sources with small angular extent ($\lesssim 60''$) at the cost of higher contamination in the ML characterization. When we assume that the detection comes from similar angular scales, the region with most of the misclassified AGNs is excluded when we apply our maximally clean threshold of 7σ (extension likelihood of approximately 50) and the extent cut of $60''$ to Fig. 9 of [Clerc et al. \(2018\)](#). Our detection algorithm naturally excludes this highly contaminated region and does not require

tuning of extended-source parameters like in the classical wavelet or sliding-cell approach. Thus, both detection methods can be used complementary or individually to determine discrepancies in the recovered cosmological parameters. Above $60''$, the detection probability stays roughly constant for clusters with larger core radius and does not decrease for clusters up to $200''$ because the cluster fluxes are spread over a larger area. Thus, our detection algorithm outperforms the sliding-cell plus ML characterization routine (see Fig. 3.7) for large extended sources above approximately $80''$. In Fig. 3.7 we also show the 90% completeness level of the 5σ detection threshold. This threshold corresponds to a similar number of detected clusters per square degree between the sliding-cell plus ML characterization algorithm and our method (see below). At the expense of purity, the sliding-cell method is more sensitive for extended sources with core radii smaller than approximately $40''$, which correspond to clusters with r_{500} values below $2'$. For the eROSITA survey, this gain in sensitivity is a minor effect because the flux of these objects is expected to be close to zero. Our proposed scheme shows an improvement in detection for flat sources, which are considered as background in other techniques. A more realistic treatment of cluster shapes requires a library of real cluster images, also to properly scale the cool-core emission. This is left for a future study. The classical wavelet approach for eROSITA source detection is under development, and we can only compare to the existing study based on the sliding-cell algorithm. The main difference is a change in input list because it also requires an ML characterization.

Similar to the description in Sect. 3.4, we used the input temperature to convert the input flux into a luminosity and also used the XXL scaling relations to calculate the galaxy cluster mass, $M_{500,ML}$. The extended source detection efficiency as a function of mass and redshift is shown in Fig. 3.8. The increasing apparent size toward low redshift causes a drop in the detection efficiency.

We folded the 5σ and 7σ selection on the $1-4'$ scale (Figs. 3.7 and 3.8), as well as the sliding-cell selection (Clerc et al., 2018, Appendix A), into the calculation of the differential number of clusters per square degree by multiplying the mass function in Eq. 3.5 with the probability of detecting a cluster of the given mass, that is, the selection function $\theta(M)$,

$$\frac{dN}{dz \text{ deg}^2} = \int_{M_{\min}=10^{13} M_{\odot}}^{M_{\max}=10^{16} M_{\odot}} \frac{dn}{dM} \frac{dV}{dz} \theta(M) dM. \quad (3.7)$$

In practice, we analytically parameterized the selection as a function of core radius and flux. The overall functional form of the detection efficiency is described by an error function, which was scaled to range between zero and one. The overall shape of the error function is defined by its argument. Compared to Clerc et al. (2018), we required a more complex functional form of the argument because it needs to describe a change in slope for different core radii in addition to an offset in flux for different core radius values. The goal is to find a functional form that is as simple as possible but still accounts for these observed features. The functional form of the argument is found by iteratively adding more complexity to it until the detection efficiency is described well. Then, the free parameters are optimized using a Markov chain Monte Carlo posterior sampling technique. Therefore, the functional form has no physical motivation. To improve the iterative finding of the functional form, we reduced the dynamical range of the core radius and flux by

Table 3.1: Best-fit parameters of the analytic selection function (Eq. 3.8) for the 5σ and 7σ detection thresholds.

Detection threshold	a	b	c	d
5σ	1.40	2.86	3.35	1.66
7σ	0.77	3.42	4.78	2.43

taking the logarithm and subtracted the corresponding means to rescale the offsets. The selection function is described best according to

$$\begin{aligned}
 \theta(R, F) &= 0.5 + 0.5 \cdot \operatorname{erf}(a + b \cdot R + c \cdot F + \exp(d \cdot R)) \\
 R &= \log(r_c / [\text{arcsec}]) - 2 \\
 F &= \log(\text{flux} / [\text{erg s}^{-1} \text{cm}^{-2}]) + 13.
 \end{aligned}
 \tag{3.8}$$

The parameters a , b , c , and d depend on the detection threshold. We show the models and their parameters in Fig. 3.9 and Table 3.1 for the 5σ and 7σ thresholds. These simple models cannot capture the complexity of the selection, but they provide a good estimate of the detection efficiency. The impact of the different selection functions on the differential number counts is shown in Fig. 3.10. The expected number of galaxy clusters per square degree for the [Clerc et al. \(2018\)](#) and the 5σ selection is approximately 4.2. At the cost of reduced purity, high-redshift clusters are detected more efficiently by the sliding-cell algorithm plus ML fitting technique, while the method based on wavelet decomposition performs much better in detecting the local population, that is, in particular galaxy groups. The 7σ selection reduces the contamination by more than two orders of magnitude (see Sect. 3.5.2), but the number of detected clusters per square degree is, with approximately 1.7, more than halved.

We require better knowledge of how the background behaves in reality to securely forecast the detection of very extended low-redshift objects for which the core radius limits are larger than $200''$. The uncertainty on small scales is dominated by the unknown shape of the survey PSF. The eROSITA PSF does not vary much over the eROSITA field of view compared to other X-ray instruments like *Chandra* and is, to first approximation, constant in survey mode. An interesting planned implementation for our proposed method is therefore subtracting point sources using a precise PSF model in the ML fitting routine.

3.5.2 Selection

We address the question how well the detection through cluster outskirts resembles a favored step-function-like selection. Figure 3.11 shows the detection efficiency on two angular scales and different core radius bins as a function of predicted model counts, which are independent of PSF effects. For a given number of predicted counts, clusters with larger extent are detected more efficiently. In other words, even with a larger number of predicted counts, clusters with

smaller extent are harder to detect. The interesting finding that gradually increasing counts toward smaller core radii are required is summarized in Fig. 3.12, showing the predicted model counts for a given detection efficiency as a function of core radius. In addition, it shows values of the model count ratio on the 0–1′ over the 1–4′ and 1–16′ radial range, respectively. This emphasizes that for a given detection efficiency, the required counts in the outskirts increase with increasing inner-to-outer counts ratios. Considering an additional contribution of AGN in cluster centers, this is particularly challenging for clusters above a redshift of 0.6, where simulations indicate that the distribution of the ratio becomes broader and exhibits a significant fraction larger than two (Biffi et al., 2018). These findings motivate the estimation of contamination due to bright sources and due to low photon statistics separately because the flux distribution of faint sources is different from that of bright sources. We studied these two effects by creating two extended source catalogs, setting the detection thresholds of cataloging to 4σ and 7σ for the maximally sensitive and maximally clean selection, respectively. The number of false detections as a function of detection threshold is shown in Fig. 3.13. We obtain close to 1.1 and 0.008 spurious or misclassified extended sources per square degree in equatorial fields for the 4σ and 7σ detection thresholds, respectively. Detection thresholds greater than 7σ show zero contamination but also a lower detection efficiency in regimes of low photon statistics. The extended source detection efficiency as a function of detection threshold is exemplified, showing mass and redshift dependencies in Fig. 3.14. In several cases, the efficiency for the 2σ threshold drops because the algorithm keeps so much structure that the extracted sources cannot be associated with the correct input within the given matching radius.

3.6 Summary and conclusions

Large-area X-ray cluster surveys are powerful tools for deriving cosmological parameters when the selection effects are well understood. We proposed and characterized an algorithm based on a wavelet decomposition to detect extended source for the upcoming eROSITA mission. This technique produces well-defined cluster catalogs with simple selection functions. We detect clusters by their large-scale emission, which minimizes the predominant impact of excess cool-core emission. Our main result is that progressively more counts are required with decreasing cluster extent to achieve a specific detection efficiency. In addition, our analytical calculation shows that an increasing number of total counts toward low redshift is required, meaning a larger angular extent, to detect clusters as extended sources. These two findings disagree with the assumption that a fixed minimum number of total photons are necessary to identify clusters (e.g., Pillepich et al., 2012; Borm et al., 2014). We predict redshift-dependent cluster observables and mass limits for an equatorial, intermediate, and deep final eROSITA survey field by assuming a minimum number of 40 and 80 counts to identify a cluster on a 1–4′ and 1–16′ angular scale, respectively. The counts in the cluster outskirts define an easy-to-measure observable, and applying a minimum photon threshold provides a selection that approximately resembles a step function. We tested the performance of our detection scheme through Monte Carlo simulations of a final equatorial eROSITA survey field of approximately 1 ks net exposure time. Our maximally clean detection method requires larger photon statistics on objects with core radii smaller than 60″ to minimize

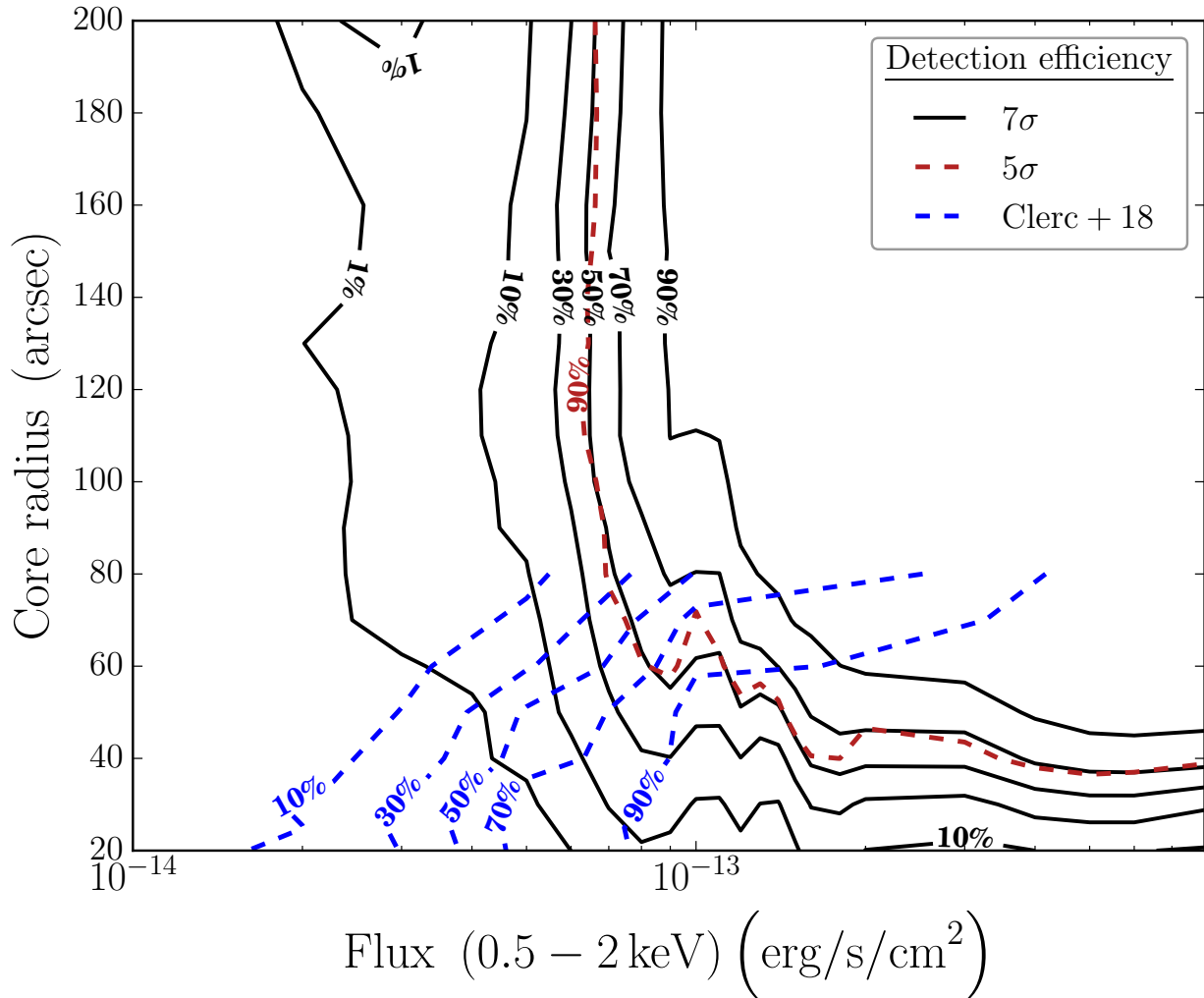


Figure 3.7: Extended source detection efficiency of our maximally clean (7σ threshold, black contours), our 5σ threshold (brown contour), and the Clerc et al. (2018) threshold (blue contours) in the core radius vs. input flux plain for an equatorial eROSITA survey field of approximately 1 ks exposure.

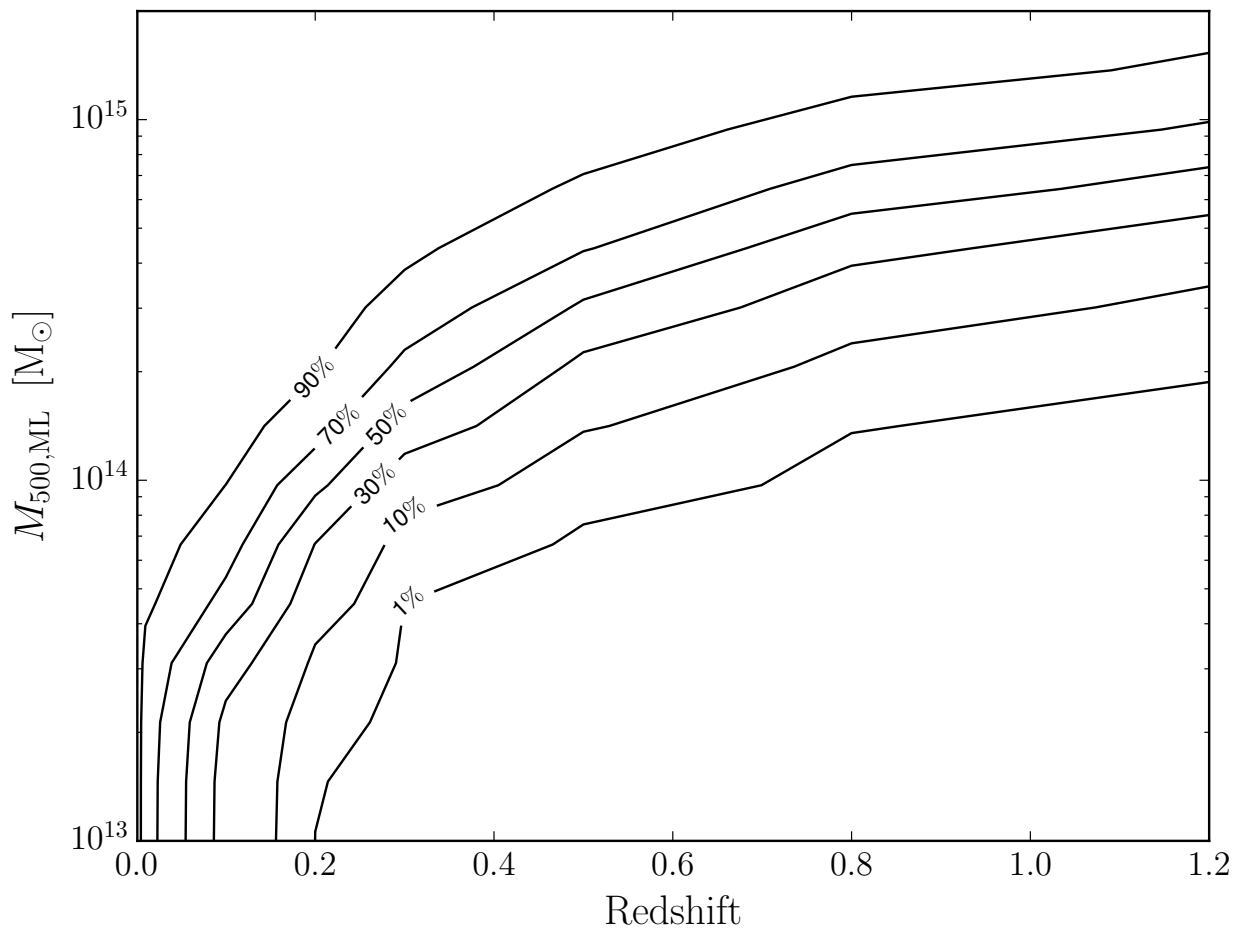


Figure 3.8: Maximally clean (7σ) extended source detection efficiency (black contours) in the mass vs. redshift plane for an equatorial eROSITA survey field of approximately 1 ks exposure.

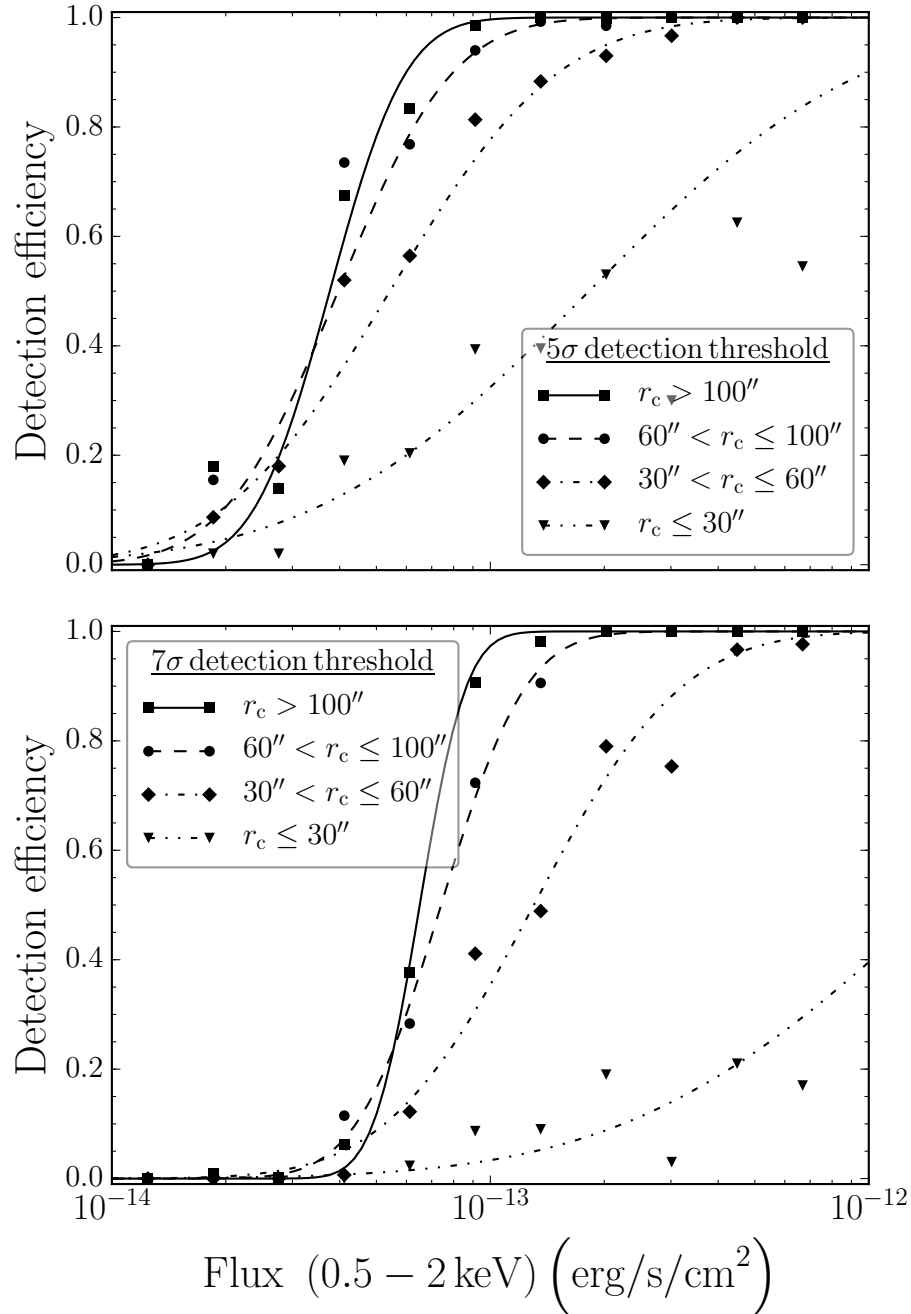


Figure 3.9: Detection efficiency as a function of input flux for four core radii bins of the 5σ (upper panel) and 7σ (lower panel) detection thresholds. Lines correspond to the model expectation of Eq. 3.8 for core radii of $25''$, $50''$, $85''$, and $150''$.

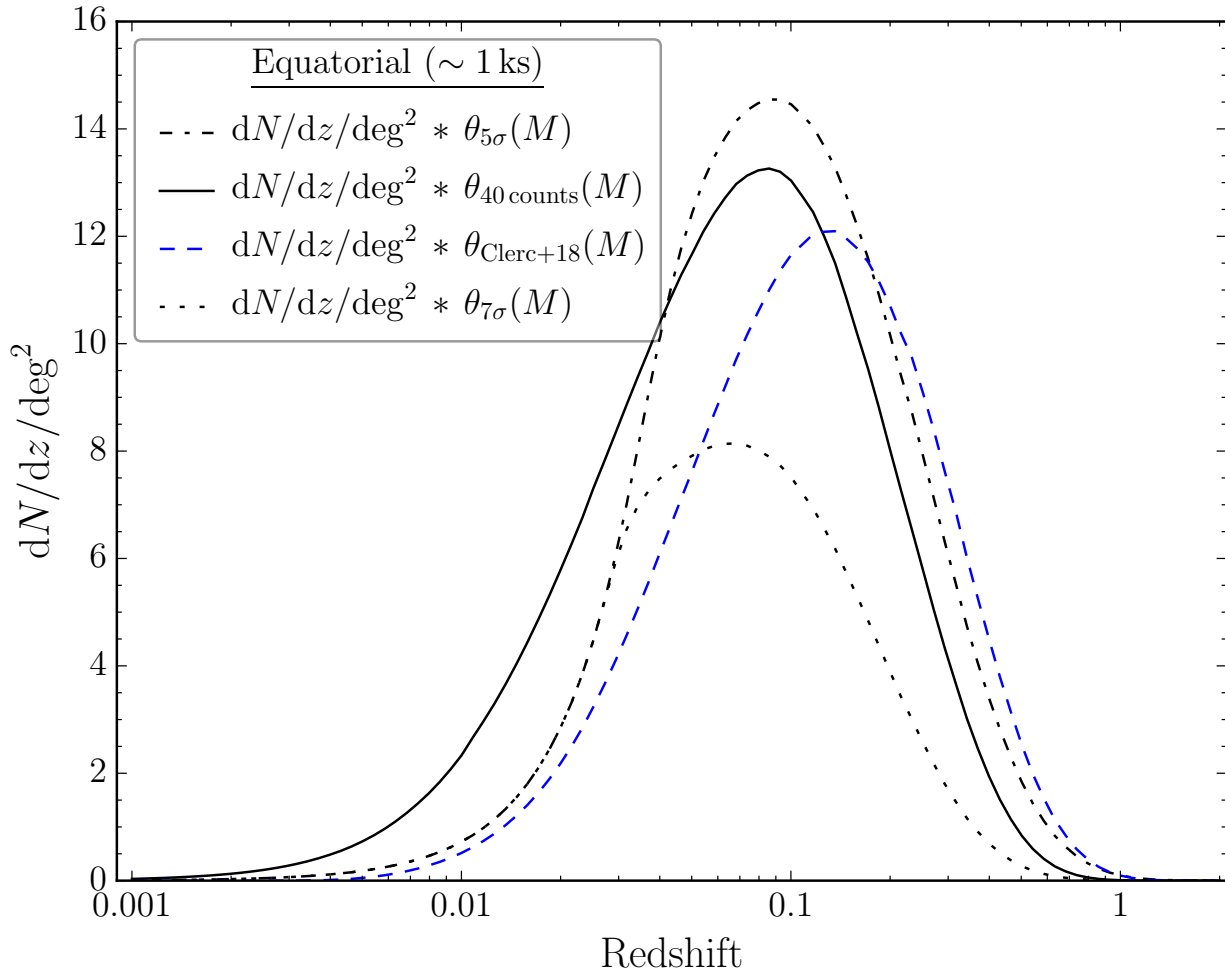


Figure 3.10: Expected differential number of galaxy clusters per square degree as a function of redshift for the final equatorial eROSITA survey field with different selection functions folded in. The solid line serves as comparison and show the 40 aperture count selection on the 1–4′ scale of Fig. 3.6.

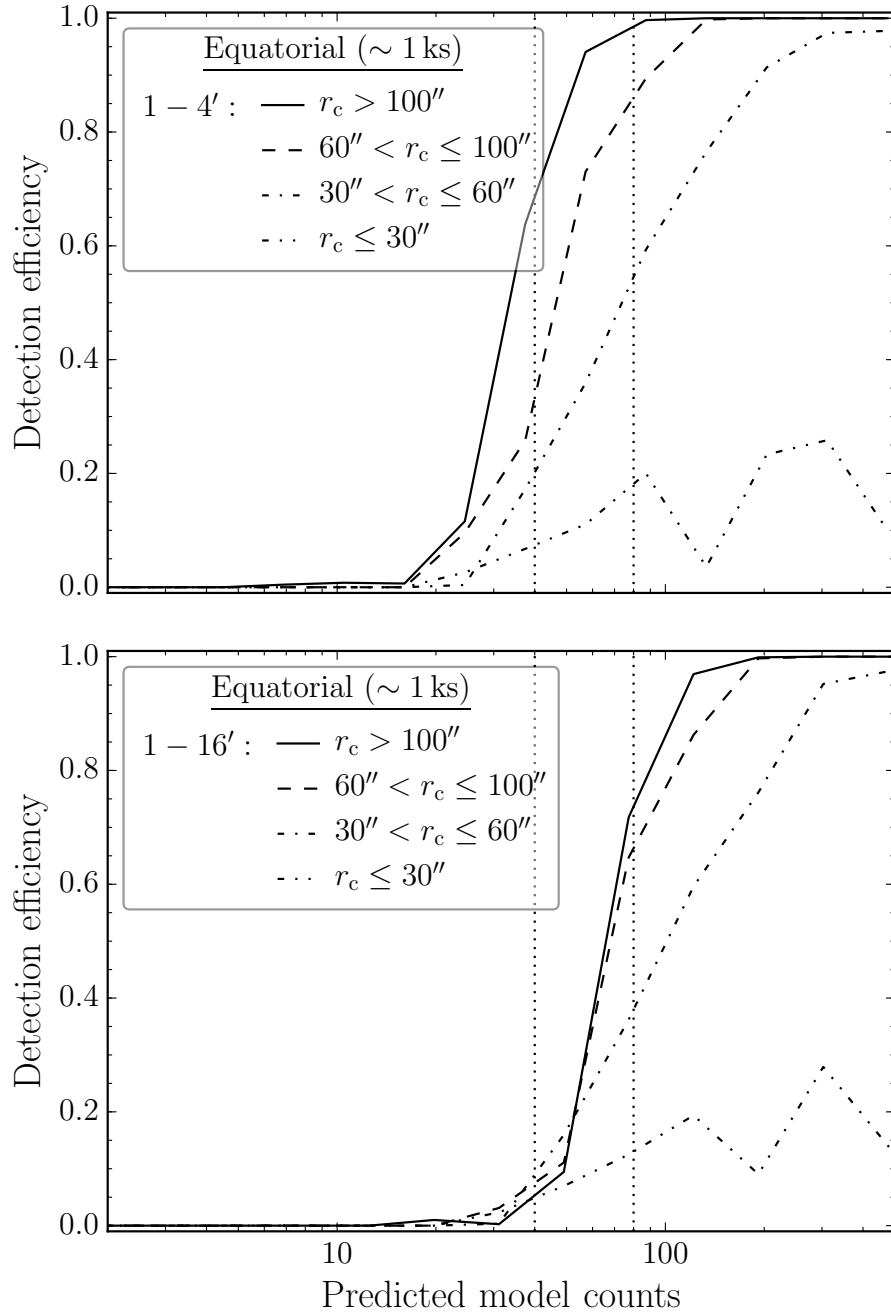


Figure 3.11: Detection efficiency as a function of predicted model counts on the 1–4' (upper panel) and 1–16' (lower panel) radial scale for four core radius bins. The dotted vertical lines correspond to 40 and 80 aperture counts, respectively.

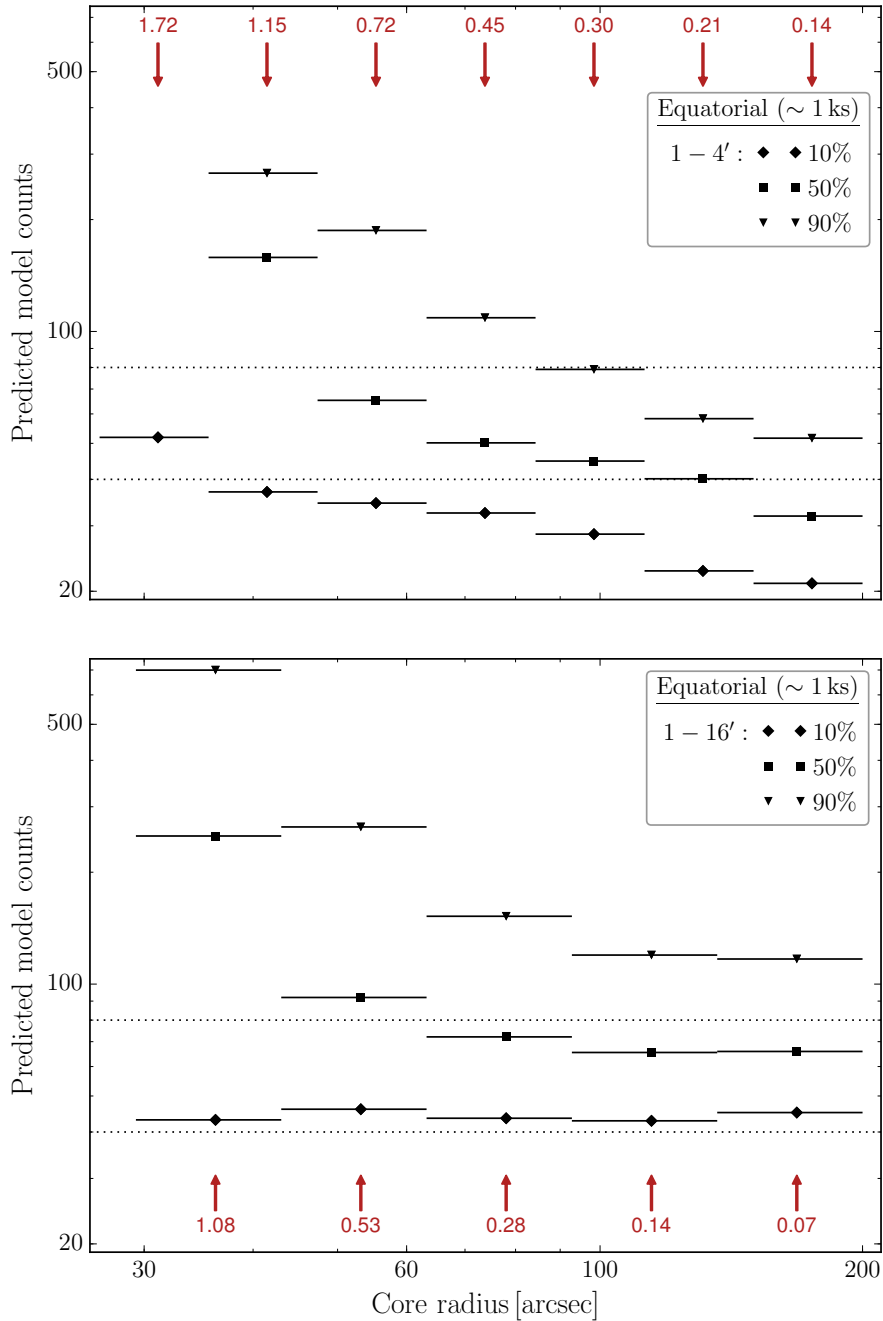


Figure 3.12: Predicted model counts for a 10%, 50%, and 90% detection efficiency as a function of core radius on the 1–4' (upper panel) and 1–16' (lower panel) radial scale. The brown values indicate the ratio of the model counts in the 0–1' and the corresponding angular scale of the individual core radius bin. The dotted horizontal lines correspond to 40 and 80 aperture counts, respectively.

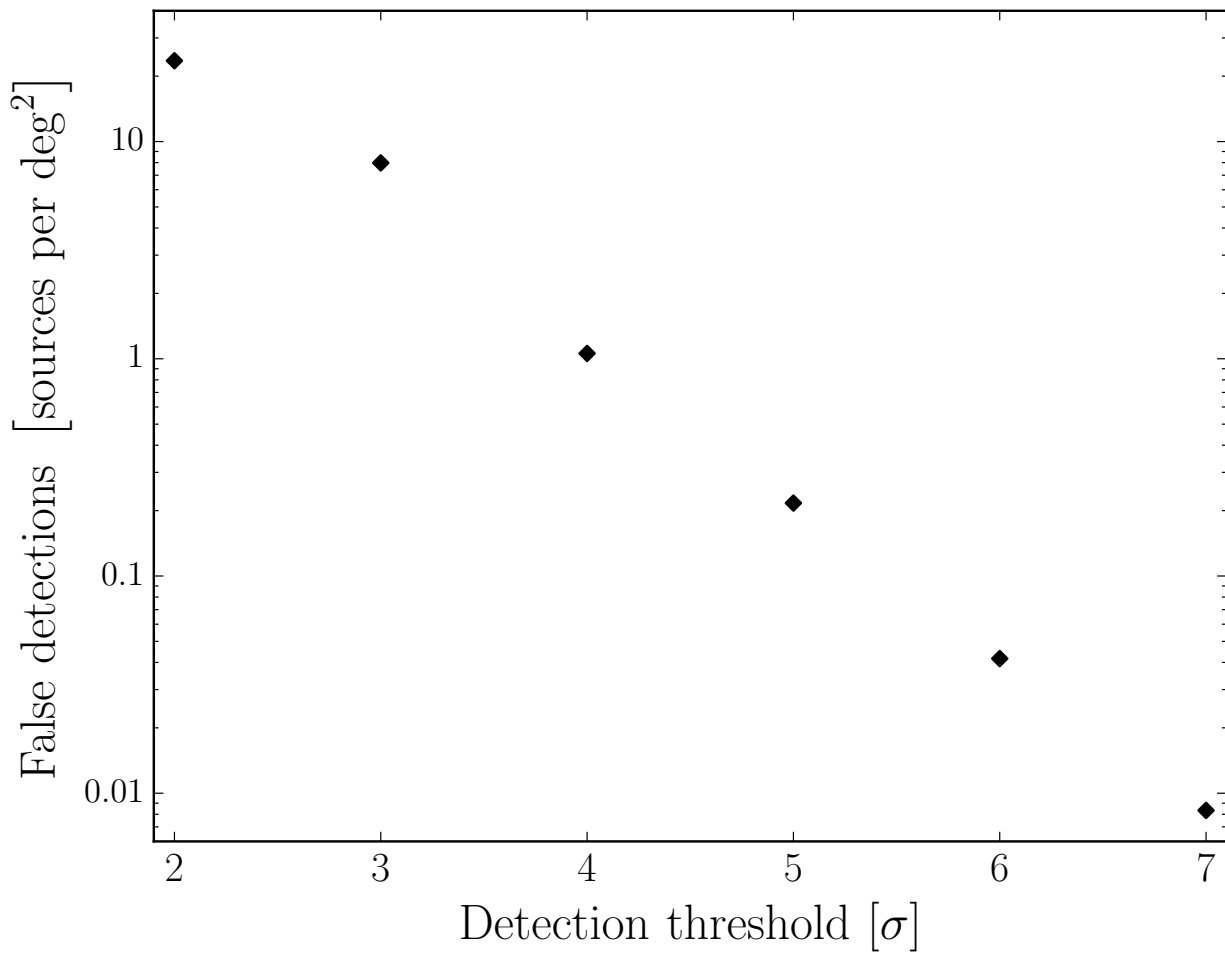


Figure 3.13: Number density of spurious and misclassified extended sources as a function of detection threshold for an eROSITA survey exposure of approximately 1 ks.

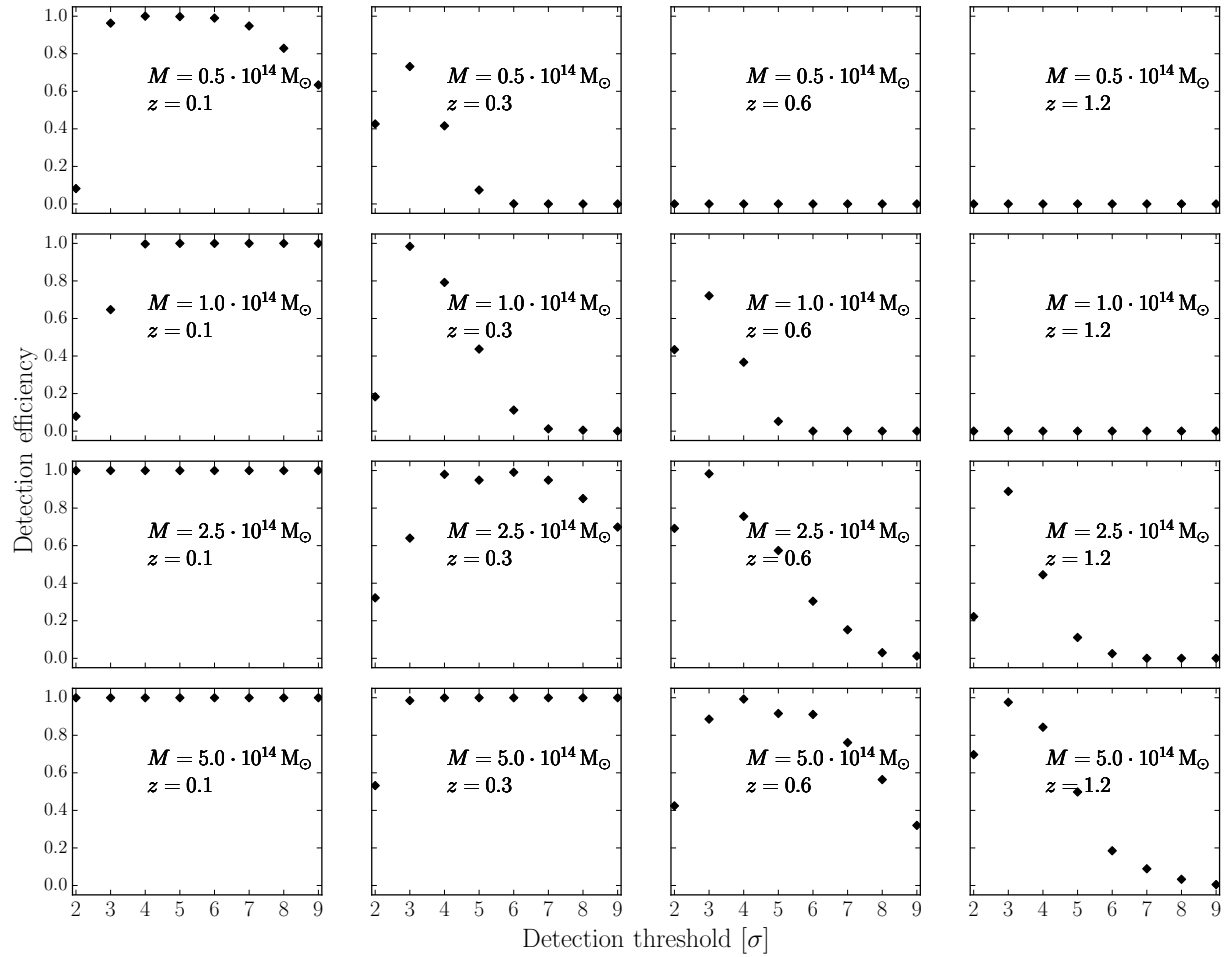


Figure 3.14: Detection efficiency of extended sources as a function of detection threshold for snapshots in redshift and mass for an eROSITA survey exposure of approximately 1 ks.

point-source contamination and has an approximately 90% detection efficiency at input fluxes of 10^{-13} erg s $^{-1}$ cm $^{-2}$ for clusters with larger extent. This is complementary to the sliding-cell algorithm plus ML fitting technique that is currently implemented as default in eSASS, which shows a drop in detection efficiency at this flux for clusters with core radii larger than 60'' (Clerc et al., 2018). We note that this blind analysis approach increases the contamination of the final catalog by misclassified AGNs and spurious extended sources. At a similar level of completeness, our catalogs are approximately 2.5 times purer than the current eSASS default. Our performance results are limited because we worked with pre-flight assumptions of instrumental and astrophysical characteristics. The proposed pipeline has the advantage that the final tuning, that is, the point-source model training due to a different in-orbit PSF or the optimized selection of the detection thresholds, is easy to implement, robust, and can be achieved very fast during the PV phase. An in-flight calibration of the pipeline below 5% is expected to keep the loss of clusters through central AGN contributions below 1%.

Chapter 4

Future prospects

The novel procedures and the scientific interpretations described in this work have significant value for future studies. In the following sections we introduce and discuss three promising ideas for future work.

4.1 Measurement of the core-excised luminosity in the eROSITA cluster survey

The characterization of galaxy clusters plays a key role in their use as cosmological probes. At the current state of research the aim is to discover X-ray clusters at a limit of photon statistics, which limits their characterization (Borm et al., 2014). If the redshift of the cluster is known, the X-ray luminosity can be measured even with tens of photons. The X-ray luminosity is therefore widely used to characterize clusters in survey data, such as the all-sky survey performed by eROSITA. On the other hand, the correlation of the total luminosity with total mass is not as tight compared to other observables like temperature. The larger scatter of the luminosity-mass scaling relation is mostly driven by clusters which show centrally peaked surface-brightness profiles, meaning clusters which exhibit cool cores. Excising the cluster centers reduces this scatter and the core-excised X-ray luminosity has been identified as a low-scatter galaxy cluster mass proxy (e.g., Maughan, 2007; Zhang et al., 2007; Pratt et al., 2009; Mantz et al., 2018).

So far, the measurement of the core-excised luminosity itself has only been considered once the cluster mass has been measured. Mantz et al. (2018) propose a measurement of core-excised luminosity using follow-up data and a scaling relation between core-excised luminosity and mass. However, following up a large amount of eROSITA clusters can be time consuming. In addition, the approach complicates the modelling of the cluster selection. Nevertheless, the attention given to the computation of the core-excised luminosity by various authors shows the importance of the problem, as well as the complexity of such an estimate. In this study, we make use of the self-similar behavior of galaxy-cluster outskirts (e.g., Zhang et al., 2007; Ghirardini et al., 2018a; Käfer et al., 2019), that is the universality of the shape of the X-ray emission. A similar problem has been successfully addressed by thermal Sunyaev-Zel'dovich-effect cluster surveys by performing an iterative reconstruction of the signal based on the knowledge of the

cluster profile.

In X-ray galaxy cluster surveys, the cluster selection is associated with a key measurement to characterize the extended emission. This selection needs to be simple and easy to model. Current cluster catalogs also lack a universal definition of the luminosity and in particular the radius at which this is defined. In the ROSAT-ESO Flux Limited X-ray (REFLEX) galaxy cluster survey catalog (Böhringer et al., 2004), for example, the value of the radius in which the luminosity is measured is not provided. Piffaretti et al. (2011) compiled publicly available serendipitous and ROSAT All-Sky Survey (RASS) cluster catalogs into the Meta-Catalog of X-ray detected Clusters of galaxies (MCXC), in which the luminosity is consistently measured within the overdensity radius r_{500} . In the XMM-Newton Large-Scale Structure (XMM-LSS, Pierre et al., 2007) and the XMM-XXL (Adami et al., 2018) catalogs a full luminosity measurement within a radius of 300 kpc has been introduced, suitable for the expected low masses of the systems. Core-excised luminosities are cataloged in a number of deep surveys (Finoguenov et al., 2009, 2010b, 2015; Gozaliasl et al., 2019) and show good correspondence with tSZ expectations.

In X-ray surveys, measuring the flux in an annulus is a straightforward and simple approach to obtain the core-excised luminosity. The main problem is that this annulus is typically defined in angular units. The outmost radial extent of the annulus can be adjusted based on the quality of the data. The inner radius however, is fixed by the instrumental characteristics and not by the properties of the cluster. Measuring the flux in such a fixed angular aperture will probe different physical zones of galaxy clusters, depending on their masses and redshifts. This introduces a scatter between the extraction region in angular units and the probed physical region of the cluster. These effects with cluster masses and redshifts need to be characterized and understood, which is one of the goals of this study. In addition, the scatter values are covariant with the signal-to-noise ratio when varying the size of the annulus. This covariance is an undesired complication for the cosmological goals of eROSITA.

Galaxy cluster profiles can be modeled with a self-similar evolution of the cluster outskirts and a non-evolving central part (McDonald et al., 2017). This has been verified using massive clusters detected by the South Pole Telescope (SPT), as well as in Chapter 2 for a mass range of approximately 10^{14} – $10^{15} M_{\odot}$, which includes the lower mass end expected for eROSITA clusters (e.g., Merloni et al., 2012; Pillepich et al., 2012). Based on these findings we developed a galaxy-cluster-detection scheme in Chapter 3, which allows to measure the scatter of simplified core-excised luminosity measurements due to the variety of cluster shapes.

The next logical step is to create a suitable framework to characterize the galaxy clusters after, or even during, detection. We focus on the reconstruction of the luminosities and the associated total cluster masses, as for SZ catalogs. Providing these products for the eROSITA survey increases accessibility and visibility of the survey, because they are simpler to use without detailed modelling of the selection. Therefore, they can also be used by astronomers that are not necessarily interested in a high precision of the mass determination.

4.1.1 Method

The typical quality of the eROSITA survey data precludes fitting of surface-brightness models with many free parameters. This includes, but is not limited to, additional free parameters to

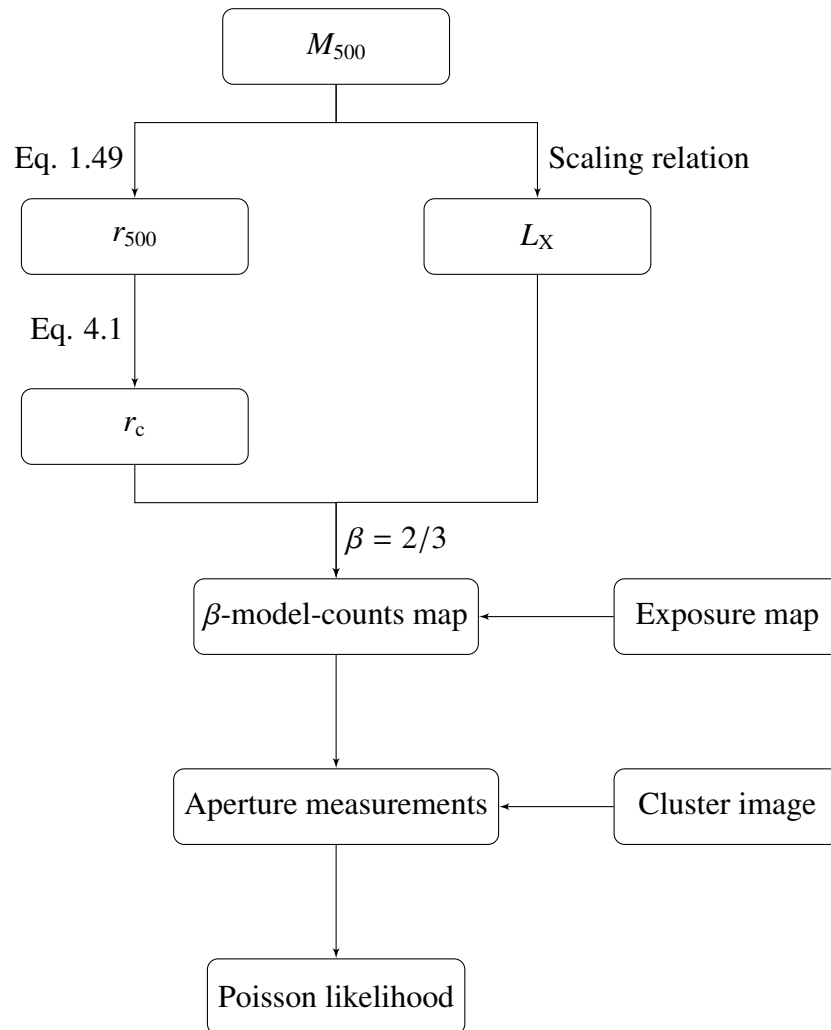


Figure 4.1: Illustrative flow chart to reconstruct the galaxy cluster mass using an MCMC posterior sampling technique with a Poisson likelihood to compare the measured aperture photon counts to the β -model predictions for a given mass estimate.

model the core region, which are generally degenerate with other surface-brightness parameters. The key feature of the proposed method is to fix the profile shapes in the cluster outskirts. Then, the surface-brightness model fits the data better outside the core region. In addition, we study aperture estimates where the poorly resolved inner part of the cluster is excised, instead of being fitted.

In the simplest application of the method, this reduces the amount of free parameters to one, the cluster mass. A flow chart of the procedure for a given mass estimate is shown in Fig. 4.1 for visualization. An initial guess of the cluster mass allows the computation of the overdensity radius r_{500} according to Eq. 1.49. From our analysis in Chapter 2 we know that the extent parameter of a single β -model in the cluster outskirts scales with the overdensity radius through

$$r_c = \frac{r_{500}}{3}. \quad (4.1)$$

Together with the exposure map and assuming a fixed β -parameter, this allows the computation of the β -model counts in a predefined aperture. With the initial mass guess, the core-excised luminosity can be calculated through a scaling relation. Given the already discussed differences in the definition of the luminosity, the mass-luminosity scaling relation is generally less well understood. This might change with the availability of eROSITA survey data, as well as Dark Energy Survey (DES) and Hyper Suprime-Cam (HSC) lensing data over large areas of the sky. In this work we will use the mass-luminosity relation of [Kettula et al. \(2015\)](#). The calculated luminosity defines the β -model normalization.

We note that the conversion between luminosity and count rate requires the redshift of the cluster to be known. Photometric redshifts with a sub-percent quality ([Klein et al., 2018](#)) are sufficient for this task. At the current stage, we also assume that the cluster temperature is known to calculate the conversion factor between luminosity and count rate. In practice, the cluster temperature will be estimated similar to the luminosity, meaning from the mass estimate through a temperature-mass scaling relation. [Grandis et al. \(2018\)](#) suggested to define a characteristic luminosity by dropping the K-correction to avoid using a mass-temperature relation. This, however, increases the demands on the redshift-dependent calibration and might change the assumption of a simple power-law scaling between mass and luminosity.

We use an MCMC posterior sampling technique ([Foreman-Mackey et al., 2013](#)) with a Poisson likelihood to compare the obtained β -model counts to the measured counts in the predefined aperture. The aperture can be fixed or defined by the data, for example by calculating the $0.2-0.5 r_{500}$ from the mass estimate in each iteration. When the aperture is fixed, the difference compared to simply using a scaling relation with a fixed aperture is that the cluster counts are compared to the counts of a β -model, whose core radius depends on the mass estimate.

The method allows the inclusion of background components and point-source flux by adding them to the β -model counts. The current implementation of the code¹ does not yet take PSF effects into account. The two dimensional approach takes exposure variations across the extraction region into account and is easily extendable to more complex models, for example to consider ellipticity.

¹<https://github.com/KaeferFlorian/mrec>

4.1.2 Validation of the method

To validate our method we reconstruct galaxy cluster masses in simulated eROSITA data (Comparat et al., 2020). For this idealized performance check, clusters are considered isolated and without background or point-source contamination. We pick a random equatorial sky tile of approximately 170 square degrees and roughly 1 ks net exposure time. The field contains 240 simulated clusters with halo masses above $2 \cdot 10^{13} M_{\odot}$.

Aperture definition

The choice of the aperture to calibrate the core-excised luminosity is largely missing in the literature and the definition of the excised regions varies between 0.1 and $0.2 r_{500}$. To characterize our method we discuss four cases of aperture definitions, which are summarized in Table 4.1.

- [1] First, we fix the aperture to the true 0.0 – $0.5 r_{500}$ range, known from the input of the simulation. This radial range is the baseline to compare the scatter in the core-excised mass determinations.
- [2] Second, the aperture is fixed to the true 0.2 – $0.5 r_{500}$ range from the input of the simulation.
- [3] Third, we adjust the 0.2 – $0.5 r_{500}$ range as part of the fitting procedure, meaning that the extraction radius is newly calculated in each iteration of the mass determination, as opposed to use the fixed simulation input.
- [4] Fourth, we choose a fixed angular range which tries to match the 0.2 – $0.5 r_{500}$ interval. However, the angular size of a cluster depends on its redshift and mass. The study of the cluster size as a function of redshift in the eROSITA survey has been presented in Chapter 3 (see e.g., Fig. 3.3). For this study, we consider three redshift intervals to determine the size of the angular extraction region. A redshift of approximately 0.6 is a natural division of clusters into small and large in terms of their angular scale, which defines our high redshift bin ($z > 0.6$). In addition we define a low ($z < 0.3$) and an intermediate ($0.3 < z < 0.6$) redshift bin. The choice of the extraction boundaries is a trade-off due to the mass range in each redshift bin. Ideally, the extraction region is maximally close to the 0.2 – $0.5 r_{500}$ interval and optimally not outside the 0.1 – $1 r_{500}$ radial range. However, for the eROSITA survey the smallest radii suitable for the flux extraction starts at approximately $0.4'$ due to the instrument's PSF. On the other hand, the overlap of eROSITA sky tiles is $12'$ and it is therefore not convenient to deal with source extraction areas that exceed $6'$, as more than one tile has to be used. These two factors define the lower and upper boundary for the extraction regions, respectively. Therefore, our definitions of the extraction regions are 0.4 – $1.0'$, 1.0 – $2.5'$, and 2.5 – $6.0'$ for the low, intermediate, and high redshift bin, respectively.

Table 4.1: Overview of the chosen extraction regions and the corresponding redshift ranges for the four cases of aperture definitions. The last two columns show the median mass ratios between reconstructed and input masses \tilde{M}_{ratio} as well as the corresponding intrinsic scatter values $\lambda_{\tilde{M}}$.

Case	Extraction region		Redshift range	\tilde{M}_{ratio}	$\lambda_{\tilde{M}}$
[1]	Fixed	0.0–0.5 r_{500}	Full	0.98	0.59 ± 0.03
[2]	Fixed	0.2–0.5 r_{500}		0.82	0.47 ± 0.03
[3]	Free	0.2–0.5 r_{500}		0.83	0.50 ± 0.03
[4]	Fixed	0.4–1.0'	$z > 0.6$	0.73	0.48 ± 0.03
		1.0–2.5'	$0.3 < z \leq 0.6$		
		2.5–6.0'	$z \leq 0.3$		

Median-mass determination

First, we determine how accurate our algorithm computes the masses of individual clusters, M_n , with their corresponding 1σ errors, $\sigma_{M,n}$, in the idealized eROSITA simulation. The performance of our method is then quantified by calculating the median mass ratio between reconstructed and input masses, \tilde{M}_{ratio} . The intrinsic scatter of the median mass ratio, $\lambda_{\tilde{M}}$, is calculated in linear space using an MCMC posterior sampling technique (Foreman-Mackey et al., 2013) and adapting a Gaussian likelihood function

$$\mathcal{L} = \prod_{n=1}^N \frac{1}{\sqrt{2\pi}\sigma_n} \exp\left(-\frac{1}{2}\left(\frac{M_n - \tilde{M}}{\sigma_n}\right)^2\right) \quad (4.2)$$

$$\sigma_n = \sqrt{\sigma_{M,n}^2 + \lambda_{\tilde{M}}^2}. \quad (4.3)$$

The results for the different apertures are summarized in Table 4.1.

The ratio of the reconstructed mass over the input mass as a function of central emissivity for the different aperture definitions is shown in Fig. 4.2. Clusters with larger central emissivity values have surface-brightness profiles that are more peaked and represent cool-core objects. The data points are gray-scale-coded by the axis-ratio parameter, meaning that black points are more elliptical than white points.

The median values of the mass ratios are biased low by a factor of 0.83 and 0.73 for case [3] and [4], respectively. We assume that there is no hydrostatic mass bias, based on the work of Smith et al. (2016), who studied a well defined sample of Local Cluster Substructure Survey (LoCuSS) cluster. They concluded that the reported differences between X-ray and weak lensing masses correspond to poorly understood cluster selection at higher redshift rather than mass bias.

One possible explanation for this offset is that the simulated clusters do not follow the used luminosity-mass scaling relation. The simulations follow by construction the XXL, HIFLUGCS, as well as X-COP data and are therefore also in good agreement with the Kettula et al. (2015)

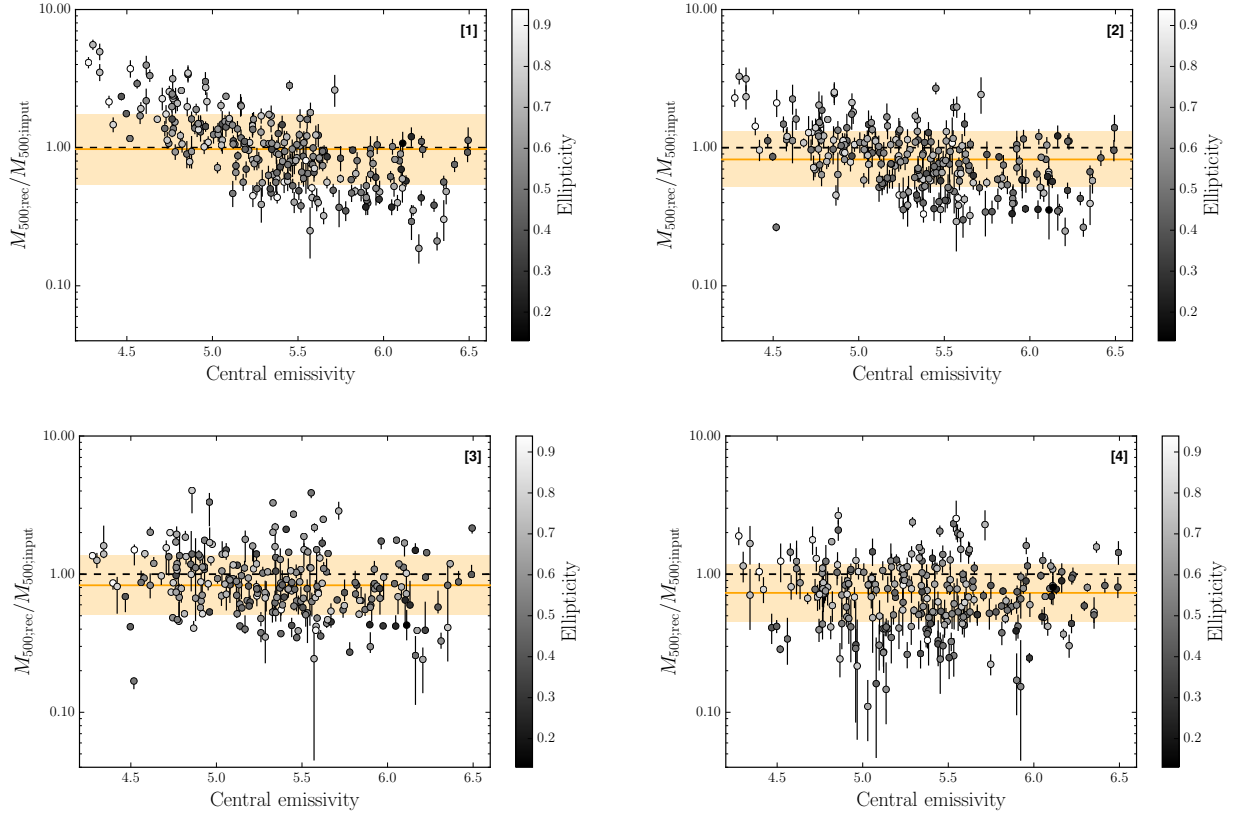


Figure 4.2: Reconstructed over input mass ratio as a function of central emissivity. The panels correspond to the four discussed extraction regions ([1]-[4]) as summarized in Table 4.1. Data points are gray-scale-coded by their ellipticity. The orange lines and the shaded regions correspond to the median values of the mass ratios and their intrinsic 1σ scatter values.

scaling relation. There is no significant trend in the mass determination with respect to the input mass (see Fig. 4.3). Thus, we conclude that the reconstructed mass bias is most likely not driven by the slope of the scaling relation but might be due to the scaling relation normalization. Increasing the normalization by 18%, which is within the 1σ error, increases the median values of the mass ratios by 5%.

Currently, we investigate other possible explanation for the mass ratio offset. In addition to the scaling relation normalization there might be effects due to the aperture filtering, the self-similar assumption, or the instrument’s PSF.

Correlation between reconstructed mass and central emissivity

In case [1], the masses of clusters with lower central emissivity are systematically overestimated when including the cluster core in the mass determination. This results from a flux cut at $8 \cdot 10^{-14} \text{ erg s}^{-1} \text{ cm}^{-2}$ in the simulation. This selection effect introduces a correlation between halo mass and central emissivity, resulting in these objects with low cluster masses that are scattered up. These clusters are well below the selection threshold of the eROSITA survey and a cut

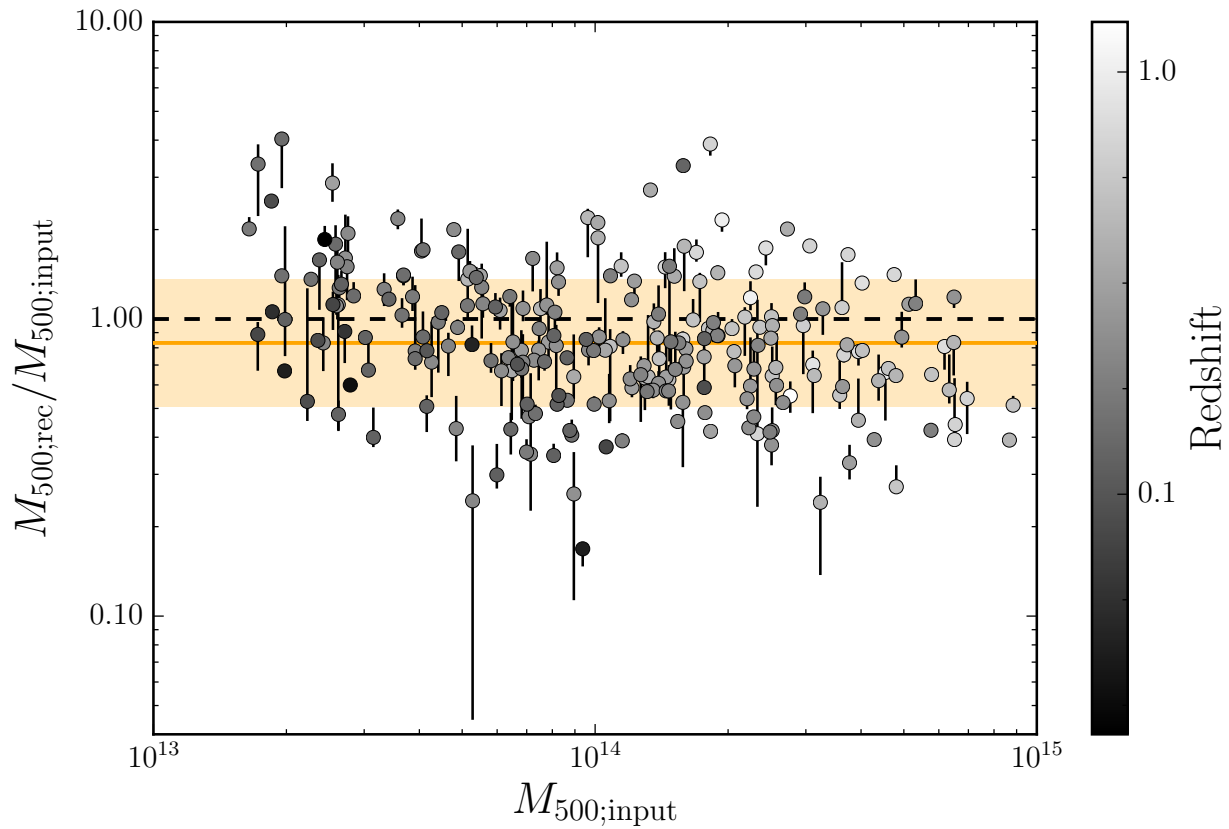


Figure 4.3: Reconstructed over input mass ratio as a function of input mass for the non-fixed $0.2-0.5 r_{500}$ extraction region. Data points are logarithmically gray-scale-coded by their redshift. The orange line and the shaded region correspond to the median value of the mass ratio and its intrinsic 1σ scatter value.

in mass, for example at $10^{14} M_{\odot}$ minimizes the impact of the selection in the simulation. It is important to understand such effects because variations in the cluster shape can bias cosmological results (Vikhlinin et al., 1998; Pacaud et al., 2018). When excising a fixed $0.2 r_{500}$ range in case [2], the selection effect due to the flux cut is minimized but still visible. The influence of the core emission on the mass determination is reduced when the $0.2\text{--}0.5 r_{500}$ range is free to vary (case [3]) or when the apertures are fixed to angular scales outside the redshift-dependent core region (case [4]).

Correlation between reconstructed mass and other cluster parameters

Figure 4.2 illustrates that there is no significant trend between the mass determination and the shape of the profile, that is the ellipticity and how peaked the profile is. There are also no significant trends between the mass ratio and the galaxy cluster fluxes or redshifts. In addition, there is no significant correlation between reconstructed masses and photon counts in the selected aperture. A count threshold in the outskirts defines a sub-sample of relatively well characterized sources, for which a reconstruction of the surface-brightness profiles is possible (Eckert et al., 2020) and the cluster detection is uncontaminated (Käfer et al., 2020). To fully benefit from low-scatter mass proxies, the measurement errors should not dominate the error budget. This sets practical limits of, for example 25 or 100 source counts in the cluster outskirts to achieve 20% or 10% scatter, respectively.

Calibration of the mass determination

The scatter of simulation parameters around their corresponding scaling relations is large and a calibration of our method on real data is needed. One way to calibrate our method is through *Chandra* observations of an SPT selected cluster sample (e.g., Sanders et al., 2018). The cluster selection can be taken into account following Bulbul et al. (2017). If we assume that there is no covariance between the SPT selection of cluster and their X-ray properties, a change in the X-ray scaling relation would not affect the cluster selection. This simplifies the likelihood computation for the calibration. By mimicking the mass distribution of the SPT sample, the sampling function can be calculated by the fraction of clusters observed by *Chandra* as a function of mass and redshift. Typically only the model prediction of the scaling relation is changed, while the proposed method allows us to also change the measurement of the core-excised luminosity itself at each step of the MCMC chain.

PSF effects

We study PSF effects on reconstructed morphological and photometric properties of cluster in more detail in Eckert et al. (2020). I contributed to the writing of this paper, but not to the code development. In this paper, the general method to reconstruct profiles is based on a linear decomposition of the observed profile onto a basis of King functions. For eROSITA, the impact of the PSF on the reconstructed cluster profile can be significant, especially on compact sources

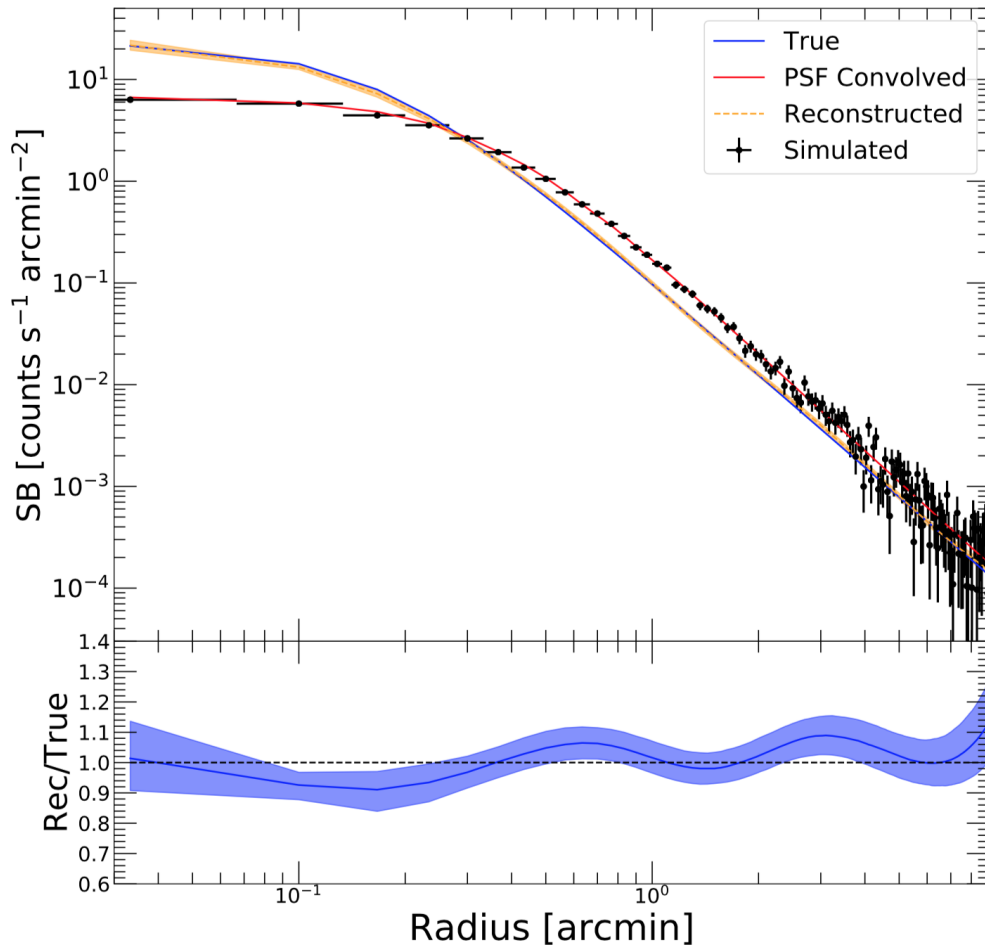


Figure 4.4: Reconstruction (orange curve) of the true cluster image (blue curve) from a Poisson realization (black points) of the PSF-convolved image (red curve). The ratio between reconstructed and input profile is shown in the bottom panel. Figure taken from [Eckert et al. \(2020\)](#).

(see Fig. 4.4). When the true PSF and the background are known, the PSF-reconstruction technique recovers the true cluster profile with differences below 5% down to the eROSITA-survey detection threshold. Compared to the simple extraction method presented in Sect. 4.1.1, the PSF-reconstruction technique does not show significant biases in the recovered core-excised luminosity or cluster mass (see Fig. 4.5). Thus we conclude that the preferred method shall be to include the PSF in the profile reconstruction. The intrinsic scatter of the recovered parameters is then approximately 16%.

4.2 Scaling relations of galaxy groups

To exploit the full potential of the eROSITA survey in using galaxy clusters as a precision cosmological probe, we require an accurate determination of the total cluster mass down to the group regime. Individual weak lensing or hydrostatic mass measurements are unfeasible for the

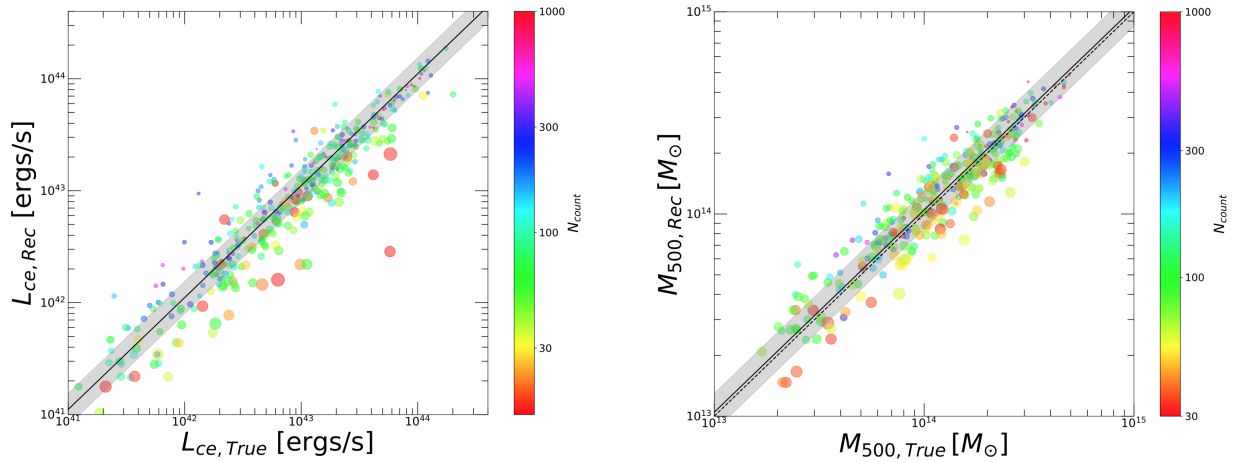


Figure 4.5: Reconstructed core-excised luminosity as a function of input core-excised luminosity (left panel), as well as reconstructed mass as a function of input mass (right panel). The number of reconstructed photon counts is shown as a color code. The solid lines and shaded regions represent the best-fit linear relation and their intrinsic scatter. The dashed line shows the one-to-one relation. Figures taken from [Eckert et al. \(2020\)](#).

majority of the expected number of detected objects and one is interested in well-calibrated and well-understood scaling relations. Due to their shallower potential well, galaxy groups are more affected by non-gravitational processes than galaxy clusters. In addition, line emission at galaxy group masses becomes significant on top of the bremsstrahlung continuum. Depending on the metallicity, more than 50% of the total X-ray emission can be contributed by line emission. This line emission is not included in the self-similar model. Therefore, galaxy groups seem more luminous and hotter for their mass relative to clusters in scaling relations. This leads, for example, to a steepening of the slope of the mass-luminosity scaling relation toward low masses ([Kettula et al., 2015](#)). This observed mass dependence of scaling relations, together with the fact that the self-similar model neglects the line emission component completely, implies that more complicated scaling-relation models need to be investigated. However, there are no other suitable functional forms from the theoretical point of view and existing galaxy-cluster samples are too small to model more complicated scaling relations. This will change with the eROSITA all-sky survey, which provides enough statistics to explore scaling-relation models beyond a single power-law. Therefore, it would be valuable to intend to constrain galaxy group scaling relations and quantify the influence of the non-gravitational physics in a future project.

4.3 Probing the link between the scatter of galaxy cluster characteristics and the mass accretion history

In addition to study the scaling relations of galaxy groups in the eROSITA all-sky survey, it is important to understand the scatter of the galaxy group mass proxies better. This helps to interpret potential systematic effects in cosmological studies. The ellipticity of the X-ray emission and the

concentration of the dark matter are shaped by the mass accretion history and we plan to explore the correlation between them and the scatter in the core-excised X-ray luminosity. This includes cluster physics in scaling relations and the formalism can easily be extended to additional galaxy group properties, for example optical richness. Additional work is needed to develop combined group mass proxies and to understand the completeness of group selection using X-rays.

Chapter 5

Brief summary

The primary goal of the work presented in this thesis is to outline how to use the X-ray emission from galaxy cluster outskirts for cosmological studies. In Chapter 2, we start by characterizing the X-ray emission of a well defined galaxy cluster sample using a novel approach. The method models the excess emission in cool-core clusters using wavelet decomposition, which provides a better fit to the cluster outskirts. This model provides an unbiased measurement of the extent parameter and the cluster flux in the outskirts with respect to the different core types. In contrast, a widely used classical β -model tends to underestimate the flux in the cluster outskirts up to over 40% and the extent parameters are biased low for cool-core clusters. Additionally, we study the scaling of the shape parameters with temperature and the covariances between shape parameters and luminosity at a fixed temperature. For the same mass, more compact objects tend to be more luminous. In Chapter 3 we utilise the findings of Chapter 2 and propose a scheme to detect galaxy clusters with eROSITA through cluster outskirts. Avoiding the cluster centers in source detection minimizes the bias toward cool-core clusters. We determine the detection efficiency of this method by simulations and find that one requires more and more counts with decreasing extent of the cluster to obtain a specific detection efficiency. The method requires better photon statistics for compact clusters to successfully classify the object as extended. The payoffs of this approach are cluster catalogs that are well characterized and have simple selection functions. Compared to the current eROSITA detection and characterization method, the obtained catalogs are purer at a similar level of completeness. After successful detection in the eROSITA all-sky survey, the galaxy groups and clusters need to be characterized. A self-consistent way to measure the core-excised luminosity will be part of a future study and is presented in Chapter 4. This method makes use of the self-similar shape of galaxy clusters in the outskirts and predicts the core-excised luminosity and the total mass based on an aperture measurement of the cluster flux. First idealized tests on simulations show a scatter of approximately 36%, which likely sets an upper performance bound of this method when PSF effects are not taken into account. We present a similar method based on the linear decomposition of observed profiles in [Eckert et al. \(2020\)](#). Applying a proper PSF-reconstruction technique reduces the intrinsic scatter of the core-excised luminosity and mass to approximately 16% without measurable bias. The inferred galaxy cluster parameters are beneficial for cosmological studies. On the one hand, the distribution of the reconstructed total masses can be compared to theoretical predictions to directly infer

cosmological parameters. On the other hand, the reconstructed core-excised luminosities can be utilized in scaling relations. The expected large amount of detected galaxy groups and clusters with eROSITA allows us to study scaling relations in unprecedented detail. This includes studying more complex functional forms and the scatter between the different mass proxies. This will help to understand potential systematic effects in cosmological constraints.

Appendix A

Appendix for the characterization of X-ray galaxy clusters

A.1 Mass comparison

In this section we compare our previous emission measure ratio results of Sect. 2.3 to profiles that are re-scaled by a characteristic radii according to hydrostatic mass estimates by [Schellenberger and Reiprich \(2017\)](#). We adapt their preferred "NFW Freeze" model, where a NFW profile ([Navarro et al., 1996, 1997](#)) is fit to the outermost measured mass profiles of *Chandra* observations and a concentration-mass relation is used to reduce the degrees of freedom. We are interested in the difference between individual core-types and not in the bias between the *Planck* and hydrostatic masses. Therefore, we assume that the bias is constant for all clusters. To probe the masses at the same radii, we recalculate the hydrostatic masses at the *Planck* r_{500} values according to Formula (31) of [Schellenberger and Reiprich \(2017\)](#)

$$M_{500,GS17}^* (< r_{500,Planck}) = M_{500,GS17} \frac{Y\left(\frac{r_{500,Planck}}{r_{500,GS17}} c_{500,GS17}\right)}{Y(c_{500,GS17})}, \quad (\text{A.1})$$

where c_{500} denotes the NFW concentration parameter and $Y(u) = \ln(1 + u) - u/(1 + u)$. These recalculated masses are on average lower than the corresponding masses in the *Planck* catalog. The median of the NCC cluster masses is approximately 13% larger than that of the SCC objects (see Fig. A.1), increasing the SCC to NCC weighted mean ratio effect in the 0.2–0.5 r_{500} range to 40%. This increase due to the dynamical states is also seen in simulations, for example in different fractions of non-thermal pressure for different mass accretion rates ([Nelson et al., 2014](#)). The differences can thus be explained by assuming that NCC clusters are merging objects and that they contain more non-thermal energy. An alternative explanation is that the differences come from the assumed concentration-mass relation. We expect different core-types to have different shapes of the dark matter halo and therefore different concentrations at a given radius. However, fitting for the concentration in [Schellenberger and Reiprich \(2017\)](#) results in some cases to unrealistic high or low masses, potentially because of limited radial coverage due to the relatively small *Chandra* field-of-view.

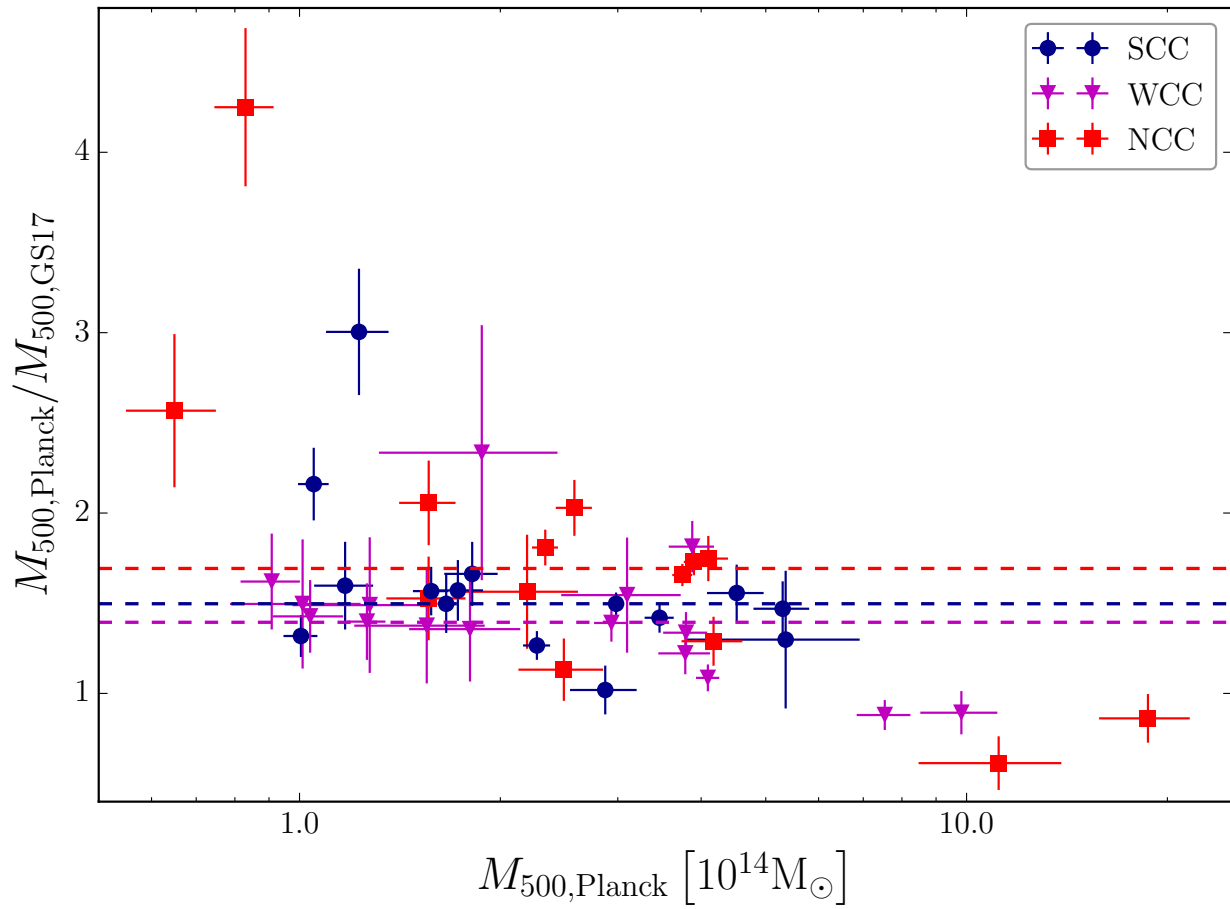


Figure A.1: Comparison between *Planck* and hydrostatic mass estimates of HIFLUGCS objects with temperatures greater than 3 keV.

A.2 Priors

We list the priors used for the analysis in Chapter 2 in Table A.1. They are chosen to be weakly- or non-informative and varying them does not influence the results of this study significantly.

Table A.1: List of parameters and their priors. We note that the prior of the scaling relation slope is assumed to be uniform in $\sin(\Theta)$ (VanderPlas, 2016), with Θ being the angle between the best-fit line and the x -axis. The term "pos-normal" refers to a probability distribution that follows an ordinary normal distribution but is set to zero for negative parameter values, meaning that the parameter is restricted to be positive.

Parameter	Description	Prior
β	β -model slope	pos-normal(0.67,10)
r_c	β -model core radius in arcminutes	pos-normal(0,100)
m	Scaling relation slope	$\propto (1 + m^2)^{-3/2}$
b	Scaling relation intercept	non-informative uniform
λ_y	Intrinsic scatter in y	pos-normal(0,10)
λ_{xy}	Correlation coefficient between x and y	uniform[-1,1]

A.3 HIFLUGCS parameters

Table A.2: Galaxy cluster parameters. Column (1) gives the cluster name. Columns (2) and (3) list the equatorial coordinates of the cluster center in decimal degrees based on the large-scale wavelet image. Column (4) gives the offset to an iteratively determined two-dimensional 'center of mass' using an aperture radius of $3'$ (Reiprich and Böhringer, 2002). Column (5) and (6) list the cluster redshift (Reiprich and Böhringer, 2002) and core-excised temperature (Hudson et al., 2010), respectively. Column (7) and (8) give the β -model slope and core radius for a core-modeled fit. Column (9) lists the luminosity in the 0.1–2.4 keV energy range. The cool-core classification according to Hudson et al. (2010) is given in column (10). Column (11) lists the characteristic radius where the density corresponds to 500 times the critical density at the cluster redshift. Galaxy clusters, whose r_{500} value is marked with a \dagger do not have SZ mass estimates (Planck Collaboration et al., 2016) and the Schellenberger and Reiprich (2017) mass estimate is used to determine the wavelet small scales. These clusters are excluded from further analysis steps which comprise characteristic radii. Column (12) gives the measured large scale ellipticity. The physical to angular scale conversion at the cluster redshift is given in column (13).

Cluster	R.A.	Dec.	Offset	z	T	β	r_c	L	CCC	r_{500}	Ellipticity	Scale
name	J2000		"		keV		kpc	10^{44} erg s $^{-1}$		Mpc		kpc/"
A0085	10.4600	-9.3110	23.5	0.0556	$5.50^{+0.10}_{-0.10}$	$0.731^{+0.010}_{-0.009}$	$283.33^{+6.72}_{-6.43}$	5.034 ± 0.030	SCC	1.18	0.102	1.08
A0119	14.0610	-1.2490	14.1	0.0440	$5.26^{+0.30}_{-0.26}$	$0.681^{+0.017}_{-0.017}$	$371.94^{+13.49}_{-13.22}$	1.725 ± 0.016	NCC	1.05	0.177	0.87
A0133	15.6740	-21.8800	1.9	0.0569	$3.72^{+0.07}_{-0.09}$	$0.634^{+0.008}_{-0.007}$	$115.90^{+3.79}_{-3.59}$	1.514 ± 0.012	SCC	1.00	0.240	1.10
NGC507	20.9080	33.2560	9.1	0.0165	$1.44^{+0.08}_{-0.10}$	$0.420^{+0.005}_{-0.005}$	$34.35^{+2.17}_{-2.10}$	0.127 ± 0.002	SCC	0.47^\dagger	0.047	0.34
A0262	28.1960	36.1600	26.2	0.0161	$2.39^{+0.03}_{-0.04}$	$0.483^{+0.007}_{-0.006}$	$57.07^{+2.55}_{-2.45}$	0.534 ± 0.020	SCC	0.73	0.303	0.33
A0400	44.4110	6.0050	44.8	0.0240	$2.23^{+0.09}_{-0.11}$	$0.544^{+0.010}_{-0.010}$	$126.97^{+5.06}_{-4.91}$	0.352 ± 0.004	NCC	0.54^\dagger	0.371	0.48
A0399	44.4680	13.0440	9.3	0.0715	$6.11^{+0.12}_{-0.12}$	$0.551^{+0.014}_{-0.013}$	$120.71^{+13.25}_{-12.93}$	3.634 ± 0.196	NCC	1.20	0.051	1.36
A0401	44.7380	13.5790	3.7	0.0748	$7.70^{+0.30}_{-0.19}$	$0.527^{+0.004}_{-0.004}$	$69.55^{+3.83}_{-3.68}$	6.452 ± 0.071	NCC	1.30	0.346	1.42
A3112	49.4910	-44.2370	0.5	0.0750	$4.39^{+0.10}_{-0.11}$	$0.646^{+0.009}_{-0.008}$	$107.81^{+4.26}_{-4.03}$	3.832 ± 0.042	SCC	0.99	0.246	1.42
FORNAX	54.6490	-35.3640	202.9	0.0046	$1.34^{+0.00}_{-0.00}$	$0.613^{+0.025}_{-0.023}$	$101.54^{+4.12}_{-4.02}$	0.042 ± 0.002	SCC	0.38^\dagger	0.061	0.09
2A0335	54.6660	9.9710	9.5	0.0349	$3.34^{+0.09}_{-0.11}$	$0.731^{+0.012}_{-0.011}$	$141.70^{+4.23}_{-4.13}$	2.462 ± 0.020	SCC	0.92	0.177	0.69
IIIZw54	55.3150	15.3970	46.4	0.0311	$2.44^{+0.04}_{-0.05}$	$0.736^{+0.120}_{-0.078}$	$166.98^{+44.75}_{-34.00}$	0.427 ± 0.033	WCC	0.56^\dagger	0.104	0.62
A3158	55.7260	-53.6300	4.0	0.0590	$4.62^{+0.06}_{-0.06}$	$0.697^{+0.020}_{-0.018}$	$234.54^{+11.72}_{-11.41}$	2.899 ± 0.043	NCC	1.12	0.207	1.14
A0478	63.3550	10.4660	1.3	0.0900	$6.67^{+0.16}_{-0.17}$	$0.731^{+0.007}_{-0.006}$	$186.43^{+3.65}_{-3.58}$	9.083 ± 0.054	SCC	1.31	0.240	1.68
NGC1550	64.9130	2.4070	37.9	0.0123	$1.34^{+0.00}_{-0.00}$	$0.615^{+0.047}_{-0.038}$	$55.14^{+11.39}_{-9.43}$	0.155 ± 0.008	SCC	0.44^\dagger	0.054	0.25
EXO0422	66.4670	-8.5620	16.4	0.0390	$2.81^{+0.11}_{-0.11}$	$0.688^{+0.030}_{-0.026}$	$70.53^{+8.55}_{-7.91}$	1.036 ± 0.064	SCC	0.69^\dagger	0.205	0.77
A3266	67.8810	-61.4260	86.3	0.0594	$8.52^{+0.31}_{-0.32}$	$0.933^{+0.018}_{-0.018}$	$560.18^{+12.57}_{-12.26}$	4.483 ± 0.031	WCC	1.30	0.397	1.15
A0496	68.4080	-13.2590	8.2	0.0328	$4.50^{+0.04}_{-0.05}$	$0.651^{+0.010}_{-0.010}$	$146.49^{+4.75}_{-4.67}$	1.972 ± 0.014	SCC	0.97	0.217	0.65
A3376	90.5000	-39.9670	52.0	0.0455	$3.58^{+0.10}_{-0.09}$	$0.675^{+0.029}_{-0.026}$	$375.21^{+22.79}_{-21.94}$	1.118 ± 0.016	NCC	0.93	0.495	0.89
A3391	96.5800	-53.6980	30.2	0.0531	$5.30^{+0.27}_{-0.32}$	$0.762^{+0.038}_{-0.034}$	$292.76^{+21.42}_{-19.82}$	1.379 ± 0.026	NCC	0.98	0.398	1.03
A3395s	96.6970	-54.5460	11.2	0.0498	$4.47^{+0.23}_{-0.23}$	$0.699^{+0.127}_{-0.086}$	$286.63^{+77.07}_{-57.77}$	1.096 ± 0.042	NCC	1.03	0.330	0.97
A0576	110.3530	55.7930	103.9	0.0381	$3.83^{+0.07}_{-0.09}$	$0.716^{+0.107}_{-0.072}$	$210.87^{+52.62}_{-39.80}$	0.962 ± 0.065	WCC	0.90	0.255	0.76
A0754	137.3110	-9.6830	82.6	0.0528	$9.99^{+0.34}_{-0.38}$	$0.767^{+0.016}_{-0.015}$	$405.13^{+11.92}_{-11.60}$	2.052 ± 0.033	NCC	1.32	0.455	1.03
HYDRA-A	139.5230	-12.0940	2.7	0.0538	$3.27^{+0.07}_{-0.08}$	$0.719^{+0.007}_{-0.007}$	$126.94^{+2.68}_{-2.63}$	3.049 ± 0.018	SCC	0.84^\dagger	0.237	1.05
A1060	159.1680	-27.5280	41.9	0.0114	$3.02^{+0.04}_{-0.04}$	$0.602^{+0.007}_{-0.007}$	$98.62^{+1.92}_{-1.97}$	0.284 ± 0.009	WCC	0.68^\dagger	0.062	0.23
A1367	176.2100	19.7030	68.4	0.0216	$3.38^{+0.05}_{-0.05}$	$0.670^{+0.022}_{-0.021}$	$346.02^{+13.68}_{-12.76}$	0.619 ± 0.005	NCC	0.83	0.089	0.44

Table A.2: Continued.

Cluster name	R.A. J2000	Dec. "	Offset "	z	T keV	β	r_c kpc	L $10^{44} \text{ erg s}^{-1}$	CCC	r_{500} Mpc	Ellipticity	Scale kpc/'
MKW4	181.1020	1.8990	38.1	0.0200	$2.01^{+0.04}_{-0.04}$	$0.566^{+0.011}_{-0.011}$	$79.67^{+4.05}_{-3.89}$	0.200 ± 0.003	SCC	0.51^\dagger	0.275	0.41
ZwCl1215	184.4200	3.6590	7.2	0.0750	$5.74^{+0.28}_{-0.25}$	$0.748^{+0.018}_{-0.017}$	$248.82^{+10.78}_{-10.45}$	2.693 ± 0.035	NCC	1.01^\dagger	0.268	1.42
NGC4636	190.7310	2.7600	272.0	0.0037	$0.90^{+0.02}_{-0.02}$	$2.043^{+1.127}_{-0.682}$	$149.01^{+45.65}_{-35.73}$	0.012 ± 0.001	SCC	0.34^\dagger	0.176	0.08
A3526	192.2300	-41.3000	89.3	0.0103	$3.68^{+0.02}_{-0.02}$	$0.551^{+0.003}_{-0.003}$	$110.89^{+1.30}_{-1.29}$	0.637 ± 0.014	SCC	0.77	0.280	0.21
A1644	194.2900	-17.3990	14.0	0.0474	$4.70^{+0.08}_{-0.08}$	$0.688^{+0.084}_{-0.062}$	$296.25^{+68.92}_{-54.79}$	1.993 ± 0.102	SCC	1.07	0.050	0.93
A1650	194.6700	-1.7590	6.4	0.0845	$5.33^{+0.05}_{-0.06}$	$0.642^{+0.048}_{-0.038}$	$171.84^{+31.73}_{-26.11}$	3.754 ± 0.248	WCC	1.13	0.160	1.59
A1651	194.8390	-4.1950	9.0	0.0860	$5.80^{+0.24}_{-0.24}$	$0.696^{+0.012}_{-0.012}$	$180.93^{+6.75}_{-6.44}$	4.109 ± 0.049	WCC	1.18	0.152	1.61
COMA	194.9480	27.9300	30.6	0.0232	$8.26^{+0.15}_{-0.14}$	$0.874^{+0.004}_{-0.004}$	$449.21^{+2.37}_{-2.39}$	4.067 ± 0.057	NCC	1.35	0.295	0.47
NGC5044	198.8640	-16.3860	38.8	0.0090	$1.22^{+0.03}_{-0.04}$	$0.664^{+0.014}_{-0.013}$	$65.97^{+2.19}_{-2.13}$	0.099 ± 0.000	SCC	0.41^\dagger	0.063	0.18
A1736	201.7500	-27.1580	108.3	0.0461	$2.98^{+0.10}_{-0.11}$	$0.591^{+0.062}_{-0.048}$	$337.18^{+70.00}_{-56.53}$	1.657 ± 0.104	NCC	0.99	0.065	0.91
A3558	202.0050	-31.5130	57.3	0.0480	$4.58^{+0.11}_{-0.13}$	$0.656^{+0.007}_{-0.006}$	$265.23^{+4.67}_{-4.54}$	3.401 ± 0.017	WCC	1.17	0.289	0.94
A3562	203.3960	-31.6650	13.1	0.0499	$4.13^{+0.18}_{-0.14}$	$0.585^{+0.011}_{-0.010}$	$192.27^{+7.73}_{-7.30}$	1.603 ± 0.014	WCC	0.94	0.230	0.98
A3571	206.8670	-32.8520	12.3	0.0397	$6.38^{+0.11}_{-0.11}$	$0.692^{+0.010}_{-0.010}$	$199.73^{+5.33}_{-5.15}$	4.181 ± 0.029	WCC	1.16	0.336	0.79
A1795	207.2190	26.5980	14.7	0.0616	$5.57^{+0.06}_{-0.06}$	$0.732^{+0.003}_{-0.003}$	$166.95^{+1.52}_{-1.49}$	5.205 ± 0.016	SCC	1.14	0.262	1.19
A3581	211.8790	-27.0180	22.3	0.0214	$1.97^{+0.07}_{-0.07}$	$0.509^{+0.018}_{-0.017}$	$25.47^{+5.36}_{-4.78}$	0.337 ± 0.011	SCC	0.63^\dagger	0.210	0.43
MKW8	220.1690	3.4710	35.7	0.0270	$2.88^{+0.11}_{-0.11}$	$0.543^{+0.061}_{-0.044}$	$100.58^{+34.75}_{-26.45}$	0.405 ± 0.034	NCC	0.72	0.151	0.54
A2029	227.7310	5.7440	7.8	0.0767	$7.48^{+0.08}_{-0.08}$	$0.693^{+0.006}_{-0.006}$	$160.89^{+3.15}_{-3.15}$	8.897 ± 0.053	SCC	1.32	0.282	1.45
A2052	229.1880	7.0260	19.5	0.0348	$3.18^{+0.02}_{-0.02}$	$0.791^{+0.022}_{-0.020}$	$163.91^{+6.83}_{-6.39}$	1.259 ± 0.013	SCC	0.67^\dagger	0.207	0.69
MKW3S	230.4660	7.7060	4.5	0.0450	$3.66^{+0.08}_{-0.08}$	$0.707^{+0.009}_{-0.008}$	$102.22^{+2.57}_{-2.47}$	1.473 ± 0.015	SCC	0.86	0.277	0.88
A2065	230.6080	27.7170	18.8	0.0721	$4.98^{+0.18}_{-0.10}$	$1.147^{+0.467}_{-0.209}$	$510.85^{+182.02}_{-103.71}$	2.858 ± 0.174	WCC	1.10	0.275	1.37
A2063	230.7790	8.6110	18.5	0.0354	$3.55^{+0.05}_{-0.05}$	$0.570^{+0.011}_{-0.010}$	$60.75^{+5.21}_{-4.99}$	1.168 ± 0.015	WCC	0.86	0.160	0.70
A2142	239.6000	27.2220	70.9	0.0899	$7.60^{+0.88}_{-0.67}$	$0.923^{+0.013}_{-0.013}$	$556.15^{+10.25}_{-10.08}$	10.960 ± 0.099	WCC	1.41	0.388	1.68
A2147	240.5640	15.9550	14.4	0.0351	$3.81^{+0.10}_{-0.11}$	$0.359^{+0.021}_{-0.017}$	$85.48^{+24.73}_{-19.42}$	1.500 ± 0.048	NCC	1.06	0.088	0.70
A2163	243.9410	-6.1470	13.6	0.2010	$14.17^{+0.71}_{-0.71}$	$0.738^{+0.015}_{-0.014}$	$368.75^{+14.01}_{-13.65}$	17.179 ± 0.258	NCC	1.67	0.151	3.31
A2199	247.1580	39.5480	2.0	0.0302	$4.07^{+0.06}_{-0.06}$	$0.751^{+0.005}_{-0.005}$	$182.12^{+1.96}_{-1.93}$	2.140 ± 0.039	SCC	0.99	0.201	0.60
A2204	248.1960	5.5760	10.2	0.1523	$8.06^{+0.63}_{-0.53}$	$0.707^{+0.020}_{-0.018}$	$173.91^{+10.89}_{-10.33}$	13.715 ± 0.219	SCC	1.33	0.046	2.65
A2244	255.6740	34.0590	4.9	0.0970	$5.31^{+0.09}_{-0.10}$	$0.642^{+0.015}_{-0.014}$	$126.79^{+7.91}_{-7.43}$	4.345 ± 0.091	WCC	1.12	0.145	1.80
A2256	255.9750	78.6400	31.0	0.0601	$6.91^{+0.57}_{-0.55}$	$1.041^{+0.014}_{-0.013}$	$547.10^{+7.58}_{-7.35}$	4.793 ± 0.067	NCC	1.27	0.341	1.16
A2255	258.2080	64.0650	26.5	0.0800	$5.33^{+0.17}_{-0.18}$	$0.851^{+0.029}_{-0.027}$	$502.79^{+21.65}_{-20.19}$	2.829 ± 0.034	NCC	1.21	0.209	1.51
A3667	303.1450	-56.8430	17.3	0.0560	$5.84^{+0.04}_{-0.04}$	$0.567^{+0.007}_{-0.006}$	$260.96^{+7.05}_{-6.82}$	4.949 ± 0.035	WCC	1.33	0.341	1.09
S1101	348.4940	-42.7270	1.3	0.0580	$2.50^{+0.11}_{-0.11}$	$0.783^{+0.011}_{-0.011}$	$115.72^{+3.27}_{-3.15}$	1.850 ± 0.017	SCC	0.79	0.178	1.12
A2589	350.9880	16.7720	10.7	0.0416	$3.65^{+0.04}_{-0.04}$	$0.671^{+0.017}_{-0.016}$	$148.38^{+7.35}_{-6.86}$	0.989 ± 0.013	WCC	0.84	0.285	0.82
A2597	351.3320	-12.1250	1.9	0.0852	$3.79^{+0.06}_{-0.06}$	$0.702^{+0.014}_{-0.013}$	$106.77^{+5.42}_{-5.02}$	3.535 ± 0.042	SCC	0.93	0.192	1.60
A2634	354.6090	27.0130	61.9	0.0312	$3.04^{+0.10}_{-0.10}$	$0.680^{+0.030}_{-0.027}$	$297.03^{+17.64}_{-16.72}$	0.518 ± 0.008	WCC	0.80	0.554	0.62
A2657	356.2290	9.1940	16.4	0.0404	$3.33^{+0.11}_{-0.10}$	$0.555^{+0.006}_{-0.006}$	$96.03^{+3.05}_{-3.00}$	0.911 ± 0.008	WCC	0.79	0.125	0.80
A4038	356.9320	-28.1450	13.3	0.0283	$3.00^{+0.03}_{-0.04}$	$0.620^{+0.014}_{-0.013}$	$98.38^{+5.08}_{-4.88}$	1.005 ± 0.013	WCC	0.80	0.313	0.57
A4059	359.2520	-34.7580	7.1	0.0460	$3.94^{+0.03}_{-0.03}$	$0.705^{+0.020}_{-0.018}$	$168.53^{+9.33}_{-8.62}$	1.477 ± 0.019	SCC	0.94	0.255	0.90

A.4 HIFLUGCS images and surface brightness profiles

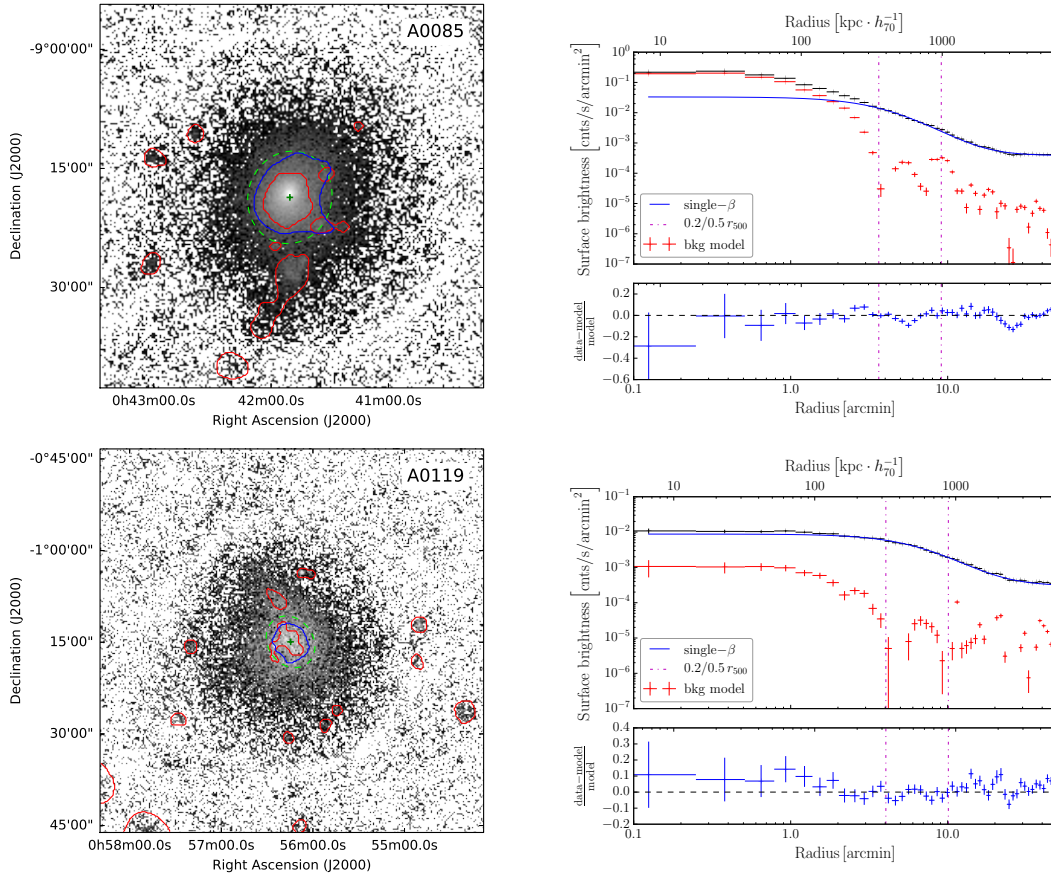


Figure A.2: Left panels: ROSAT count rate images for individual galaxy clusters. The large-scale centers are shown as green plus signs. Red contours correspond to wavelet scales used for background modeling. The large scales (the ones above $0.2 r_{500}$) are shown as blue contours. These large scales are used to calculate the center and ellipticities. The extracted SExtractor ellipses are displayed in dashed green. Each box size corresponds to the outer significance radius of the shown cluster. Right panels: The top panels show the measured (black points) surface brightness profiles of individual galaxy clusters. The background models used for the single β -model fits (solid blue lines) are shown as red points. The bottom panels show the residuals of the core-modelled single β -model fits.

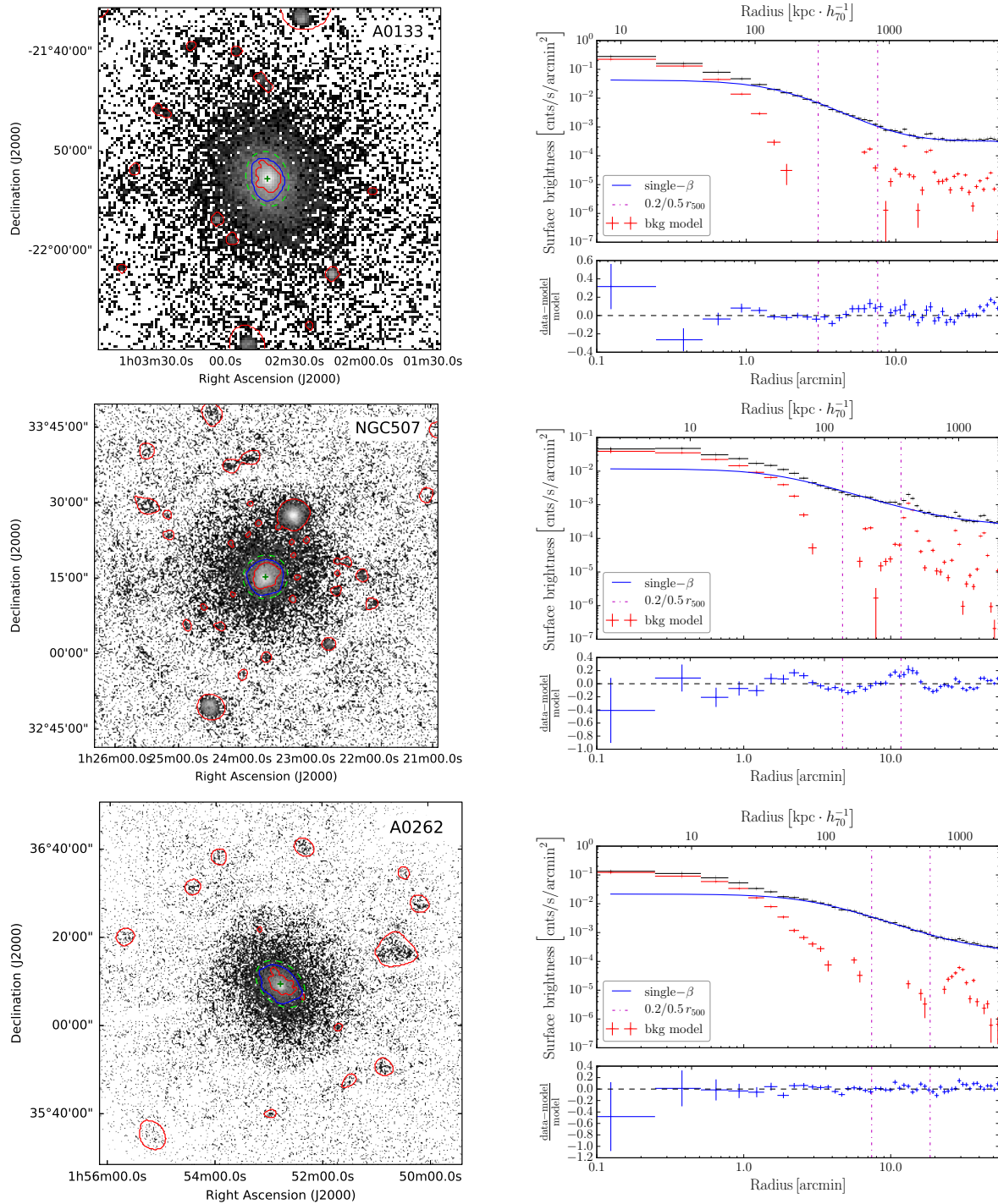


Figure A.2: Continued.

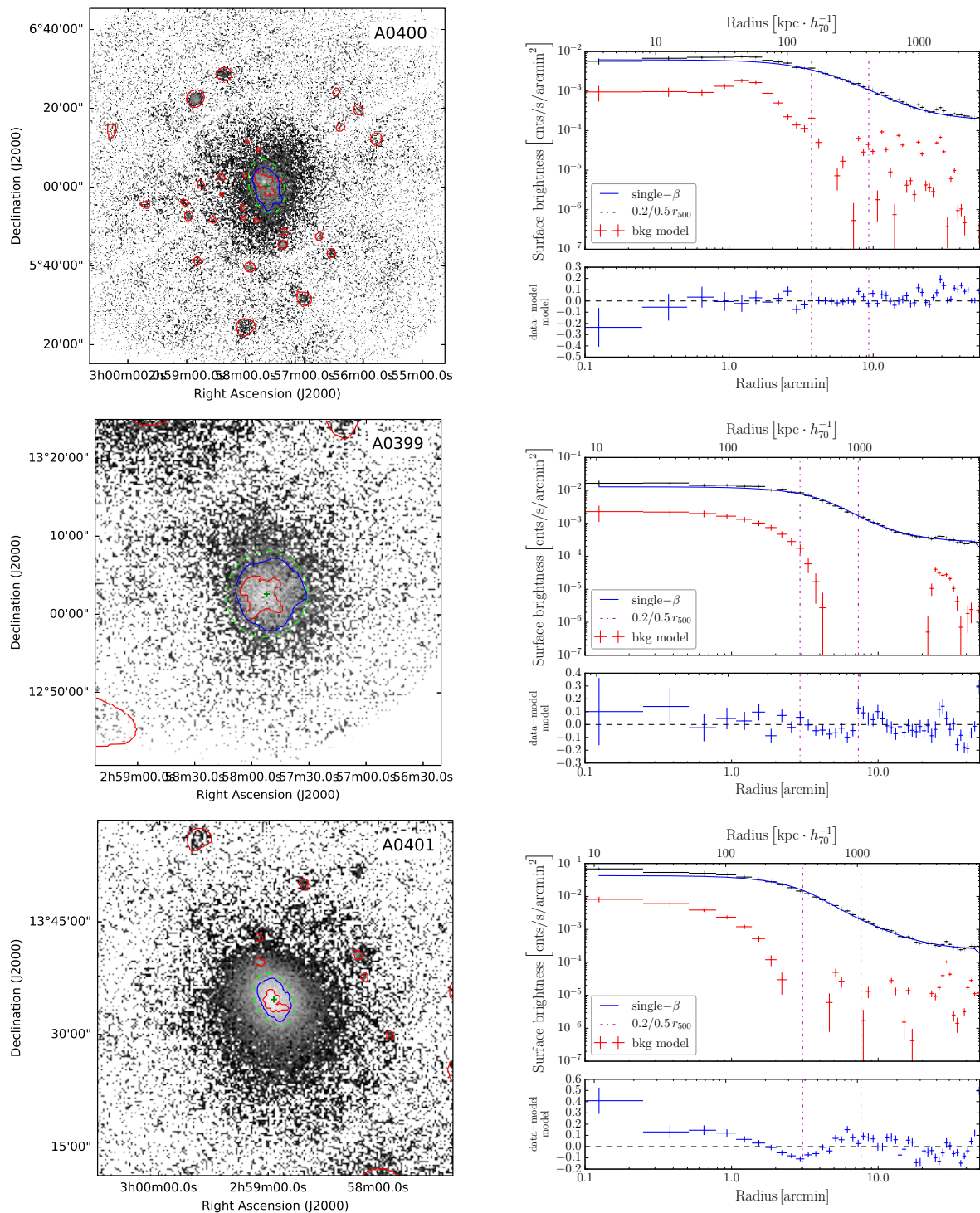


Figure A.2: Continued.

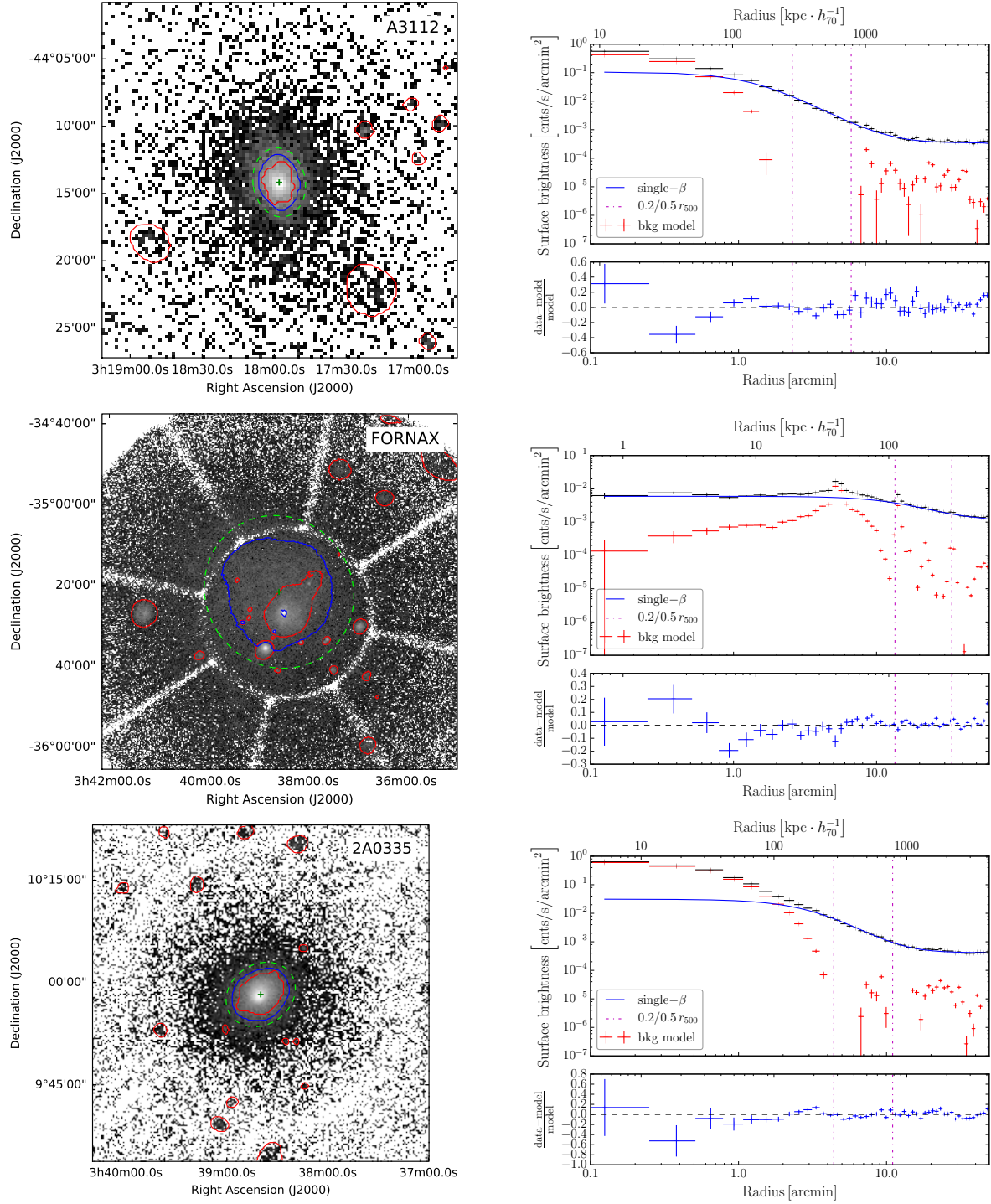


Figure A.2: Continued.

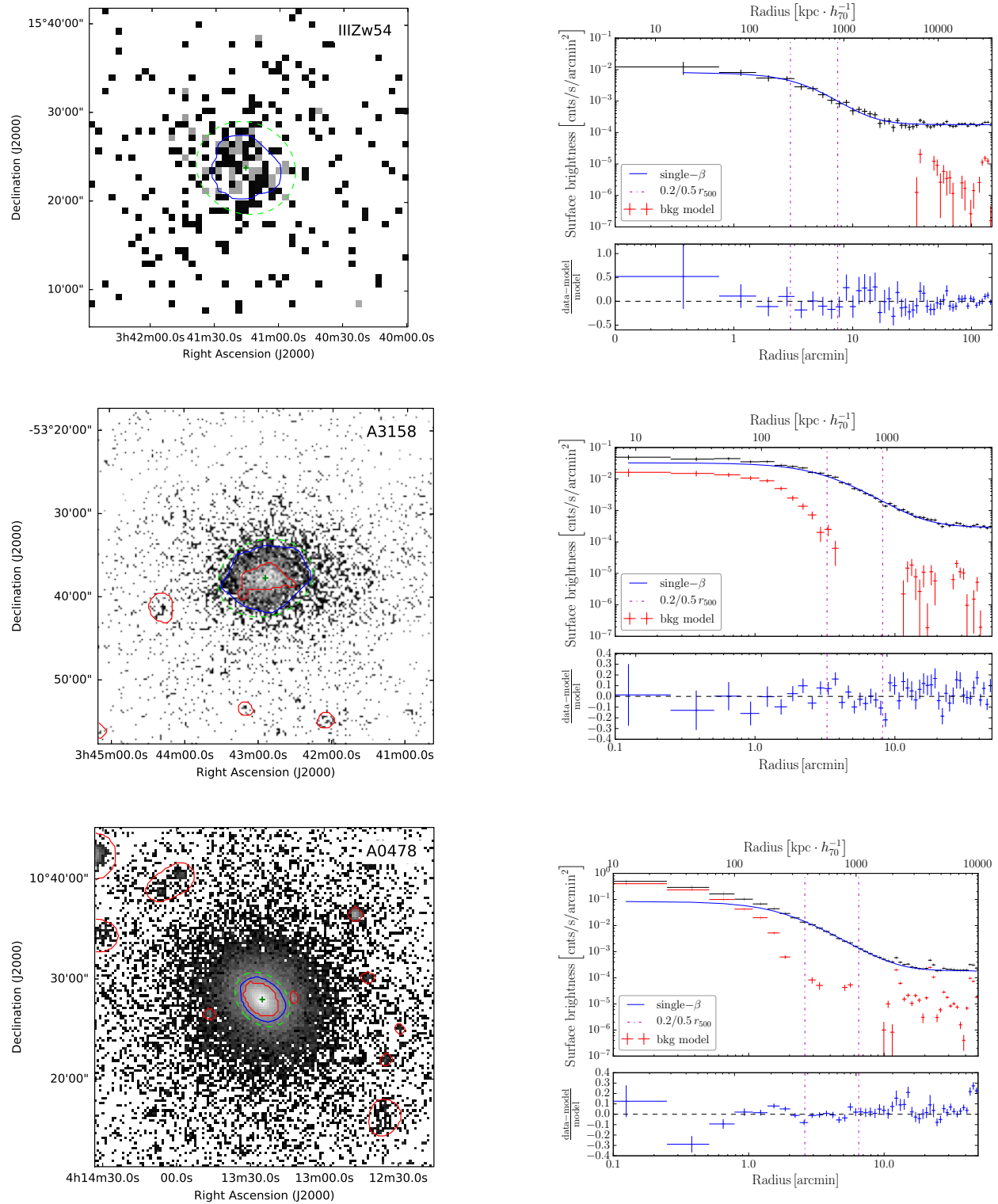


Figure A.2: Continued.

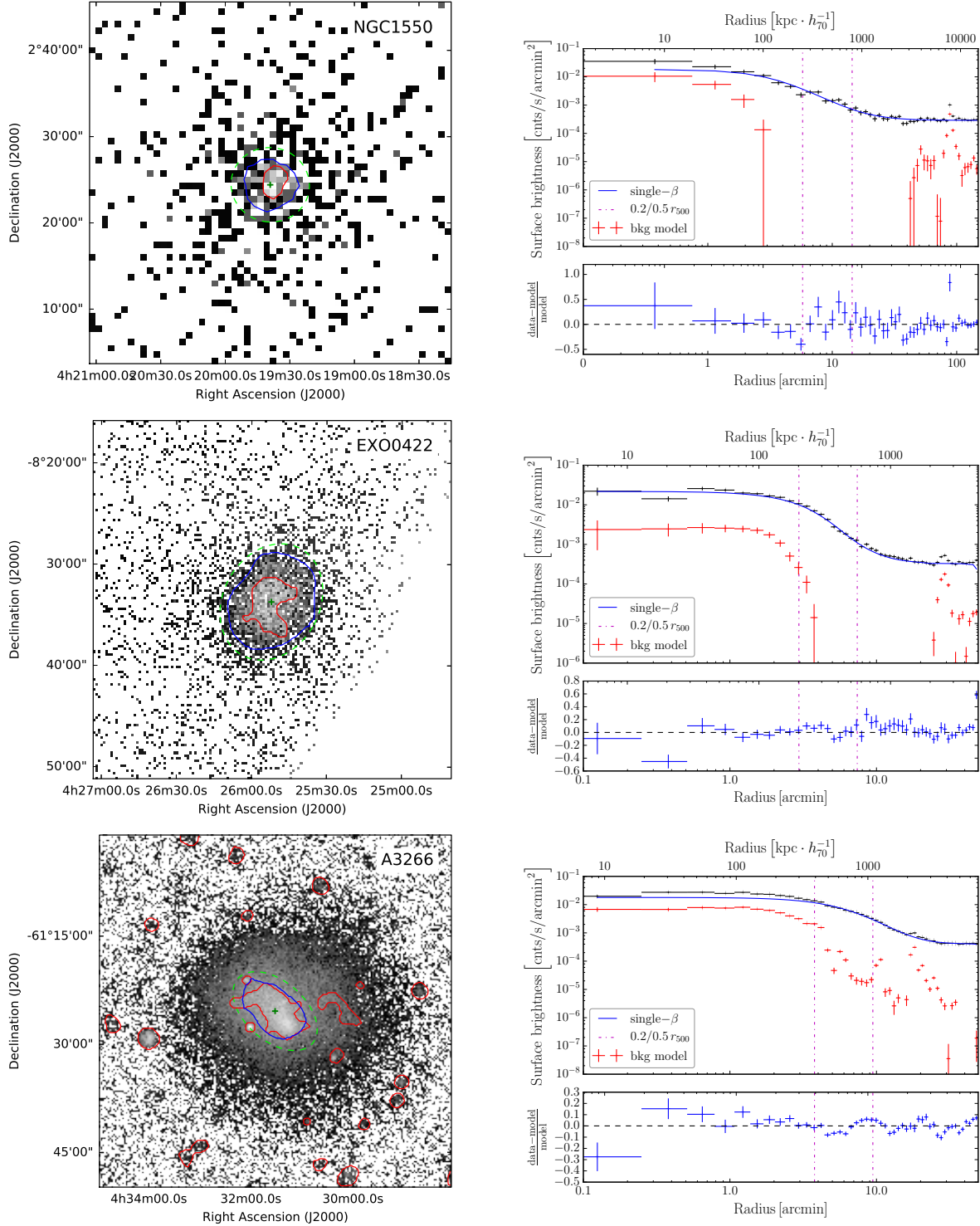


Figure A.2: Continued.

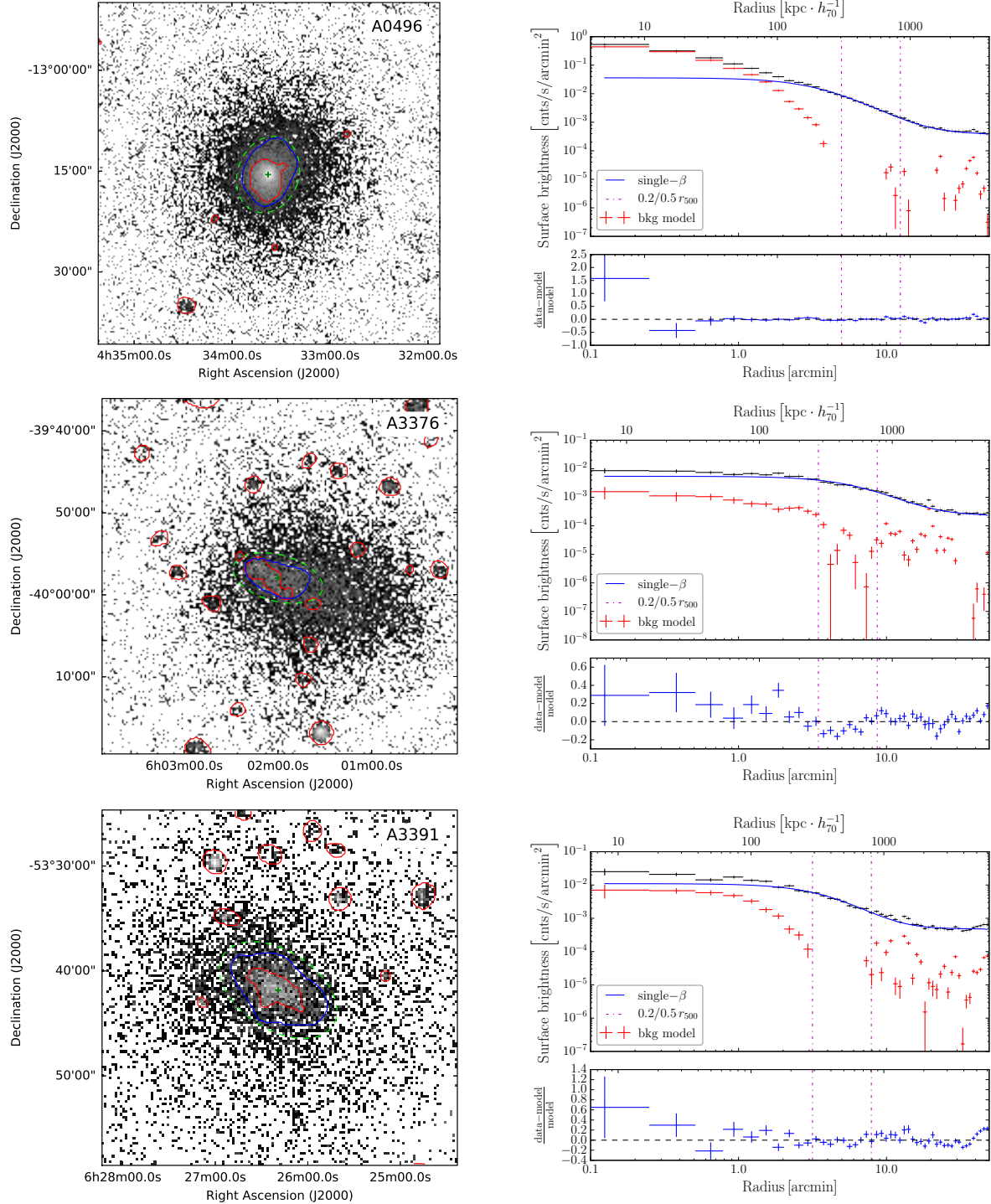


Figure A.2: Continued.

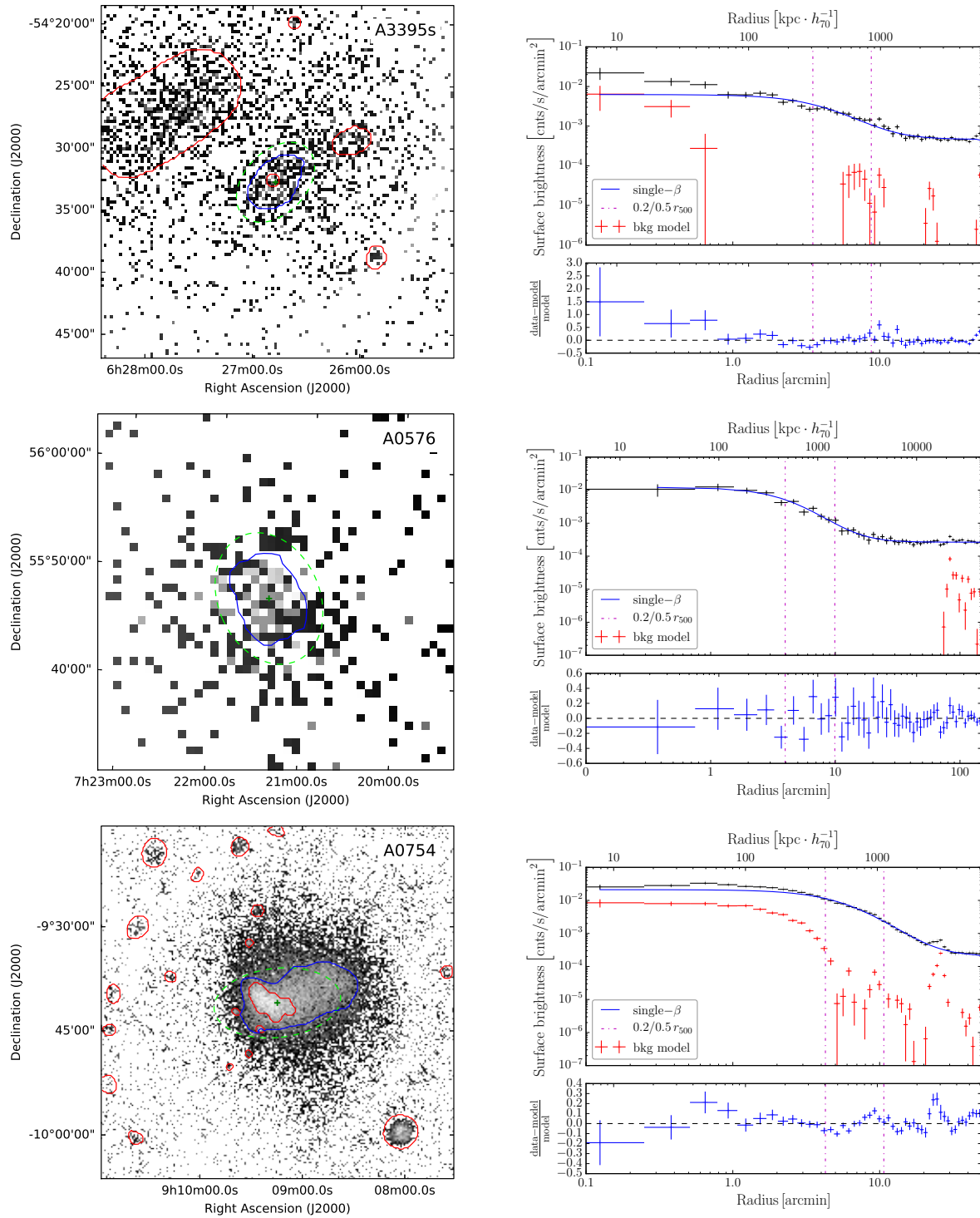


Figure A.2: Continued.

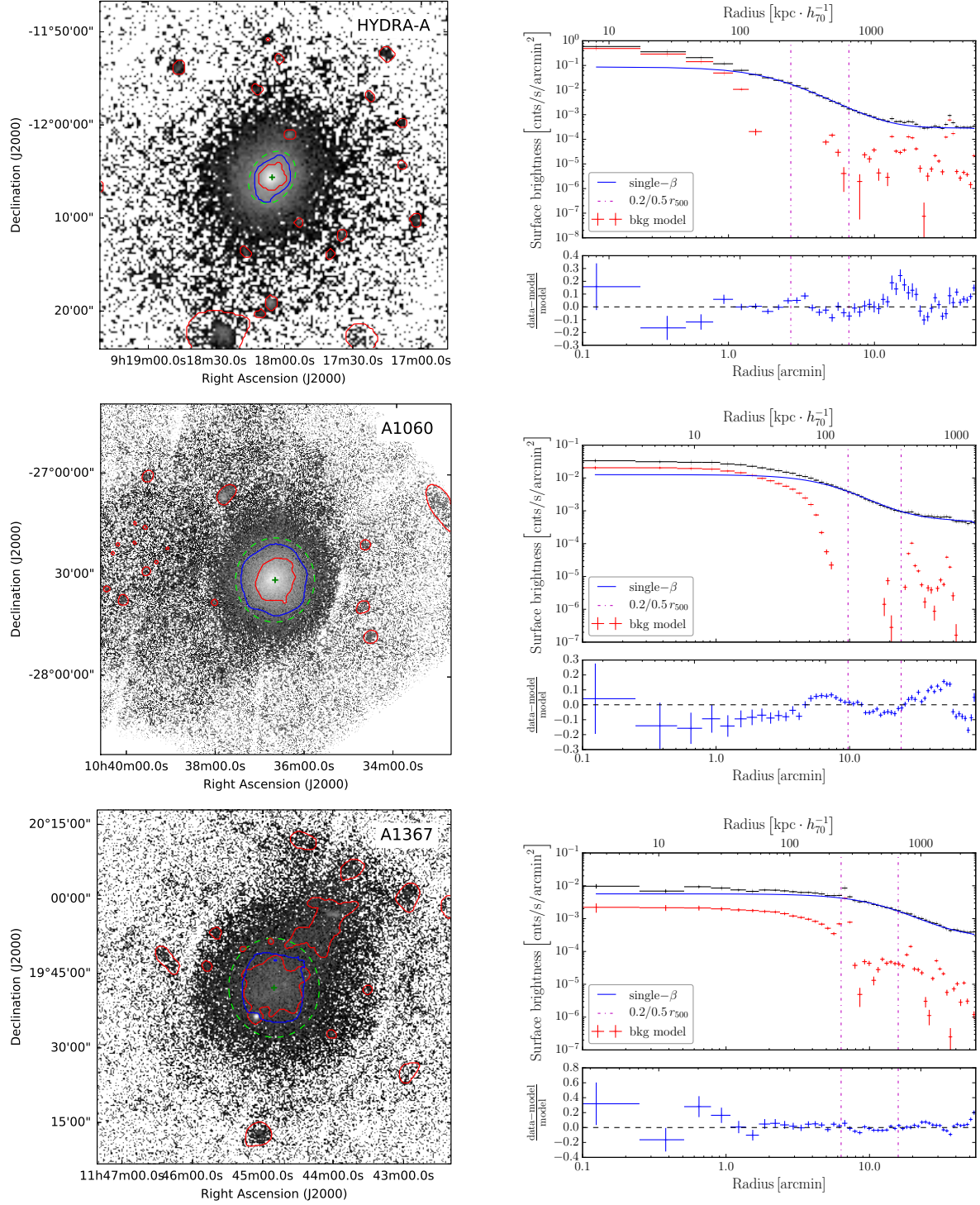


Figure A.2: Continued.

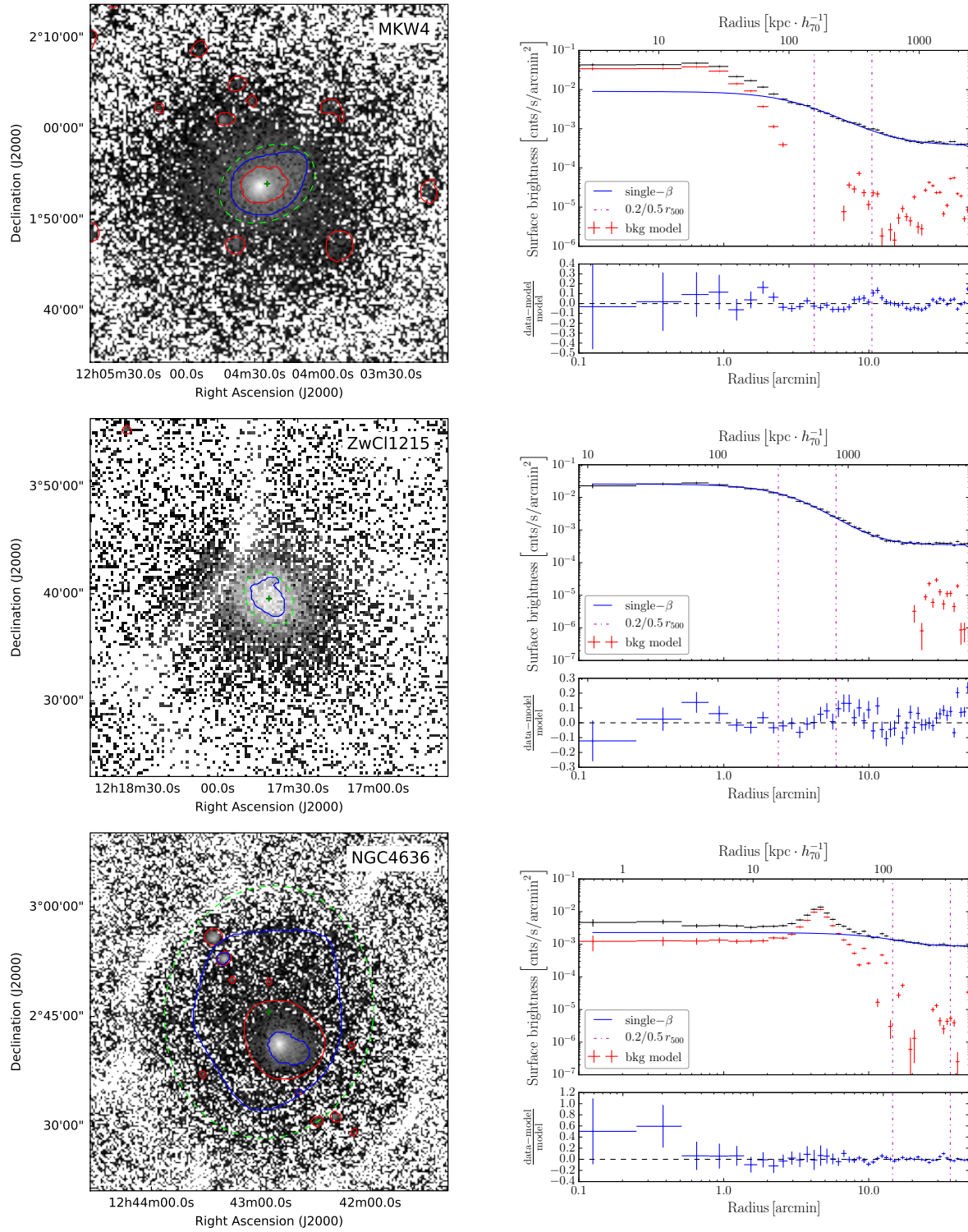


Figure A.2: Continued.

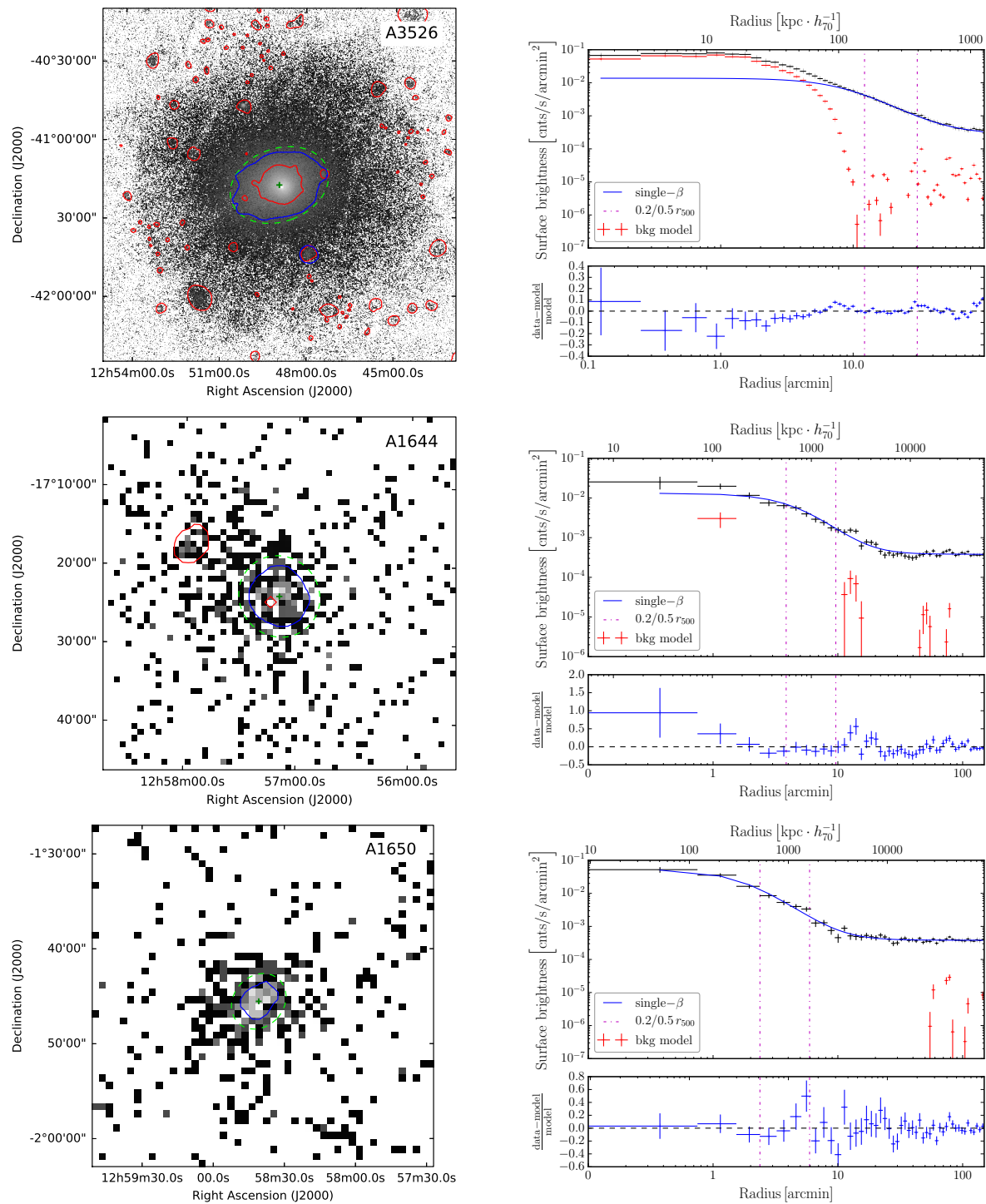


Figure A.2: Continued.

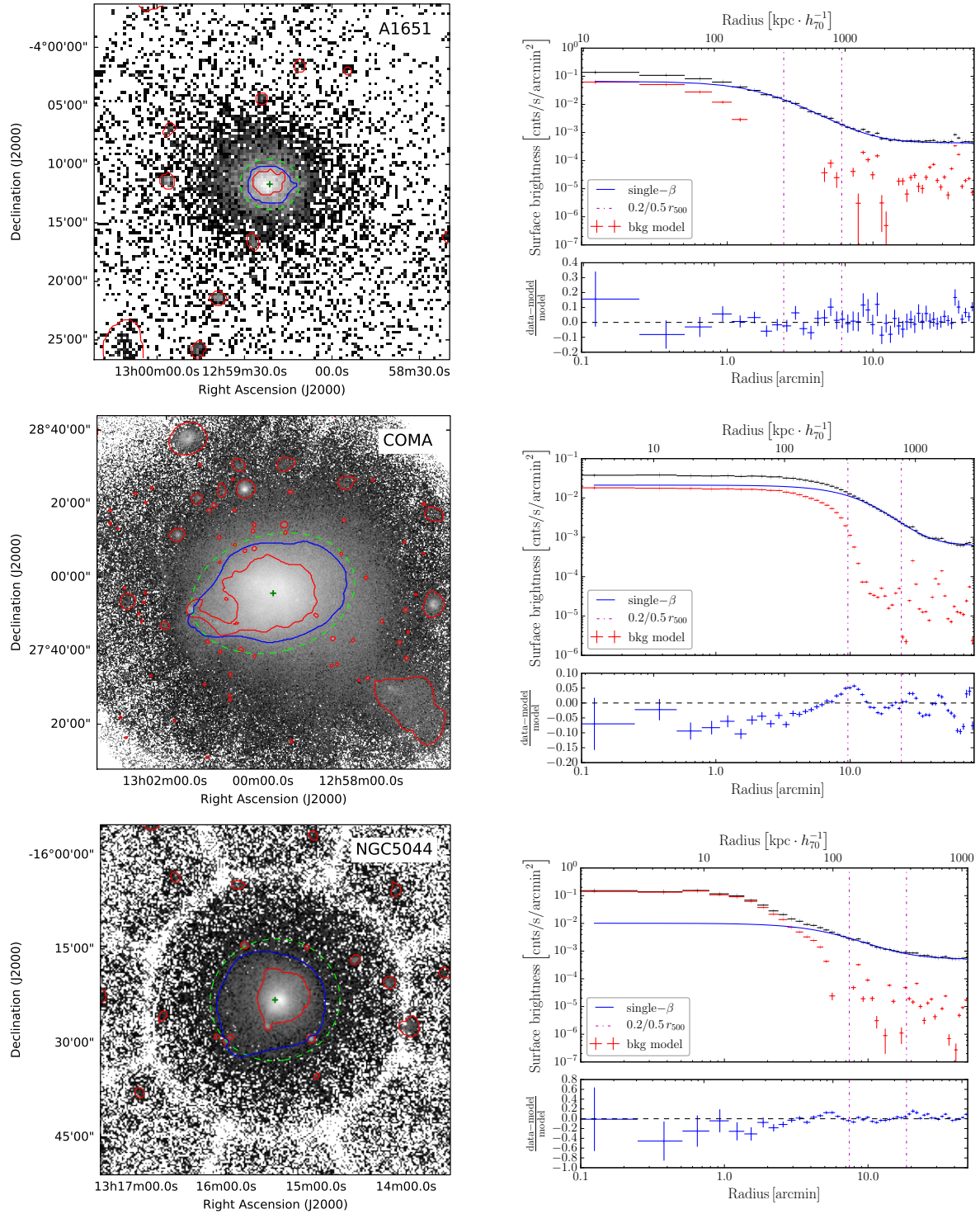


Figure A.2: Continued.

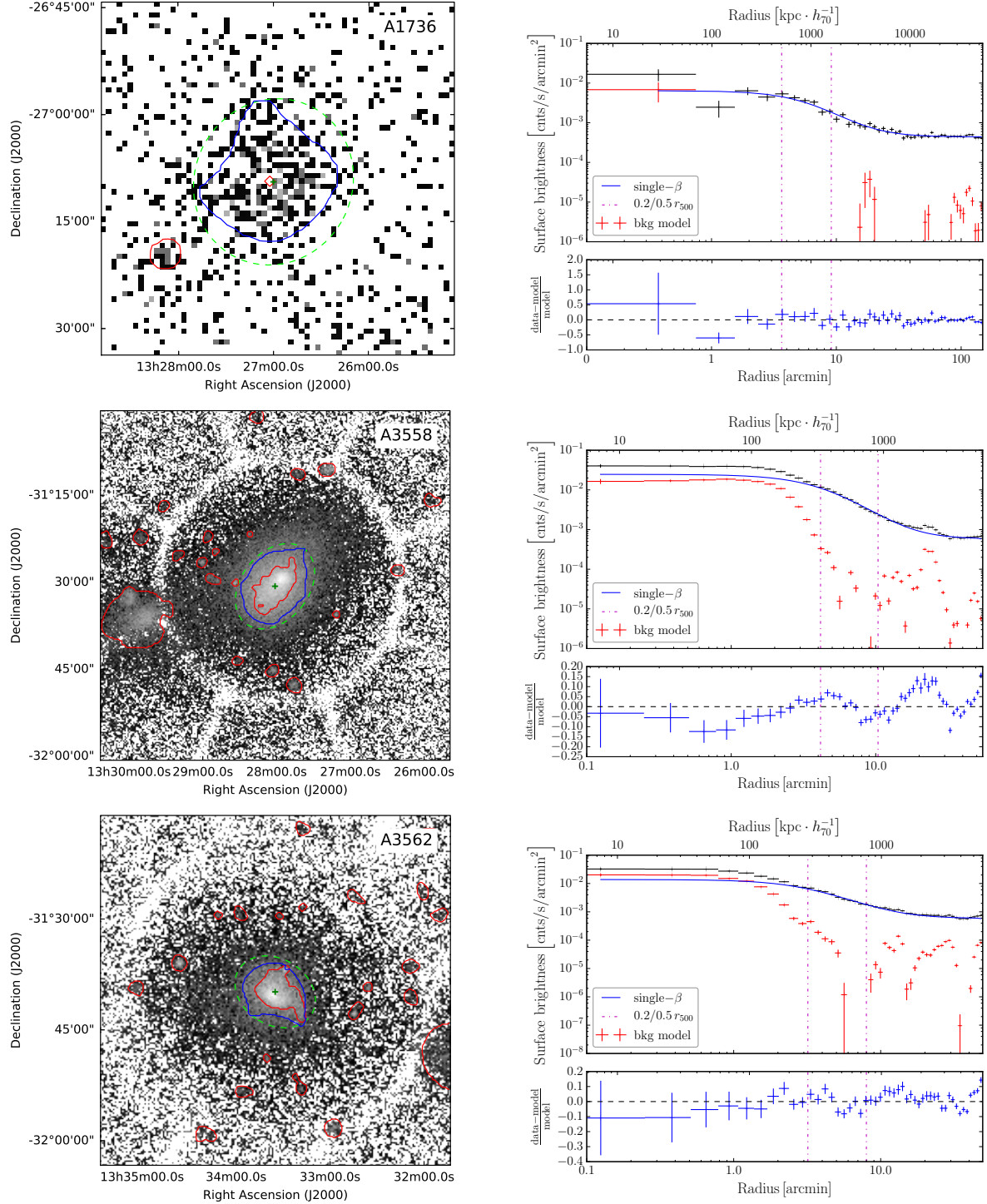


Figure A.2: Continued.

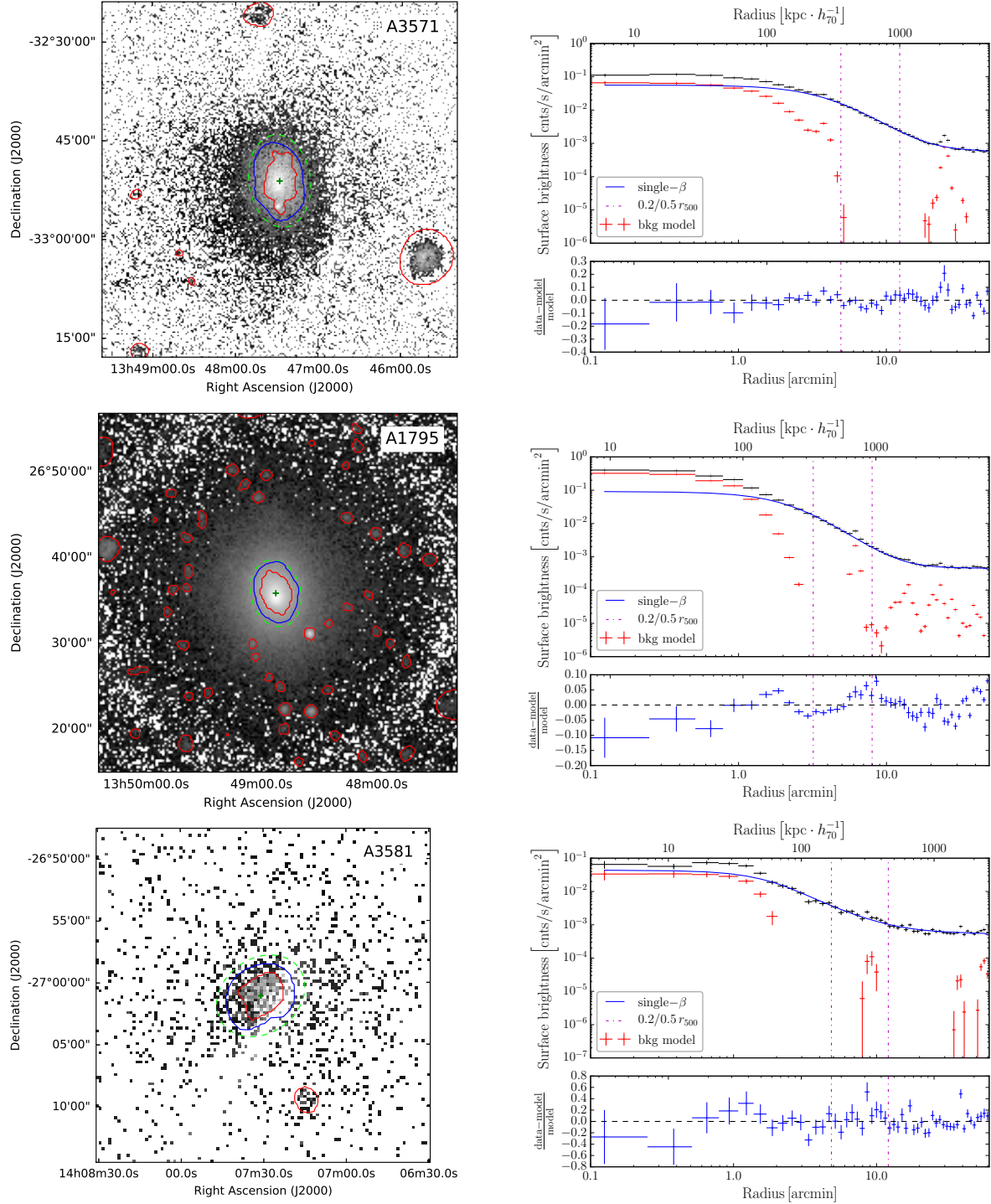


Figure A.2: Continued.

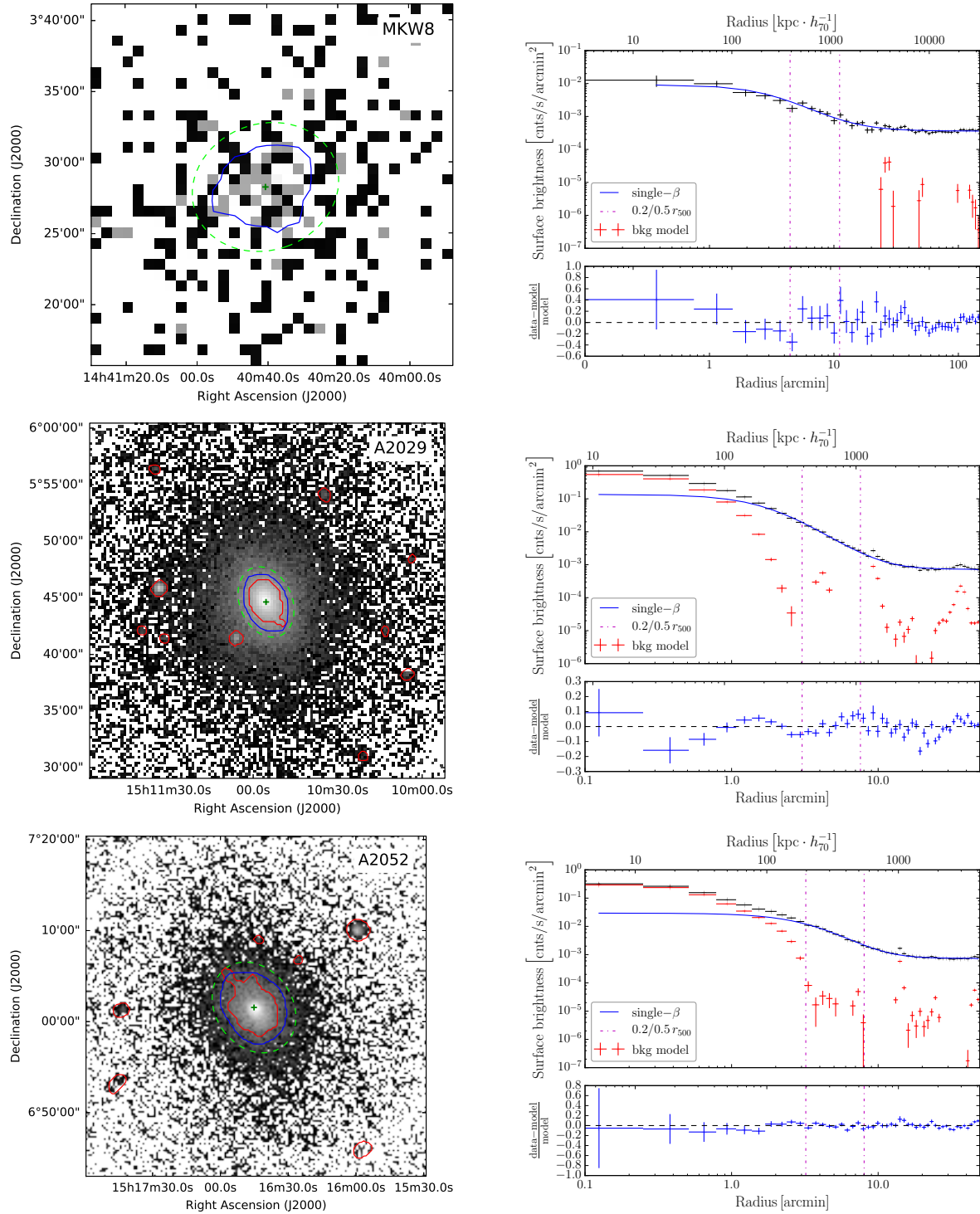


Figure A.2: Continued.

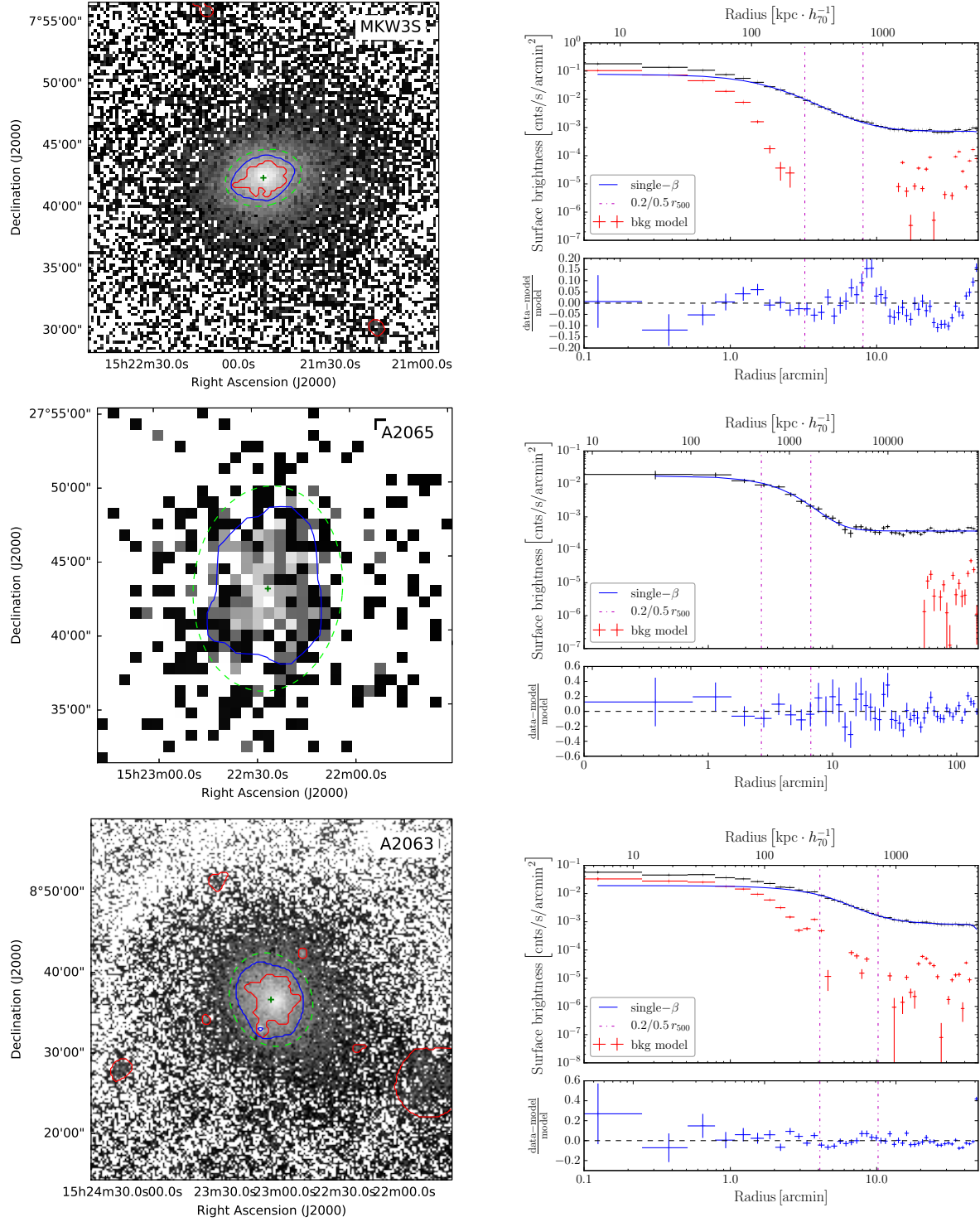


Figure A.2: Continued.

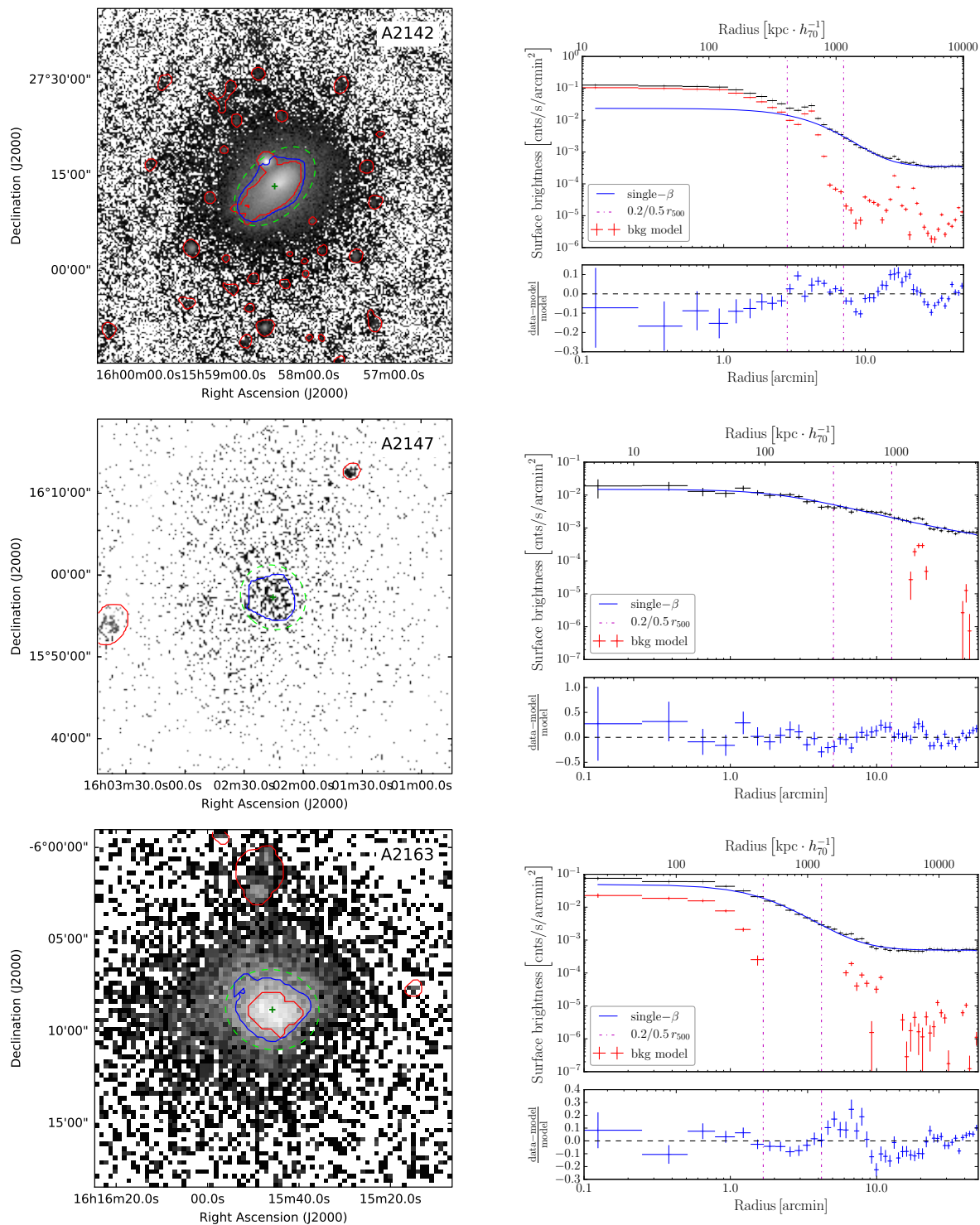


Figure A.2: Continued.

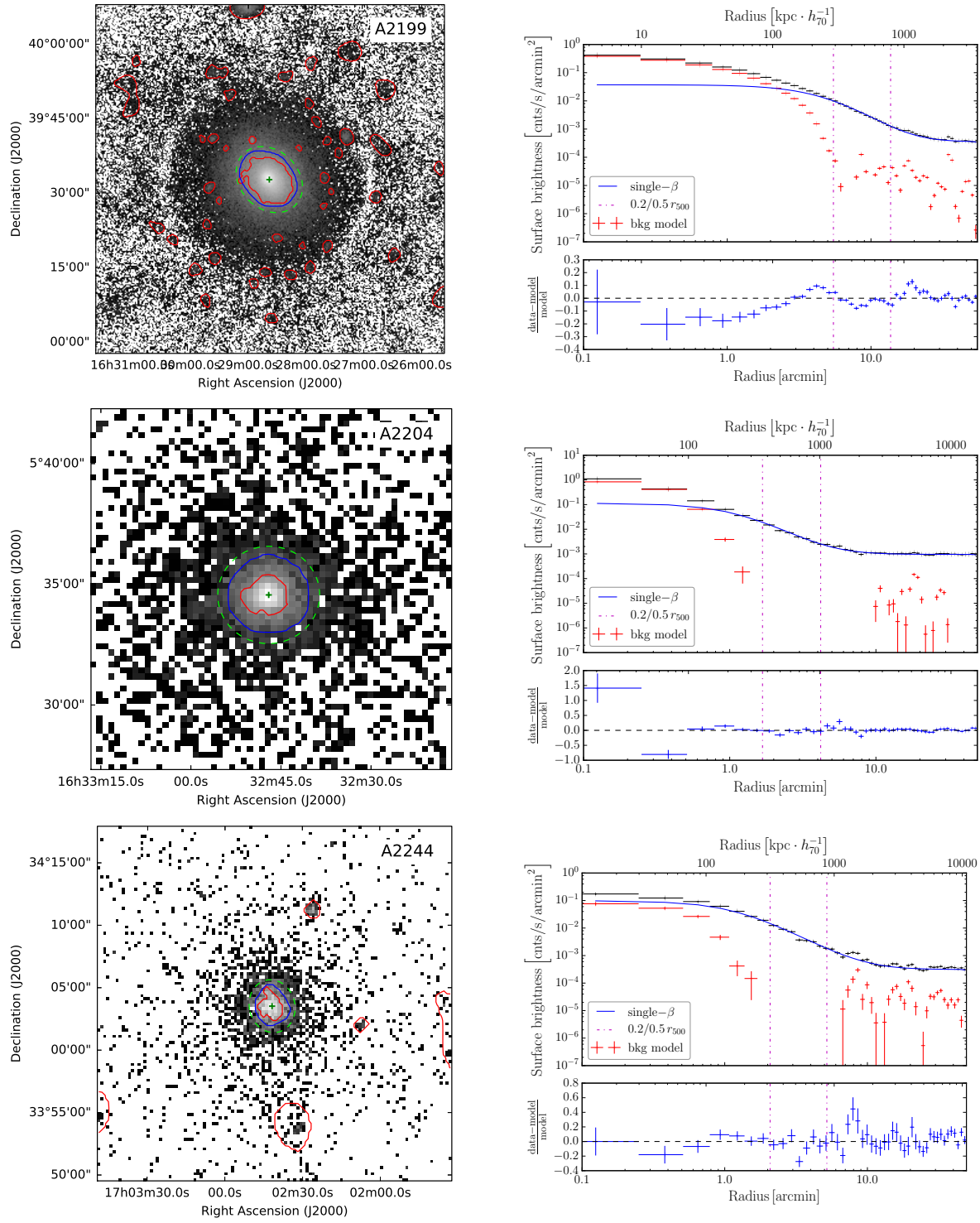


Figure A.2: Continued.

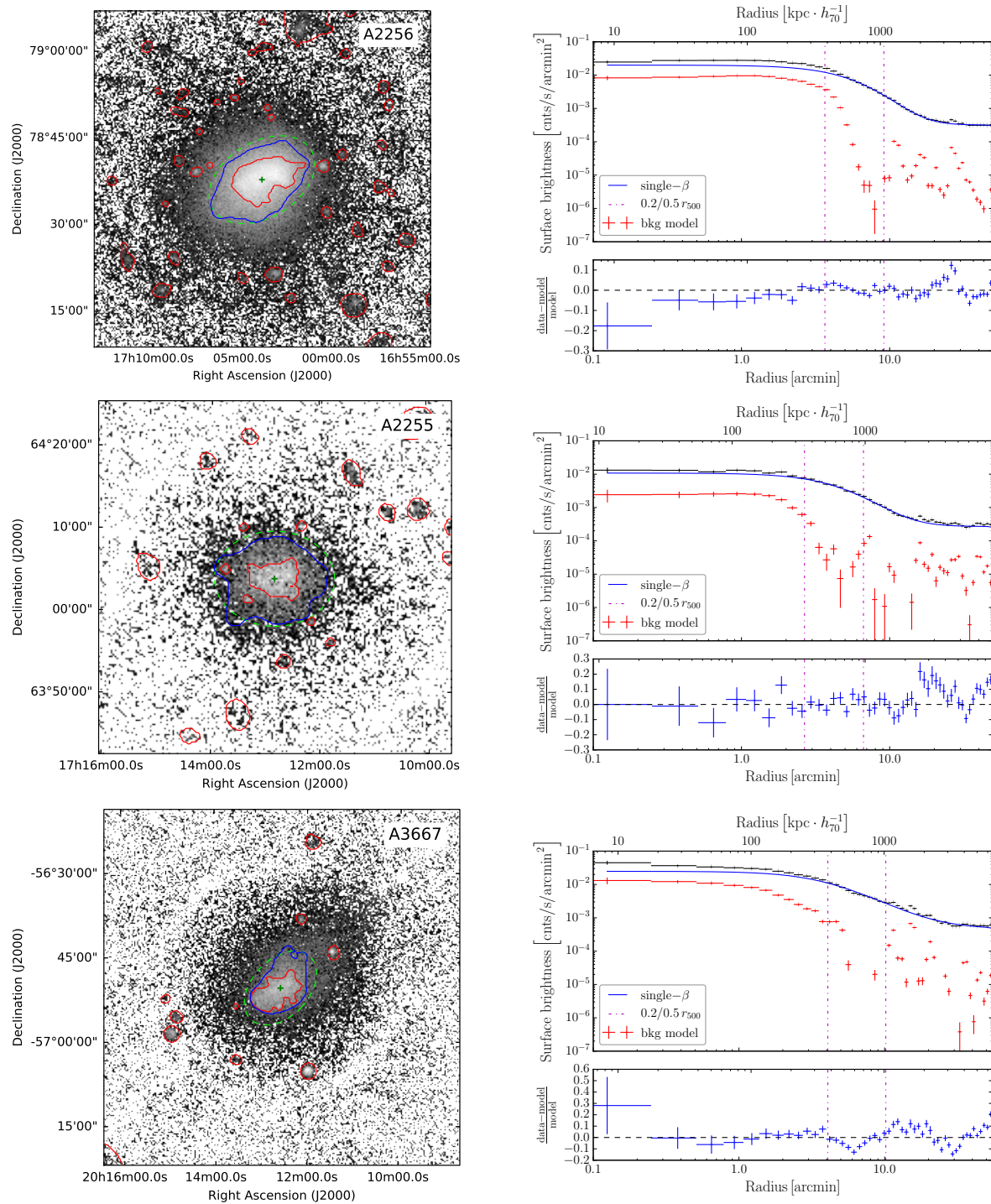


Figure A.2: Continued.

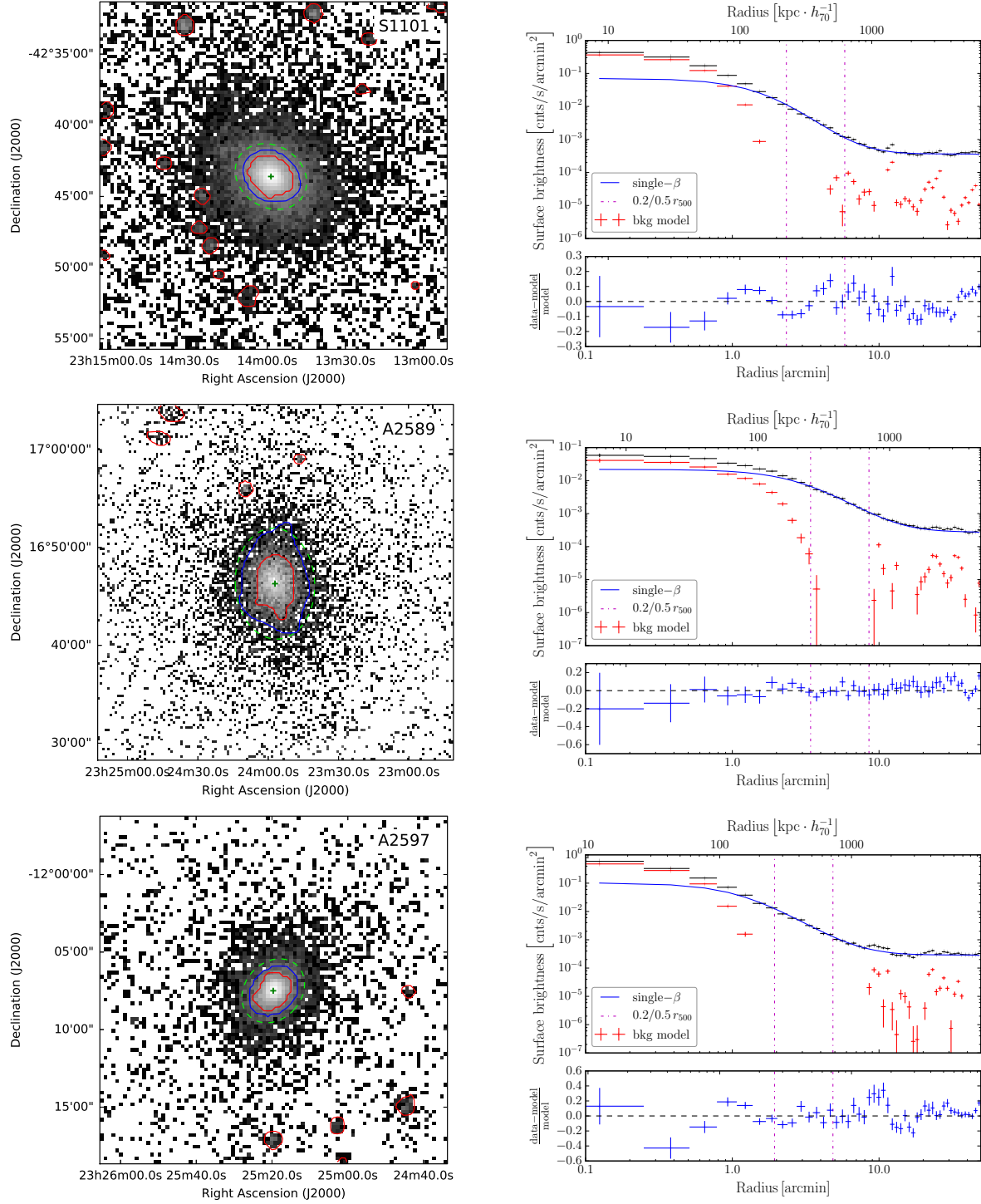


Figure A.2: Continued.

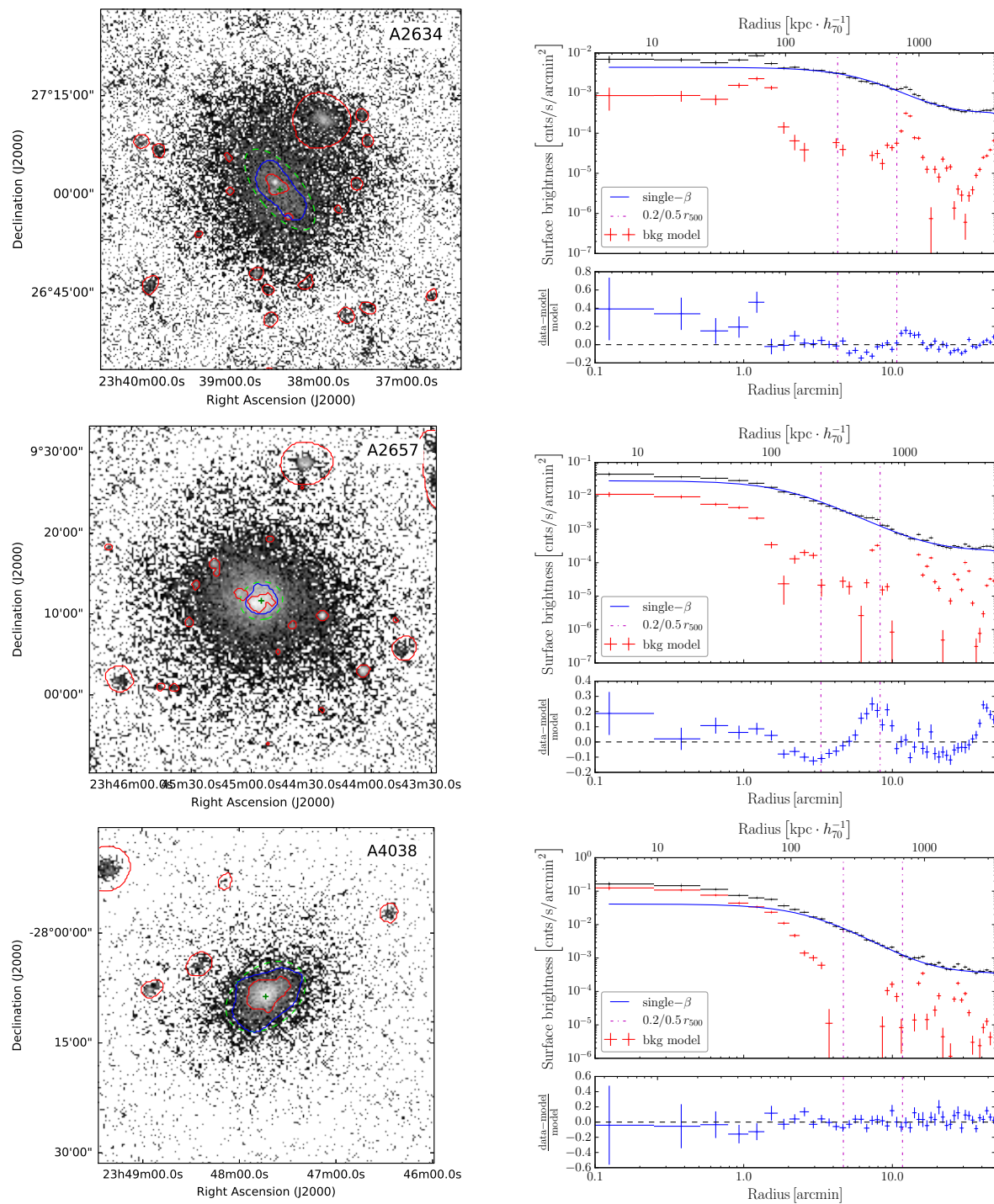


Figure A.2: Continued.

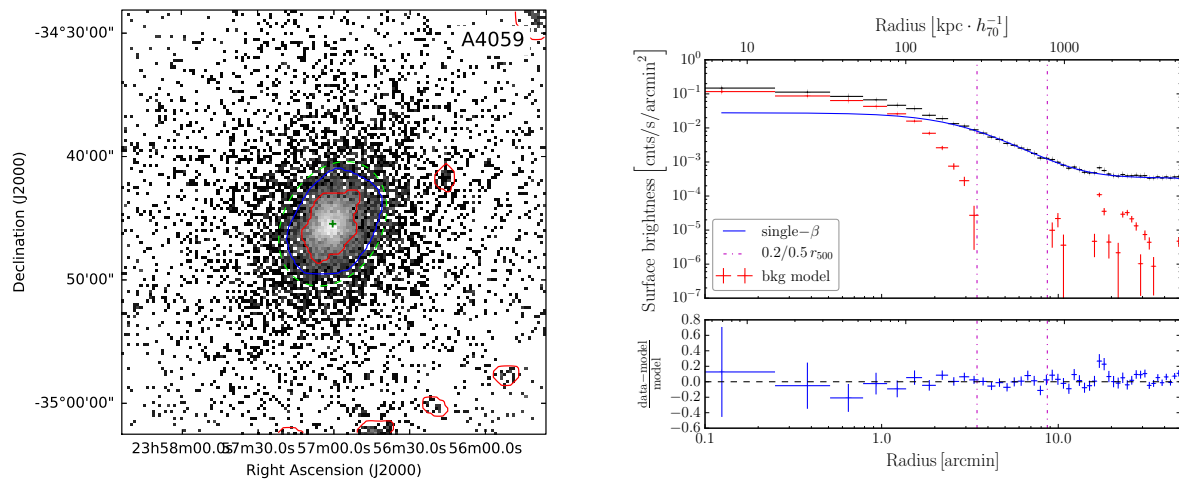


Figure A.2: Continued.

Bibliography

- Abell, G. O. (1958). The Distribution of Rich Clusters of Galaxies. *Astrophysical Journal, Supplement*, 3:211.
- Adami, C., Giles, P., Koulouridis, E., Pacaud, F., Caretta, C. A., Pierre, M., Eckert, D., Ramos-Ceja, M. E., Gastaldello, F., Fotopoulou, S., Guglielmo, V., Lidman, C., Sadibekova, T., Iovino, A., Maughan, B., Chiappetti, L., Alis, S., Altieri, B., Baldry, I., Bottini, D., Birkinshaw, M., Bremer, M., Brown, M., Cucciati, O., Driver, S., Elmer, E., Ettori, S., Evrard, A. E., Faccioli, L., Granett, B., Grootes, M., Guzzo, L., Hopkins, A., Horellou, C., Lefèvre, J. P., Liske, J., Malek, K., Marulli, F., Maurogordato, S., Owers, M., Paltani, S., Poggianti, B., Polletta, M., Plionis, M., Pollo, A., Pompei, E., Ponman, T., Rapetti, D., Ricci, M., Robotham, A., Tuffs, R., Tasca, L., Valtchanov, I., Vergani, D., Wagner, G., Willis, J., and XXL Consortium (2018). The XXL Survey. XX. The 365 cluster catalogue. *Astronomy and Astrophysics*, 620:A5.
- Allen, S. W., Evrard, A. E., and Mantz, A. B. (2011). Cosmological Parameters from Observations of Galaxy Clusters. *Annual Review of Astron and Astrophys*, 49(1):409–470.
- Alleinato, V., Finoguenov, A., Hasinger, G., Miyaji, T., Cappelluti, N., Salvato, M., Zamorani, G., Gilli, R., George, M. R., Tanaka, M., Brusa, M., Silverman, J., Civano, F., Elvis, M., and Shankar, F. (2012). Occupation of X-Ray-selected Galaxy Groups by X-Ray Active Galactic Nuclei. *Astrophysical Journal*, 758:47.
- Allgood, B., Flores, R. A., Primack, J. R., Kravtsov, A. V., Wechsler, R. H., Faltenbacher, A., and Bullock, J. S. (2006). The shape of dark matter haloes: dependence on mass, redshift, radius and formation. *Monthly Notices of the RAS*, 367:1781–1796.
- Anders, E. and Grevesse, N. (1989). Abundances of the elements - Meteoritic and solar. *Geochimica Cosmochimica Acta*, 53:197–214.
- Anderson, L., Aubourg, E., Bailey, S., Bizyaev, D., Blanton, M., Bolton, A. S., Brinkmann, J., Brownstein, J. R., Burden, A., Cuesta, A. J., da Costa, L. A. N., Dawson, K. S., de Putter, R., Eisenstein, D. J., Gunn, J. E., Guo, H., Hamilton, J.-C., Harding, P., Ho, S., Honscheid, K., Kazin, E., Kirkby, D., Kneib, J.-P., Labatie, A., Loomis, C., Lupton, R. H., Malanushenko, E., Malanushenko, V., Mandelbaum, R., Manera, M., Maraston, C., McBride, C. K., Mehta, K. T., Mena, O., Montesano, F., Muna, D., Nichol, R. C., Nuza, S. E., Olmstead, M. D., Oravetz,

- D., Padmanabhan, N., Palanque-Delabrouille, N., Pan, K., Parejko, J., Pâris, I., Percival, W. J., Petitjean, P., Prada, F., Reid, B., Roe, N. A., Ross, A. J., Ross, N. P., Samushia, L., Sánchez, A. G., Schlegel, D. J., Schneider, D. P., Scóccola, C. G., Seo, H.-J., Sheldon, E. S., Simmons, A., Skibba, R. A., Strauss, M. A., Swanson, M. E. C., Thomas, D., Tinker, J. L., Tojeiro, R., Magaña, M. V., Verde, L., Wagner, C., Wake, D. A., Weaver, B. A., Weinberg, D. H., White, M., Xu, X., Yèche, C., Zehavi, I., and Zhao, G.-B. (2012). The clustering of galaxies in the SDSS-III Baryon Oscillation Spectroscopic Survey: baryon acoustic oscillations in the Data Release 9 spectroscopic galaxy sample. *Monthly Notices of the RAS*, 427(4):3435–3467.
- Andrade-Santos, F., Jones, C., Forman, W. R., Lovisari, L., Vikhlinin, A., van Weeren, R. J., Murray, S. S., Arnaud, M., Pratt, G. W., Démoclès, J., Kraft, R., Mazzotta, P., Böhringer, H., Chon, G., Giacintucci, S., Clarke, T. E., Borgani, S., David, L., Douspis, M., Pointecouteau, E., Dahle, H., Brown, S., Aghanim, N., and Rasia, E. (2017). The Fraction of Cool-core Clusters in X-Ray versus SZ Samples Using Chandra Observations. *Astrophysical Journal*, 843:76.
- Applegate, D. E., Mantz, A., Allen, S. W., von der Linden, A., Morris, R. G., Hilbert, S., Kelly, P. L., Burke, D. L., Ebeling, H., Rapetti, D. A., and Schmidt, R. W. (2016). Cosmology and astrophysics from relaxed galaxy clusters - IV. Robustly calibrating hydrostatic masses with weak lensing. *Monthly Notices of the RAS*, 457(2):1522–1534.
- Arnaud, K. A. (1996). XSPEC: The First Ten Years. In Jacoby, G. H. and Barnes, J., editors, *Astronomical Data Analysis Software and Systems V*, volume 101 of *Astronomical Society of the Pacific Conference Series*, page 17.
- Arnaud, M., Aghanim, N., and Neumann, D. M. (2002). The X-ray surface brightness profiles of hot galaxy clusters up to $z \sim 0.8$: Evidence for self-similarity and constraints on Ω_{m0} . *Astronomy and Astrophysics*, 389:1–18.
- Arnaud, M., Rothenflug, R., Boulade, O., Vigroux, L., and Vangioni-Flam, E. (1992). Some constraints on the origin of the iron enriched intra-cluster medium. *Astronomy and Astrophysics*, 254:49–64.
- Astropy Collaboration, Price-Whelan, A. M., Sipőcz, B. M., Günther, H. M., Lim, P. L., Crawford, S. M., Conseil, S., Shupe, D. L., Craig, M. W., Dencheva, N., Ginsburg, A., VanderPlas, J. T., Bradley, L. D., Pérez-Suárez, D., de Val-Borro, M., Aldcroft, T. L., Cruz, K. L., Robitaille, T. P., Tollerud, E. J., Ardelean, C., Babej, T., Bach, Y. P., Bachetti, M., Bakanov, A. V., Bamford, S. P., Barentsen, G., Barmby, P., Baumbach, A., Berry, K. L., Biscani, F., Boquien, M., Bostroem, K. A., Bouma, L. G., Brammer, G. B., Bray, E. M., Breytenbach, H., Buddelmeijer, H., Burke, D. J., Calderone, G., Cano Rodríguez, J. L., Cara, M., Cardoso, J. V. M., Cheedella, S., Copin, Y., Corrales, L., Crichton, D., D’Avella, D., Deil, C., Depagne, É., Dietrich, J. P., Donath, A., Droettboom, M., Earl, N., Erben, T., Fabbro, S., Ferreira, L. A., Finethy, T., Fox, R. T., Garrison, L. H., Gibbons, S. L. J., Goldstein, D. A., Gommers, R., Greco, J. P., Greenfield, P., Groener, A. M., Grollier, F., Hagen, A., Hirst, P., Homeier, D., Horton, A. J., Hosseinzadeh, G., Hu, L., Hunkeler, J. S., Ivezić, Ž., Jain, A., Jenness, T.,

- Kanarek, G., Kendrew, S., Kern, N. S., Kerzendorf, W. E., Khvalko, A., King, J., Kirkby, D., Kulkarni, A. M., Kumar, A., Lee, A., Lenz, D., Littlefair, S. P., Ma, Z., Macleod, D. M., Mastropietro, M., McCully, C., Montagnac, S., Morris, B. M., Mueller, M., Mumford, S. J., Muna, D., Murphy, N. A., Nelson, S., Nguyen, G. H., Ninan, J. P., Nöthe, M., Ogaz, S., Oh, S., Parejko, J. K., Parley, N., Pascual, S., Patil, R., Patil, A. A., Plunkett, A. L., Prochaska, J. X., Rastogi, T., Reddy Janga, V., Sabater, J., Sakurikar, P., Seifert, M., Sherbert, L. E., Sherwood-Taylor, H., Shih, A. Y., Sick, J., Silbiger, M. T., Singanamalla, S., Singer, L. P., Sladen, P. H., Sooley, K. A., Sornarajah, S., Streicher, O., Teuben, P., Thomas, S. W., Tremblay, G. R., Turner, J. E. H., Terrón, V., van Kerkwijk, M. H., de la Vega, A., Watkins, L. L., Weaver, B. A., Whitmore, J. B., Woillez, J., Zabalza, V., and Astropy Contributors (2018). The Astropy Project: Building an Open-science Project and Status of the v2.0 Core Package. *Astronomical Journal*, 156:123.
- Astropy Collaboration, Robitaille, T. P., Tollerud, E. J., Greenfield, P., Droettboom, M., Bray, E., Aldcroft, T., Davis, M., Ginsburg, A., Price-Whelan, A. M., Kerzendorf, W. E., Conley, A., Crighton, N., Barbary, K., Muna, D., Ferguson, H., Grollier, F., Parikh, M. M., Nair, P. H., Unther, H. M., Deil, C., Woillez, J., Conseil, S., Kramer, R., Turner, J. E. H., Singer, L., Fox, R., Weaver, B. A., Zabalza, V., Edwards, Z. I., Azalee Bostroem, K., Burke, D. J., Casey, A. R., Crawford, S. M., Dencheva, N., Ely, J., Jenness, T., Labrie, K., Lim, P. L., Pierfederici, F., Pontzen, A., Ptak, A., Refsdal, B., Servillat, M., and Streicher, O. (2013). Astropy: A community Python package for astronomy. *Astronomy and Astrophysics*, 558:A33.
- Balogh, M. L., Babul, A., and Patton, D. R. (1999). Pre-heated isentropic gas in groups of galaxies. *Monthly Notices of the RAS*, 307:463–479.
- Balucinska-Church, M. and McCammon, D. (1992). Photoelectric absorption cross sections with variable abundances. *Astrophysical Journal*, 400:699.
- Bartelmann, M. and Steinmetz, M. (1996). A Comparison of X-ray and Strong Lensing Properties of Simulated X-ray Clusters. *Monthly Notices of the RAS*, 283:431–446.
- Bertin, E. and Arnouts, S. (1996). SExtractor: Software for source extraction. *Astronomy and Astrophysics, Supplement*, 117:393–404.
- Bianconi, M., Ettori, S., and Nipoti, C. (2013). Gas rotation in galaxy clusters: signatures and detectability in X-rays. *Monthly Notices of the RAS*, 434:1565–1575.
- Biffi, V., Dolag, K., and Merloni, A. (2018). AGN contamination of galaxy-cluster thermal X-ray emission: predictions for eRosita from cosmological simulations. *Monthly Notices of the RAS*, 481:2213–2227.
- Bocquet, S., Saro, A., Dolag, K., and Mohr, J. J. (2016). Halo mass function: baryon impact, fitting formulae, and implications for cluster cosmology. *Monthly Notices of the RAS*, 456(3):2361–2373.

- Boese, F. G. (2000). The ROSAT point spread functions and associates. *Astronomy and Astrophysics, Supplement*, 141:507–521.
- Böhringer, H., Schuecker, P., Guzzo, L., Collins, C. A., Voges, W., Cruddace, R. G., Ortiz-Gil, A., Chincarini, G., De Grandi, S., Edge, A. C., MacGillivray, H. T., Neumann, D. M., Schindler, S., and Shaver, P. (2004). The ROSAT-ESO Flux Limited X-ray (REFLEX) Galaxy cluster survey. V. The cluster catalogue. *Astronomy and Astrophysics*, 425:367–383.
- Böhringer, H., Voges, W., Huchra, J. P., McLean, B., Giacconi, R., Rosati, P., Burg, R., Mader, J., Schuecker, P., Simiç, D., Komossa, S., Reiprich, T. H., Retzlaff, J., and Trümper, J. (2000). The Northern ROSAT All-Sky (NORAS) Galaxy Cluster Survey. I. X-Ray Properties of Clusters Detected as Extended X-Ray Sources. *The Astrophysical Journal, Supplement*, 129:435–474.
- Bonafede, A., Intema, H. T., Brüggén, M., Girardi, M., Nonino, M., Kantharia, N., van Weeren, R. J., and Röttgering, H. J. A. (2014). Evidence for Particle Re-acceleration in the Radio Relic in the Galaxy Cluster PLCKG287.0+32.9. *Astrophysical Journal*, 785(1):1.
- Bonamente, M., Joy, M. K., LaRoque, S. J., Carlstrom, J. E., Reese, E. D., and Dawson, K. S. (2006). Determination of the Cosmic Distance Scale from Sunyaev-Zel'dovich Effect and Chandra X-Ray Measurements of High-Redshift Galaxy Clusters. *Astrophysical Journal*, 647(1):25–54.
- Borgani, S. and Kravtsov, A. (2011). Cosmological Simulations of Galaxy Clusters. *Advanced Science Letters*, 4(2):204–227.
- Borm, K., Reiprich, T. H., Mohammed, I., and Lovisari, L. (2014). Constraining galaxy cluster temperatures and redshifts with eROSITA survey data. *Astronomy and Astrophysics*, 567:A65.
- Brickhouse, N. S., Smith, R. K., Raymond, J. C., and Liedahl, D. A. (2000). The Astrophysical Plasma Emission Code. In *AAS/High Energy Astrophysics Division #5*, volume 32 of *Bulletin of the American Astronomical Society*, page 1227.
- Bryan, G. L. and Norman, M. L. (1998). Statistical Properties of X-Ray Clusters: Analytic and Numerical Comparisons. *Astrophysical Journal*, 495:80–99.
- Bulbul, E., Chiu, I., McDonald, M., Bautz, M. W., Benson, B., Bleem, L., Miller, E. D., and Mohr, J. J. (2017). X-ray Scaling Relations of SPT Selected Galaxy Clusters Observed with XMM-Newton. In *American Astronomical Society Meeting Abstracts #229*, volume 229 of *American Astronomical Society Meeting Abstracts*, page 404.09.
- Bulbul, E., Markevitch, M., Foster, A., Smith, R. K., Loewenstein, M., and Randall, S. W. (2014). Detection of an Unidentified Emission Line in the Stacked X-Ray Spectrum of Galaxy Clusters. *Astrophysical Journal*, 789:13.

- Burenin, R. A., Vikhlinin, A., Hornstrup, A., Ebeling, H., Quintana, H., and Mescheryakov, A. (2007). The 400 Square Degree ROSAT PSPC Galaxy Cluster Survey: Catalog and Statistical Calibration. *Astrophysical Journal, Supplement*, 172:561–582.
- Carlstrom, J. E., Holder, G. P., and Reese, E. D. (2002). Cosmology with the Sunyaev-Zel'dovich Effect. *Annual Review of Astron and Astrophys*, 40:643–680.
- Cash, W. (1979). Parameter estimation in astronomy through application of the likelihood ratio. *Astrophysical Journal*, 228:939–947.
- Cavaliere, A. and Fusco-Femiano, R. (1976). X-rays from hot plasma in clusters of galaxies. *Astronomy and Astrophysics*, 49:137–144.
- Cavaliere, A. and Fusco-Femiano, R. (1978). The Distribution of Hot Gas in Clusters of Galaxies. *Astronomy and Astrophysics*, 70:677.
- Chen, Y., Reiprich, T. H., Böhringer, H., Ikebe, Y., and Zhang, Y.-Y. (2007). Statistics of X-ray observables for the cooling-core and non-cooling core galaxy clusters. *Astronomy and Astrophysics*, 466:805–812.
- Clerc, N., Ramos-Ceja, M. E., Ridl, J., Lamer, G., Brunner, H., Hofmann, F., Comparat, J., Pacaud, F., Käfer, F., Reiprich, T. H., Merloni, A., Schmid, C., Brand, T., Wilms, J., Friedrich, P., Finoguenov, A., Dauser, T., and Kreykenbohm, I. (2018). Synthetic simulations of the extragalactic sky seen by eROSITA. I. Pre-launch selection functions from Monte-Carlo simulations. *Astronomy and Astrophysics*, 617:A92.
- Colless, M., Dalton, G., Maddox, S., Sutherland, W., Norberg, P., Cole, S., Bland-Hawthorn, J., Bridges, T., Cannon, R., Collins, C., Couch, W., Cross, N., Deeley, K., De Propriis, R., Driver, S. P., Efstathiou, G., Ellis, R. S., Frenk, C. S., Glazebrook, K., Jackson, C., Lahav, O., Lewis, I., Lumsden, S., Madgwick, D., Peacock, J. A., Peterson, B. A., Price, I., Seaborne, M., and Taylor, K. (2001). The 2dF Galaxy Redshift Survey: spectra and redshifts. *Monthly Notices of the RAS*, 328(4):1039–1063.
- Comparat, J., Eckert, D., Finoguenov, A., Schmidt, R., Sanders, J., Nagai, D., Lau, E. T., Käfer, F., Pacaud, F., Clerc, N., Reiprich, T. H., Bulbul, E., Ider Chitham, J., Chuang, C.-H., Ghirardini, V., Gonzalez-Perez, V., Gozali, G., Kirkpatrick, C. C., Klypin, A., Merloni, A., Nandra, K., Liu, T., Prada, F., Ramos-Ceja, M. E., Salvato, M., Seppi, R., Tempel, E., and Yepes, G. (2020). Full-sky photon simulation of clusters and active galactic nuclei in the soft X-rays for eROSITA. *arXiv e-prints*, page arXiv:2008.08404.
- Connelly, J. L., Wilman, D. J., Finoguenov, A., Hou, A., Mulchaey, J. S., McGee, S. L., Balogh, M. L., Parker, L. C., Saglia, R., Henderson, R. D. E., and Bower, R. G. (2012). Exploring the Diversity of Groups at $0.1 < z < 0.8$ with X-Ray and Optically Selected Samples. *Astrophysical Journal*, 756(2):139.

- Damiani, F., Maggio, A., Micela, G., and Sciortino, S. (1997). A Method Based on Wavelet Transforms for Source Detection in Photon-counting Detector Images. I. Theory and General Properties. *Astrophysical Journal*, 483(1):350–369.
- Dauser, T., Falkner, S., Lorenz, M., Kirsch, C., Peille, P., Cucchetti, E., Schmid, C., Brand, T., Oertel, M., Smith, R., and Wilms, J. (2019). SIXTE – The Generic X-ray Instrument Simulation Toolkit. *arXiv e-prints*.
- Davis, M. and Peebles, P. J. E. (1983). A survey of galaxy redshifts. V. The two-point position and velocity correlations. *Astrophysical Journal*, 267:465–482.
- Dennerl, K., Burkert, W., Burwitz, V., Freyberg, M., Friedrich, P., and Hartner, G. (2012). Determination of the eROSITA mirror half energy width (HEW) with subpixel resolution. In *Space Telescopes and Instrumentation 2012: Ultraviolet to Gamma Ray*, volume 8443 of *Proceedings of the SPIE*, page 844350.
- Despali, G., Giocoli, C., Angulo, R. E., Tormen, G., Sheth, R. K., Baso, G., and Moscardini, L. (2016). The universality of the virial halo mass function and models for non-universality of other halo definitions. *Monthly Notices of the RAS*, 456(3):2486–2504.
- Diemer, B. (2018). COLOSSUS: A Python Toolkit for Cosmology, Large-scale Structure, and Dark Matter Halos. *Astrophysical Journal, Supplement*, 239:35.
- Eckert, D., Finoguenov, A., Ghirardini, V., Grandis, S., Kaefer, F., Sanders, J. S., and Ramos-Ceja, M. (2020). Low-scatter galaxy cluster mass proxies for the eROSITA all-sky survey. *arXiv e-prints*, page arXiv:2009.03944.
- Eckert, D., Ghirardini, V., Ettori, S., Rasia, E., Biffi, V., Pointecouteau, E., Rossetti, M., Molendi, S., Vazza, F., Gastaldello, F., Gaspari, M., De Grandi, S., Ghizzardi, S., Bourdin, H., Tchernin, C., and Roncarelli, M. (2019). Non-thermal pressure support in X-COP galaxy clusters. *Astronomy and Astrophysics*, 621:A40.
- Eckert, D., Molendi, S., and Paltani, S. (2011). The cool-core bias in X-ray galaxy cluster samples. I. Method and application to HIFLUGCS. *Astronomy and Astrophysics*, 526:A79.
- Eckert, D., Vazza, F., Ettori, S., Molendi, S., Nagai, D., Lau, E. T., Roncarelli, M., Rossetti, M., Snowden, S. L., and Gastaldello, F. (2012). The gas distribution in the outer regions of galaxy clusters. *Astronomy and Astrophysics*, 541:A57.
- Eckmiller, H. J., Hudson, D. S., and Reiprich, T. H. (2011). Testing the low-mass end of X-ray scaling relations with a sample of Chandra galaxy groups. *Astronomy and Astrophysics*, 535:A105.
- Eisenstein, D. J., Weinberg, D. H., Agol, E., Aihara, H., Allende Prieto, C., Anderson, S. F., Arns, J. A., Aubourg, É., Bailey, S., Balbinot, E., Barkhouser, R., Beers, T. C., Berlind, A. A., Bickerton, S. J., Bizyaev, D., Blanton, M. R., Bochanski, J. J., Bolton, A. S., Bosman,

- C. T., Bovy, J., Brandt, W. N., Breslauer, B., Brewington, H. J., Brinkmann, J., Brown, P. J., Brownstein, J. R., Burger, D., Busca, N. G., Campbell, H., Cargile, P. A., Carithers, W. C., Carlberg, J. K., Carr, M. A., Chang, L., Chen, Y., Chiappini, C., Comparat, J., Connolly, N., Cortes, M., Croft, R. A. C., Cunha, K., da Costa, L. N., Davenport, J. R. A., Dawson, K., De Lee, N., Porto de Mello, G. F., de Simoni, F. o., Dean, J., Dhital, S., Ealet, A., Ebelke, G. L., Edmondson, E. M., Eiting, J. M., Escoffier, S., Esposito, M., Evans, M. L., Fan, X., Femenía Castellá, B., Dutra Ferreira, L., Fitzgerald, G., Fleming, S. W., Font-Ribera, A., Ford, E. B., Frinchaboy, P. M., García Pérez, A. E., Gaudi, B. S., Ge, J., Ghezzi, L., Gillespie, B. A., Gilmore, G., Girardi, L., Gott, J. R., Gould, A., Grebel, E. K., Gunn, J. E., Hamilton, J.-C., Harding, P., Harris, D. W., Hawley, S. L., Hearty, F. R., Hennawi, J. F., González Hernández, J. I., Ho, S., Hogg, D. W., Holtzman, J. A., Honscheid, K., Inada, N., Ivans, I. I., Jiang, L., Jiang, P., Johnson, J. A., Jordan, C., Jordan, W. P., Kauffmann, G., Kazin, E., Kirkby, D., Klaene, M. A., Knapp, G. R., Kneib, J.-P., Kochanek, C. S., Koesterke, L., Kollmeier, J. A., Kron, R. G., Lampeitl, H., Lang, D., Lawler, J. E., Le Goff, J.-M., Lee, B. L., Lee, Y. S., Leisenring, J. M., Lin, Y.-T., Liu, J., Long, D. C., Loomis, C. P., Lucatello, S., Lundgren, B., Lupton, R. H., Ma, B., Ma, Z., MacDonald, N., Mack, C., Mahadevan, S., Maia, M. A. G., Majewski, S. R., Makler, M., Malanushenko, E., Malanushenko, V., Mand elbaum, R., Maraston, C., Margala, D., Maseman, P., Masters, K. L., McBride, C. K., McDonald, P., McGreer, I. D., McMahan, R. G., Mena Requejo, O., Ménard, B., Miralda-Escudé, J., Morrison, H. L., Mullally, F., Muna, D., Murayama, H., Myers, A. D., Naugle, T., Neto, A. F., Nguyen, D. C., Nichol, R. C., Nidever, D. L., O'Connell, R. W., Ogando, R. L. C., Olmstead, M. D., Oravetz, D. J., Padmanabhan, N., Paegert, M., Palanque-Delabrouille, N., Pan, K., Pandey, P., Parejko, J. K., Pâris, I., Pellegrini, P., Pepper, J., Percival, W. J., Petitjean, P., Pfaffenberger, R., Pforr, J., Phleps, S., Pichon, C., Pieri, M. M., Prada, F., Price-Whelan, A. M., Raddick, M. J., Ramos, B. H. F., Reid, I. N., Reyle, C., Rich, J., Richards, G. T., Rieke, G. H., Rieke, M. J., Rix, H.-W., Robin, A. C., Rocha-Pinto, H. J., Rockosi, C. M., Roe, N. A., Rollinde, E., Ross, A. J., Ross, N. P., Rossetto, B., Sánchez, A. G., Santiago, B., Sayres, C., Schiavon, R., Schlegel, D. J., Schlesinger, K. J., Schmidt, S. J., Schneider, D. P., Sellgren, K., Shelden, A., Sheldon, E., Shetrone, M., Shu, Y., Silverman, J. D., Simmerer, J., Simmons, A. E., Sivarani, T., Skrutskie, M. F., Slosar, A., Smee, S., Smith, V. V., Snedden, S. A., Stassun, K. G., Steele, O., Steinmetz, M., Stockett, M. H., Stollberg, T., Strauss, M. A., Szalay, A. S., Tanaka, M., Thakar, A. R., Thomas, D., Tinker, J. L., Tofflemire, B. M., Tojeiro, R., Tremonti, C. A., Vargas Magaña, M., Verde, L., Vogt, N. P., Wake, D. A., Wan, X., Wang, J., Weaver, B. A., White, M., White, S. D. M., Wilson, J. C., Wisniewski, J. P., Wood-Vasey, W. M., Yanny, B., Yasuda, N., Yèche, C., York, D. G., Young, E., Zasowski, G., Zehavi, I., and Zhao, B. (2011). SDSS-III: Massive Spectroscopic Surveys of the Distant Universe, the Milky Way, and Extra-Solar Planetary Systems. *Astronomical Journal*, 142(3):72.
- Erfanianfar, G., Finoguenov, A., Tanaka, M., Lerchster, M., Nandra, K., Laird, E., Connelly, J. L., Bielby, R., Mirkazemi, M., Faber, S. M., Kocevski, D., Cooper, M., Newman, J. A., Jeltema, T., Coil, A. L., Brimiouille, F., Davis, M., McCracken, H. J., Willmer, C., Gerke, B., Cappelluti, N., and Gwyn, S. (2013). X-Ray Groups of Galaxies in the AEGIS Deep and Wide Fields. *Astrophysical Journal*, 765:117.

- Finoguenov, A., Connelly, J. L., Parker, L. C., Wilman, D. J., Mulchaey, J. S., Saglia, R. P., Balogh, M. L., Bower, R. G., and McGee, S. L. (2009). The Roadmap for Unification in Galaxy Group Selection. I. A Search for Extended X-ray Emission in the CNOC2 Survey. *Astrophysical Journal*, 704:564–575.
- Finoguenov, A., Davis, D. S., Zimer, M., and Mulchaey, J. S. (2006). The Two-dimensional XMM-Newton Group Survey: $z \lesssim 0.012$ Groups. *Astrophysical Journal*, 646(1):143–160.
- Finoguenov, A., Ponman, T. J., Osmond, J. P. F., and Zimer, M. (2007). XMM-Newton study of $0.012 \lesssim z \lesssim 0.024$ groups - I. Overview of the IGM thermodynamics. *Monthly Notices of the RAS*, 374(2):737–760.
- Finoguenov, A., Sarazin, C. L., Nakazawa, K., Wik, D. R., and Clarke, T. E. (2010a). XMM-Newton Observation of the Northwest Radio Relic Region in A3667. *Astrophysical Journal*, 715:1143–1151.
- Finoguenov, A., Tanaka, M., Cooper, M., Allevalo, V., Cappelluti, N., Choi, A., Heymans, C., Bauer, F. E., Ziparo, F., Ranalli, P., Silverman, J., Brandt, W. N., Xue, Y. Q., Mulchaey, J., Howes, L., Schmid, C., Wilman, D., Comastri, A., Hasinger, G., Mainieri, V., Luo, B., Tozzi, P., Rosati, P., Capak, P., and Popesso, P. (2015). Ultra-deep catalog of X-ray groups in the Extended Chandra Deep Field South. *Astronomy and Astrophysics*, 576:A130.
- Finoguenov, A., Watson, M. G., Tanaka, M., Simpson, C., Cirasuolo, M., Dunlop, J. S., Peacock, J. A., Farrah, D., Akiyama, M., Ueda, Y., Smolčić, V., Stewart, G., Rawlings, S., van Breukelen, C., Almaini, O., Clewley, L., Bonfield, D. G., Jarvis, M. J., Barr, J. M., Foucaud, S., McLure, R. J., Sekiguchi, K., and Egami, E. (2010b). X-ray groups and clusters of galaxies in the Subaru-XMM Deep Field. *Monthly Notices of the RAS*, 403:2063–2076.
- Foreman-Mackey, D., Hogg, D. W., Lang, D., and Goodman, J. (2013). emcee: The MCMC Hammer. *Publications of the ASP*, 125:306.
- Friedrich, P., Rohé, C., Gaida, R., Hartwig, J., Soller, F., Bräuninger, H., Budau, B., Burkert, W., Burwitz, V., Eder, J., Hartner, G., Menz, B., and Predehl, P. (2014). The eROSITA x-ray baffle. In *Space Telescopes and Instrumentation 2014: Ultraviolet to Gamma Ray*, volume 9144 of *Proceedings of the SPIE*, page 91444R.
- Geller, M. J. and Huchra, J. P. (1989). Mapping the Universe. *Science*, 246(4932):897–903.
- Ghirardini, V., Eckert, D., Ettori, S., Pointecouteau, E., Molendi, S., Gaspari, M., Rossetti, M., De Grandi, S., Roncarelli, M., Bourdin, H., Mazzotta, P., Rasia, E., and Vazza, F. (2018a). The universal thermodynamic properties of the intracluster medium over two decades in radius in the X-COP sample. *ArXiv e-prints*.
- Ghirardini, V., Eckert, D., Ettori, S., Pointecouteau, E., Molendi, S., Gaspari, M., Rossetti, M., De Grandi, S., Roncarelli, M., Bourdin, H., Mazzotta, P., Rasia, E., and Vazza, F. (2019). Universal thermodynamic properties of the intracluster medium over two decades in radius in the X-COP sample. *Astronomy and Astrophysics*, 621:A41.

- Ghirardini, V., Ettori, S., Eckert, D., Molendi, S., Gastaldello, F., Pointecouteau, E., Hurier, G., and Bourdin, H. (2018b). The XMM Cluster Outskirts Project (X-COP): Thermodynamic properties of the intracluster medium out to R_{200} in Abell 2319. *Astronomy and Astrophysics*, 614:A7.
- Giacconi, R., Gursky, H., Paolini, F. R., and Rossi, B. B. (1962). Evidence for x Rays From Sources Outside the Solar System. *Physical Review Letters*, 9:439–443.
- Giacconi, R., Kellogg, E., Gorenstein, P., Gursky, H., and Tananbaum, H. (1971). An X-Ray Scan of the Galactic Plane from UHURU. *Astrophysical Journal, Letters*, 165:L27.
- Giles, P. A., Maughan, B. J., Pacaud, F., Lieu, M., Clerc, N., Pierre, M., Adami, C., Chiappetti, L., Démoclés, J., Ettori, S., Le Fèvre, J. P., Ponman, T., Sadibekova, T., Smith, G. P., Willis, J. P., and Ziparo, F. (2016). The XXL Survey. III. Luminosity-temperature relation of the bright cluster sample. *Astronomy and Astrophysics*, 592:A3.
- Giodini, S., Lovisari, L., Pointecouteau, E., Ettori, S., Reiprich, T. H., and Hoekstra, H. (2013). Scaling Relations for Galaxy Clusters: Properties and Evolution. *Space Science Reviews*, 177:247–282.
- Gladders, M. D. and Yee, H. K. C. (2000). A New Method For Galaxy Cluster Detection. I. The Algorithm. *Astronomical Journal*, 120(4):2148–2162.
- Gott, J. Richard, I., Jurić, M., Schlegel, D., Hoyle, F., Vogeley, M., Tegmark, M., Bahcall, N., and Brinkmann, J. (2005). A Map of the Universe. *Astrophysical Journal*, 624(2):463–484.
- Gozaliasl, G., Finoguenov, A., Tanaka, M., Dolag, K., Montanari, F., Kirkpatrick, C. C., Vardoulaki, E., Khosroshahi, H. G., Salvato, M., Laigle, C., McCracken, H. J., Ilbert, O., Cappelluti, N., Daddi, E., Hasinger, G., Capak, P., Scoville, N. Z., Toft, S., Civano, F., Griffiths, R. E., Balogh, M., Li, Y., Ahoranta, J., Mei, S., Iovino, A., Henriques, B. M. B., and Erfanianfar, G. (2019). Chandra centres for COSMOS X-ray galaxy groups: differences in stellar properties between central dominant and offset brightest group galaxies. *Monthly Notices of the RAS*, 483:3545–3565.
- Grandis, S., Mohr, J. J., Dietrich, J. P., Bocquet, S., Saro, A., Klein, M., Paulus, M., and Capasso, R. (2018). Impact of Weak Lensing Mass Calibration on eROSITA Galaxy Cluster Cosmological Studies – a Forecast. *arXiv e-prints*.
- Greiner, J., Burgess, J. M., Savchenko, V., and Yu, H.-F. (2016). On the Fermi-GBM Event 0.4 s after GW150914. *Astrophysical Journal, Letters*, 827:L38.
- Guth, A. H. (1981). Inflationary universe: A possible solution to the horizon and flatness problems. *Physical Review D*, 23(2):347–356.
- Hashimoto, Y., Böhringer, H., Henry, J. P., Hasinger, G., and Szokoly, G. (2007). Robust quantitative measures of cluster X-ray morphology, and comparisons between cluster characteristics. *Astronomy and Astrophysics*, 467:485–499.

- Hinshaw, G., Larson, D., Komatsu, E., Spergel, D. N., Bennett, C. L., Dunkley, J., Nolta, M. R., Halpern, M., Hill, R. S., Odegard, N., Page, L., Smith, K. M., Weiland, J. L., Gold, B., Jarosik, N., Kogut, A., Limon, M., Meyer, S. S., Tucker, G. S., Wollack, E., and Wright, E. L. (2013). Nine-year Wilkinson Microwave Anisotropy Probe (WMAP) Observations: Cosmological Parameter Results. *Astrophysical Journal, Supplement*, 208:19.
- Hitomi Collaboration, Aharonian, F., Akamatsu, H., Akimoto, F., Allen, S. W., Anabuki, N., Angelini, L., Arnaud, K., Audard, M., Awaki, H., Axelsson, M., Bamba, A., Bautz, M., Blandford, R., Brenneman, L., Brown, G. V., Bulbul, E., Cackett, E., Chernyakova, M., Chiao, M., Coppi, P., Costantini, E., de Plaa, J., den Herder, J.-W., Done, C., Dotani, T., Ebisawa, K., Eckart, M., Enoto, T., Ezoe, Y., Fabian, A. C., Ferrigno, C., Foster, A., Fujimoto, R., Fukazawa, Y., Furuzawa, A., Galeazzi, M., Gallo, L., Gandhi, P., Giustini, M., Goldwurm, A., Gu, L., Guainazzi, M., Haba, Y., Hagino, K., Hamaguchi, K., Harrus, I., Hatsukade, I., Hayashi, K., Hayashi, T., Hayashida, K., Hiraga, J., Hornschemeier, A., Hoshino, A., Hughes, J., Iizuka, R., Inoue, H., Inoue, Y., Ishibashi, K., Ishida, M., Ishikawa, K., Ishisaki, Y., Itoh, M., Iyomoto, N., Kaastra, J., Kallman, T., Kamae, T., Kara, E., Kataoka, J., Katsuda, S., Katsuta, J., Kawaharada, M., Kawai, N., Kelley, R., Khangulyan, D., Kilbourne, C., King, A., Kitaguchi, T., Kitamoto, S., Kitayama, T., Kohmura, T., Kokubun, M., Koyama, S., Koyama, K., Kretschmar, P., Krimm, H., Kubota, A., Kunieda, H., Laurent, P., Lebrun, F., Lee, S.-H., Leutenegger, M., Limousin, O., Loewenstein, M., Long, K. S., Lumb, D., Madejski, G., Maeda, Y., Maier, D., Makishima, K., Markevitch, M., Matsumoto, H., Matsushita, K., McCammon, D., McNamara, B., Mehdipour, M., Miller, E., Miller, J., Mineshige, S., Mitsuda, K., Mitsuishi, I., Miyazawa, T., Mizuno, T., Mori, H., Mori, K., Moseley, H., Mukai, K., Murakami, H., Murakami, T., Mushotzky, R., Nagino, R., Nakagawa, T., Nakajima, H., Nakamori, T., Nakano, T., Nakashima, S., Nakazawa, K., Nobukawa, M., Noda, H., Nomachi, M., O'Dell, S., Odaka, H., Ohashi, T., Ohno, M., Okajima, T., Ota, N., Ozaki, M., Paerels, F., Paltani, S., Parmar, A., Petre, R., Pinto, C., Pohl, M., Porter, F. S., Pottschmidt, K., Ramsey, B., Reynolds, C., Russell, H., Safi-Harb, S., Saito, S., Sakai, K., Sameshima, H., Sato, G., Sato, K., Sato, R., Sawada, M., Schartel, N., Serlemitsos, P., Seta, H., Shidatsu, M., Simionescu, A., Smith, R., Soong, Y., Stawarz, L., Sugawara, Y., Sugita, S., Szymkowiak, A., Tajima, H., Takahashi, H., Takahashi, T., Takeda, S., Takei, Y., Tamagawa, T., Tamura, K., Tamura, T., Tanaka, T., Tanaka, Y., Tanaka, Y., Tashiro, M., Tawara, Y., Terada, Y., Terashima, Y., Tombesi, F., Tomida, H., Tsuboi, Y., Tsujimoto, M., Tsunemi, H., Tsuru, T., Uchida, H., Uchiyama, H., Uchiyama, Y., Ueda, S., Ueda, Y., Ueno, S., Uno, S., Urry, M., Ursino, E., de Vries, C., Watanabe, S., Werner, N., Wik, D., Wilkins, D., Williams, B., Yamada, S., Yamaguchi, H., Yamaoka, K., Yamasaki, N. Y., Yamauchi, M., Yamauchi, S., Yaqoob, T., Yatsu, Y., Yonetoku, D., Yoshida, A., Yuasa, T., Zhuravleva, I., and Zoghbi, A. (2016). The quiescent intracluster medium in the core of the Perseus cluster. *Nature*, 535(7610):117–121.
- Holschneider, M., Kronland-Martinet, R., Morlet, J., and Tchamitchian, P. (1989). A Real-Time Algorithm for Signal Analysis with the Help of the Wavelet Transform. In Combes, J.-M., Grossmann, A., and Tchamitchian, P., editors, *Wavelets. Time-Frequency Methods and Phase Space*, page 286.

- Hu, W. and Dodelson, S. (2002). Cosmic Microwave Background Anisotropies. *Annual Review of Astron and Astrophys*, 40:171–216.
- Hudson, D. S., Mittal, R., Reiprich, T. H., Nulsen, P. E. J., Andernach, H., and Sarazin, C. L. (2010). What is a cool-core cluster? a detailed analysis of the cores of the X-ray flux-limited HIFLUGCS cluster sample. *Astronomy and Astrophysics*, 513:A37.
- Jelić, V., Zaroubi, S., Labropoulos, P., Bernardi, G., de Bruyn, A. G., and Koopmans, L. V. E. (2010). Realistic simulations of the Galactic polarized foreground: consequences for 21-cm reionization detection experiments. *Monthly Notices of the RAS*, 409:1647–1659.
- Jenkins, A., Frenk, C. S., White, S. D. M., Colberg, J. M., Cole, S., Evrard, A. E., Couchman, H. M. P., and Yoshida, N. (2001). The mass function of dark matter haloes. *Monthly Notices of the RAS*, 321(2):372–384.
- Käfer, F., Finoguenov, A., Eckert, D., Clerc, N., Ramos-Ceja, M. E., Sanders, J. S., and Ghirardini, V. (2020). Toward the low-scatter selection of X-ray clusters. Galaxy cluster detection with eROSITA through cluster outskirts. *Astronomy and Astrophysics*, 634:A8.
- Käfer, F., Finoguenov, A., Eckert, D., Sanders, J. S., Reiprich, T. H., and Nandra, K. (2019). Toward a characterization of X-ray galaxy clusters for cosmology. *Astronomy and Astrophysics*, 628:A43.
- Kaiser, N. (1986). Evolution and clustering of rich clusters. *Monthly Notices of the RAS*, 222:323–345.
- Karzas, W. J. and Latter, R. (1961). Electron Radiative Transitions in a Coulomb Field. *Astrophysical Journal, Supplement*, 6:167.
- Kellogg, E., Baldwin, J., and Koch, D. (1975). Studies of cluster x-ray sources. energy spectra for the perseus, virgo, and coma clusters. *The Astrophysical Journal*, 199:299–306.
- Kelly, B. C. (2007). Some Aspects of Measurement Error in Linear Regression of Astronomical Data. *Astrophysical Journal*, 665:1489–1506.
- Kettula, K., Giodini, S., van Uitert, E., Hoekstra, H., Finoguenov, A., Lerchster, M., Erben, T., Heymans, C., Hildebrandt, H., Kitching, T. D., Mahdavi, A., Mellier, Y., Miller, L., Mirkazemi, M., Van Waerbeke, L., Coupon, J., Egami, E., Fu, L., Hudson, M. J., Kneib, J. P., Kuijken, K., McCracken, H. J., Pereira, M. J., Rowe, B., Schrabback, T., Tanaka, M., and Velander, M. (2015). CFHTLenS: weak lensing calibrated scaling relations for low-mass clusters of galaxies. *Monthly Notices of the RAS*, 451(2):1460–1481.
- King, I. (1962). The structure of star clusters. I. an empirical density law. *The Astronomical Journal*, 67:471.

- Klein, M., Mohr, J. J., Desai, S., Israel, H., Allam, S., Benoit-Lévy, A., Brooks, D., Buckley-Geer, E., Carnero Rosell, A., Carrasco Kind, M., Cunha, C. E., da Costa, L. N., Dietrich, J. P., Eifler, T. F., Evrard, A. E., Frieman, J., Gruen, D., Gruendl, R. A., Gutierrez, G., Honscheid, K., James, D. J., Kuehn, K., Lima, M., Maia, M. A. G., March, M., Melchior, P., Menanteau, F., Miquel, R., Plazas, A. A., Reil, K., Romer, A. K., Sanchez, E., Santiago, B., Scarpine, V., Schubnell, M., Sevilla-Noarbe, I., Smith, M., Soares-Santos, M., Sobreira, F., Suchyta, E., Swanson, M. E. C., Tarle, G., and DES Collaboration (2018). A multicomponent matched filter cluster confirmation tool for eROSITA: initial application to the RASS and DES-SV data sets. *Monthly Notices of the RAS*, 474(3):3324–3343.
- Kravtsov, A. V., Nagai, D., and Vikhlinin, A. A. (2005). Effects of Cooling and Star Formation on the Baryon Fractions in Clusters. *Astrophysical Journal*, 625:588–598.
- Kravtsov, A. V., Vikhlinin, A., and Nagai, D. (2006). A New Robust Low-Scatter X-Ray Mass Indicator for Clusters of Galaxies. *Astrophysical Journal*, 650:128–136.
- Lau, E. T., Nagai, D., Kravtsov, A. V., Vikhlinin, A., and Zentner, A. R. (2012). Constraining Cluster Physics with the Shape of X-Ray Clusters: Comparison of Local X-Ray Clusters Versus Λ CDM Clusters. *Astrophysical Journal*, 755:116.
- Liedahl, D. A., Osterheld, A. L., and Goldstein, W. H. (1995). New calculations of Fe L-shell X-ray spectra in high-temperature plasmas. *Astrophysical Journal, Letters*, 438:L115–L118.
- Lieu, M., Smith, G. P., Giles, P. A., Ziparo, F., Maughan, B. J., Démoclès, J., Pacaud, F., Pierre, M., Adami, C., Bahé, Y. M., Clerc, N., Chiappetti, L., Eckert, D., Ettori, S., Lavoie, S., Le Fevre, J. P., McCarthy, I. G., Kilbinger, M., Ponman, T. J., Sadibekova, T., and Willis, J. P. (2016). The XXL Survey . IV. Mass-temperature relation of the bright cluster sample. *Astronomy and Astrophysics*, 592:A4.
- Lin, H. W., McDonald, M., Benson, B., and Miller, E. (2015). Cool Core Bias in Sunyaev-Zel'dovich Galaxy Cluster Surveys. *Astrophysical Journal*, 802:34.
- Linde, A. D. (1982). A new inflationary universe scenario: A possible solution of the horizon, flatness, homogeneity, isotropy and primordial monopole problems. *Physics Letters B*, 108(6):389–393.
- Lovisari, L., Forman, W. R., Jones, C., Ettori, S., Andrade-Santos, F., Arnaud, M., Démoclès, J., Pratt, G. W., Randall, S., and Kraft, R. (2017). X-Ray Morphological Analysis of the Planck ESZ Clusters. *Astrophysical Journal*, 846:51.
- Lumb, D. H., Warwick, R. S., Page, M., and De Luca, A. (2002). X-ray background measurements with XMM-Newton EPIC. *Astronomy and Astrophysics*, 389:93–105.
- Macciò, A. V., Dutton, A. A., and van den Bosch, F. C. (2008). Concentration, spin and shape of dark matter haloes as a function of the cosmological model: WMAP1, WMAP3 and WMAP5 results. *Monthly Notices of the RAS*, 391:1940–1954.

- Mahdavi, A., Hoekstra, H., Babul, A., Bildfell, C., Jeltema, T., and Henry, J. P. (2013). Joint Analysis of Cluster Observations. II. Chandra/XMM-Newton X-Ray and Weak Lensing Scaling Relations for a Sample of 50 Rich Clusters of Galaxies. *Astrophysical Journal*, 767:116.
- Mana, A., Giannantonio, T., Weller, J., Hoyle, B., Hütsi, G., and Sartoris, B. (2013). Combining clustering and abundances of galaxy clusters to test cosmology and primordial non-Gaussianity. *Monthly Notices of the RAS*, 434(1):684–695.
- Mantz, A., Allen, S. W., Ebeling, H., Rapetti, D., and Drlica-Wagner, A. (2010). The observed growth of massive galaxy clusters - II. X-ray scaling relations. *Monthly Notices of the RAS*, 406:1773–1795.
- Mantz, A. B., Allen, S. W., Morris, R. G., and von der Linden, A. (2018). Centre-excised X-ray luminosity as an efficient mass proxy for future galaxy cluster surveys. *Monthly Notices of the RAS*, 473:3072–3079.
- Mantz, A. B., Allen, S. W., Morris, R. G., von der Linden, A., Applegate, D. E., Kelly, P. L., Burke, D. L., Donovan, D., and Ebeling, H. (2016). Weighing the giants- V. Galaxy cluster scaling relations. *Monthly Notices of the RAS*, 463:3582–3603.
- Mantz, A. B., von der Linden, A., Allen, S. W., Applegate, D. E., Kelly, P. L., Morris, R. G., Rapetti, D. A., Schmidt, R. W., Adhikari, S., Allen, M. T., Burchat, P. R., Burke, D. L., Cataneo, M., Donovan, D., Ebeling, H., Shand era, S., and Wright, A. (2015). Weighing the giants - IV. Cosmology and neutrino mass. *Monthly Notices of the RAS*, 446(3):2205–2225.
- Markevitch, M. (1998). The L_X -T Relation and Temperature Function for Nearby Clusters Revisited. *Astrophysical Journal*, 504:27–34.
- Massey, R., Hoekstra, H., Kitching, T., Rhodes, J., Cropper, M., Amiaux, J., Harvey, D., Mellier, Y., Meneghetti, M., Miller, L., Paulin-Henriksson, S., Pires, S. r., Scaramella, R., and Schrabback, T. (2013). Origins of weak lensing systematics, and requirements on future instrumentation (or knowledge of instrumentation). *Monthly Notices of the RAS*, 429(1):661–678.
- Maughan, B. J. (2007). The L_X - Y_X Relation: Using Galaxy Cluster X-Ray Luminosity as a Robust, Low-Scatter Mass Proxy. *Astrophysical Journal*, 668:772–780.
- Maughan, B. J., Giles, P. A., Randall, S. W., Jones, C., and Forman, W. R. (2012). Self-similar scaling and evolution in the galaxy cluster X-ray luminosity-temperature relation. *Monthly Notices of the RAS*, 421:1583–1602.
- McDonald, M., Allen, S. W., Bayliss, M., Benson, B. A., Bleem, L. E., Brodwin, M., Bulbul, E., Carlstrom, J. E., Forman, W. R., Hlavacek-Larrondo, J., Garmire, G. P., Gaspari, M., Gladders, M. D., Mantz, A. B., and Murray, S. S. (2017). The Remarkable Similarity of Massive Galaxy Clusters from $z = 0$ to $z = 1.9$. *Astrophysical Journal*, 843(1):28.

- McDonald, M., Benson, B. A., Vikhlinin, A., Stalder, B., Bleem, L. E., de Haan, T., Lin, H. W., Aird, K. A., Ashby, M. L. N., Bautz, M. W., Bayliss, M., Bocquet, S., Brodwin, M., Carlstrom, J. E., Chang, C. L., Cho, H. M., Clocchiatti, A., Crawford, T. M., Crites, A. T., Desai, S., Dobbs, M. A., Dudley, J. P., Foley, R. J., Forman, W. R., George, E. M., Gettings, D., Gladders, M. D., Gonzalez, A. H., Halverson, N. W., High, F. W., Holder, G. P., Holzappel, W. L., Hoover, S., Hrubes, J. D., Jones, C., Joy, M., Keisler, R., Knox, L., Lee, A. T., Leitch, E. M., Liu, J., Lueker, M., Luong-Van, D., Mantz, A., Marrone, D. P., McMahon, J. J., Mehl, J., Meyer, S. S., Miller, E. D., Mocanu, L., Mohr, J. J., Montroy, T. E., Murray, S. S., Nurgaliev, D., Padin, S., Plagge, T., Pryke, C., Reichardt, C. L., Rest, A., Ruel, J., Ruhl, J. E., Saliwanchik, B. R., Saro, A., Sayre, J. T., Schaffer, K. K., Shirokoff, E., Song, J., Šuhada, R., Spieler, H. G., Stanford, S. A., Staniszewski, Z., Stark, A. A., Story, K., van Engelen, A., Vand erlinde, K., Vieira, J. D., Williamson, R., Zahn, O., and Zenteno, A. (2013). The Growth of Cool Cores and Evolution of Cooling Properties in a Sample of 83 Galaxy Clusters at $0.3 < z < 1.2$ Selected from the SPT-SZ Survey. *Astrophysical Journal*, 774(1):23.
- Meidinger, N., Andritschke, R., Bornemann, W., Coutinho, D., Emberger, V., Hälker, O., Kink, W., Mican, B., Müller, S., Pietschner, D., Predehl, P., and Reiffers, J. (2014). Report on the eROSITA camera system. In *Proceedings of the SPIE*, volume 9144 of *Society of Photo-Optical Instrumentation Engineers (SPIE) Conference Series*, page 91441W.
- Meneghetti, M., Rasia, E., Merten, J., Bellagamba, F., Ettori, S., Mazzotta, P., Dolag, K., and Marri, S. (2010). Weighing simulated galaxy clusters using lensing and X-ray. *Astronomy and Astrophysics*, 514:A93.
- Merloni, A., Predehl, P., Becker, W., Böhringer, H., Boller, T., Brunner, H., Brusa, M., Dennerl, K., Freyberg, M., Friedrich, P., Georgakakis, A., Haberl, F., Hasinger, G., Meidinger, N., Mohr, J., Nandra, K., Rau, A., Reiprich, T. H., Robrade, J., Salvato, M., Santangelo, A., Sasaki, M., Schwobe, A., Wilms, J., and German eROSITA Consortium, t. (2012). eROSITA Science Book: Mapping the Structure of the Energetic Universe. *ArXiv e-prints*.
- Mewe, R., Gronenschild, E. H. B. M., and van den Oord, G. H. J. (1985). Calculated X-radiation from optically thin plasmas. V. *Astronomy and Astrophysics, Supplement*, 62:197–254.
- Mewe, R., Lemen, J. R., and van den Oord, G. H. J. (1986). Calculated X-radiation from optically thin plasmas. VI - Improved calculations for continuum emission and approximation formulae for nonrelativistic average Gaunt factors. *Astronomy and Astrophysics, Supplement*, 65:511–536.
- Mirkazemi, M., Finoguenov, A., Pereira, M. J., Tanaka, M., Lerchster, M., Brimiouille, F., Egami, E., Kettula, K., Erfanianfar, G., McCracken, H. J., Mellier, Y., Kneib, J. P., Rykoff, E., Seitz, S., Erben, T., and Taylor, J. E. (2015). Brightest X-Ray Clusters of Galaxies in the CFHTLS Wide Fields: Catalog and Optical Mass Estimator. *Astrophysical Journal*, 799:60.
- Mittal, R., Hicks, A., Reiprich, T. H., and Jaritz, V. (2011). The $L_X - T_{vir}$ relation in galaxy clusters: effects of radiative cooling and AGN heating. *Astronomy and Astrophysics*, 532:A133.

- Mittal, R., Hudson, D. S., Reiprich, T. H., and Clarke, T. (2009). AGN heating and ICM cooling in the HIFLUGCS sample of galaxy clusters. *Astronomy and Astrophysics*, 501:835–850.
- Moscardini, L., Matarrese, S., De Grandi, S., and Lucchin, F. (2000). The correlation function of X-ray galaxy clusters in the ROSAT All-Sky Survey 1 Bright Sample. *Monthly Notices of the RAS*, 314(3):647–656.
- Nagai, D., Kravtsov, A. V., and Vikhlinin, A. (2007). Effects of Galaxy Formation on Thermodynamics of the Intracluster Medium. *Astrophysical Journal*, 668:1–14.
- Navarro, J. F., Frenk, C. S., and White, S. D. M. (1995). Simulations of X-ray clusters. *Monthly Notices of the RAS*, 275:720–740.
- Navarro, J. F., Frenk, C. S., and White, S. D. M. (1996). The Structure of Cold Dark Matter Halos. *Astronomy and Astrophysics*, 462:563.
- Navarro, J. F., Frenk, C. S., and White, S. D. M. (1997). A Universal Density Profile from Hierarchical Clustering. *Astronomy and Astrophysics*, 490:493–508.
- Nelson, K., Lau, E. T., and Nagai, D. (2014). Hydrodynamic Simulation of Non-thermal Pressure Profiles of Galaxy Clusters. *Astrophysical Journal*, 792:25.
- Oh, S., Mulchaey, J. S., Woo, J.-H., Finoguenov, A., Tanaka, M., Cooper, M. C., Ziparo, F., Bauer, F. E., and Matsuoka, K. (2014). The Active Galactic Nucleus Population in X-Ray-selected Galaxy Groups at $0.5 < z < 1.1$. *Astrophysical Journal*, 790(1):43.
- Pacaud, F., Clerc, N., Giles, P. A., Adami, C., Sadibekova, T., Pierre, M., Maughan, B. J., Lieu, M., Le Fèvre, J. P., Alis, S., Altieri, B., Ardila, F., Baldry, I., Benoist, C., Birkinshaw, M., Chiappetti, L., Démoclès, J., Eckert, D., Evrard, A. E., Faccioli, L., Gastaldello, F., Guennou, L., Horellou, C., Iovino, A., Koulouridis, E., Le Brun, V., Lidman, C., Liske, J., Maurogordato, S., Menanteau, F., Owers, M., Poggianti, B., Pomarède, D., Pompei, E., Ponman, T. J., Rapetti, D., Reiprich, T. H., Smith, G. P., Tuffs, R., Valageas, P., Valtchanov, I., Willis, J. P., and Ziparo, F. (2016). The XXL Survey. II. The bright cluster sample: catalogue and luminosity function. *Astronomy and Astrophysics*, 592:A2.
- Pacaud, F., Pierre, M., Adami, C., Altieri, B., Andreon, S., Chiappetti, L., Detal, A., Duc, P.-A., Galaz, G., Gueguen, A., Le Fèvre, J.-P., Hertling, G., Libbrecht, C., Melin, J.-B., Ponman, T. J., Quintana, H., Refregier, A., Sprimont, P.-G., Surdej, J., Valtchanov, I., Willis, J. P., Alloin, D., Birkinshaw, M., Bremer, M. N., Garcet, O., Jean, C., Jones, L. R., Le Fèvre, O., Maccagni, D., Mazure, A., Proust, D., Röttgering, H. J. A., and Trinchieri, G. (2007). The XMM-LSS survey: the Class 1 cluster sample over the initial 5 deg^2 and its cosmological modelling. *Monthly Notices of the RAS*, 382:1289–1308.
- Pacaud, F., Pierre, M., Melin, J.-B., Adami, C., Evrard, A. E., Galli, S., Gastaldello, F., Maughan, B. J., Sereno, M., Alis, S., Altieri, B., Birkinshaw, M., Chiappetti, L., Faccioli, L., Giles, P. A., Horellou, C., Iovino, A., Koulouridis, E., Le Fèvre, J.-P., Lidman, C., Lieu, M., Maurogordato,

- S., Moscardini, L., Poggianti, B. M., Pompei, E., Sadibekova, T., Valtchanov, I., and Willis, J. P. (2018). The XXL Survey XXV. Cosmological analysis of the C1 cluster number counts. *Astronomy and Astrophysics*, 620:A10.
- Pacaud, F., Pierre, M., Refregier, A., Gueguen, A., Starck, J.-L., Valtchanov, I., Read, A. M., Altieri, B., Chiappetti, L., Gandhi, P., Garcet, O., Gosset, E., Ponman, T. J., and Surdej, J. (2006). The XMM Large-Scale Structure survey: the X-ray pipeline and survey selection function. *Monthly Notices of the RAS*, 372:578–590.
- Perlmutter, S., Aldering, G., Boyle, B. J., Castro, P. G., Couch, W. J., Deustua, S., Fabbro, S., Ellis, R. S., Filippenko, A. V., Fruchter, A., Goldhaber, G., Goobar, A., Groom, D. E., Hook, I. M., Irwin, M., Kim, A. G., Kim, M. Y., Knop, R. A., Lee, J. C., Matheson, T., McMahon, R. G., Newberg, H. J. M., Lidman, C., Nugent, P., Nunes, N. J., Pain, R., Panagia, N., Pennypacker, C. R., Quimby, R., Ruiz-Lapuente, P., Schaefer, B., Walton, N., and Supernova Cosmology Project (1998). Measurements of Omega and Lambda from 42 High-Redshift Supernovae. In Paul, J., Montmerle, T., and Aubourg, E., editors, *19th Texas Symposium on Relativistic Astrophysics and Cosmology*, page 146.
- Pierre, M., Chiappetti, L., Pacaud, F., Gueguen, A., Libbrecht, C., Altieri, B., Aussel, H., Gandhi, P., Garcet, O., Gosset, E., Païoro, L., Ponman, T. J., Read, A. M., Refregier, A., Starck, J.-L., Surdej, J., Valtchanov, I., Adami, C., Alloin, D., Alshino, A., Andreon, S., Birkinshaw, M., Bremer, M., Detal, A., Duc, P.-A., Galaz, G., Jones, L., Le Fèvre, J.-P., Le Fèvre, O., Maccagni, D., Mazure, A., Quintana, H., Röttgering, H. J. A., Sprimont, P.-G., Tasse, C., Trinchieri, G., and Willis, J. P. (2007). The XMM-Large Scale Structure catalogue: X-ray sources and associated optical data. Version I. *Monthly Notices of the RAS*, 382:279–290.
- Piffaretti, R., Arnaud, M., Pratt, G. W., Pointecouteau, E., and Melin, J.-B. (2011). The MCXC: a meta-catalogue of x-ray detected clusters of galaxies. *Astronomy and Astrophysics*, 534:A109.
- Pillepich, A., Porciani, C., and Reiprich, T. H. (2012). The X-ray cluster survey with eRosita: forecasts for cosmology, cluster physics and primordial non-Gaussianity. *Monthly Notices of the RAS*, 422:44–69.
- Planck Collaboration, Ade, P. A. R., Aghanim, N., Arnaud, M., Ashdown, M., Aumont, J., Baccigalupi, C., Banday, A. J., Barreiro, R. B., Barrena, R., and et al. (2016). Planck 2015 results. XXVII. The second Planck catalogue of Sunyaev-Zeldovich sources. *Astronomy and Astrophysics*, 594:A27.
- Planck Collaboration, Aghanim, N., Akrami, Y., Ashdown, M., Aumont, J., Baccigalupi, C., Ballardini, M., Banday, A. J., Barreiro, R. B., Bartolo, N., Basak, S., Battye, R., Benabed, K., Bernard, J.-P., Bersanelli, M., Bielewicz, P., Bock, J. J., Bond, J. R., Borrill, J., Bouchet, F. R., Boulanger, F., Bucher, M., Burigana, C., Butler, R. C., Calabrese, E., Cardoso, J.-F., Carron, J., Challinor, A., Chiang, H. C., Chluba, J., Colombo, L. P. L., Combet, C., Contreras, D., Crill, B. P., Cuttaia, F., de Bernardis, P., de Zotti, G., Delabrouille, J., Delouis, J.-M., Di

- Valentino, E., Diego, J. M., Doré, O., Douspis, M., Ducout, A., Dupac, X., Dusini, S., Efstathiou, G., Elsner, F., Enßlin, T. A., Eriksen, H. K., Fantaye, Y., Farhang, M., Fergusson, J., Fernandez-Cobos, R., Finelli, F., Forastieri, F., Frailis, M., Franceschi, E., Frolov, A., Galeotta, S., Galli, S., Ganga, K., Génova-Santos, R. T., Gerbino, M., Ghosh, T., González-Nuevo, J., Górski, K. M., Gratton, S., Gruppuso, A., Gudmundsson, J. E., Hamann, J., Handley, W., Herranz, D., Hivon, E., Huang, Z., Jaffe, A. H., Jones, W. C., Karakci, A., Keihänen, E., Keskitalo, R., Kiiveri, K., Kim, J., Kisner, T. S., Knox, L., Krachmalnicoff, N., Kunz, M., Kurki-Suonio, H., Lagache, G., Lamarre, J.-M., Lasenby, A., Lattanzi, M., Lawrence, C. R., Le Jeune, M., Lemos, P., Lesgourgues, J., Levrier, F., Lewis, A., Liguori, M., Lilje, P. B., Lilley, M., Lindholm, V., López-Cañiego, M., Lubin, P. M., Ma, Y.-Z., Macías-Pérez, J. F., Maggio, G., Maino, D., Mandolesi, N., Mangilli, A., Marcos-Caballero, A., Maris, M., Martin, P. G., Martinelli, M., Martínez-González, E., Matarrese, S., Mauri, N., McEwen, J. D., Meinhold, P. R., Melchiorri, A., Mennella, A., Migliaccio, M., Millea, M., Mitra, S., Miville-Deschênes, M.-A., Molinari, D., Montier, L., Morgante, G., Moss, A., Natoli, P., Nørgaard-Nielsen, H. U., Pagano, L., Paoletti, D., Partridge, B., Patanchon, G., Peiris, H. V., Perrotta, F., Pettorino, V., Piacentini, F., Polastri, L., Polenta, G., Puget, J.-L., Rachen, J. P., Reinecke, M., Remazeilles, M., Renzi, A., Rocha, G., Rosset, C., Roudier, G., Rubiño-Martín, J. A., Ruiz-Granados, B., Salvati, L., Sandri, M., Savelainen, M., Scott, D., Shellard, E. P. S., Sirignano, C., Sirri, G., Spencer, L. D., Sunyaev, R., Suur-Uski, A.-S., Tauber, J. A., Tavagnacco, D., Tenti, M., Toffolatti, L., Tomasi, M., Trombetti, T., Valenziano, L., Valiviita, J., Van Tent, B., Vibert, L., Vielva, P., Villa, F., Vittorio, N., Wandelt, B. D., Wehus, I. K., White, M., White, S. D. M., Zacchei, A., and Zonca, A. (2018). Planck 2018 results. VI. Cosmological parameters. *arXiv e-prints*.
- Pointecouteau, E., Arnaud, M., and Pratt, G. W. (2005). The structural and scaling properties of nearby galaxy clusters. I. The universal mass profile. *Astronomy and Astrophysics*, 435(1):1–7.
- Ponman, T. J., Bourner, P. D. J., Ebeling, H., and Böhringer, H. (1996). A ROSAT survey of Hickson’s compact galaxy groups. *Monthly Notices of the RAS*, 283:690–708.
- Pratt, G. W., Croston, J. H., Arnaud, M., and Böhringer, H. (2009). Galaxy cluster X-ray luminosity scaling relations from a representative local sample (REXCESS). *Astronomy and Astrophysics*, 498:361–378.
- Predehl, P., Andritschke, R., Böhringer, H., Bornemann, W., Bräuninger, H., Brunner, H., Brusa, M., Burkert, W., Burwitz, V., Cappelluti, N., Churazov, E., Dennerl, K., Eder, J., Elbs, J., Freyberg, M., Friedrich, P., Fürmetz, M., Gaida, R., Hälker, O., Hartner, G., Hasinger, G., Hermann, S., Huber, H., Kendziorra, E., von Kienlin, A., Kink, W., Kreykenbohm, I., Lamer, G., Lapchov, I., Lehmann, K., Meidinger, N., Mican, B., Mohr, J., Mühlegger, M., Müller, S., Nandra, K., Pavlinsky, M., Pfeffermann, E., Reiprich, T., Robrade, J., Rohé, C., Santangelo, A., Schächner, G., Schanz, T., Schmid, C., Schmitt, J., Schreib, R., Schrey, F., Schwobe, A., Steinmetz, M., Strüder, L., Sunyaev, R., Tenzer, C., Tiedemann, L., Vongehr, M., and Wilms, J. (2010). eROSITA on SRG. In *Space Telescopes and Instrumentation 2010: Ultraviolet to Gamma Ray*, volume 7732 of *Proceedings of the SPIE*, page 77320U.

- Predehl, P., Bornemann, W., Bräuninger, H., Brunner, H., Burwitz, V., Coutinho, D., Dennerl, K., Eder, J., Friedrich, P., Fürmetz, M., Hartner, G., von Kienlin, A., Kink, W., Meidinger, N., Mican, B., Müller, S., Nandra, K., Pfeffermann, E., Rohé, C., and Yaroshenko, V. (2018). eROSITA mated with SRG. In *Space Telescopes and Instrumentation 2018: Ultraviolet to Gamma Ray*, volume 10699 of *Society of Photo-Optical Instrumentation Engineers (SPIE) Conference Series*, page 106995H.
- Reed, D., Gardner, J., Quinn, T., Stadel, J., Fardal, M., Lake, G., and Governato, F. (2003). Evolution of the mass function of dark matter haloes. *Monthly Notices of the RAS*, 346(2):565–572.
- Reed, D. S., Bower, R., Frenk, C. S., Jenkins, A., and Theuns, T. (2007). The halo mass function from the dark ages through the present day. *Monthly Notices of the RAS*, 374(1):2–15.
- Refregier, A. (2003). Shapelets - I. A method for image analysis. *Monthly Notices of the RAS*, 338:35–47.
- Reichert, A., Böhringer, H., Fassbender, R., and Mühlegger, M. (2011). Observational constraints on the redshift evolution of X-ray scaling relations of galaxy clusters out to $z \sim 1.5$. *Astronomy and Astrophysics*, 535:A4.
- Reiprich, T. H., Basu, K., Ettori, S., Israel, H., Lovisari, L., Molendi, S., Pointecouteau, E., and Roncarelli, M. (2013). Outskirts of Galaxy Clusters. *Space Science Reviews*, 177:195–245.
- Reiprich, T. H. and Böhringer, H. (2002). The Mass Function of an X-Ray Flux-limited Sample of Galaxy Clusters. *Astrophysical Journal*, 567:716–740.
- Riess, A. G., Filippenko, A. V., Challis, P., Clocchiatti, A., Diercks, A., Garnavich, P. M., Gilliland, R. L., Hogan, C. J., Jha, S., Kirshner, R. P., Leibundgut, B., Phillips, M. M., Reiss, D., Schmidt, B. P., Schommer, R. A., Smith, R. C., Spyromilio, J., Stubbs, C., Suntzeff, N. B., and Tonry, J. (1998). Observational Evidence from Supernovae for an Accelerating Universe and a Cosmological Constant. *Astronomical Journal*, 116:1009–1038.
- Robertson, H. P. (1935). Kinematics and World-Structure. *Astrophysical Journal*, 82:284.
- Rossetti, M., Gastaldello, F., Eckert, D., Della Torre, M., Pantiri, G., Cazzoletti, P., and Molendi, S. (2017). The cool-core state of Planck SZ-selected clusters versus X-ray-selected samples: evidence for cool-core bias. *Monthly Notices of the RAS*, 468:1917–1930.
- Rossetti, M., Gastaldello, F., Ferioli, G., Bersanelli, M., De Grandi, S., Eckert, D., Ghizzardi, S., Maino, D., and Molendi, S. (2016). Measuring the dynamical state of Planck SZ-selected clusters: X-ray peak - BCG offset. *Monthly Notices of the RAS*, 457:4515–4524.
- Sanders, J. S., Fabian, A. C., Russell, H. R., and Walker, S. A. (2018). Hydrostatic Chandra X-ray analysis of SPT-selected galaxy clusters - I. Evolution of profiles and core properties. *Monthly Notices of the RAS*, 474(1):1065–1098.

- Sanderson, A. J. R., Ponman, T. J., and O'Sullivan, E. (2006). A statistically selected Chandra sample of 20 galaxy clusters - I. Temperature and cooling time profiles. *Monthly Notices of the RAS*, 372:1496–1508.
- Santos, J. S., Rosati, P., Tozzi, P., Böhringer, H., Ettori, S., and Bignamini, A. (2008). Searching for cool core clusters at high redshift. *Astronomy and Astrophysics*, 483:35–47.
- Sarazin, C. L. (1986). X-ray emission from clusters of galaxies. *Reviews of Modern Physics*, 58(1):1–115.
- Schellenberger, G. and Reiprich, T. H. (2017). HICOSMO - cosmology with a complete sample of galaxy clusters - I. Data analysis, sample selection and luminosity-mass scaling relation. *Monthly Notices of the RAS*, 469:3738–3761.
- Schneider, P., Ehlers, J., Falco, E. E., and Bleyer, U. (1993). Book-Review - Gravitational Lenses. *Astronomische Nachrichten*, 314(4):314.
- Sharp, N. A. (1986). The whole-sky distribution of galaxies. *Publications of the ASP*, 98:740–754.
- Sheth, R. K. and Tormen, G. (1999). Large-scale bias and the peak background split. *Monthly Notices of the RAS*, 308(1):119–126.
- Slezak, E., Bijaoui, A., and Mars, G. (1990). Identification of structures from galaxy counts : use of the wavelet transform. *Astronomy and Astrophysics*, 227:301–316.
- Slezak, E., Durret, F., and Gerbal, D. (1994). A Wavelet Analysis Search for Substructures in Eleven X-Ray Clusters of Galaxies. *Astronomical Journal*, 108:1996.
- Smith, G. P., Mazzotta, P., Okabe, N., Ziparo, F., Mulroy, S. L., Babul, A., Finoguenov, A., McCarthy, I. G., Lieu, M., Bahé, Y. M., Bourdin, H., Evrard, A. E., Futamase, T., Haines, C. P., Jauzac, M., Marrone, D. P., Martino, R., May, P. E., Taylor, J. E., and Umetsu, K. (2016). LoCuSS: Testing hydrostatic equilibrium in galaxy clusters. *Monthly Notices of the RAS*, 456(1):L74–L78.
- Snowden, S. L., McCammon, D., Burrows, D. N., and Mendenhall, J. A. (1994). Analysis procedures for ROSAT XRT/PSPC observations of extended objects and the diffuse background. *Astrophysical Journal*, 424:714–728.
- Springel, V., Frenk, C. S., and White, S. D. M. (2006). The large-scale structure of the Universe. *Nature*, 440(7088):1137–1144.
- Springel, V., White, S. D. M., Jenkins, A., Frenk, C. S., Yoshida, N., Gao, L., Navarro, J., Thacker, R., Croton, D., Helly, J., Peacock, J. A., Cole, S., Thomas, P., Couchman, H., Evrard, A., Colberg, J., and Pearce, F. (2005). Simulations of the formation, evolution and clustering of galaxies and quasars. *Nature*, 435(7042):629–636.

- Starck, J. L. and Bijaoui, A. (1991). Filtering and Restoration with the Wavelet Transform. In Grosbøl, P. J. and Warmels, R. H., editors, *European Southern Observatory Conference and Workshop Proceedings*, volume 38 of *European Southern Observatory Conference and Workshop Proceedings*, page 17.
- Starck, J.-L. and Murtagh, F. (2006). *Astronomical Image and Data Analysis*.
- Starck, J.-L. and Pierre, M. (1998). Structure detection in low intensity X-ray images. *Astronomy and Astrophysics, Supplement*, 128:397–407.
- Sunyaev, R. A. and Zeldovich, Y. B. (1972). The Observations of Relic Radiation as a Test of the Nature of X-Ray Radiation from the Clusters of Galaxies. *Comments on Astrophysics and Space Physics*, 4:173.
- Tenzer, C., Warth, G., Kendziorra, E., and Santangelo, A. (2010). Geant4 simulation studies of the eROSITA detector background. In *High Energy, Optical, and Infrared Detectors for Astronomy IV*, volume 7742 of *Proceedings of the SPIE*, page 77420Y.
- Tinker, J., Kravtsov, A. V., Klypin, A., Abazajian, K., Warren, M., Yepes, G., Gottlöber, S., and Holz, D. E. (2008). Toward a Halo Mass Function for Precision Cosmology: The Limits of Universality. *Astrophysical Journal*, 688:709–728.
- Truemper, J. (1982). The ROSAT mission. *Advances in Space Research*, 2:241–249.
- Valtchanov, I., Pierre, M., and Gastaud, R. (2001). Comparison of source detection procedures for XMM-Newton images. *Astronomy and Astrophysics*, 370:689–706.
- VanderPlas, J. (2016). *Python Data Science Handbook: Essential Tools for Working with Data*. O'Reilly Media, Inc., 1st edition.
- Vikhlinin, A., Burenin, R., Forman, W. R., Jones, C., Hornstrup, A., Murray, S. S., and Quintana, H. (2007). Lack of Cooling Flow Clusters at $z \lesssim 0.5$. In Böhringer, H., Pratt, G. W., Finoguenov, A., and Schuecker, P., editors, *Heating versus Cooling in Galaxies and Clusters of Galaxies*, page 48.
- Vikhlinin, A., Burenin, R. A., Ebeling, H., Forman, W. R., Hornstrup, A., Jones, C., Kravtsov, A. V., Murray, S. S., Nagai, D., Quintana, H., and Voevodkin, A. (2009a). Chandra Cluster Cosmology Project. II. Samples and X-Ray Data Reduction. *Astrophysical Journal*, 692:1033–1059.
- Vikhlinin, A., Forman, W., and Jones, C. (1999). Outer Regions of the Cluster Gaseous Atmospheres. *Astrophysical Journal*, 525:47–57.
- Vikhlinin, A., Forman, W., Jones, C., and Murray, S. (1995). Matched Filter Source Detection Applied to the ROSAT PSPC and the Determination of the Number-Flux Relation. *Astrophysical Journal*, 451:542.

- Vikhlinin, A., Kravtsov, A. V., Burenin, R. A., Ebeling, H., Forman, W. R., Hornstrup, A., Jones, C., Murray, S. S., Nagai, D., Quintana, H., and Voevodkin, A. (2009b). Chandra Cluster Cosmology Project III: Cosmological Parameter Constraints. *Astrophysical Journal*, 692:1060–1074.
- Vikhlinin, A., McNamara, B. R., Forman, W., Jones, C., Quintana, H., and Hornstrup, A. (1998). A Catalog of 200 Galaxy Clusters Serendipitously Detected in the ROSAT PSPC Pointed Observations. *Astrophysical Journal*, 502:558–581.
- Voges, W., Aschenbach, B., Boller, T., Bräuninger, H., Briel, U., Burkert, W., Dennerl, K., Englhauser, J., Gruber, R., Haberl, F., Hartner, G., Hasinger, G., Kürster, M., Pfeffermann, E., Pietsch, W., Predehl, P., Rosso, C., Schmitt, J. H. M. M., Trümper, J., and Zimmermann, H. U. (1999). The ROSAT all-sky survey bright source catalogue. *Astronomy and Astrophysics*, 349:389–405.
- Voit, G. M. (2005). Expectations for evolution of cluster scaling relations. *Advances in Space Research*, 36(4):701–705.
- Walker, A. G. (1935). On the formal comparison of Milne’s kinematical system with the systems of general relativity. *Monthly Notices of the RAS*, 95:263–269.
- Warren, M. S., Abazajian, K., Holz, D. E., and Teodoro, L. (2006). Precision Determination of the Mass Function of Dark Matter Halos. *Astrophysical Journal*, 646(2):881–885.
- Watson, W. A., Iliev, I. T., D’Aloisio, A., Knebe, A., Shapiro, P. R., and Yepes, G. (2013). The halo mass function through the cosmic ages. *Monthly Notices of the RAS*, 433(2):1230–1245.
- Willingale, R., Starling, R. L. C., Beardmore, A. P., Tanvir, N. R., and O’Brien, P. T. (2013). Calibration of X-ray absorption in our Galaxy. *Monthly Notices of the RAS*, 431:394–404.
- Wolter, H. (1952). Spiegelsysteme streifenden Einfalls als abbildende Optiken für Röntgenstrahlen. *Annalen der Physik*, 445:94–114.
- Zhang, Y.-Y., Finoguenov, A., Böhringer, H., Kneib, J.-P., Smith, G. P., Czoske, O., and Soucail, G. (2007). Scaling relations and mass calibration of the X-ray luminous galaxy clusters at redshift ~ 0.2 : XMM-Newton observations. *Astronomy and Astrophysics*, 467:437–457.
- Zhang, Y.-Y., Finoguenov, A., Böhringer, H., Kneib, J.-P., Smith, G. P., Kneissl, R., Okabe, N., and Dahle, H. (2008). LoCuSS: comparison of observed X-ray and lensing galaxy cluster scaling relations with simulations. *Astronomy and Astrophysics*, 482:451–472.
- Zwicky, F. (1933). Die Rotverschiebung von extragalaktischen Nebeln. *Helvetica Physica Acta*, 6:110–127.
- Zwicky, F. (1937). On the Masses of Nebulae and of Clusters of Nebulae. *Astrophysical Journal*, 86:217.

Acknowledgements

I would like to express my deepest gratitude to my supervisors Prof. Dr. Alexis Finoguenov and Dr. Jeremy S. Sanders for their consistent guidance and support during my PhD. I am grateful for the assistance and encouragement of Dr. Dominique Eckert. I thank my official supervisor, Prof. Dr. Kirpal Nandra, and his outstanding secretary, Birgit Boller, for giving me the opportunity to work on this interesting research project and for providing valuable resources. I also thank the remaining co-authors of my publications Dr. Nicolas Clerc, Prof. Dr. Thomas H. Reiprich, Dr. Miriam E. Ramos-Ceja, and Dr. Vittorio Ghirardini for their constructive comments and advice. Additionally, I would like to thank the remaining committee members Prof. Dr. Jochen Weller, PD Dr. Klaus Dolag, Prof. Dr. Thomas Kuhr, and Prof. Dr. Tilman Birnstiel. Thank you to Dr. Esra Bulbul for giving me the opportunity to work on a project including actual eROSITA data. I thank all remaining personal of the High-Energy Astrophysics group and the members of the eROSITA consortium for their support over the last 3.5 years, in particular Dr. Johan Comparat, Dr. Hermann Brunner, Dr. Matthias Klein, Dr. Johannes Buchner, and Dr. J. Michael Burgess.

I would like to express a special thanks to Linda Baronchelli, Shweta Agarwal-Eames, and Alejandra Fresco for all the fun times and for being the best office mates. I am deeply thankful for the support and encouragement of my girlfriend Maria and the help of my family that got me to this point. I thank Fauli for the consistent inspiration.

This research was made possible by the International Max Planck Research School on Astrophysics at the Ludwig-Maximilians University Munich, as well as their funding received from the Max-Planck Society.

The simulated eROSITA data shown here were processed using the eSASS software system developed by the German eROSITA consortium. This research has made use of NASA's Astrophysics Data System. This research has made use of SAOImage DS9, developed by Smithsonian Astrophysical Observatory. I have made use of the ROSAT Data Archive of the Max-Planck-Institut für extraterrestrische Physik (MPE) at Garching, Germany.

Reproduced with permission from Astronomy & Astrophysics, © ESO.